LOWER EXTREMITY BIOMECHANICAL RESPONSE OF FEMALE AND MALE POST-MORTEM HUMAN SURROGATES TO HIGH-RATE VERTICAL LOADING DURING SIMULATED UNDER-BODY BLAST EVENTS

Danielle Marie Cristino

Dissertation submitted to the faculty of the Virginia Polytechnic Institute and State University in partial fulfillment of the requirements for the degree of

Doctor of Philosophy
In
Biomedical Engineering

Warren N. Hardy, Chair
John H. Bolte IV
John M. Cavanaugh
Kerry A. Danelson
Andrew R. Kemper

December 13, 2018
Blacksburg, VA

Keywords: Under-Body Blast, Biomechanics, Lower Extremity, Cadaver, Injury

LOWER EXTREMITY BIOMECHANICAL RESPONSE OF FEMALE AND MALE POST-MORTEM HUMAN SURROGATES TO HIGH-RATE VERTICAL LOADING DURING SIMULATED UNDER-BODY BLAST EVENTS

Danielle Marie Cristino

ABSTRACT

During an under-body blast (UBB) event, an improvised explosive device (IED) delivers a high-energy blast beneath a military vehicle, exposing mounted Warfighters to considerable risk of severe lower extremity injuries. Loftis and Gillich (2014) determined that the lower leg and ankle region is the most common body region to sustain skeletal injury in military mounted combat events, comprising twenty-one percent of cases reported in the Joint Trauma Analysis and Prevention of Injuries in Combat (JTAPIC) database between 2010 and 2012. Injuries of the lower extremity are not always life-threatening. However, from a survivability standpoint, these injuries may affect the ability of the Warfighter to self-extricate and ambulate in the immediate aftermath of an UBB event. In addition, lower extremity injuries can lead to long term health complications and reduced quality of life (Dischinger et al., 2004). While some comparisons can be drawn from the study of civilian automotive crashes; the impact level, rate, location, and directions in UBB are fundamentally different for the lower extremity. Therefore, substantial research efforts to characterize and assess injuries unique to UBB are essential. The Warrior Injury Assessment Manikin (WIAMan), the Tech Demonstrator version of which was introduced by Pietsch et al. (2016), is the only anthropomorphic test device (ATD) designed to evaluate injury patterns in UBB conditions. However, there are no known injury assessment tools for the female Warfighter at this time. The overarching goal of this research effort is to determine the origin of potential differences in the response of females and males in UBB conditions. The results of this work contribute to the body of research concerning high-rate axial loading of the lower extremity and form the first detailed biomechanical account of UBB effects on female PMHS. This work will inform future decisions regarding the requirements for a valid injury assessment capability for female Warfighters in the UBB environment and the subsequent research needed to support those requirements. Ultimately, advancements can be made in modeling and simulation capabilities, injury assessment criteria, test methodologies, and design approaches for safer military ground vehicles and personal protective equipment (PPE). Improvements in these technologies will reduce morbidity and mortality rates among the U.S. Warfighter population, both male and female.

LOWER EXTREMITY BIOMECHANICAL RESPONSE OF FEMALE AND MALE POST-MORTEM HUMAN SURROGATES TO HIGH-RATE VERTICAL LOADING DURING SIMULATED UNDER-BODY BLAST EVENTS

Danielle Marie Cristino

GENERAL AUDIENCE ABSTRACT

During an under-body blast (UBB) event, an improvised explosive device (IED) delivers a high-energy blast beneath a military vehicle. Energy from the explosive is imparted to the occupants primarily through the floor and seats of the vehicle, exposing the occupants to considerable risk of injuries to the lower extremity. Compared to civilian automotive crashes, the lower extremities of occupants in UBB scenarios are exposed to greater forces, applied at higher rates, and in different locations and directions. To improve current vehicle systems and personal protective equipment (PPE), it is crucial to develop tools to evaluate injuries in UBB scenarios. One such tool is a test dummy, which is designed to quantify loads, deflections, and accelerations experienced by occupants during a crash. These measured values are compared to accepted thresholds, above which injury is likely to occur. The Warrior Injury Assessment Manikin (WIAMan), which is representative of the 50th-percentile male, is the only test dummy designed to evaluate injuries in UBB conditions. However, there are no known injury assessment tools for the female Warfighter at this time. The overarching goal of this research effort is to determine the origin of potential differences in the response of females and males in UBB conditions. The results of this work contribute to the body of research concerning high-rate axial loading of the lower extremity and form the first detailed biomechanical account of UBB effects on female post-mortem human surrogates (PMHS). The results will inform the development of injury assessment tools for female Warfighters, which will ultimately lead to improvements in technologies to reduce morbidity and mortality rates among the U.S. Warfighter population, both male and female.

This dissertation is dedicated to the memory of my beloved grandfathers:

Angelo A. Cristino

A Navy Veteran of World War II

&

Willis H. Merritt II

An Army Veteran of the Korean War

Whose tenacity, wisdom, and kind hearts I aspire to emulate in my lifetime.

ACKNOWLEDGMENTS

I am thankful for the guidance of my adviser, Warren Hardy, whose experience and insights had a profound impact on my growth as a graduate student. I am also thankful for the mentorship provided by my committee members: John Bolte, John Cavanaugh, Kerry Danelson, and Andrew Kemper. I am especially appreciative of H. Clay Gabler, who introduced me to injury biomechanics and inspired me to pursue a degree in biomedical engineering.

This work was funded through the WIAMan Engineering Office of the Army Research Laboratory (ARL) under Award Number W911NF-14-2-0023. I am particularly thankful for the contributions of Jason Tice, Patricia Frounfelker, Aaron Alai, and Joshua Crookshanks. I sincerely appreciate all who have assisted in conducting the research in this dissertation, including Hollie Pietsch, Joshua McNeil, Elizabeth McNeil, Meghan Howes, Allison Guettler, Laura Watkins, Amanda Agnew, Rakshit Ramachandra, Skyler Singh, David Stark, Matthew Mason, David Mellichamp, Craig McNally, Paul Benedetto, and Nicholas Schultz.

In addition, I gratefully acknowledge the anatomical donors and their families, whose generosity made it possible to conduct the research in this dissertation and contribute to the protection of military service personnel.

I am incredibly thankful for the wonderful friendships I have developed over the past few years. My time in Blacksburg was greatly enriched by having such compassionate and uplifting friends. I am especially thankful for the endless support and comedic relief provided by Devon Albert and Amnah Eltahir.

Finally, I am truly grateful for the continuous encouragement provided by my family. Mom, Dad, and Stephanie – although Blacksburg is far from home, the feeling of your love and support has always been right here with me. Each of you supplied immeasurable motivation and wisdom as I navigated through this chapter of my life.

TABLE OF CONTENTS

LIST OF FIGURES

LIST OF TABLES

CHAPTER 1

INTRODUCTION TO UNDER-BODY BLAST

During an under-body blast (UBB) event, an improvised explosive device (IED) delivers a high-energy blast beneath a military vehicle, exposing mounted Warfighters to considerable risk of severe lower extremity injuries. A recent study revealed that the lower leg and ankle region is the most common body region to sustain skeletal injury in military mounted combat events, comprising twenty-one percent of cases reported in the Joint Trauma Analysis and Prevention of Injuries in Combat (JTAPIC) database between 2010 and 2012 (Loftis and Gillich, 2014). Substantial research to characterize these injuries is essential in the effort to reduce morbidity and mortality rates among the U.S. Warfighter population. This chapter provides background information pertaining to UBB and the associated lower extremity injuries. The objectives of the current study are presented at the conclusion of this chapter.

Blast Physics and Injury Types

Triggering a mine initiates a high-rate, explosive chemical reaction. The resulting shockwave and subsequent expansion of gas mobilize detonation products and "soil ejecta" (Ramasamy et al., 2009). During UBB, kinetic energy is transferred to the target vehicle predominantly through the high-speed flow of these particulates, which can become entrapped beneath the vehicle (Cimpoeru et al., 2017). This can cause local deformation and rupture of the vehicle hull, as well as global acceleration of the vehicle. If the vehicle is displaced vertically, a secondary impact with the ground ensues. The nature of the loading on vehicle occupants during UBB is influenced by a number of factors. These include the characteristics of the explosive, such as charge shape, charge size, casing material, burial depth, and standoff; the surrounding environment, namely soil conditions and nearby structures; and the shape and material properties of the vehicle interior and exterior.

Blast injuries are categorized into five groups. Primary blast injuries are caused by direct interaction between the high pressure blast wave and tissues of the body. Common examples include tympanic membrane rupture, blast lung, eye injuries, and concussion (Champion et al.,

2009). Isolated injuries to the extremities from blast waves are rare (Bieler et al., 2011). Secondary blast injuries are inflicted by airborne fragments and can include penetrating injuries, traumatic amputations, lacerations, fractures, and concussions. Tertiary blast injuries result from interaction between the occupants and the vehicle interior. These can include blunt injuries, crush syndrome, and compartment syndrome (Champion et al., 2009). Quaternary blast injuries include burns and inhalation injuries that result from heat or chemicals, while quinary blast injuries include toxic reactions caused by infectious, chemical, or radioactive substances (Bieler et al., 2011).

Primary blast injuries are not usually seen in under-body blast scenarios, since much of the energy from the initial pressure wave is reflected at the interface between the soil and air or diminished by the vehicle structure (Ramasamy et al., 2009). However, primary blast injuries are more likely to occur when there is a breach in the vehicle hull. The associated ingress of blast pressure, detonation products, soil ejecta, and/or debris from the rupture may interact with the occupants and cause both primary and secondary blast injuries. Given its complexity, floor rupture is considered out of scope for the research presented in this dissertation.

Tertiary blast injuries of the lower extremities are sustained in a number of ways during UBB. The encroaching floor can apply an axial load to the lower extremities. In addition, floor deflection and global vehicle displacement can lead to subsequent impacts between inadequately restrained lower extremities and the vehicle interior. If seatbelts are not used, the occupants may incur injuries from secondary impacts within the vehicle or ejection from the vehicle. In addition, loose cargo or equipment within the vehicle may strike and injure occupants.

The injuries under investigation in the current study include those induced by direct interaction between the vehicle interior (floor and seat) and the occupants, which are categorized as tertiary injuries. This study does not explore additional tertiary injuries caused by improper use of restraints, interaction with vehicle cargo and equipment, or secondary impacts with the ground. All other blast injury types are out of scope for the current study.

In-Theater Data

Data from the Joint Theater Trauma Registry (JTTR) show that between October 2001 and January 2005, 1,566 combatants sustained 6,609 wounds as a result of enemy action during Operation Iraqi Freedom (OIF) and Operation Enduring Freedom (OEF) (Owens et al., 2008). Lower extremity fractures comprised 50% (454) of the 915 extremity fractures reported in the dataset (Owens et al., 2007). The distribution of fractures to the lower extremity included 123 to the femur, 218 to the leg, and 113 to the feet. Open fractures comprised 80% (366) of the lower extremity fractures. Within this dataset, 1,146 wounded combatants sustained injuries due to explosions (i.e. IED, landmine, mortar, bomb, or grenade). IEDs were the most common injury mechanism in this category, injuring 558 combatants.

Dougherty et al. (2009) reported that 37.1% of the patients treated at Navy-Marine Corps facilities in Iraq between September 2004 and February 2005 sustained extremity wounds due to IEDs. This dataset, which was provided by the United States Navy-Marine Corps Combat Trauma Registry (CTR), included 935 combat casualties, 3,218 injuries, 166 lower extremity fractures, and 22 lower extremity amputations. With respect to extremity injuries in general, including both the upper and lower extremities, the distribution of injuries to the lower extremity included 5.1% to the upper leg and thigh, 12.2% to the leg and ankle, and 11.4% to the feet and toes.

Vasquez et al. (2018) examined injury data from mounted UBB events that occurred in OIF and OEF between 2007 and 2010. In a dataset of 555 service members with a total of 3,844 injuries, the fracture/dislocation category was the most frequent injury type in both wounded in action (WIA) and killed in action (KIA) casualties. Foot/ankle injuries were the most prevalent in the WIA casualties with 33% of individuals sustaining injuries to this region.

A more recent analysis of combat explosion episodes cited 5,091 episodes involving 4,774 male service personnel (Eskridge et al., 2012). IEDs were the predominant explosion mechanism, causing 78% of the episodes recorded in the Expeditionary Medical Encounter Database (EMED) between March 2004 and December 2007. The most frequently injured body region was the extremities (41.3%). In addition, 488 lower leg/ankle fractures and 275 foot/toe fractures were reported.

The severe and multilevel injuries to the lower extremity from blast have led to a greater incidence of lower extremity amputation. Between October 2001 and June 2008, there were over 1,100 major limb amputations of U.S. Soldiers (Tintle et al., 2010). In a study of JTTR records of UK Service Personnel who sustained calcaneal fractures from vehicle explosions between January 2006 and December 2008, 18 of 40 calcaneus fractures required amputations (Ramasamy, 2011). Eleven were performed immediately, three occurred after further surgical debridement, and four were performed due to chronic pain.

To inform efforts to mitigate UBB injuries, Alvarez (2011) presented a case study of 608 casualties reported in the JTAPIC database. Within this dataset, 456 casualties were WIA, with 1,637 total coded injuries, while 152 casualties were KIA, with 2,912 coded injuries. Fractures comprised 53% of the WIA injuries and 53% of the KIA injuries. In the WIA category, 7% of the casualties sustained fractures to the femur, 18% to the tibia and fibula, and 26% to the foot and ankle. In the KIA injury category, 33% of the casualties sustained fractures to the femur, 32% to the tibia and fibula, and 32% to the foot and ankle. While this epidemiological study provided a crucial overview of injuries sustained during UBB events at the time, it did not provide detailed information regarding injury mechanisms.

A recent study by Danelson et al. (2018) provided a thorough description of the frequency, severity, and mechanisms of injuries sustained by mounted Warfighters in UBB attacks. The dataset was compiled by screening cases reported in the Joint Trauma Analysis and Prevention of Injuries in Combat (JTAPIC) database by vehicle type, event charge weight, and injury severity level. Events that were characterized by damage levels greater than those produced in the UBB testing environment were excluded. In contrast to the Alvarez study, which included both WIA and KIA occupants, the selection criteria for Danelson et al. resulted in a dataset of WIA occupants only. While the Alvarez study reported that 18% of the WIA occupants sustained injuries of the tibia and fibula, and 26% of the foot and ankle, Danelson et al. reported that fractures of the foot, ankle, or leg were sustained by 79% of occupants. In addition, the lower extremities were identified as the most severely injured body region for 53% of the occupants. Danelson et al. also reported the proportion of occupants who sustained fractures to various locations of the lower extremity: 46% to the tibia diaphysis, 40% to the calcaneus, 37% to the forefoot, 25% to the distal tibia, 21%

to the fibula diaphysis, 21% to the midfoot, 19% to the talus, 13% to the distal fibula, and 8% to the proximal fibula.

In addition to reporting the incidence of injury, Danelson et al. provided crucial information regarding injury mechanisms. Compression alone, or compression in combination with a secondary injury mechanism, was associated with 64% of fractures to the distal portions of the tibia and fibula. Compression was identified as the injury mechanism for the majority of the calcaneus (73%) and talus (55%) injuries. Injuries of the midfoot were most commonly associated with a combination of compression and differential loading (53%). Compression alone caused 54% of forefoot fractures. The findings of this study are vital in the effort to predict and prevent injuries in UBB scenarios. The damage produced in the current study is representative of the in-theater injuries described in Danelson et al., which validates the use of the Accelerative Loading Fixture (ALF) for UBB testing.

While the occupants described in Danelson et al. (2018) were mostly male (96%), additional data reporting the incidence and mechanism of injuries to female Warfighters are imperative for the protection of a full range of service members. This is of utmost importance, as women in the armed services are being integrated into additional military occupational specialties that were previously closed to women. As of August 2014, women comprised 16% of the total DoD force and accounted for 2.4% (113) of those killed in Iraq and Afghanistan since the beginning of OIF and OEF (Powers, 2016). During this period, 32,799 U.S. service members were wounded in combat, 606 of which were women.

Dye et al. (2016) examined combat injuries in a dataset of 844 episodes involving 835 U.S. service women in OIF and OEF. Blast events were responsible for over 90% of the injury episodes recorded in the EMED, between January 2003 and May 2014. Additionally, almost 65% of the injury episodes involved more than one injury and there was an average of 2.9 injuries per episode. Lower extremity injuries comprised 29.6% of the injuries in OIF and 25.5% of injuries in OEF.

Female Injury Risk

Epidemiological evidence suggests that in general, females are at greater risk of injury, are injured more frequently, and sustain injuries with higher severity levels than men. Evans (2001) compared the fatality risk of females and males in over 200,000 traffic fatalities and discovered that between the ages of 20 and 35, females have about a 28% greater risk of death than males in similar impacts. Foret-Bruno et al. (1990) surveyed over 1,200 seat-belted casualties between the ages of 15 and 45 years old, and found that fatal accident risk is 20-to-25% higher for females. Furthermore, there are notable disparities in lower extremity injury frequency between sexes. Welsh and Lenard (2001) examined four UK crash databases and found that a greater proportion of females than males sustain leg injuries. Dischinger et al. (2016) compared injury risk of the foot/ankle between sexes in the National Automotive Sampling System/Crashworthiness Data System (NASS-CDS) for drivers in frontal crashes and found that females were 1.2 times more likely to sustain foot injuries and 1.6 times more likely to sustain ankle injuries than males in MY 2005 to 2014 vehicles. Ye et al. (2014) also determined that females have a higher likelihood of sustaining injuries of the lower extremity than males in a sample selected from the NASS between 1998 and 2010.

Evidence from cadaveric studies also suggests that females are at greater risk of fracture than males. Rib strength was investigated in 245 cadavers in the Foret-Bruno et al. study, and it was determined that female fracture resistance was 18% lower than males of the same age. Kemper et al. (2005) conducted dynamic three-point bending tests of female and male humerus bones and found that females have lower peak moments and peak strains than males. Hardy et al. (2001) found that bone mineral content, which reflects both the quantity and quality of bone and relates directly to forearm fracture tolerance, was 41% lower in female specimens than male specimens. In addition, the average mass of female post-mortem human surrogates (PMHS) arms was 32% lower than that of the male arms. Bone mineral content was linearly related to arm mass in this study. In the Foret-Bruno study, injury tolerance in females was lower than expected when considering body mass alone. Although the females weighed less and the loads on their chests were lower, they reached maximum thoracic resistance sooner in the event than males of the same age.

Axial Loading of the Lower Extremity

Traumatic injury of the lower extremities has been an area of concern in the automotive realm for many years. As improvements were made to vehicles that increased the survivability of crashes, cases involving occupants surviving with severe injuries of the lower extremities increased. Kuppa et al. (2001) determined that the lower extremities are the most frequently injured body region with an Abbreviated Injury Scale (AIS) score of 2+ reported in the NASS/CDS between 1993 and 1999. In this dataset, 33% of AIS 2+ injuries of the lower limb occurred to the foot and ankle.

The high incidence and severity of lower extremity injuries observed in automotive crashes incited numerous research efforts to understand, predict, and prevent these injuries. Some of these studies offer valuable insight into injury mechanisms observed in UBB scenarios as well. For example, Morris et al. (1997) cited axial loading directed perpendicular to the foot as the mechanism of injury for pilon, talus, and calcaneus fractures sustained in frontal collisions in England between 1983 and 1996. The most severe and disabling injuries were caused by axial loading rather than indirect rotational loading.

In an effort to characterize lower extremity injury tolerance and mechanisms from axial loading, many researchers have reproduced these injuries in a laboratory setting. Schueler et al. (1995) imparted plantar impacts to the feet of whole-body cadavers with velocities that ranged from 6.67-m/s to 12.5-m/s. Damage occurred primarily to the calcaneus. Thresholds that indicated a significant “relative risk of leg injuries” included a 9.72-m/s or greater impact speed and a 1000-g or greater acceleration of the sole of the foot. In a similar study, Klopp et al. (1997) used a pendulum-driven plate to axially load PMHS lower extremities. Damage was produced throughout the distal tibia, talus, and calcaneus, and a fifty-percent probability of injury was associated with a peak heel acceleration of 216-g. While both of these studies are in the automotive realm, the resulting damage is comparable to that seen in UBB.

The calcaneus is highly susceptible to fractures from plantar impacts. Thus, several studies have examined injury tolerance levels of the calcaneus alone. Seipel et al. (2001) produced calcaneus fractures with associated peak forces ranging from 3.6 to 11.4-kN. A fifty-percent probability of calcaneus fracture was associated with a 5.5-kN load. Comparable results were obtained by

Yoganandan et al. (1999), in which fourteen calcaneus fractures were produced. Five of the fractures were comminuted. A fifty-percent probability of calcaneus fracture was associated with a 6.2-kN force.

The aforementioned studies tested specimens in a neutral foot posture with the angle of the ankle set to 90 degrees. While this posture is implemented in the current study as well, other studies that have examined the effects of plantar flexion, dorsiflexion, inversion, and eversion may be relevant for more complex interactions between the feet and the vehicle interior during UBB events. Begeman and Prasad (1990) applied loads to the plantar surface of PMHS leg specimens that were slightly anterior to the ankle joint. This produced a combination of axial loading and dorsiflexion with impact speeds ranging from 3.0 to 8.1-m/s. Similarly, Petit et al. (1996) performed quasi-static compression of PMHS leg specimens in inversion, eversion, and dorsiflexion. Both studies produced malleolus fractures and soft tissue damage in the dorsiflexion condition. Parenteau et al. (1998) conducted similar tests to Begeman and Prasad (1990). However, the specimens were loaded to failure quasi-statically in dorsiflexion, plantar flexion, inversion, and eversion. The failure moments were 33.1 ± 16.5-Nm in dorsiflexion, 40.1 ± 9.2-Nm in plantar flexion, 34.1 ± 14.5-Nm in inversion, and 48.1 ± 12.2-Nm in eversion. Other studies have demonstrated that severe ankle and hindfoot damage can occur without much ankle rotation (McMaster et al., 2000; Klopp et al., 1997).

Damage type and location may be related to the level of loading through the foot/ankle complex. Kitagawa (1998) applied damage-inducing plantar loads anterior to the long axis of the tibia of PMHS legs. The calcaneus fractures occurred at higher loads than pilon fractures (8,115-N vs. 7,293-N). Tension in the Achilles tendon may also play a role in damage outcome. Funk et al. (2002) applied 5-m/s plantar impacts to neutrally positioned PMHS legs both with and without tension applied to the Achilles tendon. Fracture of the distal tibia was associated with Achilles tension, while fractures of the calcaneus were associated with no Achilles tension. It is unknown whether the influence of Achilles tension is maintained at the higher energy levels seen in UBB.

Yoganandan et al. (1996) combined the results of Roberts et al. (1993) and Begeman and Aekbote (1996) with an additional test series to determine probability distributions of fractures to the lower

extremity due to axial loading. Roberts used a constant speed compression device to impact PMHS leg specimens at 4.6-m/s while maintaining 20 degrees of dorsiflexion throughout the event. Begeman used a pneumatic piston to load PMHS leg specimens that were restrained from inversion/eversion and plantar flexion/dorsiflexion. Yoganandan used a pendulum impactor to load PMHS leg specimens that were mounted on a mini-sled at velocities ranging from 2.2-m/s to 7.6-m/s. The results of the combined dataset indicated that a 50% risk of injury for a 65 year old was associated with an axial load of 6.2-kN.

In addition to studies in the civilian automotive realm, research on the high-energy injuries imparted by landmines may also inform the study of UBB. Griffin et al. (2001) suspended PMHS lower extremities with the heel positioned directly over a buried land mine. The resulting damage included pilon fractures of the tibia and comminuted fractures of the calcaneus, cuboid, navicular, and talus. A fifty-percent risk of a pilon fracture was associated with an axial force of 6,800-N for a 50^{th}-percentile male.

Dosquet et al. (2004) used the Test Rig for Occupant Safety Systems (TROSS™) to launch a deformable floorplate towards lower extremity surrogates. This test apparatus used scaled detonations to replicate the conditions of a full-scale mine blast test. Barbir (2005) replicated the performance of the TROSS™ using a pneumatic linear impactor at three energy levels to axially load PMHS leg specimens. One fracture of the tibial plateau resulted from tests with an average force of 4.5-kN for 10 to 15-ms.

McKay and Bir (2009) conducted full-scale blast tests on PMHS lower extremity specimens in a neutral posture with impact speeds of 7, 10, and 12-m/s. Damage was sustained by the calcaneus, talus, tibia, fibula, and cuboid. More severe fractures with higher levels of comminution, as well as fractures of the tibia and fibula, were associated with the highest impact velocity. A fifty-percent risk of incapacitating injury was associated with a 10.8-m/s impactor speed and 6,429-N tibia load.

The introduction of under-body blast tactics in military combat incited numerous research efforts to replicate UBB conditions in a laboratory setting. The goal of these studies was to produce damage commensurate with injuries seen in-theater and to develop updated injury thresholds for

higher-energy conditions. Quenneville et al. (2010) used a pneumatically driven projectile to generate fractures of the lower extremity with short-duration and high-impulse loading. Exit speeds of the projectile ranged from 2.3 to 13.9-m/s. The authors reported that the device could produce "clinically significant injuries." A major limitation of this study was that the magnitude of the axial forces measured was influenced by the properties of the specimens.

Masouros et al. (2013) described the development of the Anti-Vehicle Underbelly Blast Injury Simulator (AnUBIS), which consists of a heavy plate that is launched at specimens. Newell et al. (2012) compared the response of three lower extremity specimens to two ATD surrogate legs using the AnUBIS. Although the loads measured in the ATDs were higher than injury tolerance levels recommended by NATO, only one PMHS specimen sustained damage, which was minor. The authors suggested that the tolerance levels of current injury criteria are too conservative. These counterintuitive results warrant continued research efforts in UBB.

Gallenberger et al. (2013) examined the influence of modulating energy input during simulated vehicle floor intrusions. This was accomplished by imparting multiple impacts to PMHS lower extremity specimens with three different pendulum masses. Almost all of the specimens sustained damage to the calcaneus and tibia. Fracture patterns were similar between neutral and dorsiflexed initial positions, which lead the authors to suggest that significant rotation of the ankle does not occur prior to damage. A fifty-percent probability of calcaneus fracture was associated with a 6,800-N force. Interestingly, the response of the specimens was more sensitive to impact speed than impact energy.

Pintar et al. (2016) examined the response of twenty-six foot and ankle complexes to non-damaging vertical loading on the Vertac (Yoganandan et al., 2015) and produced biofidelity response curves (BRCs). The specimens were tested with and without combat boots in three different initial positions at the ankle (neutral, dorsiflexed, and plantar flexed). In the neutral initial position, the average axial forces at the proximal tibia were approximately 2, 4, and 6-kN, for the 4, 6, and 8-m/s tests, respectively. The time-to-peak values for the forces ranged from 3 to 5-ms and the rise times for calcaneus acceleration ranged from 2 to 8-ms. A delay in angular movement

of the tibia was observed in the dorsiflexed position. In contrast, the plantar-flexed position allowed immediate "angular motion" upon impact.

In a study using a similar dataset and methods, Yoganandan et al. (2016) developed peak-force based fracture probability curves for foot and ankle injuries due to under-body blast. Two test fixtures, a pendulum and the Vertac, were used to apply incrementally larger axial loads to seventeen PMHS leg specimens until damage was detected. For the age of 50 years, a 6.8-kN peak force was associated with a 10% risk for the "all fractures" group, while a 7.8-kN peak force was associated with a 10% risk of injury to the tibia. A shortcoming of this and other studies is the use of multiple successive impacts to cadaveric specimens, which may lower fracture thresholds by damaging the bone in undetectable ways.

Danelson et al. (2015) provided a comparison of the impact and damage response of whole-body male PMHS to the Hybrid III 50th-percentile male ATD. Like the current study, this work was conducted on the Accelerative Loading Fixture (ALF). This important study explored the influence of charge level (mild or enhanced), occupant position (nominal 90 degree or obtuse 120 degree knee angle), the use of personal protective equipment (PPE), and floor properties (stiffer vs. softer). This study revealed that the Hybrid III 50th-percentile male dummy is not well-suited for injury prediction in the UBB environment, since it cannot assume the upright initial position on the ALF and it exhibits a stiffer response overall. Notably, the damage produced in the PMHS was commensurate with injuries seen in-theater, including numerous lower extremity fractures. Damage to the ankle (tibia, talus, and calcaneus) was frequently observed in this study. Two calcaneus fractures involved gross disruption. The talus remained relatively intact, with the exception of a single case of full transection. This was observed in the nominal position, at a mild energy level, and with a softer floor. One pilon fracture was produced in the obtuse posture with enhanced floor energy. Damage to the bones of the foot was produced in one test with a softer floor material and enhanced floor energy. This damage was attributed to longer duration of contact with the floor. In general, lower extremity fractures appeared to be related to higher acceleration and speed of the tibia and a shorter time-to-peak. The results of this study contributed to the body of knowledge pertaining to UBB in numerous ways, including the validation of the ALF for UBB

testing, characterization of the nature and timing of damage sustained by PMHS during UBB, and correlation of damage outcome with floor behavior and kinematics of the body.

An additional study by Bailey et al. (2017) pooled the results of two other studies to determine the influence of loading rate and duration on the axial force associated with fracture of PMHS legs. The first dataset used a drop tower test fixture to apply an axial load to male PMHS leg specimens with two impactor velocities (Henderson et al., 2013). The second dataset applied pneumatic linear impacts to male PMHS leg specimens at three impactor speeds. The authors stated that tibia force alone is not an appropriate predictor of injury. They recommended the incorporation of loading duration in developing injury criteria for axial loading of the leg and set forth the hypothesis that the duration of the load may influence the force measured at the time of fracture.

The underrepresentation of female specimens in matched conditions with male specimens is a major shortcoming in the current body of knowledge pertaining to lower extremity injuries, particularly those sustained at higher energy levels. Female specimens were included in several of the aforementioned studies (Begeman and Aekbote, 1996; Begeman and Prasad, 1990; Funk et al., 2002; Gallenberger et al., 2013; Griffin et al., 2001; Kitagawa et al., 1998; Parenteau et al., 1998; Roberts et al., 1993; Schueler et al., 1995; Seipel et al., 2001; Yoganandan et al., 1996; and Yoganandan et al., 1999). However, the number of female specimens was typically too low for statistical significance. Begeman and Prasad noted that five out of six female specimens in the study sustained damage, while only one of the twelve male specimens sustained damage. The authors suggested that these results reflected potential differences in tolerance due to sex, however this finding was not statistically significant. Parenteau et al. (1998) showed that female PMHS had significantly lower failure moments than male PMHS in inversion and eversion. Funk et al. (2002) reported that the risk of injury due to axial loading was dependent on sex, with a 50% risk of injury due to blunt axial loading of the foot and ankle of a 45 year old being associated with an 8.3-kN tibia load for 50^{th}-percentile males, and a 5-kN load for 5^{th}-percentile females. Although there is sufficient evidence to suggest that there are differences in injury risk and injury mechanisms between females and males, there is no known study of high-rate axial loading of female lower extremities.

Lower Extremity Anatomy

This section describes bones of the lower extremity, including the femur, patella, tibia, fibula, tarsals (talus, calcaneus, navicular, cuboid, and cuneiforms), metatarsals, and phalanges. Several joints are also described, including the hip (acetabulofemoral) joint, the knee (tibiofemoral and patellofemoral) joint, the proximal and distal tibiofibular joints, the ankle (talocrural) joint, the subtalar (talocalcaneal) joint, Chopart's joint, and the Lisfranc joint. The information presented in this overview was drawn largely from Gilroy et al. (2012), Hamill et al. (2015), and Sarrafian (2011).

Hip Joint

The proximal end of the femur, or head, articulates with the acetabulum of the pelvis to form the acetabulofemoral joint, or hip joint (Figure 1). The hip joint is a ball-and-socket type, which facilitates triaxial rotation. The acetabulum of the pelvis is oriented anteriorly, laterally, and inferiorly. This cup-like feature encloses nearly half of the head of the femur and is extended by the acetabular labrum (Hamill et al., 2015). The hip joint is relatively stable due to the geometry of the bones, the acetabular labrum, and the surrounding ligaments. Major ligaments of the hip joint include the iliofemoral, pubofemoral, and ischiofemoral ligaments.

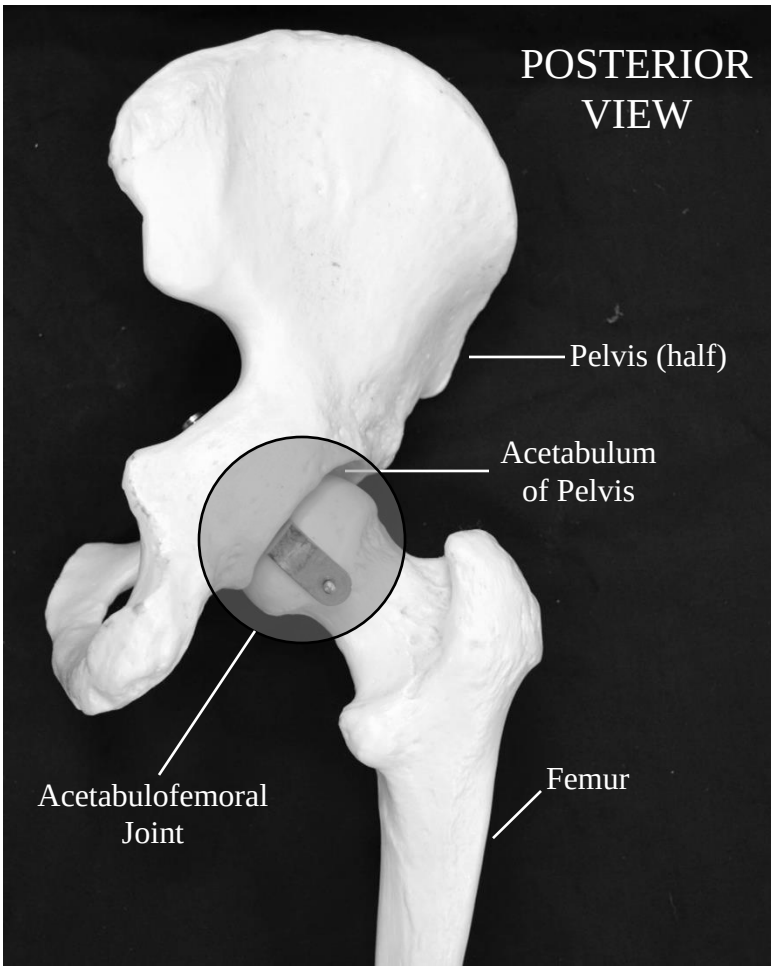

Figure 1: Right hip (acetabulofemoral) joint.

Femur

The femur supports the proximal portion of the lower extremity, or thigh (Figure 2). In an upright, standing posture, the femur is not oriented perpendicular to the ground, but rather it slopes medially, bringing the knee closer to the centerline of the body. The body (shaft) of the femur has

an approximately cylindrical cross-section, with a slight curvature making it concave posteriorly. The proximal portion of the femur includes the greater and lesser trochanters, head, and neck. The greater trochanter is a large eminence that protrudes laterally and slightly posteriorly at the proximal portion of the femur. The lesser trochanter is a bony protuberance on the posterior aspect of the femur that is oriented inferiorly and medially. Both of these landmarks serve as muscular attachment points. The head of the femur is oriented superiorly, medially, and anteriorly to the shaft of the femur. The distal end of the femur widens to form the medial and lateral epicondyles. The distal surface is comprised of the medial and lateral condyles, which articulate with the knee.

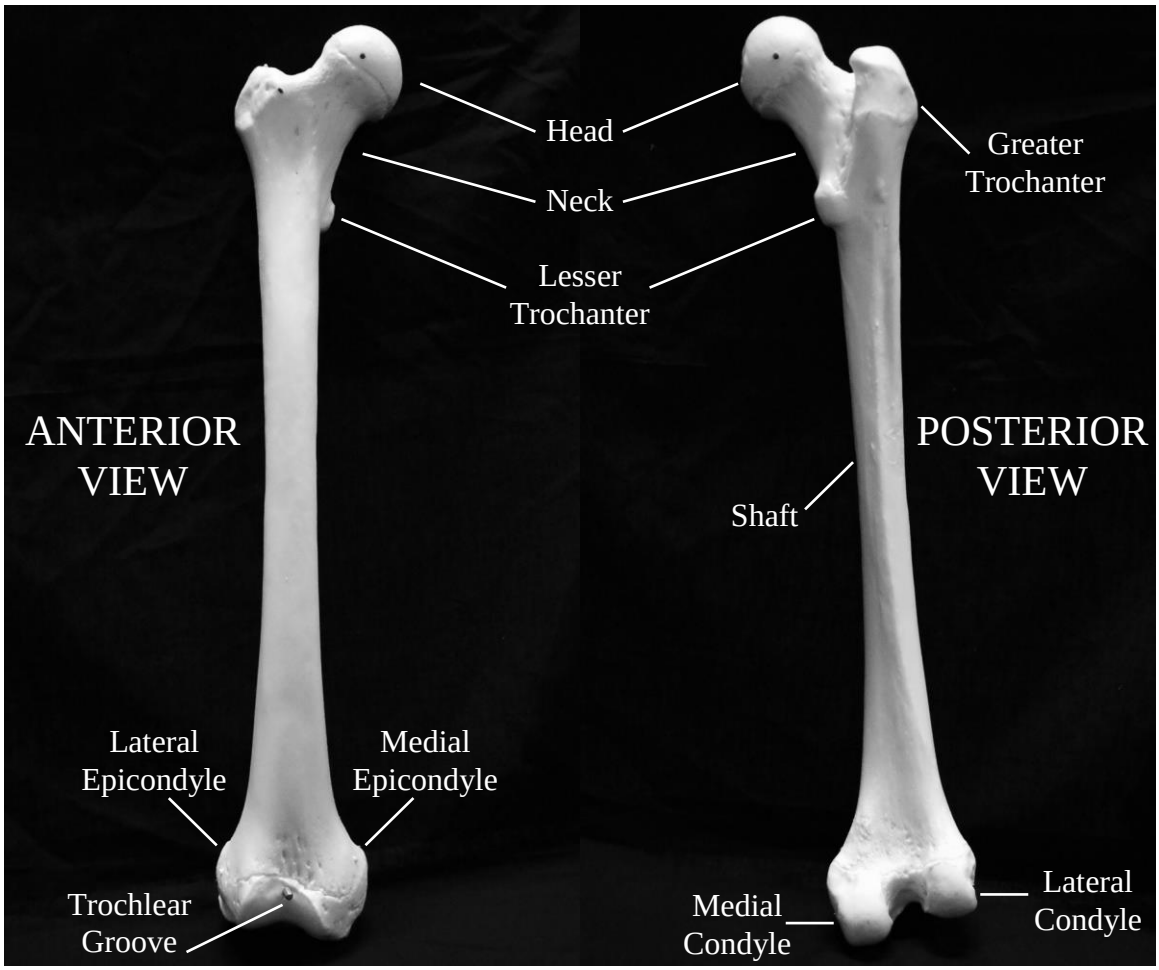

Figure 2: Right femur.

Knee Joint

Distally, the femur articulates with the tibia (shin) and patella (knee cap) to form the knee (Figure 3). The knee is a hinge joint that is modified to provide a pivot-like motion in addition to flexion and extension. It is comprised of the tibiofemoral joint, which is a double condyloid joint formed

by the articulations between the medial and lateral condyles of the femur and tibia; and the patellofemoral joint, which is formed by the articulation between the patella and the trochlear groove of the femur. The patella is a sesamoid bone that is embedded in the patellar ligament, which originates at the common tendon of the quadriceps femoris and inserts at the tibial tuberosity. The proximal tibiofibular joint is formed by the articulation between the head of the fibula and the lateral tibial condyle. The knee joint is relatively mobile, with its stability depending almost exclusively on the associated ligaments and muscles. The major ligaments of the knee include the medial and lateral collateral ligaments, as well as the anterior and posterior cruciate ligaments. The joint is cushioned by the fibrocartilaginous medial and lateral menisci, which are located between the tibial plateau and the femoral condyles. The knee joint is surrounded by the capsular ligament and the inner synovium.

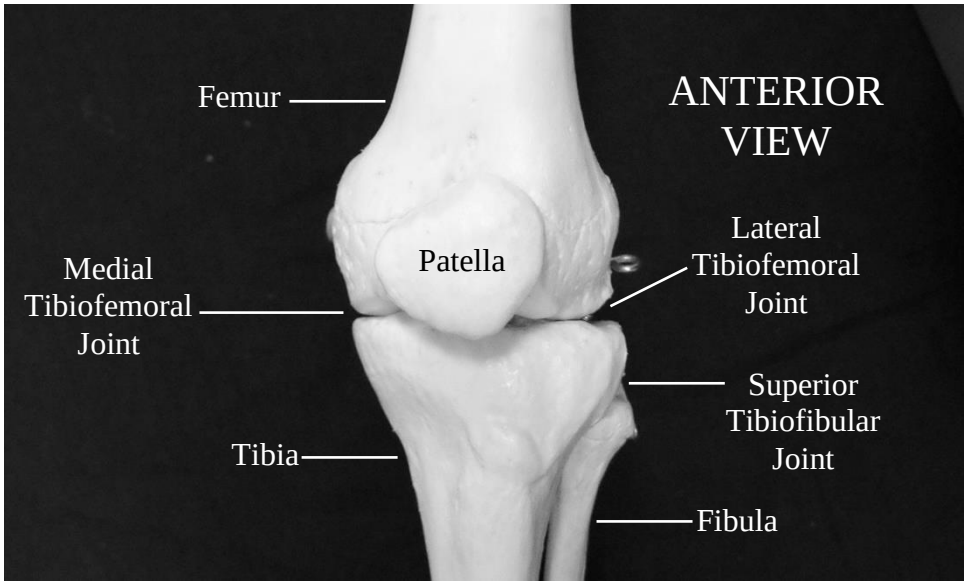

Figure 3: Left knee joint.

Tibia and Fibula

The distal portion of the lower extremity, which extends from the knee to the ankle, is called the leg (Figure 4). The tibia is the primary weight bearing bone of the leg. Its cross-section is triangular and it has a medial, lateral, and posterior surface. The proximal tibia widens to form the medial and lateral condyles. The proximal surface flattens to form the tibial plateau. Distally, the medial border of the tibia forms the medial malleolus. The inferior surface, called the tibial plafond, is concave anteroposteriorly and articulates with the superior surface of the talus. The fibula is positioned lateral to the tibia and supports approximately 16% of body weight during standing

(VanDenBogart et al., 1999). The proximal end of the fibula forms the neck and head. The distal end of the fibula extends beyond the tibia forming the lateral malleolus, which articulates with the talus. Distally, the tibia and fibula are joined by a slightly mobile fibrous joint called the distal tibiofibular joint, which is supported by the anterior inferior tibiofibular ligament and posterior inferior tibiofibular ligament of the lateral malleolus, and the interosseous membrane.

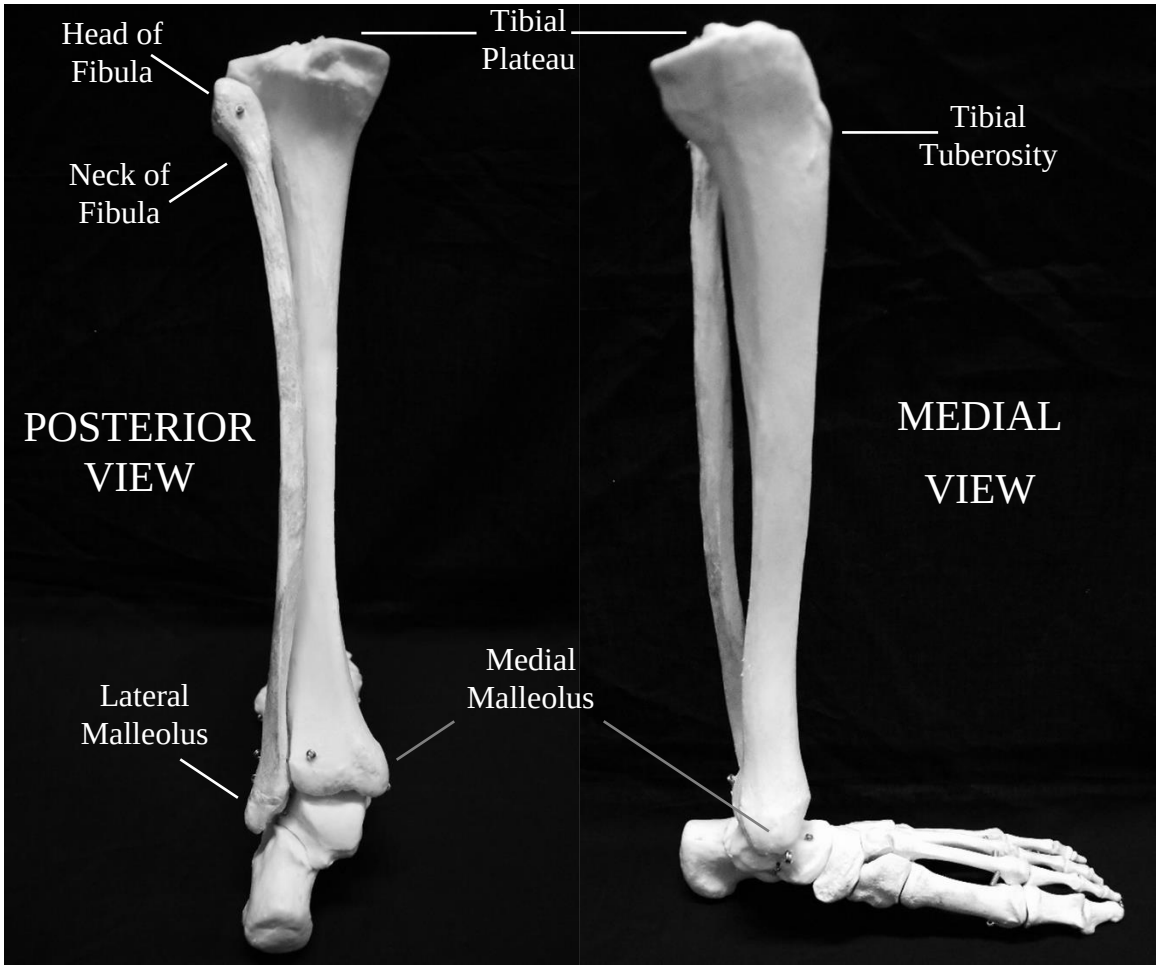

Figure 4: Left leg (tibia and fibula).

Talus

The talus is positioned between the tibia, superiorly, and the calcaneus, inferiorly (Figure 5). It is comprised of a body, neck, and head. Articular surfaces of the talus include the head anteriorly (facies articularis navicularis), which articulates with the navicular and calcaneus; the trochlear surface superiorly, which articulates with the tibia and presents the articular facets for the medial and lateral malleoli (facies malleolus medialis and facies malleolus lateralis, respectively); and the anterior, middle, and posterior facets on the inferior aspect, which articulate with the calcaneus.

Other landmarks of the talus include the medial, lateral, and posterior processes, as well as the sulcus tali. The head of the talus, which articulates with the concave surface of the navicular, is supported by the anterior lip and sustentaculum tali of the calcaneus. A "socket" for the talar head is formed by the plantar calcaneonavicular (spring) ligament (Perry, 1983).

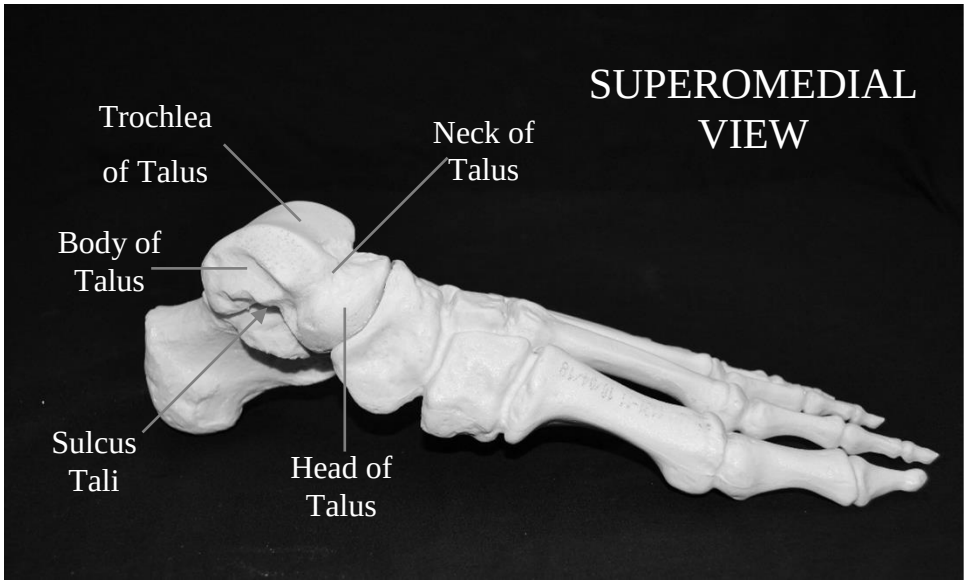

Figure 5: Left talus.

Talocrural (Ankle) Joint

The talocrural (ankle) joint is a hinge joint formed by the talus and the distal portions of the tibia and fibula (Figure 6). This joint provides dorsiflexion and plantar flexion, as well as some inversion and eversion. The superior portion of the talus (trochlea) forms a tenon that fits into a mortise formed by the inferior surface of the tibia and the malleoli of the tibia and fibula. The connective tissues that support this joint include the deltoid, anterior talofibular, posterior talofibular, and calcaneofibular ligaments, as well as the articular capsule. The axis of rotation is oblique, running slightly distal to the tips of the medial and lateral malleoli (Sarrafian, 2011).

Talocalcaneal (Subtalar) Joint

The subtalar joint is a condylar-type joint formed by three articulations (anterior, middle, and posterior) between concave facets of the talus and convex surfaces of the calcaneus (Figure 6). This joint is supported by an articular capsule and the anterior, posterior, lateral, medial, and interosseous talocalcaneal ligaments. The oblique axis of rotation of this joint, which runs from the posterolateral plantar surface to the anterior medial dorsal surface of the talus, produces tri-

planar movements (Hamill et al., 2015). The subtalar joint works in combination with the talonavicular and calcaneocuboid joints to form the “triple joint complex” (Rammelt and Zwipp, 2006), which facilitates pronation (eversion, abduction, and dorsiflexion) and supination (inversion, adduction, and plantar flexion) of the calcaneus.

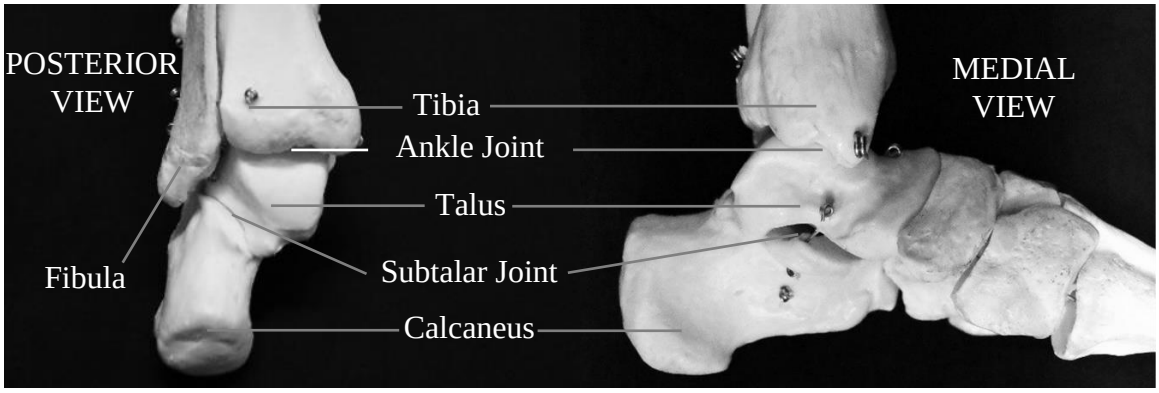

Figure 6: Left hindfoot.

Foot

The foot consists of the hindfoot, which includes the calcaneus and talus; the midfoot, which includes the navicular, cuboid, and the three cuneiforms (medial, intermediate, and lateral); and the forefoot, which includes the five metatarsal bones and the proximal, middle, and distal phalanges (Figure 7). The articulation between the hindfoot and midfoot is known as Chopart's (midtarsal) joint, and consists of the talonavicular joint and calcaneocuboid joint. The articulation between the midfoot and the forefoot is known as the Lisfranc (tarsometatarsal) joint, which includes the first, second, and third metatarsal-cuneiform joints, as well as the fourth and fifth metatarsal-cuboid joints. The metatarsals interface with the phalanges at the metatarsophalangeal joints. The joints among the phalanges include the proximal and distal interphalangeal joints. Some joints of the foot are shown in Figure 8. The metatarsals and phalanges are numbered one through five from medial to lateral.

Calcaneus

The calcaneus is an irregular bone that provides structure for the heel of the foot (Figure 6). It is inclined anteriorly and serves as a lever arm for the attachment of several soft tissue structures, including the Achilles tendon and plantar aponeurosis (fibrous band of connective tissue). The base of the calcaneus is triangular and formed by the anterior tuberosity, and the medial and lateral tuberosities. The medial tuberosity, which is broader than the lateral tuberosity, is the main weight

bearing bony structure of the calcaneus. Notably, the point of contact between the floor and the plantar surface of the calcaneus is located lateral to the ankle joint, so upward force on the calcaneus creates a valgus force on the subtalar joint (Perry, 1983), meaning the joint is pushed medially. The anteromedial portion of the calcaneus supports a shelf-like projection of bone called the sustentaculum tali, which provides the middle articular surface for the talus. Calcaneal morphology is highly variable among the population (Laidlaw, 1904). Beneath the calcaneus is a thick fat pad that serves as a shock absorber. The dermis fat cells in this thick layer of cushion are separated into individual sacs by an organized structure of fibrous tissue (septa). The fibrous septa are attached to one another in a spiral pattern that resists torsional forces (Perry, 1983). Transverse and diagonal layers of fibrous connections provide additional reinforcement to the fat pocket.

Midfoot

The midfoot includes the navicular; cuboid; and the medial, intermediate, and lateral cuneiforms (Figure 7). The navicular is a pear-shaped bone with four surfaces. The posterior aspect provides a concave surface for the head of the talus, while the anterior surface provides three convex facets for the cuneiforms. Major landmarks of the navicular include the tuberosity, which is a bony prominence on the medial surface, and the beak, which is a bony projection on the plantar surface (Sarrafian, 2011). The cuboid is a cube-shaped bone with five surfaces. The posterior surface articulates with the calcaneus, while the anterior surface articulates with the proximal surfaces of the fourth and fifth metatarsals. The medial cuneiform articulates with the navicular, posteriorly; the intermediate cuneiform, laterally; and the base of the fourth and fifth metatarsals, anteriorly. The intermediate cuneiform articulates with the navicular, posteriorly; the second metatarsal, anteriorly; and the cuneiforms medially and laterally. The lateral cuneiform articulates with the navicular, posteriorly; the third metatarsal, anteriorly; the intermediate cuneiform, medially; and the cuboid, laterally.

Forefoot

The forefoot is comprised of the metatarsal bones and the proximal, middle, and distal phalanges (Figure 7). Each metatarsal bone consists of a base, shaft, and head. Distally, they articulate with the proximal row of phalanges to form the metatarsophalangeal joints. Joints between the phalanges are called interphalangeal joints.

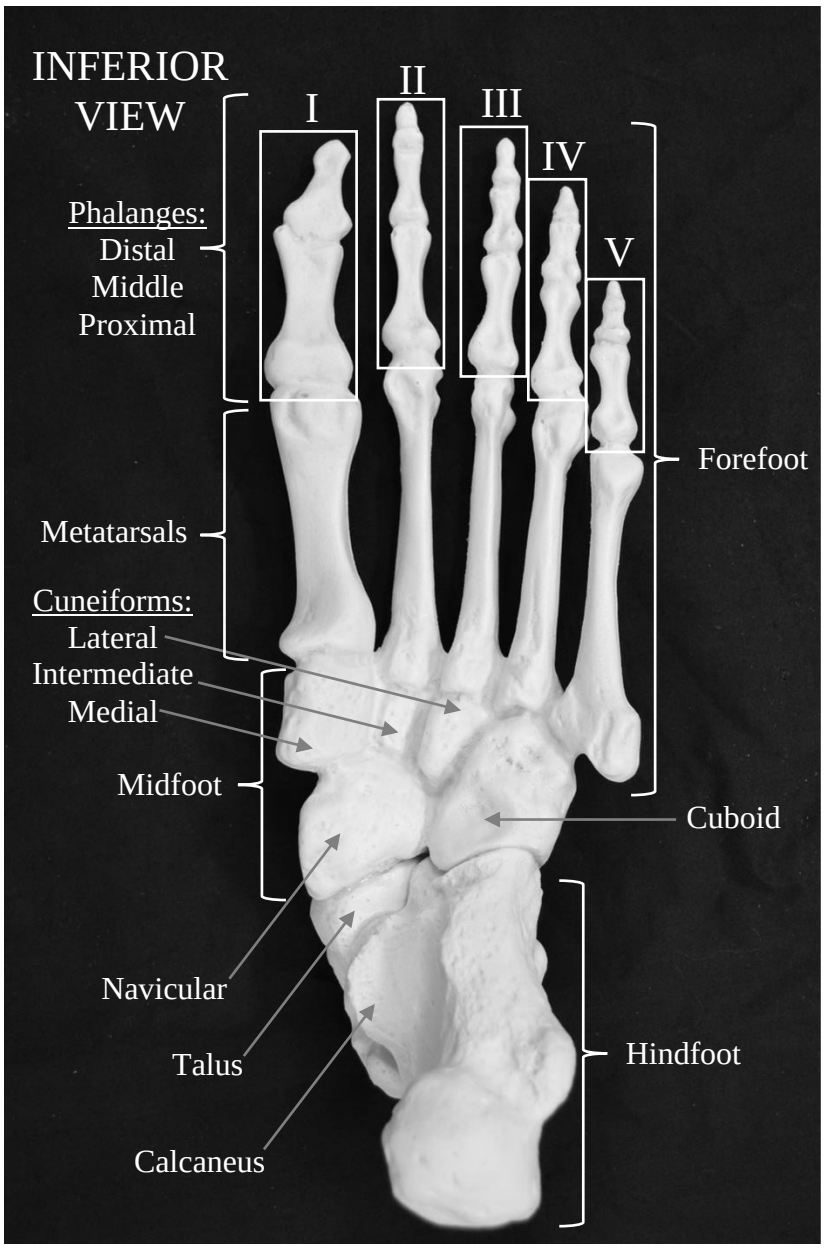

Figure 7: Bones of the left foot.

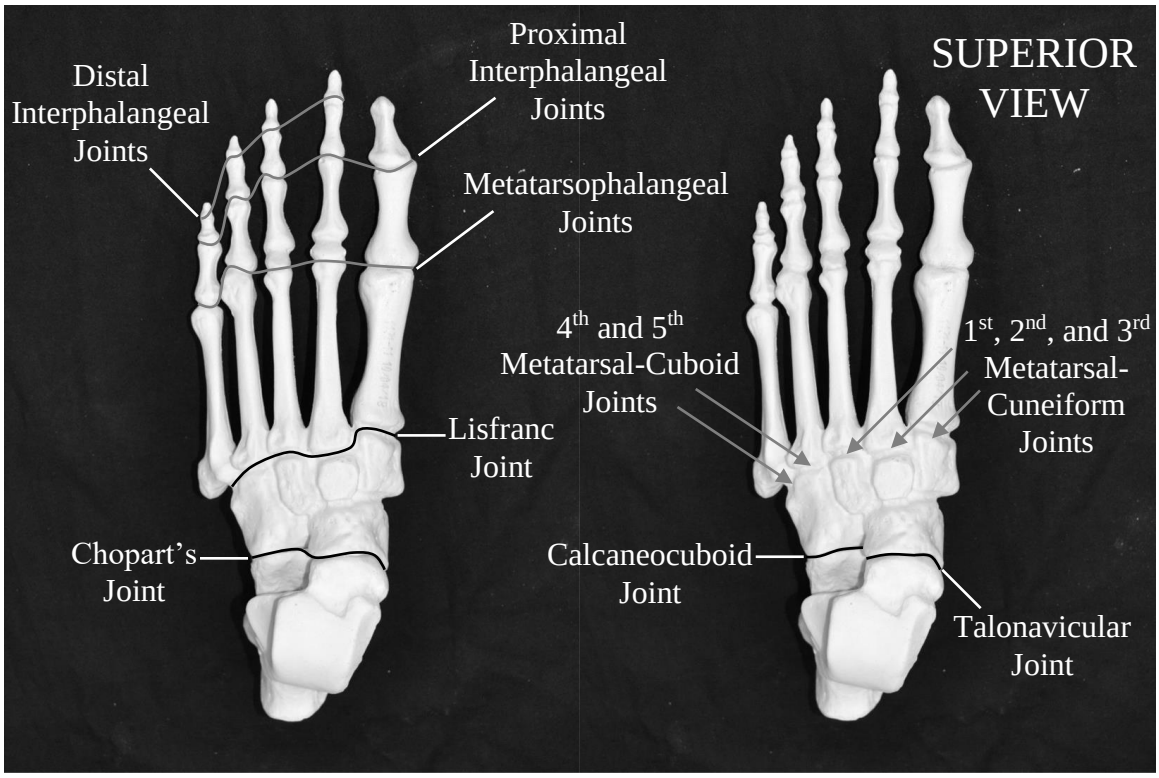

Figure 8: Joints of the left foot.

Problem Statement

In an effort to enhance ground vehicle protection measures against unconventional UBB attacks, the Live Fire Test and Evaluation (LFT&E) Program requires that military ground vehicles undergo UBB testing. This necessitates the development of validated tools, such as anthropomorphic test devices (ATDs), to assess the probability of injuries to occupants in UBB conditions. These tools were developed for the civilian automotive domain, however they are not designed to assess injuries from high-rate vertical loading (Danelson et al., 2015).

The US Army initiated the Warrior Injury Assessment Manikin (WIAMan) Project in 2011 with the goal of developing an appropriate ATD and associated injury assessment tools that are specific to UBB. A prototype of this technology was the WIAMan Technology Demonstrator (TD) ATD, which is representative of the 50th-percentile male Warfighter (Pietsch et al., 2016). The production version of the WIAMan is now being fielded. This ATD will aid in predicting injuries sustained by Warfighters in-theater and enable the development and implementation of improved vehicle systems and personal protective equipment.

At this time, WIAMan technology continues to evolve and additional supporting data are being generated. It is anticipated that the WIAMan ATD will become part of the Department of Defense Standard, Occupant-Centric Protection for Military Ground Vehicles (MIL-STD 3058). However, there is still a gap in the protection of service members whose demographics fall outside of the range represented by the 50th-percentile male Warfighter. Currently, injury assessment tools for the female Warfighter are not available.

To address this need, the Office of the Assistant Secretary of Defense for Health Affairs approved a project to be managed by the WIAMan Engineering Office. This Analysis of Alternatives (AoA) addresses knowledge gaps regarding potential differences between the responses of females and males during UBB events. The alternatives under consideration include the potential need for a new, separate female ATD for use in the UBB environment, or the potential collection of female biomechanics data to implement scaling/transformation methods to map the performance and injury prediction capabilities of the existing male ATD to that of female PMHS. The current study was conducted in support of this AoA.

Research Hypothesis

The overarching objective of the research presented in this dissertation is to conduct a comparison of female and male PMHS kinematics and damage response under UBB conditions. This was accomplished by conducting whole-body PMHS tests in both sub-damaging and damaging test conditions and drawing comparisons to existing data. The following hypothesis is made: Female and male PMHS will demonstrate notably different responses in the UBB environment in terms of kinematics response (transducer and video-based measurements) and damage response (type, incidence, and extent).

The results of this work form the first detailed biomechanical account of UBB effects on female PMHS. Further, this work assesses potential biomechanical sensitivities that can be attributed to sex differences. These findings will inform future decisions regarding the requirements for a valid injury assessment capability for female Warfighters in the UBB environment.

CHAPTER 2

METHODOLOGY

The research objectives of this study are accomplished, in part, by exposing whole-body PMHS to UBB conditions at both sub-damaging and damaging input levels. The PMHS in this portion of the study included eight 50th-percentile males, six 75th-percentile females, and six 5th-percentile females. The data collected in this study include generalized kinematics of the distal femur and distal tibia, vertical acceleration of the calcaneus, axial strain of the proximal and distal femur, axial strain of the proximal and distal tibia, superior-to-inferior strain of the calcaneus, video kinematics of the thigh and leg, and damage to the skeletal system. The impact and damage response of the PMHS in this study is compared across all specimens. Additional comparisons are drawn from existing data collected from 50th-percentile male PMHS during a study titled Task 4.2 (Danelson et al., 2015).

Specimen Selection

The PMHS in this study are tested in accordance with USMRMC ORP Award Number W911NF-14-2-0023 Log Number A-18968.2a. They are procured through the Body Donor Program at The Ohio State University, Medcure, Lonetree Medical Donation, and Science Care/Life Legacy Foundation.

The body mass index (BMI) of all PMHS types in the study must fall within 18 and 35, while the age must fall within 18 to 80 years old. The PMHS are selected within a specified range of stature and mass for a given sex and percentile (Table 1). Since it is difficult to obtain specimens falling within both the mass and stature ranges for a given category, selection within the defined mass range is prioritized over selection within the defined height range. Mass is considered to be the more important of the two measures and is used to categorize specimens having stature that fall slightly within a different range. The upper and lower bounds of the stature and mass were determined by a detailed anthropometric survey of U.S. Army Soldiers, titled ANSUR II, that was performed by the Natick Soldier Research, Development and Engineering Center (Gordon et al., 2014). In this report, the average statures for the 5th-percentile females, 75th-percentile females,

and 50th-percentile males were 152.5 cm, 167.2 cm, and 175.5 cm, respectively. The average body weights for the 5th-percentile female, 75th-percentile female, and 50th-percentile male were 51.3 kg, 74.6 kg, and 84.6 kg, respectively. The ranges of stature and mass are one standard deviation away from the average. Comprehensive anthropomorphic measurements are obtained for all PMHS in the current study (Appendix A).

Table 1: Acceptance criteria for PMHS stature and mass

PMHS	Stature (cm)	Mass (kg)
50th Male	165 - 186	64 - 106
75th Female	160.9 - 173.7	64 - 89
5th Female	145.6 - 158.4	39 - 63

To control for bone quality, detailed examinations of computed tomography (CT) scans of the entire skeleton are performed, with special attention paid to cortical thickness. In addition, dual energy X-ray absorptiometry (DeXA) scans of the second, third, and fourth lumbar vertebrae are used to determine T-score, which is required to fall within -1.0 and +2.5 standard deviations from the population average.

Further screening of the specimens includes a review of medical history and cause of death, a radiological examination, and serologic testing for HIV, hepatitis B and hepatitis C. Exclusion criteria include communicable diseases; pre-existing skeletal injuries; existing damage or trauma to any important anatomical region (i.e. spine, pelvis, or lower extremities); appreciable bone metastases, or some advanced or aggressive forms of cancer (e.g. melanoma); some surgeries, such as lower extremity amputations, unhealed orthopaedic procedures, spinal fixation/arthroplasty, or joint replacement; some disease states, such as sepsis or extreme cases of: disc degeneration, scoliosis, stenosis or osteophytic growths, rheumatoid arthritis, or osteomyelitis; congenital joint malformations or developmental anomalies (e.g. talipes equinovarus, dysplasia, etc.); spina bifida; amyotrophic lateral sclerosis (ALS), muscular dystrophy (MD), and polio as the primary cause of death; and a severely limited range of motion of the joints.

UBB Test Conditions

To ensure that UBB injuries are studied within an operationally relevant environment that accurately reproduces real-world (in-theater) loading conditions, a predetermined set of initial

conditions and dynamic parameters are used in the current study. These conditions describe the structural behavior at the interface between the vehicle interior and the occupant. They were determined from Department of Defense (DoD) ground system tests, as well as tests performed at the Aberdeen Test Center (ATC) of the Army Test and Evaluation Command (Figure 9).

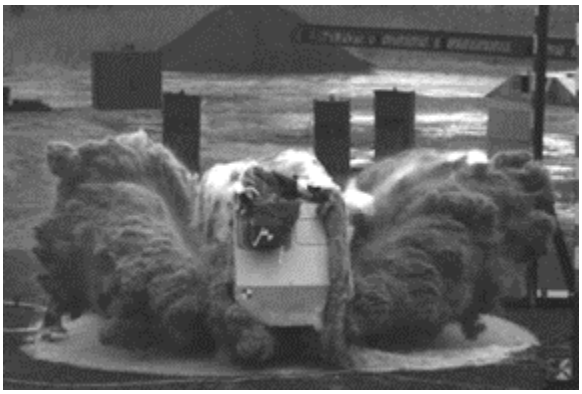

Figure 5: Generic Hull test.

Accelerative Loading Fixture

Whole-body PMHS testing is conducted on the Accelerative Loading Fixture (ALF), which is designed to generate floor and seat loading conditions at the level, rate, location, direction, and extent seen in UBB (Figure 10). The ALF was employed previously by Danelson et al. (2015), however modifications were made to stiffen the fixture and reinforce the seats for the desired loading in the current study. While there exists a number of vehicle hull designs that deflect blast energy and reduce loading on the vehicle structure, the primary direction of loading during UBB is vertical. Accordingly, the blast rig used in the current study does not include any blast attenuating features and is designed to reproduce the vertical input conditions within the predefined test conditions.

The ALF consists of an occupant platform that is driven upwards by the detonation of an explosive charge buried beneath in prepared soil having properties held to tight tolerances. The platform travels within a surrounding superstructure and is captured by a rope and cleat braking system after it passes through the apex of its travel. The floor plate, which is made of rolled homogeneous armor (RHA), undergoes plastic deformation and is replaced between each test. The occupant platform supports two rigid seats for surrogates (Figure 11). The seats have five-point harnesses.

The seat pans are 46 cm wide and 46 cm deep. The seats are incrementally adjustable in height and fore-aft position to accommodate a range of PMHS sizes. This allows the angle of the knees to be positioned at 90 degrees and the feet to be placed in a similar location on the floor with respect to the charge location beneath the deck.

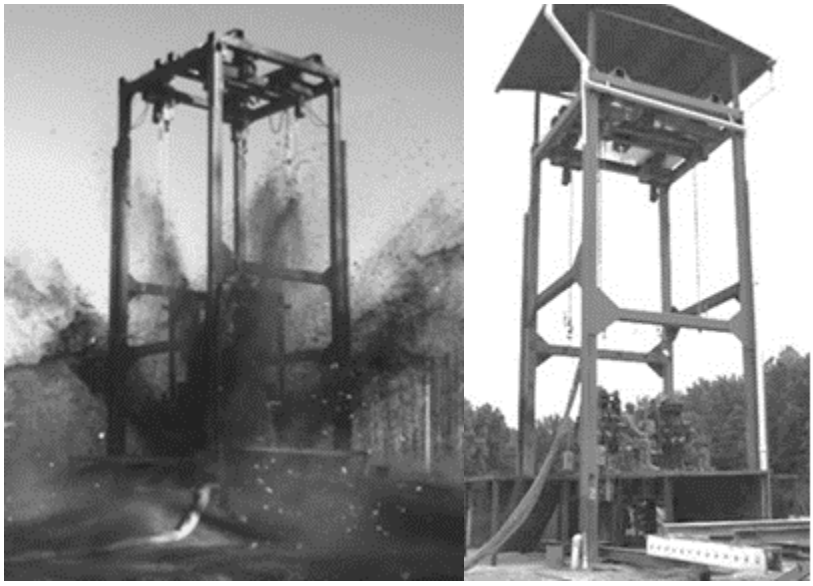

Figure 6: Accelerative Loading Fixture (ALF). Left: Photograph captured during a test from Danelson et al., 2015. Right: Pre-test photograph from the current study.

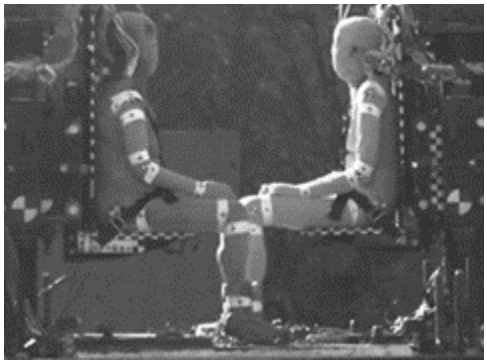

Figure 7: PMHS positioned on the ALF.

The explosive threat that drives the ALF is buried in the soil below. This soil is held at a specific temperature and moisture content, since mechanical properties of the ground are known to affect the explosive forces on a target (Cimpoeru, 2017). Changing characteristics of the charge, such as the size and standoff distance, determines the performance of the ALF. An array of accelerometers and angular rate sensors is fixed to the seats and floor of the ALF to characterize the structural response. The performance of the ALF is defined by target peak speeds and the time taken to reach

the specified peak speeds (time-to-peak or TTP) at both the seats and the floor. The behavior of the seat and floor can be modulated independently and is symmetric, predictable, and repeatable.

This study was performed in cooperation with Army Research Laboratory (ARL) personnel at the Aberdeen Proving Ground (APG) in Aberdeen, Maryland. The Aberdeen Test Center (ATC) provided some equipment, including ATDs, high-speed video cameras, structure transducers, and a Spectral Dynamics data acquisition system. The ALF is operated and maintained by the Weapons and Materials Research Directorate (WMRD) team.

Test Matrix

Twenty un-embalmed PMHS were tested during eleven under-body blast tests (Table 2). The average age of the PMHS tested was 54 years, the median was 55 years, and the range was 26 to 75 years. The PMHS in this study included 50^{th}-percentile males, 75^{th}-percentile females, and 5^{th}-percentile females. The 75^{th}-percentile females were selected because they are similar in mass and stature to 50^{th}-percentile males, thus potential differences in response between these two PMHS types are likely a result of differences in sex. The 5^{th}-percentile females represent the smallest females in the population and provide insight into the female response at one end of the spectrum. Table 3 shows the PMHS grouped by type, with average mass, stature, and BMI listed.

Each test event is referred to as a "Shot" and test occupants are designated Crew 1 or Crew 2, with Crew 1 always being the heavier surrogate. There are two test series: Series A (SA) and Series B (SB). Series A includes two shots with two 50^{th}-percentile male PMHS each (SA1 and SA2), with an additional four shots that introduced 5^{th} and 75^{th}-percentile female PMHS (SA3 through SA6). Shots SA4 and SA6 included the Hybrid III 5^{th}-percentile female ATD, which is not included in the subsequent analyses. Test Series B consisted of five shots that included 5^{th} and 75^{th}-percentile females, as well as 50^{th}-percentile males (SB1-SB5).

During Test Series A, a lower-energy floor condition was implemented to collect kinematics data in the absence of substantive damage to the lower extremities. Test Series B introduced a higher-energy floor condition to produce damaging test conditions for the lower extremities. The target test conditions are shown in Table 4.

Table 2: PMHS characteristics

Shot	Crew	PMHS	Size	Sex	Age	Tibia vBMD (mg/cm^3)		T-Score	Mass (kg)	Stature (cm)	BMI (kg/m^2)
						Left	Right				
SA1	1	SM117	50^{th}	M	58	379.19	380.14	1.6	95.10	182.9	28.4
	2	SM118	50^{th}	M	54	350.64	334.96	0.1	82.50	174.5	27.1
SA2	1	SM120	50^{th}	M	69	323.27	329.99	0.8	81.80	188.0	23.1
	2	SM119	50^{th}	M	73	340.19	342.44	-0.7	65.00	181.8	19.7
SA3	1	SF127	75^{th}	F	57	401.71	393.25	-0.9	69.25	170.9	23.7
	2	SF126	5^{th}	F	54	385.65	380.98	-0.5	47.10	159.2	18.6
SA4	1	SF128	75^{th}	F	45	406.26	447.98	0.3	66.06	161.5	25.3
	2	ATD	5^{th}	-	-	-	-	-	48.90	150.1	21.7
SA5	1	SF131	75^{th}	F	55	391.49	392.59	1.0	68.49	165.1	25.1
	2	SF132	5^{th}	F	66	387.13	383.45	1.0	66.36	165.1	24.3
SA6	1	SF133	5^{th}	F	57	324.33	327.75	-0.7	57.42	162.6	21.7
	2	ATD	5^{th}	-	-	-	-	-	48.90	150.1	21.7
SB1	1	SF138	75^{th}	F	50	328.08	321.01	1	74.74	166.6	26.9
	2	SF134	5^{th}	F	53	441.07	438.26	0.5	60.57	171.6	20.6
SB2	1	SM140	50^{th}	M	50	432.02	427.37	0.2	68.72	186.9	19.7
	2	SF135	5^{th}	F	36	326.59	320.37	2.1	56.88	160.3	22.1
SB3	1	SM141	50^{th}	M	55	359.18	361.07	0.7	93.85	168. 5	33.1
	2	SF142	75^{th}	F	75	272.99	316.69	0.1	88.13	164.3	32.6
SB4	1	SM145	50^{th}	M	68	366.39	379.92	2.4	75.30	178.0	23.8
	2	SF148	75^{th}	F	56	367.27	398.79	1.4	69.35	162.9	26.1
SB5	1	SM150	50^{th}	M	26	369.65	381.50	0.3	78.02	181.6	23.7
	2	SF151	5^{th}	F	28	334.69	336.90	-0.6	36.51	159.0	14.4

Table 3: PMHS mass and stature by sex and percentile

Shot	Crew	PMHS	Size	Sex	Mass (kg)	Stature (cm)	BMI (kg/m^2)
SA1	1	SM117	50th	M	95.10	182.9	28.4
SA1	2	SM118	50th	M	82.50	174.5	27.1
SA2	1	SM120	50th	M	81.80	188.0	23.1
SA2	2	SM119	50th	M	65.00	181.8	19.7
SB2	1	SM140	50th	M	68.72	186.9	19.7
SB3	1	SM141	50th	M	93.85	168. 5	33.1
SB4	1	SM145	50th	M	75.30	178.0	23.8
SB5	1	SM150	50th	M	78.02	181.6	23.7
					80.0 ± 10.7	**182.0 ± 4.7**	**24.8 ± 4.5**
SA3	1	SF127	75th	F	69.25	170.9	23.7
SA4	1	SF128	75th	F	66.06	161.5	25.3
SA5	1	SF131	75th	F	68.49	165.1	25.1
SB1	1	SF138	75th	F	74.74	166.6	26.9
SB3	2	SF142	75th	F	88.13	164.3	32.6
SB4	2	SF148	75th	F	69.35	162.9	26.1
					72.7 ± 8.1	**165.2 ± 3.3**	**26.6 ± 3.1**
SA3	2	SF126	5th	F	47.10	159.2	18.6
SA5	2	SF132	5th	F	66.36	165.1	24.3
SA6	1	SF133	5th	F	57.42	162.6	21.7
SB1	2	SF134	5th	F	60.57	171.6	20.6
SB2	2	SF135	5th	F	56.88	160.3	22.1
SB5	2	SF151	5th	F	36.51	159.0	14.4
					54.1 ± 10.7	**163.0 ± 4.8**	**20.3 ± 3.4**

Table 4: Test matrix

Test Series	Target Peak Floor Speed	Target Floor Time-to Peak	Target Peak Seat Speed	Target Seat Time-to-Peak
A	8 m/s	2 ms	5 m/s	4 ms
B	20 m/s	2 ms	4 m/s	7 ms

Instrumentation

The instrumentation locations that are pertinent to this study include the femora, tibiae, and the calcanei. To collect generalized kinematics of body segments in all three planes of motion, six-degree-of-freedom (6-DoF) “motion blocks” are rigidly attached to the distal femora and tibiae, bilaterally (Figure 12). Each motion block is comprised of an aluminum block (Figure 13), to which three orthogonal linear accelerometers (Endevco 7264, 7264B, or 7264C) and three

mutually orthogonal angular rate sensors (DTS ARS Pro or HG) are fixed. The motion blocks are attached to Delrin® blocks that interface between the aluminum and the bone (Figure 14). Delrin® does not create stress points that would occur with a metal interface. The Delrin® surface that is in contact with the bone has a serrated texture to improve conformation to the bone. In addition, the motion blocks that are mounted to the long bones of the lower extremity have pieces of 80-grit sandpaper adhered to the bone beneath the Delrin® to further prevent potential slippage of the motion block during the test.

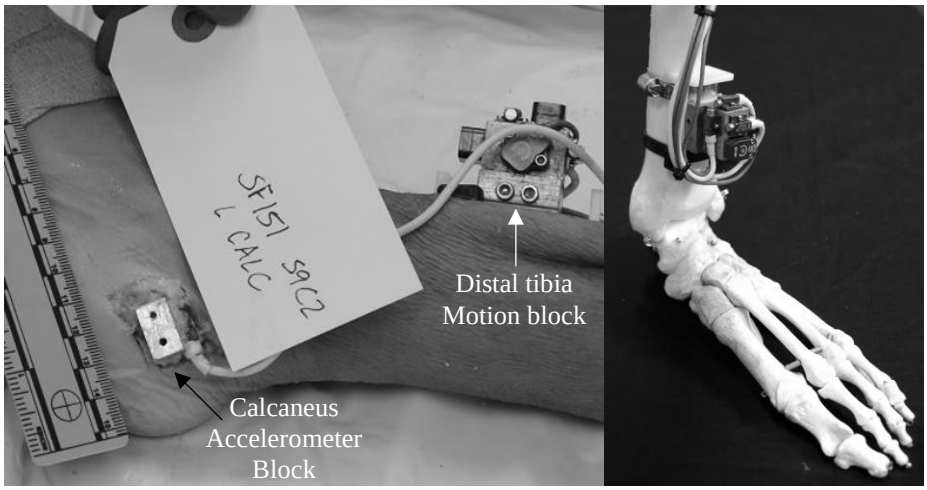

Figure 8: Left photo: left lateral view of left distal leg and foot showing distal tibia motion block and calcaneus accelerometer block. Right photo: location of distal tibia motion block.

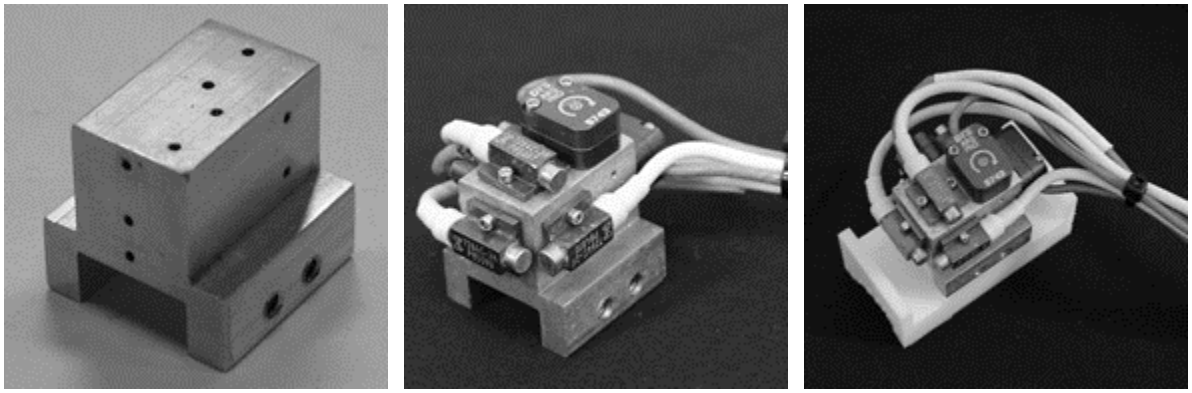

Figure 9: Left: aluminum instrumentation block. Middle: instrumentation block with transducers. Right: assembled motion block, including Delrin® interface for tibia.

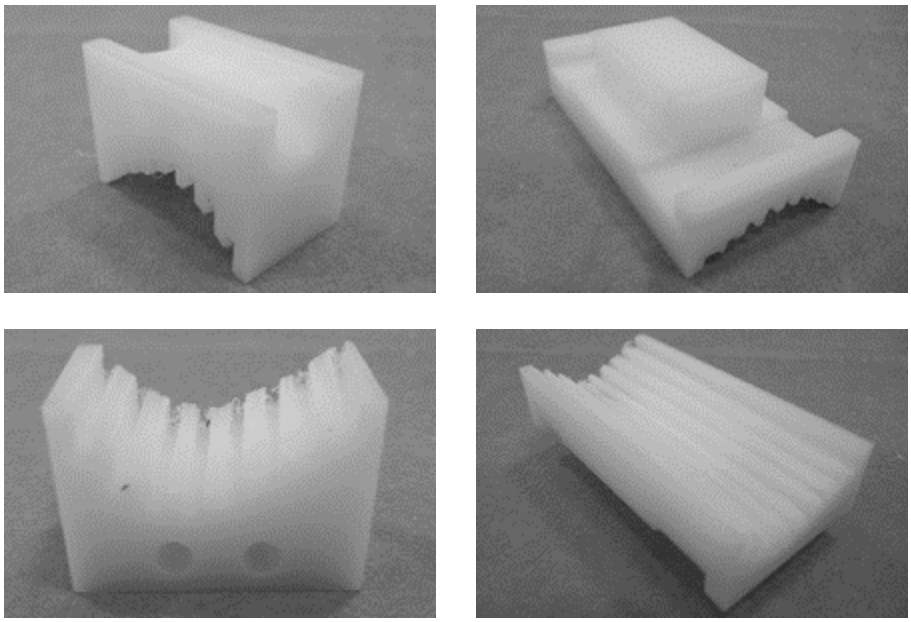

Figure 10: Delrin® interface component of motion blocks. Left column: femur interface. Right column: tibia interface.

The motion blocks are positioned at the center of incisions made at specified distances from anatomical landmarks of the lower extremity as described in the document titled “Signal Conversion Tiger Team [ScoTT] Recommendations for Anatomical Reference Rev. 0.6” (Figure 15). The distal strain gages are positioned proximal to the motion blocks, while the proximal strain gages are centered within the proximal incisions. Metal hose clamps secure the motion blocks to the femur and tibia. A single metal hose clamp is used for the femur, while both a metal hose clamp (proximally) and a 300-pound strength wire tie (distally) are used for the tibia. These are passed through the motion blocks and around the shaft of the bone.

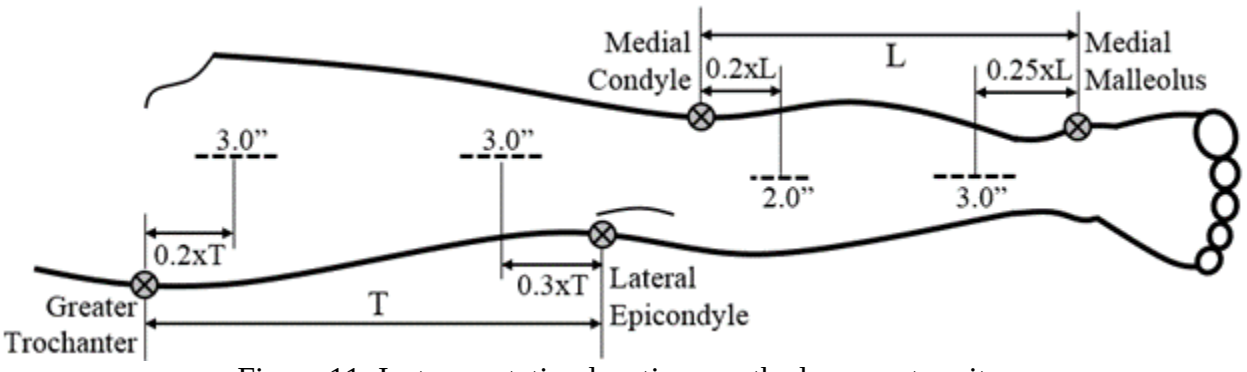

Figure 11: Instrumentation locations on the lower extremity.

Individual accelerometers (Endevco 7264D) are mounted to both calcanei with the sensing axes aligned perpendicular to the plantar surface of the foot (Figure 12). The calcaneus is accessed by making a small window incision on the medial or lateral aspect of the heel. The calcaneus accelerometers are fixed to aluminum blocks with cyanoacrylate. The aluminum blocks are attached to the surface of the calcaneus using cyanoacrylate.

A tilt sensor is rigidly attached to the right ilium of the pelvis and used to position the pelvis at the desired angle on the ALF without the need for external palpation. During pretest preparations, the voltage output of the tilt sensor that corresponds to a pelvis angle of 40 degrees with respect to vertical is determined using the following procedure: With the PMHS in a prone position, the plane of the pelvis is defined by firmly pressing a rigid Plexiglas triangle directly against the pubic symphysis and the right and left ASIS within the abdominal incision. The angle of the pelvis with respect to the coronal plane is determined by placing digital angle finder on the triangle. The cart on which the PMHS is laying is tilted until the pelvis reaches 40 degree angle and the corresponding voltage output of the tilt sensor is recorded. This number is later used to position the PMHS on the ALF.

Single axis strain gages (Micro-Measurements cea-06-250uw-350) are adhered to the lower extremities on the anterior aspect of the proximal and distal femora and tibiae, bilaterally. The sensing axes are aligned with the long axes of the bones. Strain gages are also applied to the medial or lateral aspect of the calcaneus (Micro-Measurements cea-13-062uw-350), with the sensing axes oriented perpendicular to the plantar surface of the foot.

Several steps are followed to adhere each strain gage to the bone surface. First, soft tissue is carefully removed from the bone with a scalpel. Next, the bone is sanded with 80-grit sandpaper. Fatty residue and moisture is removed with acetone. The bone is then cleaned and dried with isopropyl alcohol before applying a thin layer of cyanoacrylate. After the glue layer cures, it is lightly sanded with 120-grit sandpaper and cleaned again with alcohol to prepare for another layer of glue. These steps are repeated until a smooth layer of glue has sealed off any moisture from the bone. The strain gages are prepared for application by attaching lead wires to the solder tabs and cleaning with isopropyl alcohol. A small amount of glue is applied to the back of the strain gage

and the strain gage is gently pressed in place to fix the entire surface to the bone. The strain gage is cleaned and dried with isopropyl alcohol and at least two layers of a protective acrylic coating are applied to seal out moisture. The lead wires are soldered to the extension wire. The strain gages are connected to the signal conditioning using a three-wire configuration, with one bridge completion resistor being external to the data acquisition system and two being internal.

Wires exiting all transducers are strain-relieved to nearby tissue structures within the incisions. Each motion block is covered with a thin piece of latex that is secured with a rubber band. All incisions are stitched closed. The feet, distal tibiae, and distal femora are wrapped in self-adherent elastic wrap to protect protruding instrumentation blocks. All instrumentation cables are passed through tunnels made on the lateral aspect of the body. They exit the body near the acromion process, bilaterally. The wire bundles are strain-relieved to tissue near the scapulae. The transducers are connected to the data acquisition system and it is verified that they are functional before transporting the PMHS to the test site. The PMHS are donned in Spandex bodysuits. The only PPE used in this study are Belleville boots, which are fitted to each specimen based on the anthropometry of the feet. The boots are laced and tightened consistently for all tests.

Imaging

Full body CTs with 0.625 mm thickness slices are collected upon procurement and prior to storing the PMHS in the freezer. CTs are also collected after instrumentation is installed and after the test is conducted. X-rays of all body regions are collected before instrumentation is installed. An additional lateral x-ray of the lower extremities is taken on the ALF after final positioning of the PMHS. Photos of the PMHS on the ALF are taken before and after the test is conducted. Video is recorded using four Vision Research Phantom 9.1v CMOS video cameras operating at 1 kfps, with 50 mm lenses. There are four back-up Photron FASTCAM SA1.1 cameras operating at 10 kfps. The cameras are positioned within protected enclosures. The camera views include the coronal and lateral plane views of the PMHS. Platforms are positioned along the edges of the ALF to delay soil ejecta from blocking the camera view of the occupant platform.

Targets are applied to various anatomical landmarks and to the harness, seat, and test apparatus following the procedure defined in the document titled “WIAMan Bio PT PMHS Positioning

Procedure guidelines. Rev. 0.7". White sport tape is wrapped around the limbs on either side of each joint and cross-hairs are drawn onto the anterior, medial, and lateral aspects of the tape with black paint pens. Target stickers are also placed on palpable bony landmarks of the limbs and head.

Test Procedure

Pretest preparations are performed at the Virginia Tech Center for Injury Biomechanics Crash Sled Laboratory. After specimen preparation, a four day procedure is followed to conduct each test. On day one, specimens are transported from Virginia Tech to APG in a temperature controlled morgue within a secure trailer. Policies and guidelines of federal, state and local laws, in addition to university SOPs, are followed. Upon arrival at APG, the PMHS are transported from the trailer into a morgue in a locked building at an on-site preparation facility. On day two, after final specimen preparation, the PMHS are transported to the test site and seated on the ALF. An environmental chamber is placed over the PMHS, which are supervised overnight. Final specimen positioning and instrumentation verification is performed on the morning of day three. After the test is conducted, the PMHS are transported back to the preparation site and secured overnight. Decontamination of the ALF is performed. On day four, the PMHS are transported back to Virginia Tech for post-test procedures, including polarity checks and autopsies. The PMHS are then handled per the donors' wishes, culminating in cremation. If weather interferes with the ability to safely perform the test, the testing schedule may be extended by one day.

Positioning

The specimen positioning procedure follows the guidelines presented in the document titled "WIAMan Bio PT PMHS Positioning Procedure guidelines. Rev. 0.7". To provide specimen dimensions for the adjustable seat on the ALF, relevant measurements are collected in the laboratory with the specimen seated in the approximate position for testing on the ALF. The height of the shoulder belts is adjusted by feeding them through the appropriate slot in the seatback at the level of the top of the shoulder or slightly higher. The five-point harnesses are reused.

A series of steps are followed to position each specimen. The specimen is seated on the ALF in an approximately correct position with the torso upright against the seatback and the pelvis centered between the left and right edges of the seat. The five-point harness is used to loosely secure the

torso in place. The pelvis is shifted until the tilt sensor indicates the desired pelvis angle of 40 ± 5 degrees with respect to vertical. Once the pelvis is in place, the harness is fully tightened and the angle of the pelvis is checked again. A nominal posture of the lower extremities is implemented for all PMHS, meaning the foot is placed flat on the floor, the shank is oriented perpendicular to the floor, and the thigh is oriented parallel to the floor. This sets the angle of the knees and ankles to 90 degrees. The orientation of the leg is indicated by the position of the lateral malleolus of the fibula and the lateral epicondyle of the femur, while the orientation of the thigh is indicated by the lateral epicondyle of the femur and the H-point of the pelvis. The heels and toes are aligned in the sagittal plane and the lower extremities are positioned 10.5 inches apart, equidistant from the mid-sagittal plane. String is looped around the thighs to keep the knees from splaying open. The hands are loosely secured onto the tops of the thighs with the palms down and the fingers in line with the thighs using break-away tape. The arms rest at the sides of the chest. The head is positioned using a frangible hanging system that is fashioned to remain undisturbed until the test event. A coordinate measurement machine (FARO) is used to verify that various anatomical landmarks are positioned at specified distances relative to one another within specified tolerances.

The data acquisition hardware for each specimen is housed within a reinforced enclosure that provides internal damping for the DAS to protect from shock. Each enclosure is secured to a pedestal behind the seat. A thin layer of rubber is placed between the case and the pedestal. The wire bundles running from the PMHS to the DAS enclosures are strain relieved to the structures that reinforce the seat.

Data Processing

There are two data acquisition systems for each PMHS. The first is a 32-channel DTS G5 sampling using 100 kHz, with a 30-kHz cutoff frequency, 8^{th} order Butterworth profile, low-pass filter. The second is a 64-channel DTS TDAS Pro sampling using 20 kHz with a 4,300 Hz cutoff, 8^{th} order Butterworth profile, anti-aliasing filter. The data from the TDAS Pro are interpolated to 100,000 sps using a cubic spline algorithm. Large spikes that are unrelated to the test are removed. The data are corrected for polarity then zeroed, truncated, and filtered. Linear acceleration and angular speed are filtered following SAE J211/1 recommended practice (SAE, 2014) for Channel Frequency Class 1 kHz. The acceleration data are integrated using Simpson's rule to determine

speed. The strain gage data are adjusted to a baseline of zero and filtered with a 4,950 Hz cutoff frequency, using a 4^{th} order Butterworth profile. The data are not normalized since the differences between groups are being examined. Normalization minimizes these differences. Triggering and synchronization between the separate data acquisition systems is accomplished using a solid state sequencer to send signals through fiber optic cables to the three DAQ systems at the time of charge detonation. The signals are converted to TTL levels within the DAS enclosures and are digitized by each DAS. Triggering is accomplished via a custom interface that provides high-current though BNC cables to an optocoupled resistive switch plugged into each DAS unit.

The SAE-J211 coordinate system described in the document Instrumentation for Impact Test is used for all occupant measurements and calculations (SAE, 2014). Positive X is posterior to anterior, positive Y is left to right, and positive Z is superior to inferior. This coordinate system is based on a standing occupant, so repositioning to the seated posture on the ALF causes a corresponding change in alignment of the axis (e.g. the X direction for the thigh is aligned with vertical during specimen positioning).

Coordinate system transformations of the transducer data are performed to align the signals with the anatomical axes (Hardy et al., 2001). Local motion block coordinate systems and bone coordinate systems are defined within the global CT space. The transducer signals from each motion block are rotated from the local motion block coordinate system to the global CT space. These signals are then rotated from the CT space to the local bone system. The motion block coordinate system is defined by choosing an origin point, a point defining the X-axis direction, and a third point defining the XZ plane. The Y-axis follows from the X and Z axis definitions. A fourth point in the opposite corner of the origin is recorded to provide spatial context and is used to check the measurements and calculations. The femur coordinate system is defined by the medial and lateral epicondyles of the femur, the midpoint between the epicondyles, and the center of a sphere that is fitted to the femoral heading using a least squares sphere fit. The tibia coordinate system is defined by the medial and lateral malleolus, the midpoint between the malleoli, the center of the intercondylar eminence, and the tibial tuberosity.

Data Analysis

Damage Assessment

All PMHS are surveyed for damage to the joints and bones through an examination of post-test CT scans and autopsies. Damage is categorized using the Abbreviated Injury Scale (AIS) 2005 Update 2008, as well as the AO/OTA Classification. The Danis-Weber Classification is used for fibula fractures. The Hawkins Classification is used for talus fractures. The Sanders Classification is used for calcaneus fractures. All damage coding was performed by Kerry Danelson.

Fracture Timing Estimation

The approximate time of fracture is determined with respect to the onset of motion of the calcaneus on the right and left sides. All non-fracture cases provide right-censored timing data, while the fracture cases are left-censored. For each limb that sustained a fracture of the calcaneus, tibia, or both, a probable time of fracture is determined by examining the strain gage traces and associated kinematics collected from the motion blocks. The time at which there is an initial sharp transition in strain is assumed to indicate the onset of a fracture. In general, the first initiation of fracture is characterized by an inflection point in the distal tibia vertical speed (local minimum in acceleration), while complete failure manifests as a noticeable drop in speed, since a considerable amount of energy contributes to the fracture rather than to moving the limb. These two points were used to provide a range of time within which fracture likely occurred. Fractures of the calcaneus and tibia occur at approximately the same time.

Response Envelopes

To illustrate the natural variance in the response of each PMHS type, response envelopes are generated for the distal tibia and distal femur. The envelopes are defined by the minimum and maximum value of vertical speed or acceleration at each time point. The envelopes are created for a given surrogate type (50^{th}-percentile male, 75^{th}-percentile female, or 5^{th}-percentile female), side (right or left), and floor energy level (Series A or Series B). No scaling or shifting is applied.

Peak and Time-To-Peak (TTP)

The peak values of vertical acceleration and speed are determined for tibia Z, femur X, and the floor. The time-to-peak for the tibia and femur is determined by taking the difference between the time associated with the peak value and the time of onset of motion of the tibia or femur. The time at which the signal departs zero is the signal start time. If there are small oscillations at the beginning of the signal, the time point at which the signal crosses zero prior to the first rise is selected as the start time. If a local peak value within the first 5-ms is commensurate with the peak value for the entire event, then the first local peak is used. Otherwise, the overall peak is used. This reduces the effect of slow drift. Within the data, the distinction was unambiguous.

Bone Mineral Density and Mass Estimation

Volumetric bone mineral density (vBMD), which is the bone mineral content per volume of bone, was calculated from the pre-test CT scans at the distal tibia. CT segmentation was used to estimate the mass of the thigh, shank, and foot, bilaterally, for each specimen.

Parametric and Non-Parametric Analyses

In the current study, non-damage cases are right censored, meaning the stimulus value (i.e. peak acceleration) is below the level that will cause damage. Conversely, the damage cases are left censored, meaning the level of input has surpassed the actual threshold of injury. Because the dataset in the current study is doubly censored (mix of right and left censored data points) the consistent threshold (CT) survival analysis method is implemented (Nusholtz and Mosier, 1999). Parametric curve fits are performed to estimate the probability of fracture of the calcaneus or tibia for a given kinematic variable (i.e. peak tibia vertical acceleration). The sigmoid function employed by Hardy et al., 2001 is used, (Equation 1), where Y represents values along the continuous curve fit to the dichotomous damage outcome. The results of both methods are compared in one case: calcaneus fracture with respect to peak tibia vertical acceleration. Point biserial correlation is also conducted to examine potential relationships between the peak accelerations and speeds of the femur or tibia with corresponding damage to the tibia, talus, or calcaneus; vBMD; and mass below the knee. This correlation method is appropriate for examining relationships between binary variables and continuous variables.

$$Y = 1 / (1 + \exp(a - b * X)) \qquad \text{Eq. 1}$$

CHAPTER 3

RESULTS

Damage Response

The damage results for the lower extremity are described herein. Appendix B provides a detailed summary of the damage results for the lower extremities of all PMHS, as well as a listing of damage coding. Damage is grouped by individual PMHS and presented in the order that the PMHS were tested.

Table 5 and Table 6 present the frequency of fractures for each bone in the lower extremity from the current study and the Task 4.2/Matrix Shot dataset, respectively. Damage is distinguished between the right and left side of the body. A capitalized and bolded "**R**" or "**L**" indicates that damage to this region was major (higher in severity), while a lower case "r" or "l" indicates that the damage was minor (lower in severity). Damage is characterized as major when it compromises the structural integrity of the bone.

The current study resulted in fractures of forty-seven individual bones in the lower extremities of twelve PMHS. Damage was sustained by PMHS in all three categories (50^{th}-percentile male, 75^{th}- and 5^{th}-percentile females) on both the right and left side of the body. The only instance of pertinent lower extremity damage that occurred with the lower-energy floor condition was a case of minor damage to the talus of a 5^{th}-percentile female. One proximal femur fracture was observed on the left side of SA3C2 (SF126) in the lower-energy floor condition, however this fracture passed through a local region of cancerous bone. This femur fracture was not included in the subsequent analysis. The higher-energy floor condition resulted in numerous fractures of the lower extremity. The previous Task 4.2/Matrix Shot test series resulted in fractures of fifteen individual bones in the lower extremities of five PMHS. Damage in this test series was not observed in the tibia nor the fibula. The majority of the damage occurred to the talus and calcaneus. No open fractures were observed in either study.

Table 5: PMHS lower extremity damage summary for the current study

Test	PMHS	Type	Femur	Tibia	Fibula	Talus	Calcaneus	Midfoot	Forefoot
SA1C1	SM117	M 50th							
SA1C2	SM118	M 50th							
SA2C1	SM120	M 50th							
SA2C2	SM119	M 50th							
SA3C1	SF127	F 75th							
SA3C2	SF126	F 5th	**L**						
SA4C1	SF128	F 75th							
SA5C1	SF131	F 75th							
SA5C2	SF132	F 5th							
SA6C1	SF133	F 5th				l			
SB1C1	SF138	F 75th		r/**L**	**L**	r	**R**	r/l	l
SB1C2	SF134	F 5th	**L**	l		**R**	**R/L**	l	l
SB2C1	SM140	M 50th	**L**				**R/L**		l
SB2C2	SF135	F 5th				l	**R/L**	r	
SB3C1	SM141	M 50th					**L**		
SB3C2	SF142	F 75th		**L**	**L**	r/l	**R/L**	r	
SB4C1	SM145	M 50th		r		r	**L**		
SB4C2	SF148	F 75th		r/**L**	**L**	l	**R/L**		l
SB5C1	SM150	M 50th	**L**						
SB5C2	SF151	F 5th				r	**R/L**		

Table 6: PMHS lower extremity damage summary for Task 4.2/Matrix Shot

Test	PMHS	Type	Femur	Tibia	Fibula	Talus	Calcaneus	Midfoot	Forefoot
MS1C1	SM91	M 50th							
MS4C1	6541	M 50th					**R/L**		
MS5C1	SM85	M 50th					**R**		
MS5C2	SM90	M 50th							
MS7C1	6504	M 50th				l	**R/L**	r, l	r, l
MS11C1	SM94	M 50th				**L**	**R/L**		
MS14C1	6601	M 50th				r	**R**		

Femur

In addition to the femur fracture that occurred through cancerous bone of a small female PMHS during Series A, three femur fractures were sustained by three PMHS on the left side during Series B (higher-energy floor condition). Two were sustained by 50th-percentile males, while one was sustained by a 5th-percentile female. All femur fractures observed in this study are classified as major damage. The three non-cancer cases occurred at the mid-diaphysis and involved complete transection of the shaft of the femur with associated fragments. Examples are shown in Figure 16 and Figure 17. The fracture in Figure 16 resulted from combined bending and torsion. This fracture fits within the Müller AO 32-B1.2 classification.

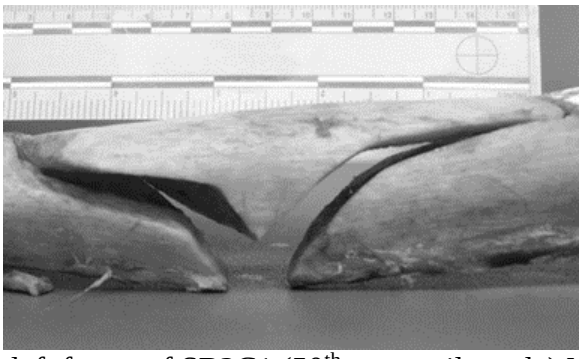

Figure 12: Fracture of the left femur of SB2C1 (50th-percentile male) Müller AO 32-B1.2. Right lateral view; right side of photo is distal.

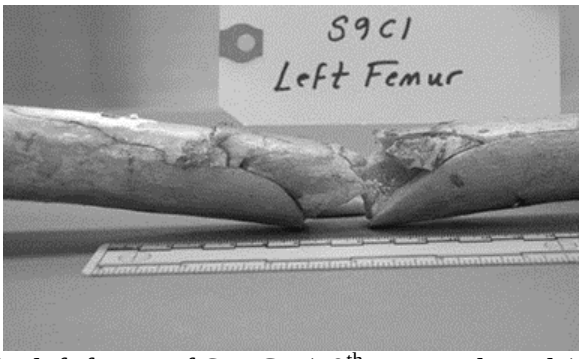

Figure 13: Fracture of the left femur of SB5C1 (50th-percentile male). Left lateral view; right side of photo is proximal.

Tibia and Fibula

Series B (higher-energy floor condition) produced seven cases of damage to the distal tibia in four female PMHS and one male. Two 75th-percentile females sustained bilateral damage to the tibia. There were four cases of minor tibia damage that occurred across all sexes and percentiles. Three of these were pilon fractures that were observed in females (Figure 18). The fourth case of minor tibia damage, which involved trivial damage to the anterior and posterior margins of the tibial plafond, was sustained by a 50th-percentile male (SB4C1, SM145). There were three cases of major damage to the distal tibia that involved considerable bone height loss (Figure 19). All three cases occurred on the left side of 75th-percentile females and had associated ipsilateral fibula fractures (Figure 20). Two of the fibula fractures involved complete transection of the distal third of the diaphysis, one of which also sustained a fracture of the head of the fibula. A third fibula sustained a fracture of the lateral malleolus.

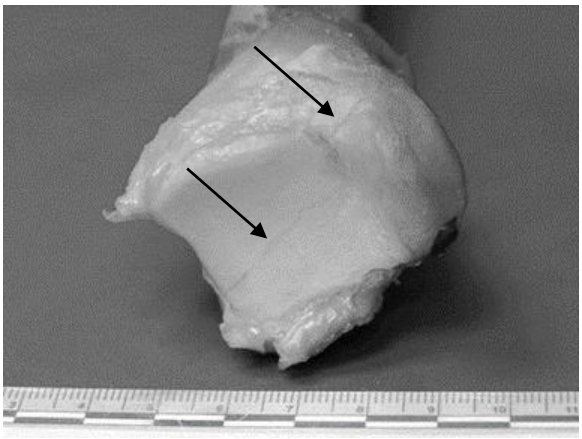

Figure 14: Pilon fracture of the right tibia of SB1C1 (75th-percentile female) oriented from the lateral aspect to the anterior colliculus. Inferior view; right side of photo is medial.

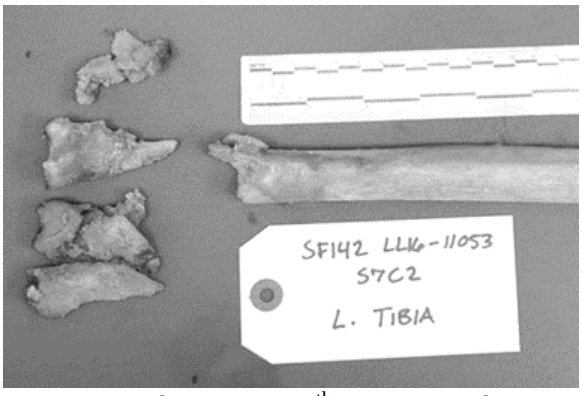

Figure 15: Shattered left distal tibia of SB3C2 (75th-percentile female). Anterior view; right side of photo is proximal.

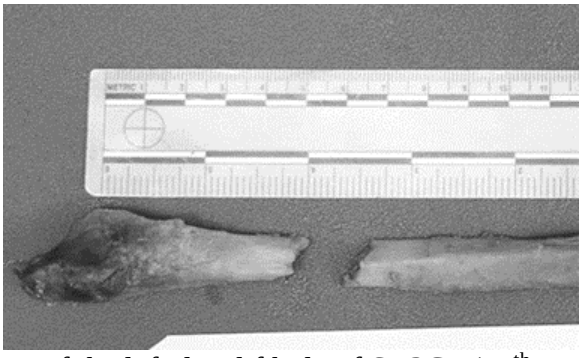

Figure 16: Oblique fracture of the left distal fibula of SB3C2 (75th-percentile female). Anterior view; right side of photo is proximal.

Talus

In Series A (lower-energy floor condition) there was a single case of minor damage to the talus of a 5th-percentile female that involved a partial fracture of the neck of the talus. In Series B (higher-energy floor condition) there were eight talus fractures sustained by seven PMHS. One 75th-percentile female sustained bilateral talus fractures. All but one of the seven cases occurred to females. Minor damage was observed across all five surfaces of the talus and in all sexes and percentiles (Figure 21). There was a single case of major damage to the talus that occurred in a 5th-percentile female (Figure 22). This fracture involved a nearly complete transection of the neck of the talus that separated the anterior and posterior portions of the bone. This fracture initiated at the sulcus tali, which is an oblique groove on the underside of the talus.

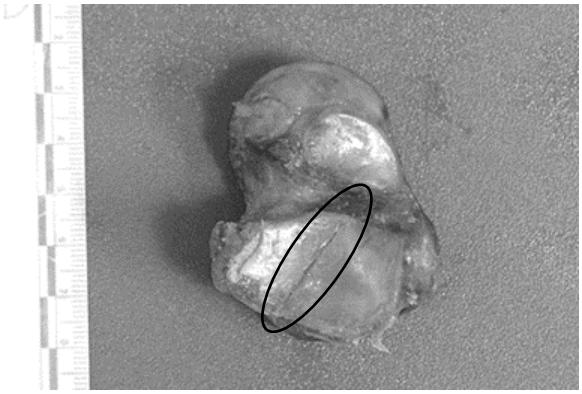

Figure 17: Fracture to the posterior calcaneal articular surface of the right talus of SB3C2 (75th-percentile female). Inferior view; right side of photo is medial.

Figure 18: Fracture of the right talus of SB1C2 (5th-percentile female). Medial view; right side of photo is posterior.

Calcaneus

Crushed calcanei were the most frequently observed fractures, with fifteen cases observed for the twenty lower extremities in Series B (higher-energy floor condition). All PMHS in this test condition sustained damage to either one or both calcanei with the exception of one 50th-percentile male. Six PMHS incurred bilateral calcaneus damage. Figure 23 shows an example of a typical calcaneus fracture. The calcaneus fractures were non-displaced, but fragmentation was revealed during autopsy. All calcaneus damage was intraarticular.

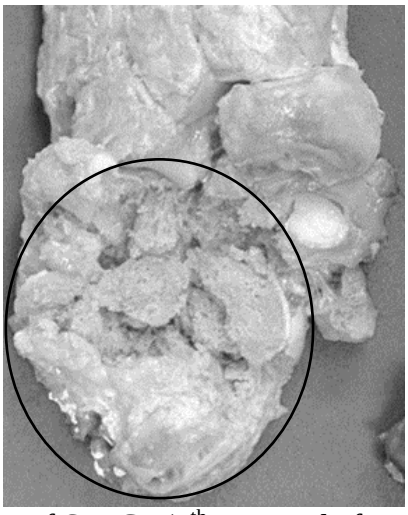

Figure 19: Crushed left calcaneus of SB1C2 (5th-percentile female). Superior view; right side of photo is medial. Tibia and talus are removed.

Midfoot

In Series B (higher-energy floor condition), there were five cases of damage to the navicular. All navicular damage occurred at the "beak" of the navicular. The two observed cuboid fractures were both associated with navicular fractures. All navicular and cuboid fractures were sustained by females. A typical example of fractures of the navicular and cuboid is shown in Figure 24.

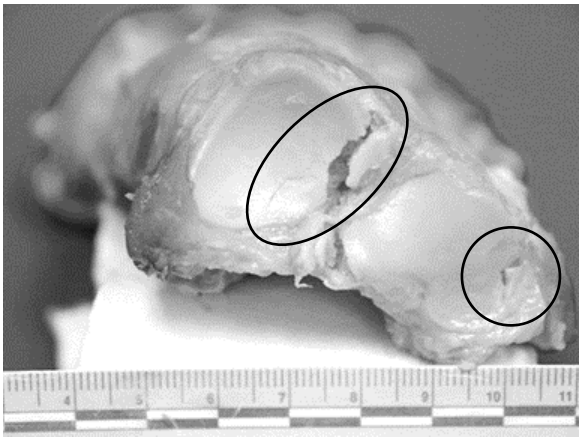

Figure 20: Fractures of the beak of the right navicular and the lateral portion of the posterior surface of the right cuboid of SB1C1 (75th-percentile female). Posterior view; right side of photo is lateral; hindfoot is removed.

Forefoot

There were four cases of forefoot damage in Series B (higher-energy floor condition). Damage was limited to the third, fourth, and fifth metatarsals and was observed across all sexes and percentiles. An example is shown in Figure 25. Damage to the fifth proximal phalange was observed in a 75th-percentile female. All forefoot damage occurred to the proximal portion of the bones and on the left lower extremity.

Figure 21: Fracture of the left proximal 4th metatarsal of SB2C1 (50th-percentile male). Superior view; right side of photo is proximal).

Fracture Timing

Table 7 provides the approximate times of fracture in Series B. For each lower extremity that sustained a fracture of the tibia and/or calcaneus, a window of time between the initiation of the fracture and complete failure is provided. In the current study, fractures of the calcaneus and tibia occurred within three milliseconds of the onset of motion of the calcaneus. Table 8 provides the fracture timing for Task 4.2/Matrix Shot test series. Femur fracture timing estimations are provided in Table 9.

Table 7: Fracture timing with respect to onset of calcaneus motion for the current study

PMHS	Side	Fracture Location(s)	Fracture Time (ms)
SB1C1	R	Tibia & Calcaneus	1.46 - 1.61
	L	Tibia	0.90 - 1.14
SB1C2	R	Calcaneus	1.23 - 1.73
	L	Tibia & Calcaneus	1.03 - 1.26
SB2C1	R	Calcaneus	1.41 - 1.94
	L	Calcaneus	0.55 - 1.04
SB2C2	R	Calcaneus	1.43 - 2.01
	L	Calcaneus	0.78 - 1.39
SB3C1	R	-	-
	L	Calcaneus	0.66 - 0.94
SB3C2	R	Calcaneus	1.45 - 1.63
	L	Tibia & Calcaneus	0.64 - 0.92
SB4C1	R	Tibia	1.98 - 1.38
	L	Calcaneus	0.73 - 0.95
SB4C2	R	Tibia & Calcaneus	0.60 - 2.37
	L	Tibia & Calcaneus	0.68 - 1.11
SB5C1	R	-	-
	L	-	-
SB5C2	R	Calcaneus	0.59 - 1.37
	L	Calcaneus	1.26 - 2.05

Table 8: Fracture timing with respect to onset of calcaneus motion for Task 4.2/Matrix Shot

PMHS	Side	Fracture Location	Fracture Time (ms)
MS1C1	R	-	-
	L	-	-
MS4C1	R	Calcaneus	8.5
	L	Calcaneus	6.8 - 7.5
MS5C1	R	Calcaneus	7.4
	L	-	-
MS5C2	R	-	-
	L	-	-
MS7C1	R	Calcaneus	2.6
	L	Calcaneus	1.6
MS11C1	R	Calcaneus	8.8
	L	Calcaneus	8.3
MS14C1	R	Calcaneus	7.9
	L	-	-

Table 9: Femur fracture timing with respect to onset of calcaneus motion for the current study

PMHS	Side	Fracture Time (ms)
SA3C2	R	-
	L	6.77*
SB1C2	R	-
	L	8.50
SB2C1	R	-
	L	7.26
SB5C1	R	-
	L	6.22

*****This fracture occurred through cancerous bone.

Kinematics Response

Video

Still frames from high-speed video are presented from 0, 2.5, 5, 7.5, 10, 15, 20, 25, and 30 milliseconds. Figure 26 shows the 75th- and 5th-percentile females from Series B Shot 1, while Figure 27 shows the 50th-percentile male and 5th-percentile female from Series B Shot 2. Appendix C provides still frames of video captured during all tests for qualitative comparison.

A visual comparison does not reveal gross differences between female and male PMHS movement. There is very little movement of the lower extremities within the first few milliseconds. The lateral view of the lower extremities shows progressive flexion of the hips, knees, and ankles throughout the duration of the event, with the vertical orientation of the shank being maintained throughout the first thirty milliseconds. The deformation profile of the floor is visible within the first several milliseconds.

Still frames showing the booted foot at time-zero and the time of calcaneus failure are shown in Figure 28 for the right lower extremity of SB1 Crew 2. At the time of fracture, the lower extremity has not begun to move and the boot/heel are being compressed.

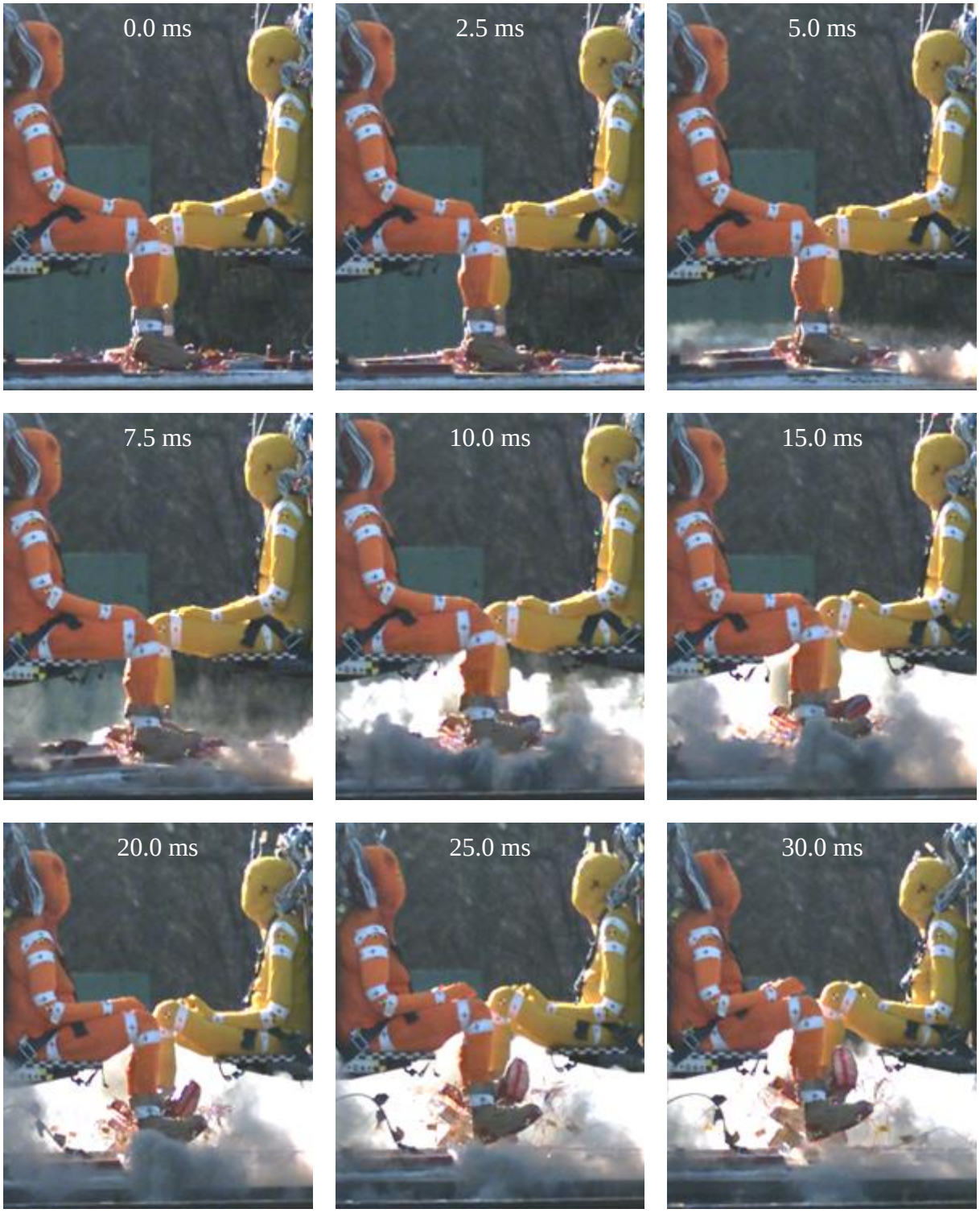

Figure 22: Series B Shot 1. 75th-percentile female (left) and 5th-percentile female (right).

Figure 23: Series B Shot 2. 50th-percentile male (left) and 5th-percentile female (right).

Figure 24: SB1 Crew 2 (yellow) right calcaneus fracture. Left photo: time-zero. Right photo: 3.5 ms from time-zero.

Transducer Data

The transducer data collected by the motion blocks on the distal femur and tibia are presented herein. Plots of global vertical speed and acceleration for both the lower-energy and higher-energy floor conditions are shown for the first twenty milliseconds of the event. Each plot contains individual traces for the left lower extremity. Appendix D provides a comprehensive catalog of individual traces.

Series A Tibia Response

In Series A (lower-energy floor condition) the general shape and duration of the tibia axial (global vertical) speeds were similar between females and males. However, the tibiae of the female PMHS generally had higher vertical speeds and they reached those speeds earlier in the event than the male PMHS (Figure 29). The tibiae of the females also reached higher peak accelerations than those of the males. Moreover, the tibiae of the 5th-percentile females reached higher peak accelerations than those of the 75th-percentile females in the lower energy floor condition (Figure 30).

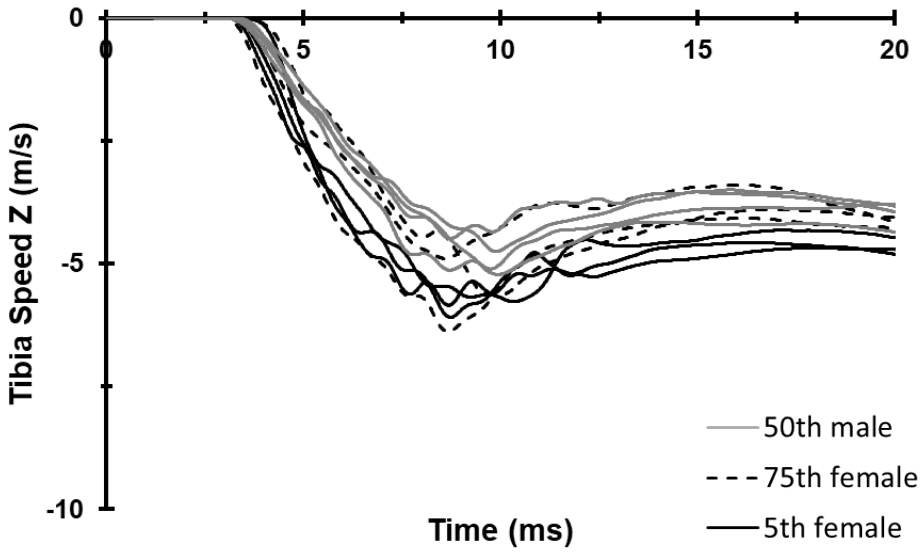

Figure 25: Series A left tibia vertical (Z-axis) speed.

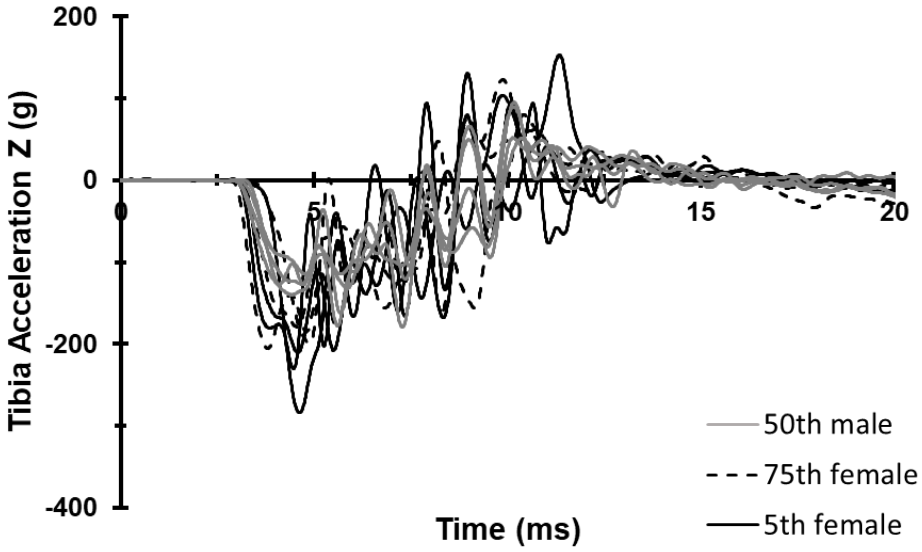

Figure 26: Series A left tibia vertical (Z-axis) acceleration.

Series B Tibia Response

In Series B, the tibia vertical speeds were approximately twice those in Series A (Figure 31). Again, the shape and durations of the tibia vertical speed responses were similar between females and males, but the differences in response between females and males were not observed in Series B. The left tibia vertical acceleration responses of the 75th-percentile females in Series B show large peaks that correspond to the three cases of major tibia damage sustained by these lower extremities (Figure 32).

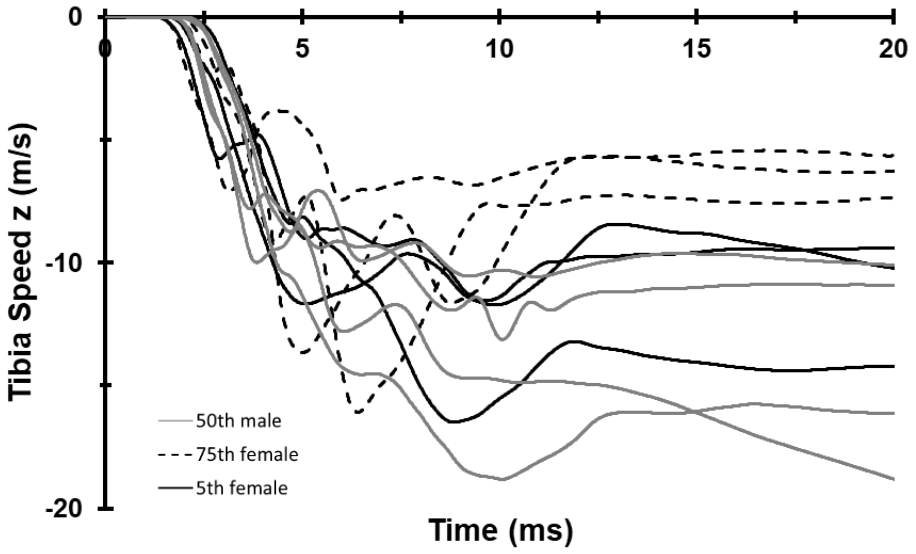

Figure 27: Series B left tibia vertical (Z-axis) speed.

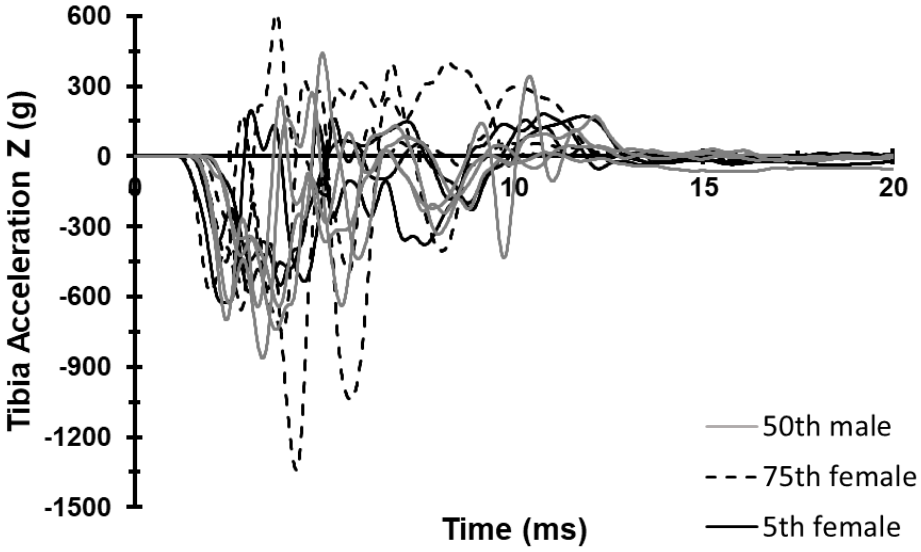

Figure 28: Series B left tibia vertical (Z-axis) acceleration.

Series A Femur Response

In Series A, the general shape of the posteroanterior (global vertical) femur speeds are similar between female and male PMHS. However, the femora of the females attain greater peak speeds, earlier in the event (Figure 33). In addition, the heavier extremities exhibit an oscillatory square unimodal response in the femur vertical acceleration response (Figure 34). The femora of the 5th-percentile female PMHS in particular undergo larger vertical accelerations earlier in the event and the acceleration response is shorter.

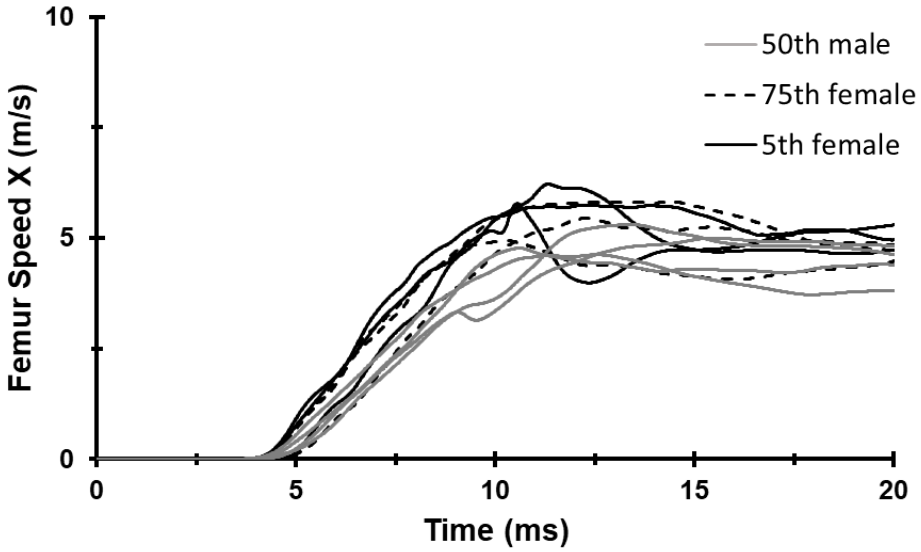

Figure 29: Series A left femur vertical (X-axis) speed.

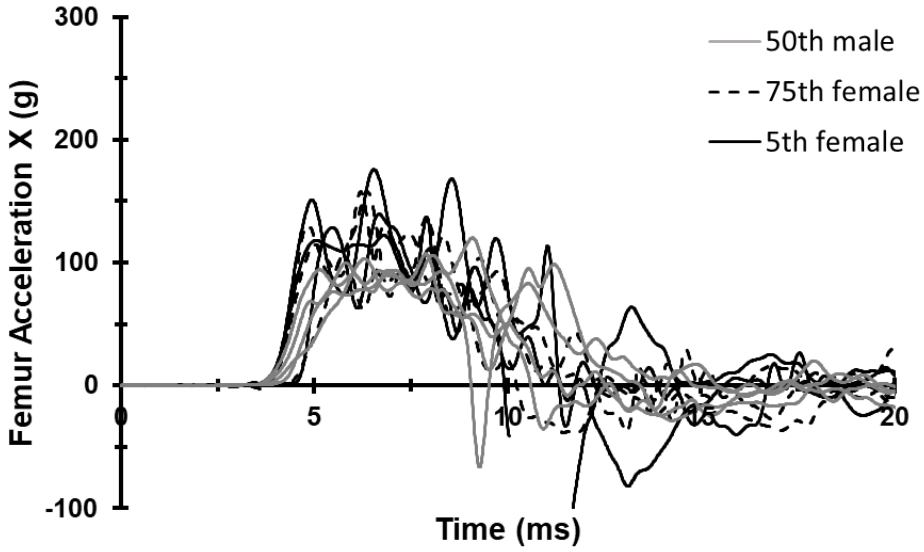

Figure 30**:** Series A left femur vertical (X-axis) acceleration.

Series B Femur Response

In Series B, the three traces with noticeable drop in speed between seven and ten milliseconds from time-zero correspond to the previously reported femur fractures (Figure 35). In addition, heavier lower extremities exhibit a second-order effect in the vertical speed response of the femur that is evident in Figure 35. The associated acceleration responses are triangular and bimodal in nature (Figure 36). The duration of posteroanterior femur acceleration is shorter for most female PMHS than male PMHS.

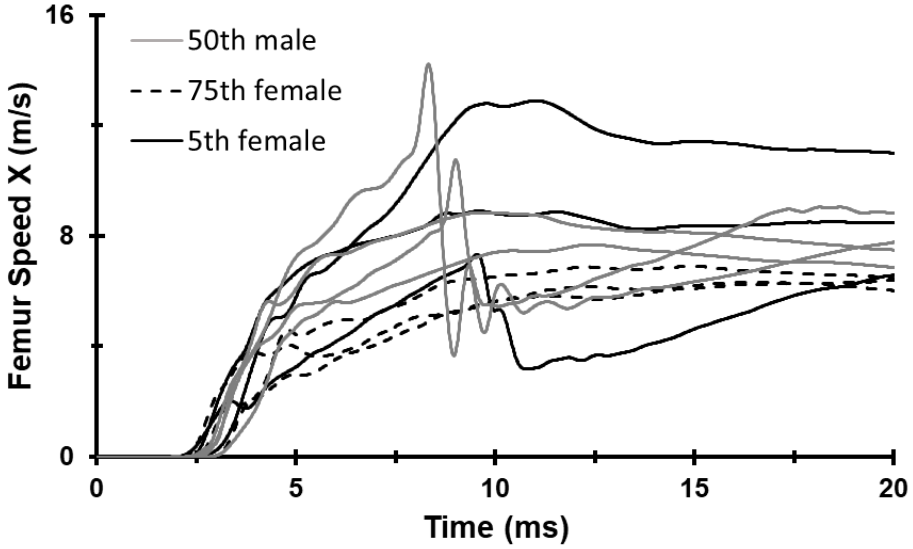

Figure 31: Series B left femur vertical (X-axis) speed.

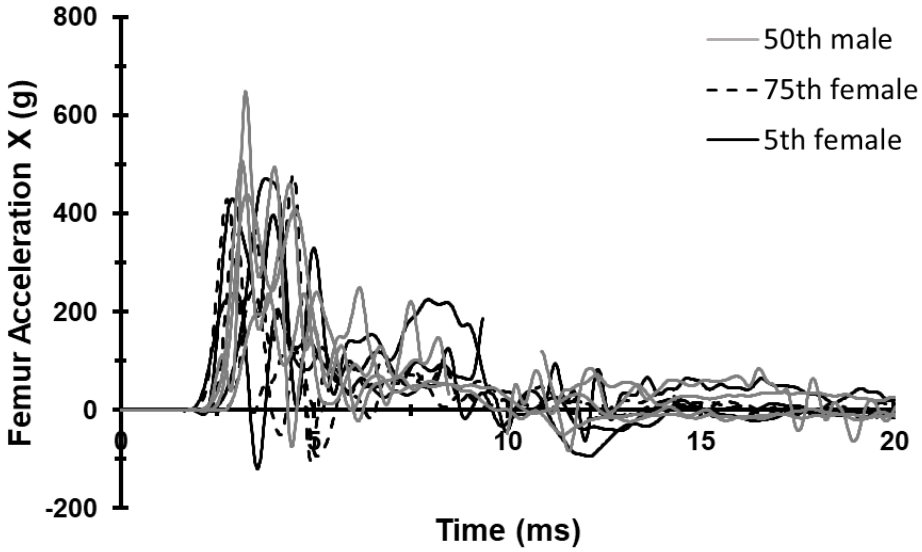

Figure 32: Series B left femur vertical (X-axis) acceleration.

Response Envelopes

Several exemplar response envelope plots are presented. Appendix E provides all response envelopes. Figure 37 and Figure 38 show the left distal tibia global vertical speed in Series A, with the 50th-percentile male envelope being common to both plots. It is evident that the 5th-percentile female envelope overlaps with that of the 50th-percentile male to a lesser extent than the 75th-percentile female envelope.

Figure 39 and Figure 40 show the left distal femur global vertical speed in Series B, with the 5th-percentile female envelope being common to both plots. The 5th-percentile females maintain greater global vertical femur speeds throughout the duration of the event than both the 50th-percentile males and the 75th-percentile females.

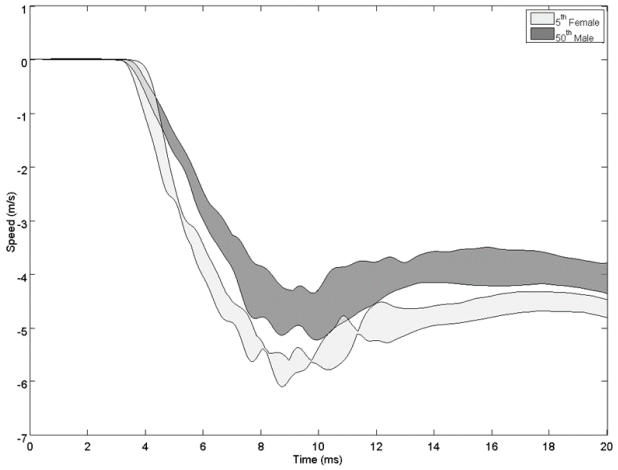

Figure 33: Series A left tibia Z-axis speed 5th-percentile females and 50th-percentile males.

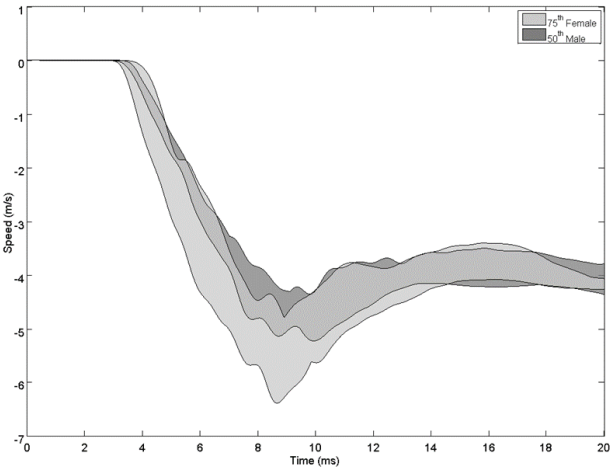

Figure 34: Series A left tibia Z-axis speed 75th-percentile females and 50th-percentile males.

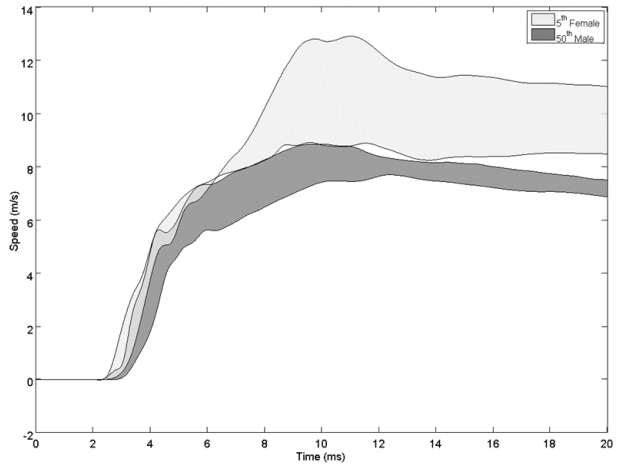

Figure 35: Series B left femur X-axis speed 5th-percentile females and 50th-percentile males.

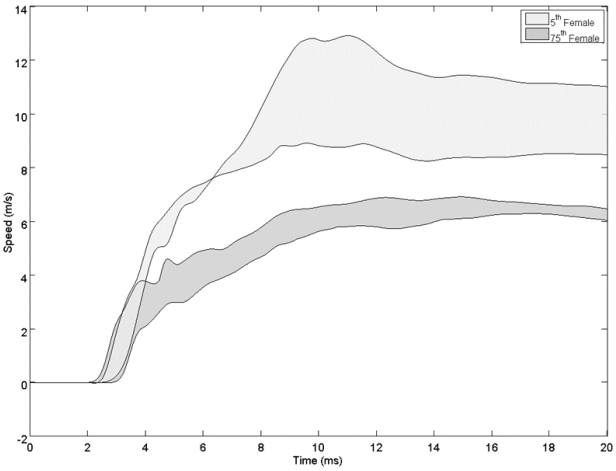

Figure 36: Series B left femur X-axis speed 5th and 75th-percentile females.

Peak Acceleration and Speed

The following figures present the damage level of the tibia, talus, or calcaneus plotted as a function of the peak acceleration or speed of the tibia or femur. Damage level is specified by the color of the marker, with light grey, dark grey, and black indicating no damage, minor damage, and major damage, respectively. The shape of the markers indicates the sex and percentile, with circles, squares, and triangles representing 50th-percentile males, 75th-percentile females, and 5th-percentile females, respectively.

Tibia Damage Level

Figure 41 and Figure 42 present damage level of the tibia as a function of peak Z-axis acceleration and speed of the distal tibia, respectively. Tibia damage is associated with higher peak axial (global vertical) accelerations, however the large number of non-damage cases at lower peak accelerations makes this trend insignificant. As peak axial (global vertical) acceleration of the distal tibia increases, the incidence of tibia fracture increases. No trend is seen for peak distal tibia axial speed and tibia fracture.

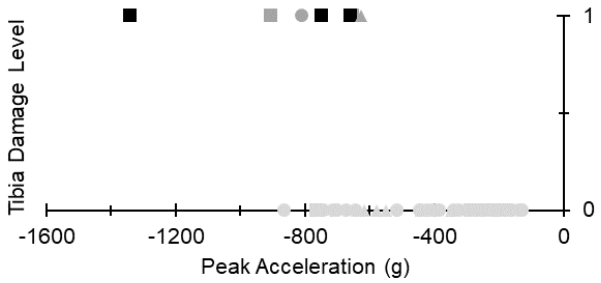

Figure 37: Tibia damage vs. peak distal tibia Z-axis acceleration.

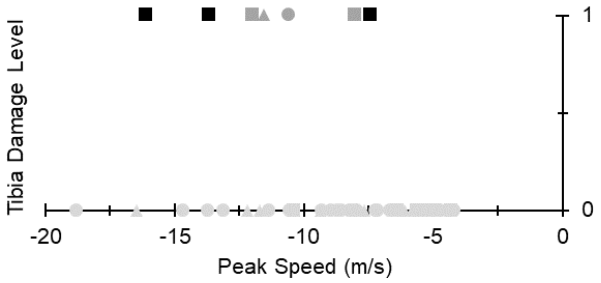

Figure 38: Tibia damage vs. peak distal tibia Z-axis speed

Figure 43 and Figure 44 present damage level of the tibia as a function of peak X-axis acceleration and speed of the distal femur, respectively. No relationship between peak distal femur posteroanterior (global vertical) acceleration and tibia fracture is evident. Tibia fracture does not appear to be related to peak distal femur posteroanterior speed either.

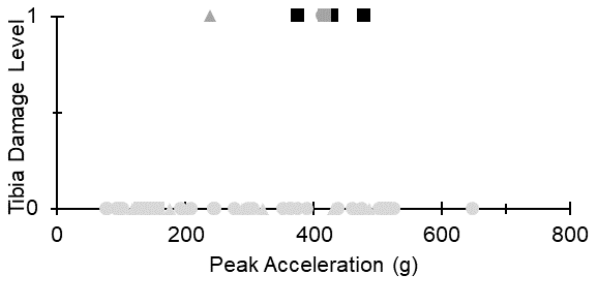

Figure 39: Tibia damage vs. peak distal femur X-axis acceleration.

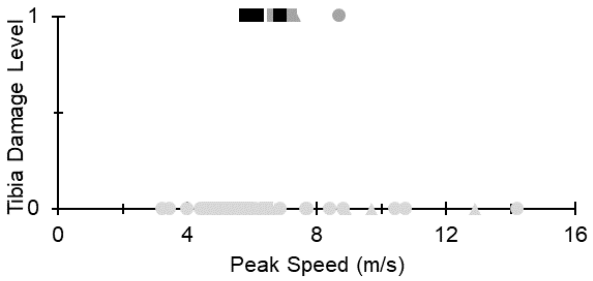

Figure 40: Tibia damage vs. peak distal femur X-axis speed.

75th female 5th female 50th male No Damage Minor Damage Major Damage

Talus Damage Level

Figure 45 and Figure 46 present damage level of the talus as a function of peak Z-axis acceleration and speed of the distal tibia, respectively. A limited trend between increasing peak axial (global vertical) acceleration of the distal tibia and increased incidence of talus fracture is demonstrated. However, the more severe talus damage is observed at lower peak accelerations, and there is only a single damage case at an acceleration higher than the highest measured for non-fracture. No relationship is observed between peak axial speed of the distal tibia and talus fracture.

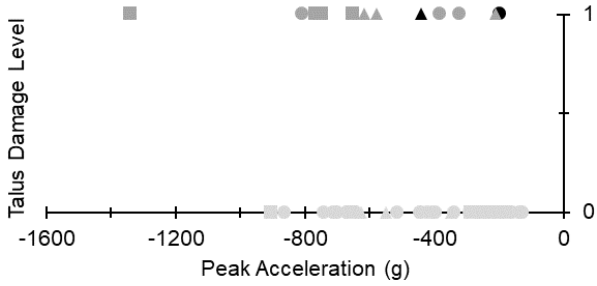

Figure 41: Talus damage vs. peak distal tibia Z-axis acceleration.

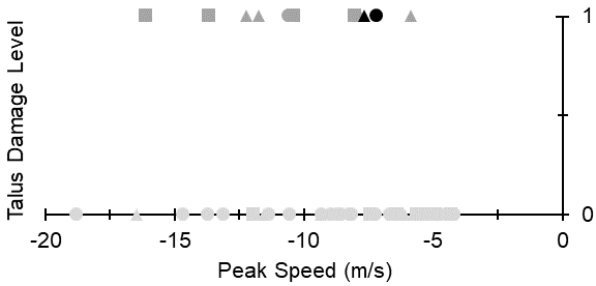

Figure 42: Talus damage vs. peak distal tibia Z-axis speed.

75th female 5th female 50th male No Damage Minor Damage Major Damage

Figure 47 and Figure 48 present damage level of the talus as a function of peak X-axis acceleration and speed of the distal femur, respectively. If the non-fracture point at the highest acceleration is excluded, there is a slight trend towards talus fractures being associated with greater peak posteroanterior (global vertical) acceleration of the distal femur. Talus fracture is not related to peak posteroanterior speed of the distal femur.

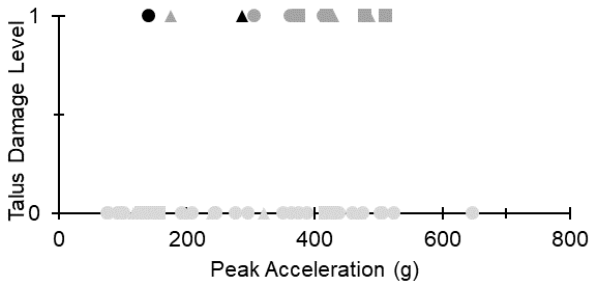

Figure 43: Talus damage vs. peak distal femur X-axis acceleration.

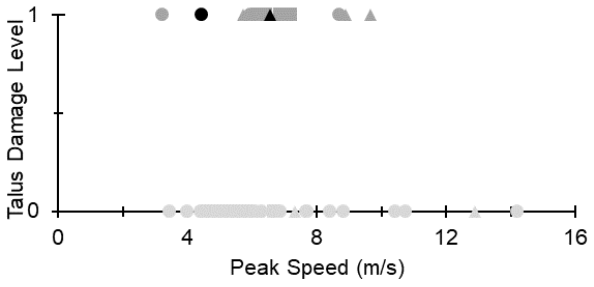

Figure 44: Talus damage vs. peak distal femur X-axis speed.

Calcaneus Damage Level

Figure 49 and Figure 50 present damage level of the calcaneus as a function of tibia peak Z-axis acceleration and speed, respectively. As peak axial (global vertical) acceleration of the distal tibia increases, the incidence of calcaneus fracture increases. No trend is seen for peak axial speed of the distal tibia and calcaneus fracture. However, if the non-fracture case having the largest speed (> 18 m/s) is ignored, a limited trend showing an increase in calcaneus fractures with increased peak speed of the distal tibia emerges.

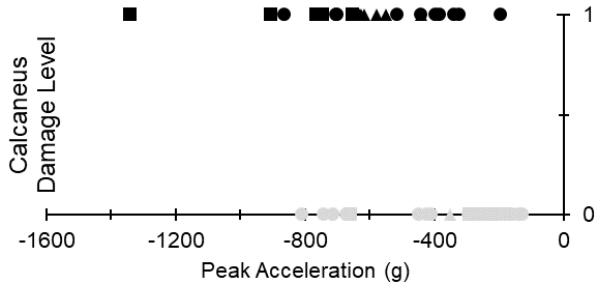

Figure 45: Calcaneus damage vs. peak distal tibia Z-axis acceleration.

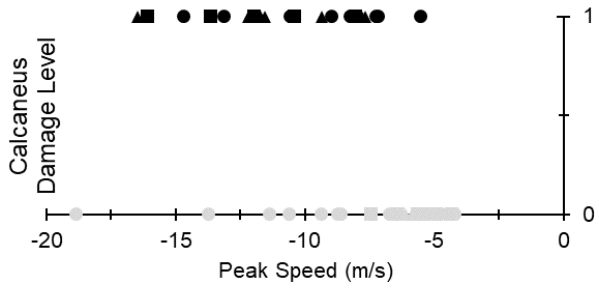

Figure 46: Calcaneus damage vs. peak distal tibia Z-axis speed.

Figure 51 and Figure 52 present damage level of the calcaneus as a function of peak X-axis acceleration and speed of the distal femur, respectively. As peak posteroanterior (global vertical) acceleration of the distal femur increases, the incidence of calcaneus fracture increases. Calcaneus fracture does not correlate with peak posteroanterior speed of the distal femur.

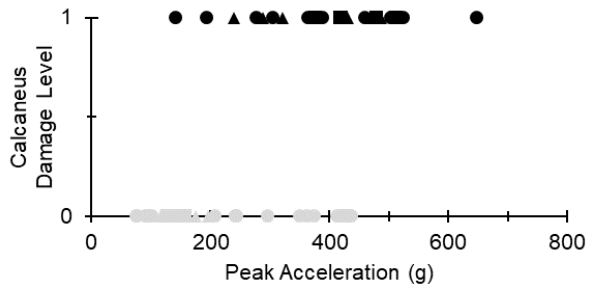

Figure 47: Calcaneus damage vs. peak distal femur X-axis acceleration.

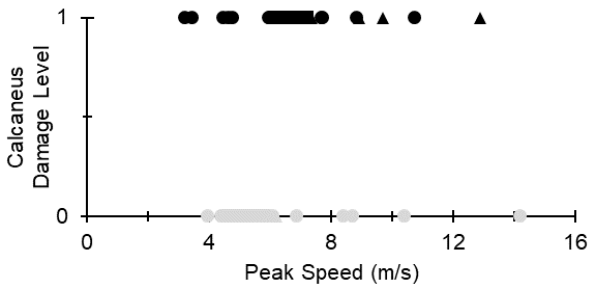

Figure 48: Calcaneus damage vs. peak distal femur X-axis speed.

Peak and Time-to-Peak Acceleration and Speed

Several "point-cloud" plots are generated to illustrate potential relationships between lower extremity kinematics and damage level. The damage under investigation in this analysis includes that of the tibia, talus, and calcaneus, since these are the primary weight bearing bones of the foot and ankle. A single peak value of acceleration or a single peak value of speed measured by the accelerometers on the distal tibia or distal femur is plotted on the vertical axis, while the time taken to reach that peak value (time-to-peak, or TTP) is plotted on the horizontal axis. These values are tabulated in Appendix F. The damage locations in this analysis include the tibia and fibula, which are grouped together and are concomitant for severe damage cases; the talus; and the calcaneus. The damage to these regions is divided into three categories: no damage, minor damage, and major damage. Damage level is specified by the color of the marker, with light grey, dark grey, and black indicating no damage, minor damage, and major damage, respectively. The shape of the markers indicates the sex and percentile, with circles, squares, and triangles representing 50th-percentile males, 75th-percentile females, and 5th-percentile females, respectively. Markers from the Task 4.2/Matrix Shot test series are distinguished by a plus (+) or minus (-) symbol. The markers for the PMHS outfitted with PPE contain a plus symbol, while all other PMHS in the Task 4.2/Matrix Shot test series are marked by a minus symbol. Lower extremities with ipsilateral damage to specified bones are indicated by a black border on the marker.

Peak Tibia Vertical Acceleration and TTP

Overall, greater peak axial acceleration of the distal tibia is required to fracture the calcaneus for a shorter time-to-peak for acceleration of the distal tibia (Figure 53). For a longer time-to-peak, ostensibly reflecting longer contact time between the boot and floor, lower levels of peak acceleration of the distal tibia can result in calcaneus fracture. For acceleration time-to-peak less than 3 ms, calcaneus fracture does not occur below 400 g. For acceleration time-to-peak greater than 3 ms, calcaneus fracture occurs below 400-g roughly 50-percent of the time within these tests. In addition, for less than 3-ms acceleration time-to-peak, the average axial acceleration of the distal tibia for which calcaneus fracture occurs is 575 ± 74 g for 5th-percentile female PMHS, 882 ± 272 g for the 75th-percentile female PMHS, and 680 ± 145 g for the 50th-percentile male PMHS. For the 5th-percentile female PMHS, the lowest distal tibia axial acceleration for which calcaneus fracture occurs is 625 g, while the highest distal tibia axial acceleration for which calcaneus fracture does not occur is 640 g (irrespective of time-to-peak acceleration). For the 75th-percentile female PMHS, the lowest distal tibia axial acceleration for which calcaneus fracture occurs is also 640 g. The highest distal tibia axial acceleration for which calcaneus fracture does not occur is 766 g. For the 50th-percentile male PMHS, the lowest distal tibia axial acceleration for which calcaneus fracture occurs is 195 g. The highest distal tibia axial acceleration for which calcaneus fracture does not occur is 807 g. When the analysis is limited to time-to-peak acceleration less than 3 ms, as described previously, the incidence of calcaneus fracture increases as peak axial acceleration of the distal tibia increases. However, the transition from no-fracture to fracture cases is more distinct.

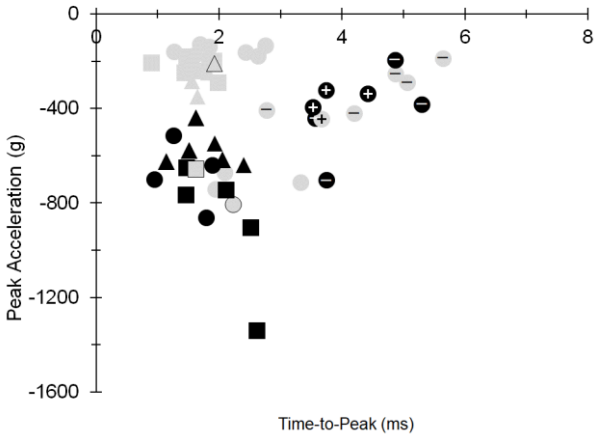

Figure 49: Peak distal tibia Z-axis acceleration vs. time-to-peak for calcaneus damage level. Markers with black borders indicate ipsilateral talus or tibia/fibula damage.

75th female 5th female 50th male No Damage Minor Damage Major Damage

With the exception of one 5th-female PMHS case, the relationship between peak axial acceleration of the distal tibia and time-to-peak acceleration follows the same trends for talus fracture as for calcaneus fracture (Figure 54). That is, for shorter time-to-peak acceleration, greater axial acceleration of the distal tibia is required to produce fracture. For the 5th-percentile females, the lowest distal tibia axial acceleration for which talus fracture occurs is 210 g. The highest distal tibia axial acceleration for which talus fracture does not occur is 640 g. For the 75th-percentile females, the lowest distal tibia axial acceleration for which talus fracture occurs is 904 g. The highest distal tibia axial acceleration for which talus fracture does not occur is 766 g. For the 50th-percentile male PMHS, the lowest distal tibia axial acceleration for which talus fracture occurs is 195-g. The highest distal tibia axial acceleration for which talus fracture does not occur is 864-g.

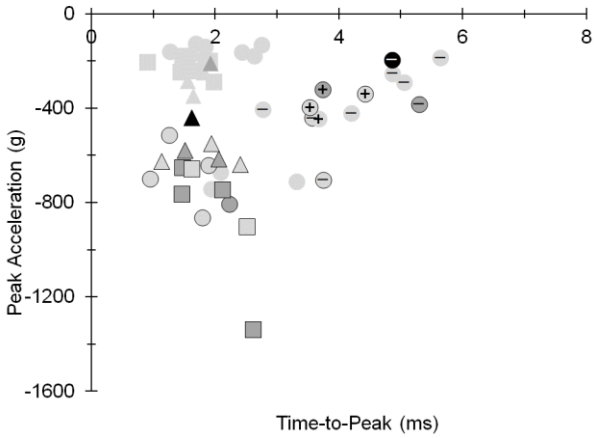

Figure 50: Peak distal tibia Z-axis acceleration vs. time-to-peak for talus damage. Markers with black borders indicate ipsilateral calcaneus or tibia/fibula damage.

75th female 5th female 50th male No Damage Minor Damage Major Damage

Few combined tibia and fibula fractures are seen overall (Figure 55). Unlike the calcaneus and talus cases, no combined distal tibia and fibula fractures occurred at the lower levels of peak axial acceleration of the distal tibia. There is one such fracture in a 5th-percentile female PMHS at 625 g, which is the lowest peak distal tibia axial acceleration for which a combined distal tibia and fibula fracture is seen. For the 5th-percentile female, the highest distal tibia axial acceleration for which a tibia/fibula fracture does not occur is 640 g. One tibia/fibula fracture is observed in a 50th-percentile male PMHS at 807 g. For the 50th-percentile male, the highest distal tibia axial acceleration for which tibia/fibula fracture does not occur is 864 g. For the 75th-percentile female

PMHS, the lowest distal tibia axial acceleration for which tibia/fibula fracture occurs is 652 g. The highest distal tibia axial acceleration for which tibia/fibula fracture does not occur is 766 g.

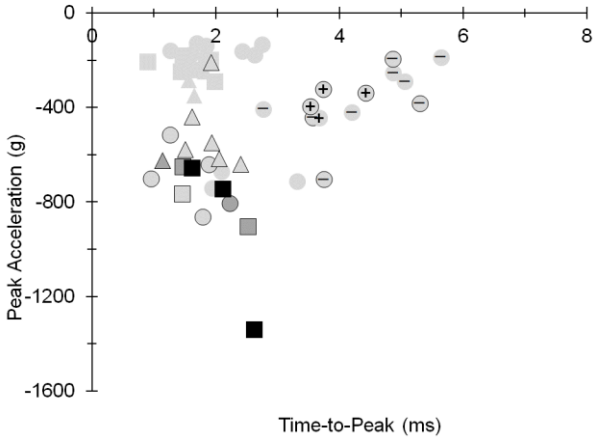

Figure 51: Peak distal tibia Z-axis acceleration vs. time-to-peak for tibia and fibula damage. Markers with black borders indicate ipsilateral talus or calcaneus damage.

Peak Tibia Vertical Speed and TTP

Figures 56, 57, and 58 show peak Z-axis speed of the tibia and TTP. All calcaneus, talus and combined tibia and fibula fractures, except one calcaneus and one talus fracture, occur above 7-m/s. Calcaneus and talus fractures in the 75th-percentile females generally occur at the shortest TTP distal tibia axial speed, while those observed in the 50th-percentile male occur at the longest TTP distal tibia axial speed, with the fractures in the small females scattered in between.

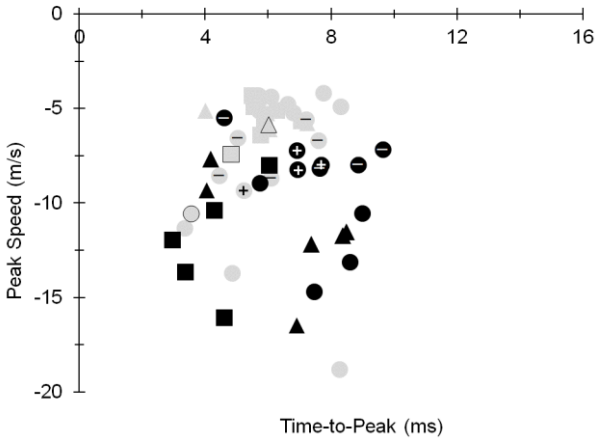

Figure 52: Peak distal tibia Z-axis speed vs. time-to-peak for calcaneus damage. Markers with black borders indicate ipsilateral talus damage.

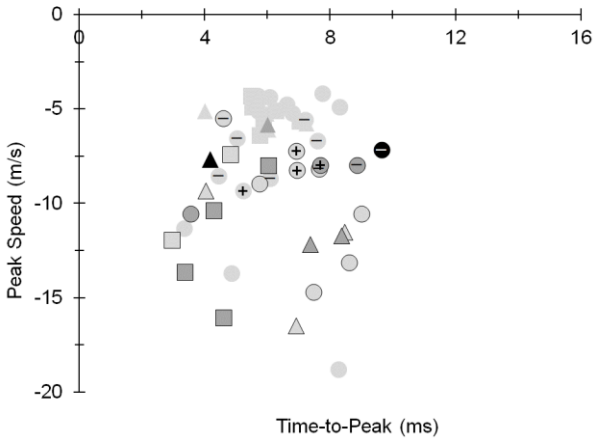

Figure 53: Peak distal tibia Z-axis speed vs. time-to-peak for talus damage. Markers with black borders indicate ipsilateral calcaneus damage.

75th female 5th female 50th male No Damage Minor Damage Major Damage

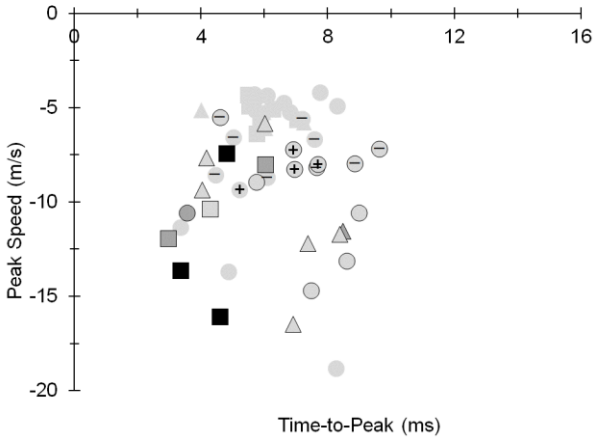

Figure 54: Peak distal tibia Z-axis speed vs. time-to-peak for tibia and fibula damage. Markers with black borders indicate ipsilateral talus and calcaneus damage.

75th female 5th female 50th male No Damage Minor Damage Major Damage

Peak Femur Vertical Acceleration and TTP

In general, peak posteroanterior acceleration of the distal femur does not follow any particular pattern other than all but two calcaneus fractures occurring above 200 g (Figure 59). For the 5th-percentile female PMHS, the lowest posteroanterior acceleration of the distal femur for which calcaneus fracture occurs is 239 g. The average peak posteroanterior acceleration of the distal femur that is associated with calcaneus fracture is 373 ± 103 g. The highest distal femur posteroanterior acceleration for which calcaneus fracture does not occur is 197 g. For the 75th-percentile female PMHS, the lowest distal femur posteroanterior acceleration for which calcaneus

fracture occurs is 376 g. The average peak distal femur posteroanterior acceleration associated with calcaneus fracture is 441 ± 54 g. The highest distal femur posteroanterior acceleration for which calcaneus fracture does not occur is 429 g. For the 50th-percentile male PMHS, the lowest distal femur posteroanterior acceleration for which calcaneus fracture occurs is 146 g. The average peak distal femur posteroanterior acceleration associated with calcaneus fracture is 399 ± 149 g. The highest distal femur posteroanterior acceleration for which calcaneus fracture does not occur is 439 g.

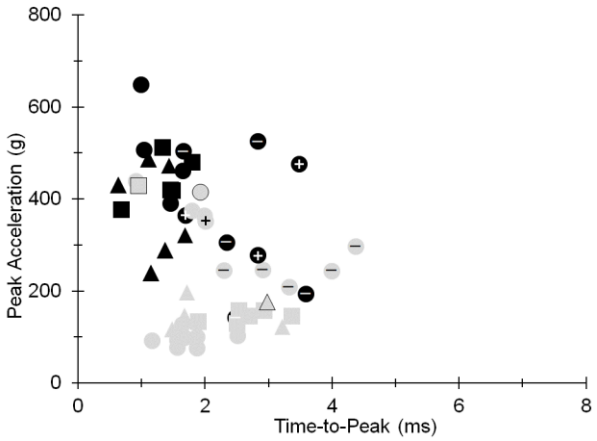

Figure 55: Peak distal femur X-axis acceleration vs. time-to-peak for calcaneus damage. Markers with black borders indicate ipsilateral talus or tibia/fibula damage.

Similarly, peak posteroanterior acceleration of the distal femur does not follow any particular pattern other than all but two talus fractures occurring above 250 g (Figure 60). However, there are far fewer talus fractures than calcaneus fractures occurring at the higher accelerations within these data. For the 5th-percentile female PMHS, the lowest distal femur posteroanterior acceleration for which talus fracture occurs is 176 g. The highest distal femur posteroanterior acceleration for which talus fracture does not occur is 471 g. For the 75th-percentile female PMHS, the lowest distal femur posteroanterior acceleration for which talus fracture occurs is 376 g (same as for the calcaneus). The highest distal femur posteroanterior acceleration for which talus fracture does not occur is 429 g (same as for the calcaneus). For the 50th-percentile male PMHS, the lowest distal femur posteroanterior acceleration for which talus fracture occurs is 142 g. The highest distal femur posteroanterior acceleration for which talus fracture does not occur is 648 g.

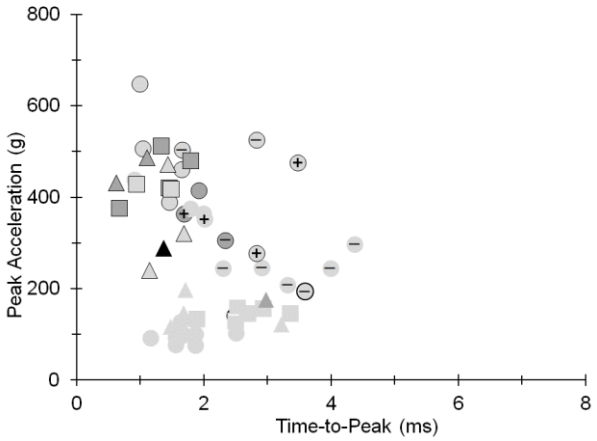

Figure 56: Peak distal femur X-axis acceleration vs. time-to-peak for talus damage. Markers with black borders indicate ipsilateral calcaneus or tibia/fibula damage.

75th female 5th female 50th male No Damage Minor Damage Major Damage

One combined distal tibia and fibula fracture occurred in a 5th-percentile female PMHS at 239 g, which is the lowest peak posteroanterior acceleration of the distal femur for which a combined distal tibia and fibula is seen (Figure 61). For the 5th-percentile female, the highest distal femur posteroanterior acceleration for which tibia/fibula fracture does not occur is 486 g. One fracture is observed in a 50th-percentile male PMHS at 415 g. For the 50th-percentile male, the highest distal femur posteroanterior acceleration for which tibia/fibula fracture does not occur is 648 g. For the 75th-percentile female, the lowest distal femur posteroanterior acceleration for which tibia/fibula fracture occurs is 376 g. The highest distal femur posteroanterior acceleration for which tibia/fibula fracture does not occur is 420 g.

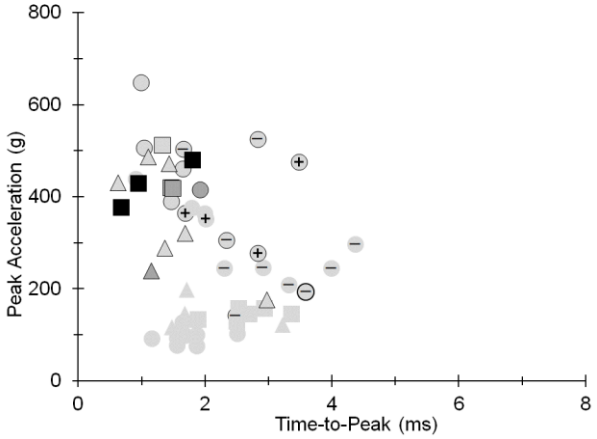

Figure 57: Peak distal femur X-axis acceleration vs. time-to-peak for tibia and fibula damage. Markers with black borders indicate ipsilateral talus and calcaneus damage.

75th female 5th female 50th male No Damage Minor Damage Major Damage

Peak Femur Vertical Speed and TTP

Figure 62, Figure 63, and Figure 64 show peak vertical speed of the femur and TTP with the markers indicating damage level of the calcaneus, talus, and tibia/fibula, respectively. No readily distinguishable relationships between peak axial speed of the distal femur and time-to-peak speed are observed for the calcaneus, talus, and combined tibia and fibula fractures.

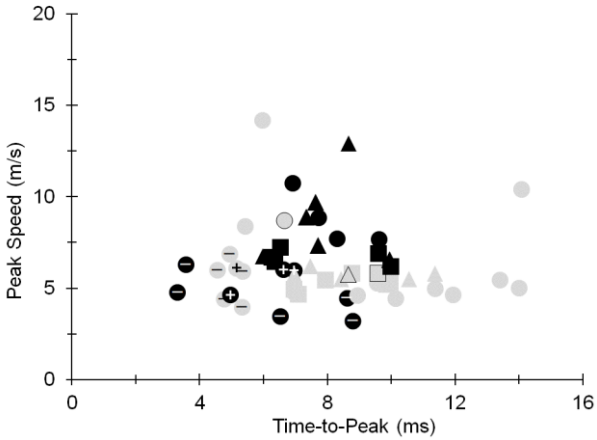

Figure 58: Peak distal femur X-axis speed vs. time-to-peak for calcaneus damage. Markers with black borders indicate ipsilateral talus or tibia/fibula damage.

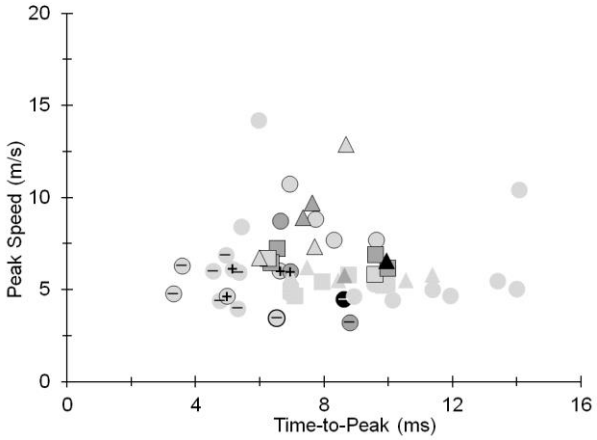

Figure 59: Peak distal femur X-axis speed vs. time-to-peak for talus damage. Markers with black borders indicate ipsilateral calcaneus or tibia/fibula damage.

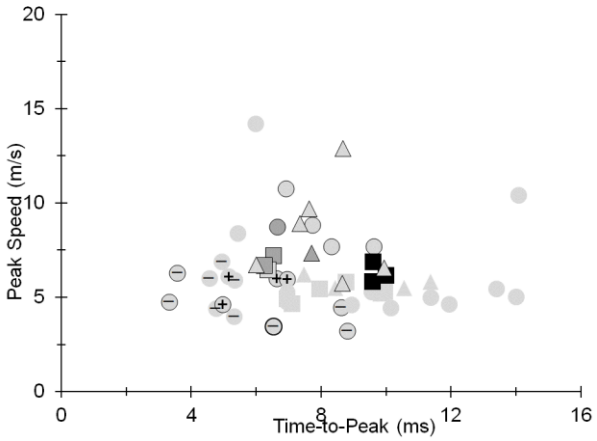

Figure 60: Peak distal femur X-axis speed vs. time-to-peak for tibia and fibula damage. Markers with black borders indicate ipsilateral talus and calcaneus damage.

Floor Kinematics

The potential relationships between floor kinematics and damage level are illustrated using point-cloud plots as well. A single peak value of acceleration or a single peak value of speed measured by the accelerometers on the floor near the right or left heel is plotted on the vertical axis, while the time taken to reach that peak value (time-to-peak or TTP) is plotted on the horizontal axis. TTP values are measured with respect to the initiation of floor acceleration, which is nearly coincident with charge detonation. As for the PMHS signal analyses, the damage locations used for this analysis include the tibia and fibula, which are grouped together; the talus; and the calcaneus. The damage to these regions is divided into three categories: no damage, minor damage, and major damage. Damage level is specified by the color of the marker, with light grey, dark grey, and black indicating no damage, minor damage, and major damage, respectively. The shape of the markers indicates the sex and percentile, with circles, squares, and triangles representing 50th-percentile males, 75th-percentile females, and 5th-percentile females, respectively. Markers from the Task 4.2/Matrix Shot test series are distinguished by a plus (+) or minus (-) symbol. The markers for the PMHS donned in PPE contain a plus symbol, while all other PMHS in the Task 4.2/Matrix Shot test series are marked by a minus symbol. Lower extremities with ipsilateral damage to specified bones are indicated by a black border on the marker.

Peak Floor Acceleration

A number of calcaneus fractures occur between a 1,000 and 3,000-g peak floor acceleration and within 1 to 3-ms TTP. However, calcaneus fractures generally occur at a lower range of acceleration with a longer TTP or higher accelerations with shorter TTP (Figure 65). There is not a distinct pattern for talus fractures (Figure 66), but similarity to the calcaneus distribution is evident given the strong association between talus and calcaneus fractures. Combined tibia/fibula fractures also generally occur at lower ranges of peak floor acceleration with longer TTP, or higher acceleration with shorter TTP (Figure 67). This trend is limited to cases having TTP less than 3-ms, as none of the Task 4.2/Matrix Shot tests (longer time-to-peak) produced tibia/fibula fracture.

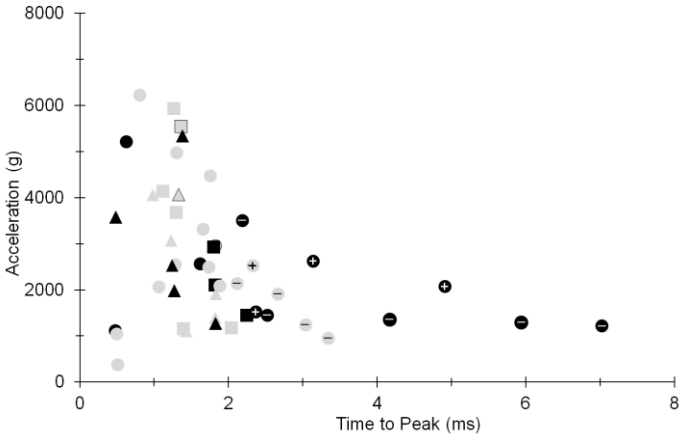

Figure 61: Peak floor vertical acceleration vs. time-to-peak. Marker color indicates calcaneus damage level. Borders indicate ipsilateral talus or tibia/fibula damage.

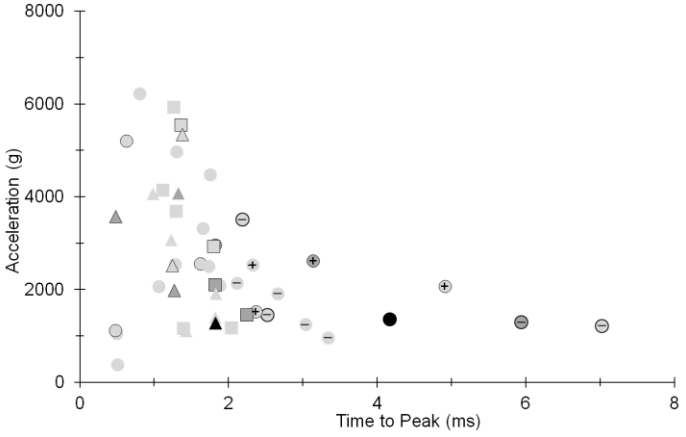

Figure 62: Peak floor vertical acceleration vs. time-to-peak. Marker color indicates talus damage level. Borders indicate ipsilateral calcaneus or tibia/fibula damage.

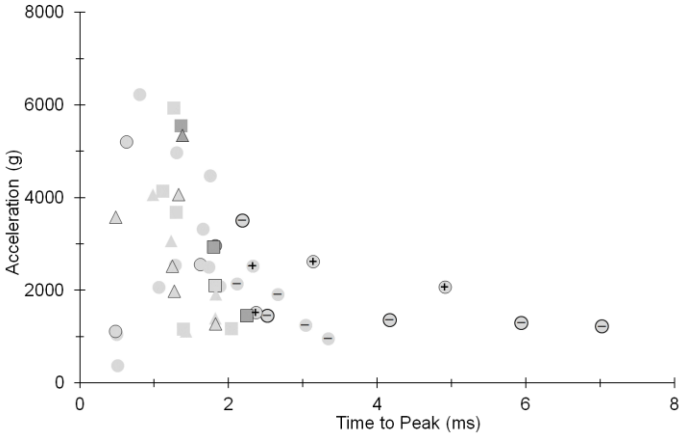

Figure 63: Peak floor vertical acceleration vs. time-to-peak. Marker color indicates tibia/fibula damage level. Borders indicate ipsilateral calcaneus or talus damage.

75th female 5th female 50th male No Damage Minor Damage Major Damage

Peak Floor Speed

Nearly all calcaneus fractures occur above a 10-m/s peak floor speed, regardless of the time-to-peak (Figure 68). However, exceeding 10 m/s does not guarantee calcaneus fracture. There is no trend observed for the incidence of talus fracture when examining peak vertical speed of the floor vs. time-to-peak speed (Figure 69), other than the association with calcaneus fracture. Similarly, there is no trend for the incidence of combined tibia and fibula fracture (Figure 70).

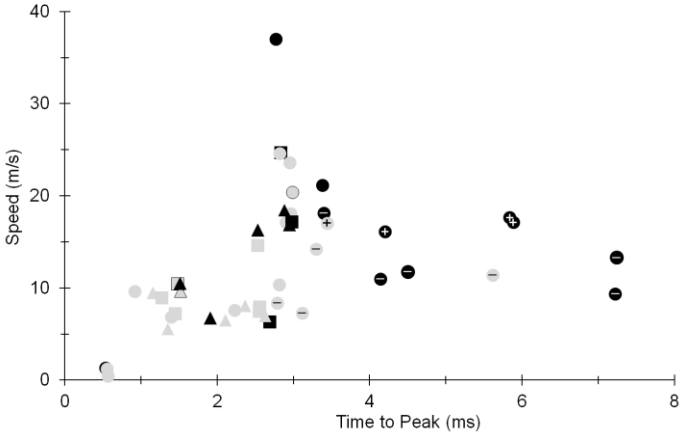

Figure 64: Peak floor vertical speed vs. time-to-peak. Marker color indicates calcaneus damage level. Borders indicate ipsilateral talus damage.

75th female 5th female 50th male No Damage Minor Damage Major Damage

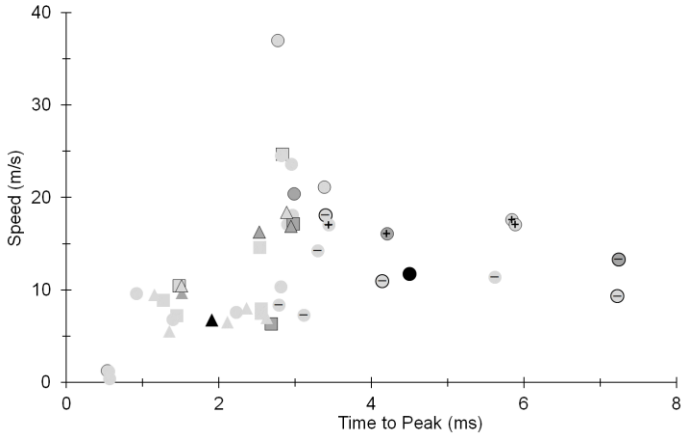

Figure 65: Peak floor vertical speed vs. time-to-peak. Marker color indicates talus damage level. Borders indicate ipsilateral calcaneus damage.

□ 75th female △ 5th female ○ 50th male No Damage Minor Damage Major Damage

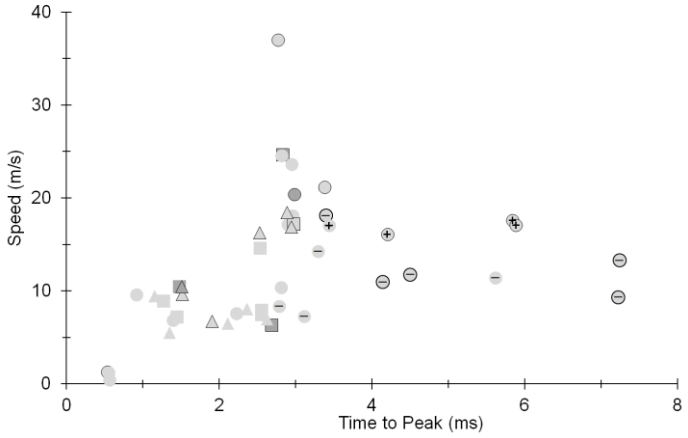

Figure 66: Peak floor vertical speed vs. time-to-peak. Marker color indicates tibia/fibula damage level. Borders indicate ipsilateral calcaneus and talus damage.

□ 75th female △ 5th female ○ 50th male No Damage Minor Damage Major Damage

Mass Below Knee

The results of the CT segmentation below-knee mass estimations are shown in Table 10. These data were not obtained for the Task 4.2/Matrix Shot tests.

Table 10: Lower Extremity Mass Estimations

Test ID	PMHS	Mass Below Knee (kg)	
		Left	Right
SA1C1	SM117	6.805	6.782
SA1C2	SM118	5.277	5.126
SA2C1	SM120	5.724	5.880
SA2C2	SM119	4.451	4.215
SA3C1	SF127	3.779	3.771
SA3C2	SF126	3.502	3.685
SA4C1	SF128	3.143	3.263
SA5C1	SF131	3.063	3.055
SA5C2	SF132	4.165	4.176
SA6C1	SF133	3.847	3.947
SB1C1	SF138	3.063	3.055
SB1C2	SF134	3.537	3.527
SB2C1	SM140	4.374	4.502
SB2C2	SF135	5.048	4.906
SB3C1	SM141	3.630	4.033
SB3C2	SF142	4.452	4.564
SB4C1	SM145	5.404	5.302
SB4C2	SF148	2.323	2.546
SB5C1	SM150	5.779	5.683
SB5C2	SF151	3.060	3.008

Figure 71 presents the mass below the knee as a function of sex and percentile. Damage level of the tibia is indicated by the color of the marker, with light grey, dark grey, and black indicating no damage, minor damage, and major damage, respectively. The 50^{th}-percentile males are in the higher range of mass below the knee, while 75^{th}-percentile females are in the lower range. The range of mass below the knee for 5^{th}-percentile females falls within the lower-end of the 50^{th}-percentile male range and the higher-end of the 75^{th}-percentile female range.

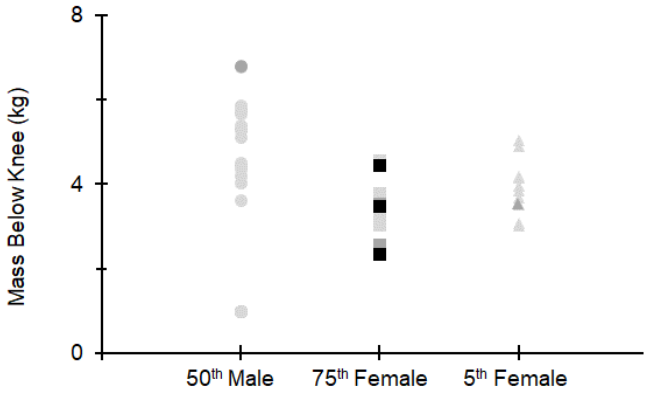

Figure 67: Mass below the knee by sex and percentile. Marker color indicates tibia damage level.

75th female 5th female 50th male No Damage Minor Damage Major Damage

Figure 72 presents these data in a different way, with the horizontal axis showing the mass of the leg and the vertical axis showing non-damage cases at a level of zero and damage cases at a level of one. There is a weak trend toward lower-mass legs being more susceptible to tibia damage. This is influenced the most by the 75th-percentile female responses. This plot does not account for other factors, such as BMD or peak acceleration.

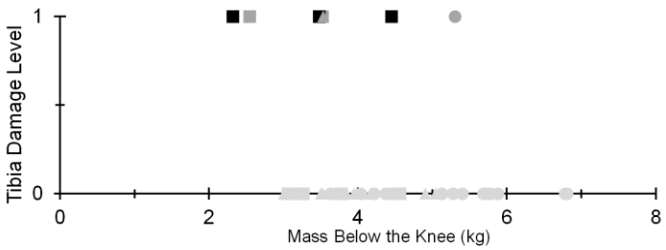

Figure 68: Tibia damage level vs. mass of the lower extremity below the knee. Marker color indicates tibia damage level.

75th female 5th female 50th male No Damage Minor Damage Major Damage

Point-cloud plots were generated with mass plotted on the horizontal axis and peak vertical acceleration or speed of the tibia or femur on the vertical axis. Damage level of the tibia is specified by the color of the marker, with light grey, dark grey, and black indicating no damage, minor damage, and major damage, respectively. The shape of the markers indicates the sex and percentile, with circles, squares, and triangles representing 50th-percentile males, 75th-percentile females, and 5th-percentile females, respectively.

In general, no trend is seen for peak axial (global vertical) acceleration of the distal tibia with respect to leg mass (Figure 73). However, if only 75th-percentile female tibia fracture cases are considered, a moderate relationship (R^2 = 0.310) is seen for peak axial acceleration of the distal tibia increasing as leg mass increases. This relationship strengthens when only the more severe fractures are considered (R^2 = 0.588). In general, no trend between peak axial (global vertical) speed of the distal tibia and leg mass is evident (Figure 74). However, if only tibia fracture cases are considered, a weak trend (R^2 = 0.082) showing an increase in peak axial speed of the tibia with decreasing leg mass exists.

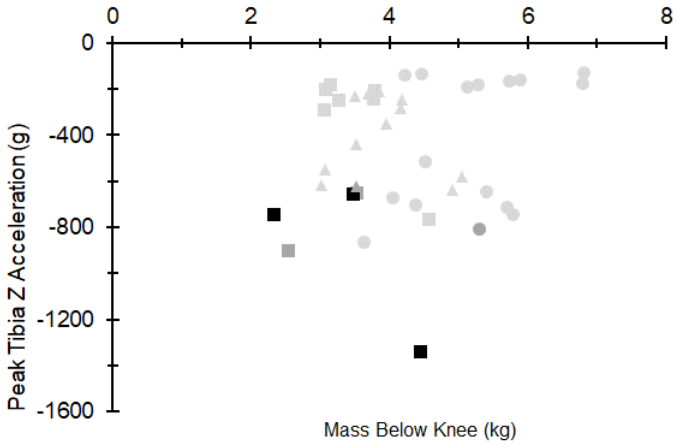

Figure 69: Peak tibia vertical acceleration vs. mass below the knee. Marker color indicates tibia damage level.

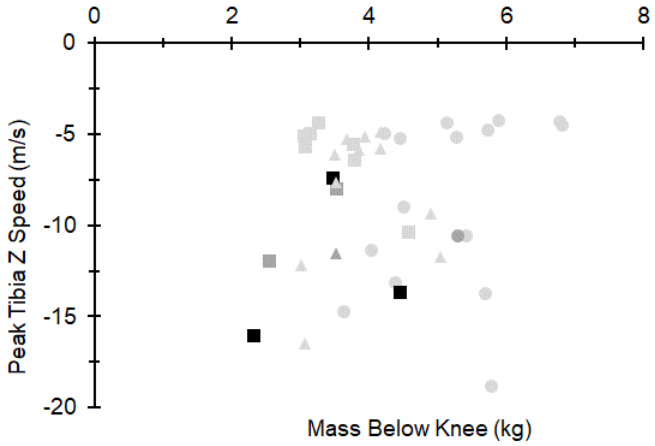

Figure 70: Peak tibia vertical speed vs. mass below the knee. Marker color indicates tibia damage level.

Overall, no trend is seen for peak posteroanterior (global vertical) acceleration of the distal femur with respect to leg mass (Figure 75). When only 75th-percentile female tibia fracture cases are considered, a moderate relationship (R^2 = 0.687) is seen for peak distal femur acceleration decreasing as leg mass increases. This relationship becomes strong when only the more severe fractures are considered (R^2 = 0.996). No trend between peak posteroanterior (global vertical) speed of the distal femur and leg mass is evident. However, tibia fracture tends to occur toward the lower end of the speed range (Figure 76).

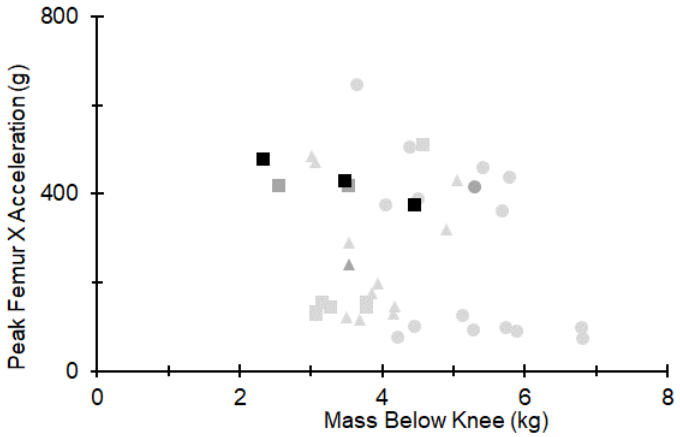

Figure 71: Peak femur vertical acceleration vs. mass below the knee. Marker color indicates tibia damage level.

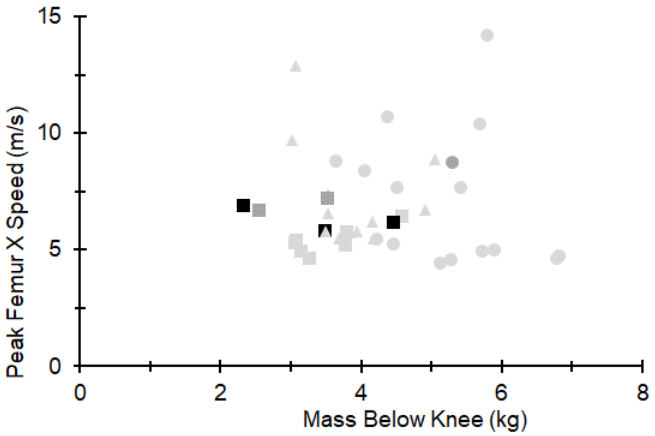

Figure 72: Peak femur vertical speed vs. mass below the knee. Marker color indicates tibia damage level.

Tibia Volumetric Bone Mineral Density

The results of the volumetric bone mineral density estimations are presented in Table 11. These data were not obtained for the Task 4.2/Matrix Shot tests.

Table 11: Volumetric bone mineral density 4% total (mg/cm^3)

Test	Crew	PMHS	Left	Right	Mean
SA1	1	SM117	379.19	380.14	379.66
	2	SM118	350.64	334.96	342.8
SA2	1	SM120	323.27	329.99	326.63
	2	SM119	340.19	342.44	341.31
SA3	1	SF127	401.71	393.25	397.48
	2	SF126	385.65	380.98	383.31
SA4	1	SF128	406.26	447.98	427.12
SA5	1	SF131	391.49	392.59	392.04
	2	SF132	387.13	383.45	385.29
SA6	1	SF133	324.33	327.75	326.04
SB1	1	SF138	328.08	321.01	324.54
	2	SF134	441.07	438.26	439.66
SB2	1	SM140	432.02	427.37	429.7
	2	SF135	326.59	320.37	323.48
SB3	1	SM141	359.18	361.07	360.13
	2	SF142	272.99	316.69	294.84
SB4	1	SM145	366.39	379.92	373.16
	2	SF148	367.27	398.79	383.03
SB5	1	SM150	369.65	381.5	375.58
	2	SF151	334.69	336.9	335.8

In the following three plots, tibia damage level is indicated by color, with light grey, dark grey, and black indicating no damage, minor damage, and major damage, respectively. The shape of the markers indicates the sex and percentile, with circles, squares, and triangles representing 50^{th}-percentile males, 75^{th}-percentile females, and 5^{th}-percentile females, respectively.

Figure 77 shows the volumetric bone mineral density (vBMD) of the tibia as a function of sex and percentile. Although fracture risk is related to quality and quantity of bone, which can help explain why the 50^{th}-percentile male and 5^{th}-percentile female fractures occur in tibiae having relatively higher vBMD, the 75^{th}-percentile female data demonstrate a trend toward increased propensity to tibia fracture as vBMD decreases. Figure 78 presents the damage level of the tibia as a function of

tibia vBMD. There is a weak trend toward tibiae with lower volumetric BMD being more susceptible to damage. This is influenced the most by the 75th-percentile female responses.

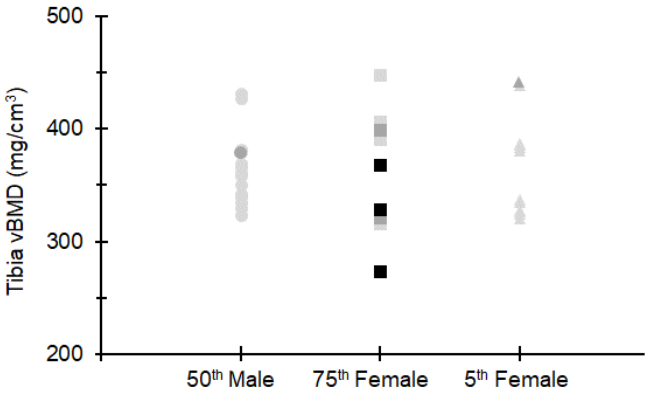

Figure 73: Tibia vBMD by sex and percentile. Marker color indicates tibia damage level.

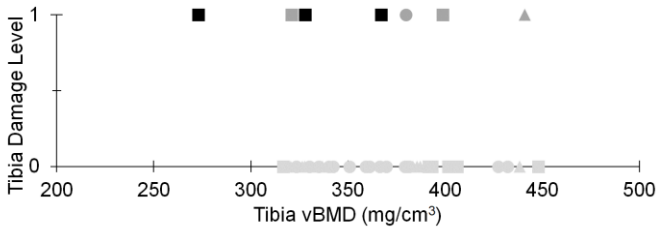

Figure 74: Tibia damage level vs. tibia vBMD. Marker color indicates tibia damage level.

Figure 79 shows tibia vBMD as a function of mass below the knee. There is no trend ($R^2 = 0.005$) between vBMD and leg mass for 50th-percentile males. There is a weak trend ($R^2 = 0.094$) toward decreasing vBMD for increasing leg mass for 5th-percentile females. There is a moderate trend ($R^2 = 0.325$) toward decreasing vBMD for increasing leg mass for 75th-percentile females. If only damaged tibiae for 75th-percentile females are considered, there is a strong trend ($R^2 = 0.896$) toward decreasing vBMD for increasing leg mass. These results present a confounding factor for the interpretation of this study. The trends for all three anthropometries are opposite those found for the upper extremity by Hardy et al., 2001, where BMD (determined via Osteogram®) and mineral content (ash mass per unit length) both increased with increasing extremity mass.

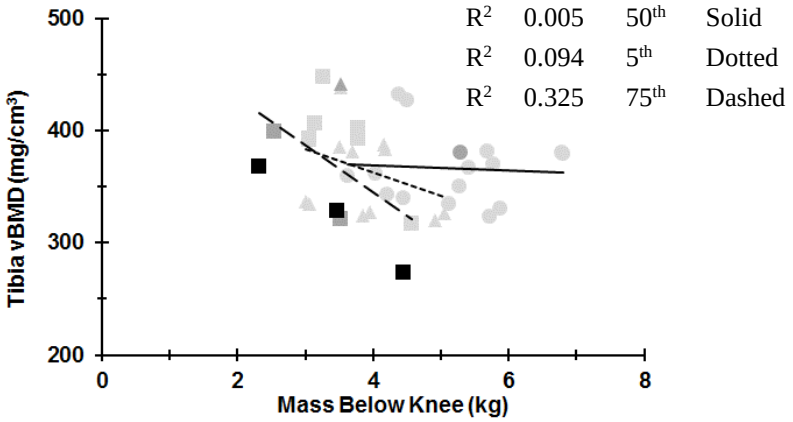

Figure 75: Tibia vBMD vs. mass below the knee. Marker color indicates tibia damage level.

Parametric and Non-Parametric Analyses

Logistical regressions are performed to assess the probability of calcaneus fracture as a function of peak vertical acceleration of the distal tibia. This is conducted with all PMHS types grouped together for all TTP (Figure 80), as well as for TTP below 3 ms (Figure 81). The R^2 value increases from 0.327 for all cases to 0.461 when cases before 3 ms are considered. Fifty-percent probability (p50) of calcaneus fracture is associated with a peak distal tibia vertical acceleration of -462.5 g for all cases and -522.5 g for cases with a TTP less than 3 ms.

For comparison, survival analysis using the CT method of Nusholtz et al., 1999 is performed to determine the cumulative probability of calcaneus fracture with respect to peak vertical acceleration of the distal tibia for all PMHS types in one group (Figure 82). This method is valuable because it accommodates right-censored non-event data points (non-damage cases) and left-censored event data points (damage cases). This method is unique in the literature in this regard. However, given the few data points overall, particularly the few data points for damage cases, the analysis does not reach a p50 value. Therefore, additional CT survival analyses are not performed.

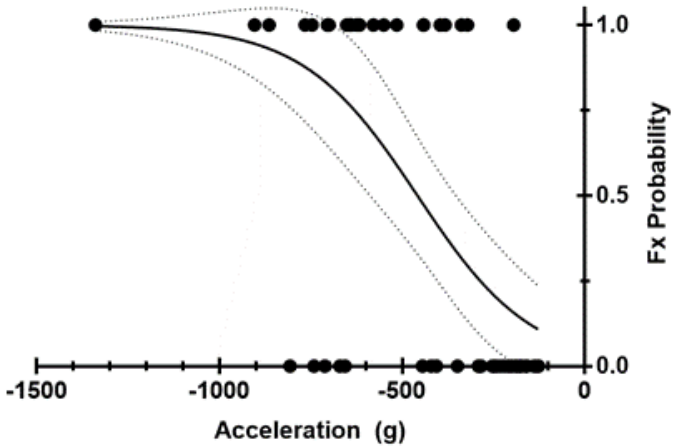

Figure 76: Logistic regression showing probability of calcaneus damage as a function of peak tibia Z-axis acceleration for all PMHS types at all TTP. $R^2 = 0.327$.

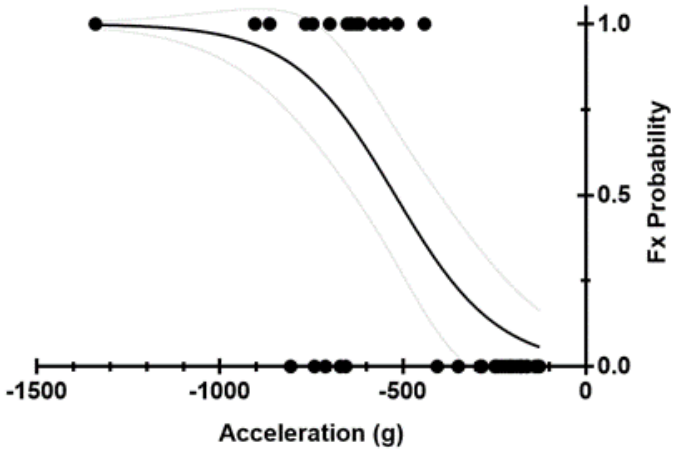

Figure 77: Logistic regression showing probability of calcaneus damage as a function of peak tibia Z-axis acceleration for TTP below 3 ms. $R^2 = 0.461$.

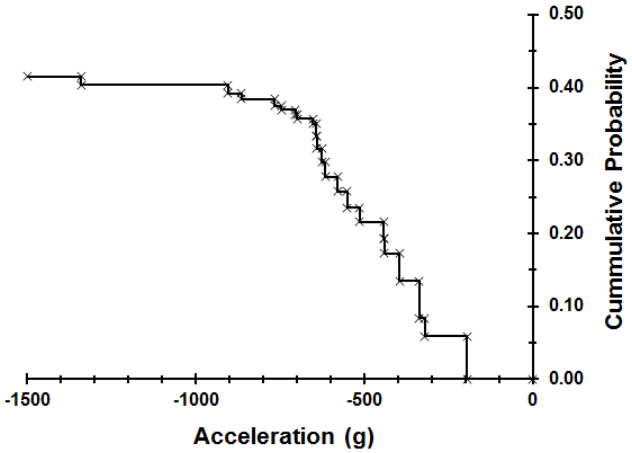

Figure 78: Survival analysis showing the probability of calcaneus damage as a function of peak tibia Z-axis acceleration for all PMHS types. p50 is never reached.

Logistic regressions to examine the probability of calcaneus damage with respect to peak vertical acceleration of the distal tibia are also conducted for cases grouped by PMHS type. The 50th-percentile males do not show a relationship between increased peak distal tibia vertical acceleration and higher likelihood of calcaneus fracture (R^2 = 0.098). This relationship is strong for 75th-percentile females (R^2 = 0.816), and maximal for 5th-percentile females (R^2 = 1.000), given the separation between non-fracture and fracture cases. Fifty-percent probability of calcaneus fracture is associated with -568-g, -650-g, and -396-g peak tibia vertical acceleration for 50th-percentile males (Figure 83), 75th-percentile females (Figure 84), and 5th-percentile females (Figure 85), respectively.

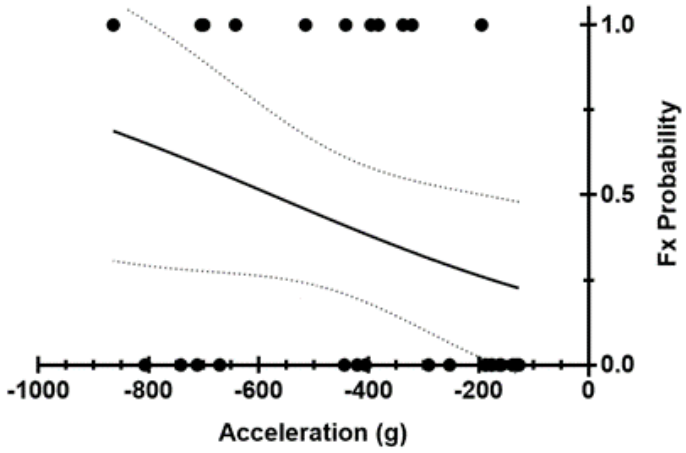

Figure 79: Logistic regression showing probability of calcaneus damage as a function of peak tibia Z-axis acceleration for 50th-percentile males. R^2 = 0.098.

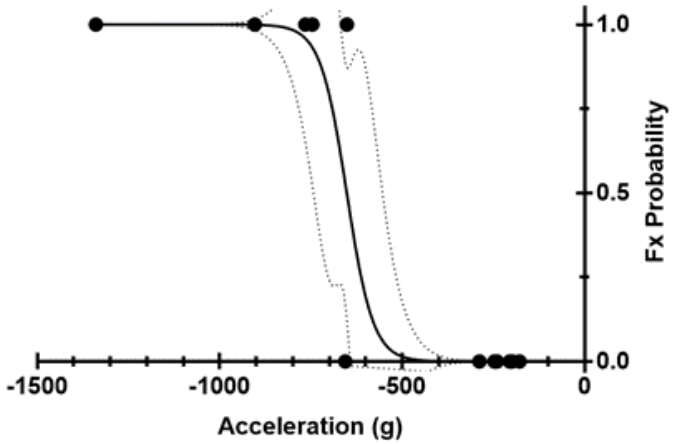

Figure 80: Logistic regression showing probability of calcaneus damage as a function of peak tibia Z-axis acceleration for 75th-percentile females. $R^2 = 0.816$.

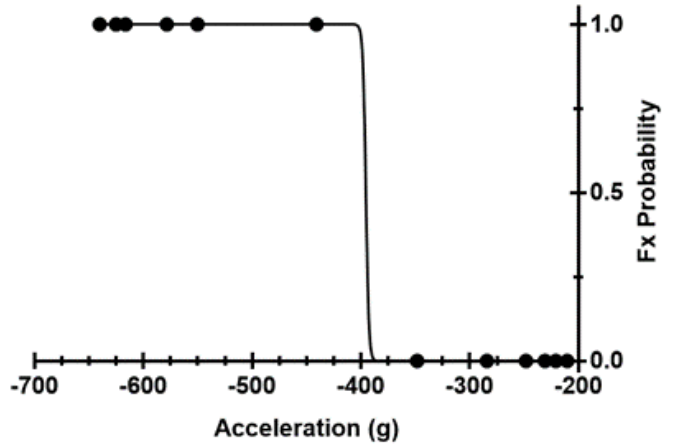

Figure 81: Logistic regression showing probability of calcaneus damage as a function of peak tibia Z-axis acceleration for 5th-percentile females. $R^2 = 1.000$.

Linear regression is conducted to assess the probability of tibia damage as a function of peak vertical acceleration of the distal tibia for all PMHS types grouped together (Figure 86). A moderate relationship between increased peak tibia vertical acceleration and increased risk of tibia fracture is seen ($R^2 = 0.376$). However this is mostly driven by a single damage case having high peak tibia vertical acceleration compared to other damage cases, as well as a collection of low-acceleration cases that did not produce damage. Fifty-percent probability of tibia fracture is associated with a -814-g peak tibia vertical acceleration.

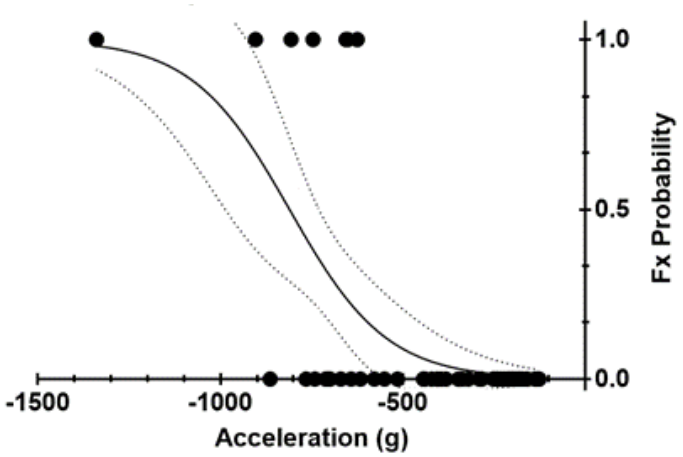

Figure 82: Logistic regression showing probability of tibia damage as a function of peak tibia Z-axis acceleration for all PMHS types and all TTP. $R^2 = 0.376$.

Logistic regression is also performed to assess the probability of calcaneus damage as a function of peak vertical acceleration of the distal femur. This is conducted with all PMHS types grouped together for all TTP, as well as by PMHS type (50^{th}-percentile male, 75^{th} and 5^{th}-percentile female). The analysis that grouped all PMHS types shows a moderate relationship between increased peak vertical acceleration of the femur and increased probability of calcaneus fracture ($R^2 = 0.426$) (Figure 87). Fifty-percent probability of calcaneus fracture was associated with a 320-g peak femur vertical acceleration for all PMHS. Similar to the peak tibia vertical acceleration regressions, the 50^{th}-percentile males show moderate relationship strength ($R^2 = 0.301$), while 75^{th}-percentile females demonstrate a better fit ($R^2 = 0.694$), and the 5^{th}-percentile females provide a maximal fit ($R^2 = 1.000$), given the separation between non-fracture and fracture cases. A fifty-percent probability of calcaneus fracture was associated with a peak femur vertical acceleration of 368 g, 332 g, and 218 g for 50^{th}-percentile males (Figure 88), 75^{th}-percentile females (Figure 89), and 5^{th}-percentile females (Figure 90), respectively.

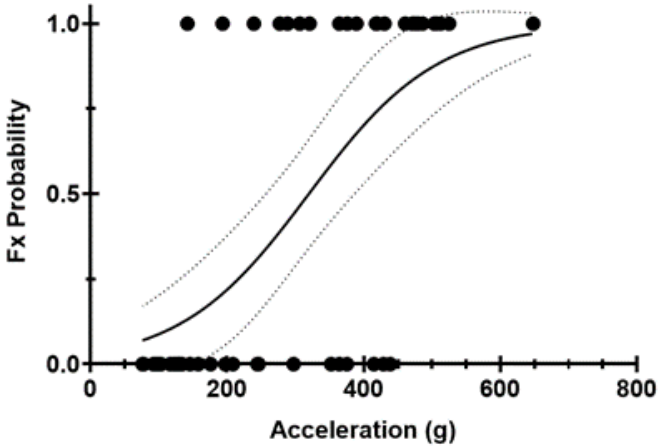

Figure 83: Logistic regression showing probability of calcaneus damage as a function of peak femur X-axis acceleration for all PMHS types and TTP. $R^2 = 0.426$.

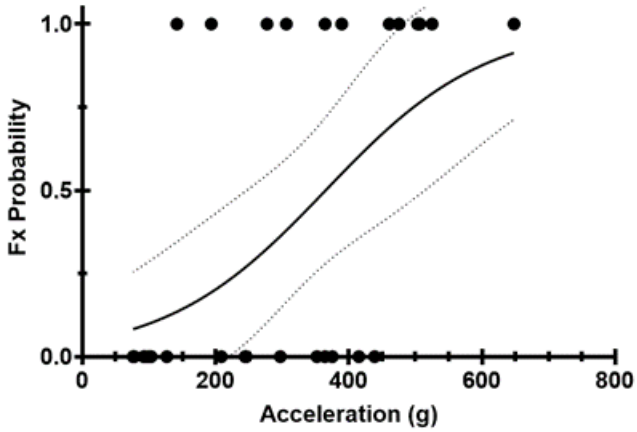

Figure 84: Logistic regression showing probability of calcaneus damage as a function of peak femur X-axis acceleration for 50^{th}-percentile males. $R^2 = 0.301$.

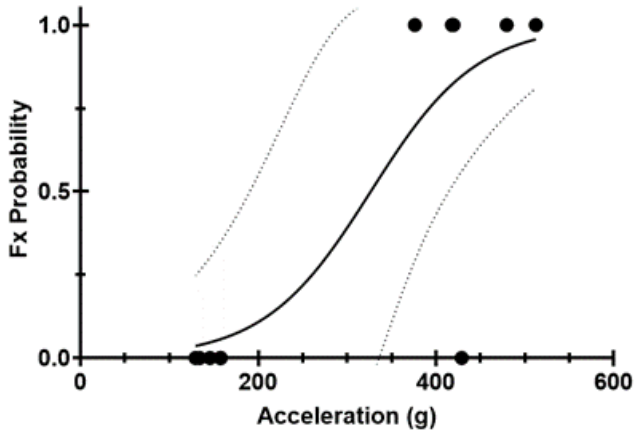

Figure 85: Logistic regression showing probability of calcaneus damage as a function of peak femur X-axis acceleration for 75th-percentile females. R^2 = 0.694.

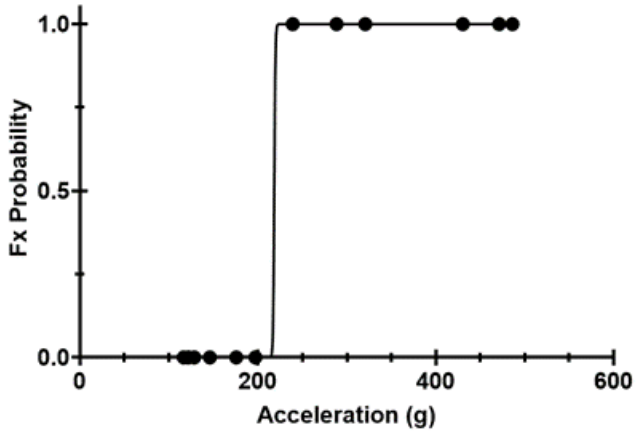

Figure 86: Logistical regression showing probability of calcaneus damage as a function of peak femur x-axis acceleration for 5th-percentile females. R^2 = 1.000.

The results of the analyses of peak acceleration of the distal tibia and distal femur are cataloged in Table 12 and Table 13, respectively. For calcaneus damage, the average tibia acceleration trend follows that of the p50 values (R^2 = 0.861), with the 5th-percentile females having the lowest values, followed by the 50th-percentile males, then the 75th-percentile females. For calcaneus damage with respect to femur acceleration, neither the average nor p50 values follow the tibia trend, nor do they follow the same trend. For the average femur acceleration, 75th-percentile female > 5th-percentile female > 50th-percentile male. For the femur acceleration p50, 50th-percentile male > 75th-percentile female > 5th-percentile female.

Table 12: Summary statistics for peak tibia acceleration

Damage Location	Peak Distal Tibia Axial Acceleration (g)	5th-Percentile Female PMHS	75th-Percentile Female PMHS	50th-Percentile Male PMHS	Overall
Calcaneus	Lowest w Fx	625	640	195	195
	Highest w/o Fx	640	766	807	807
	< 3ms Avg, ± Std.	575 ± 74	882 ± 272	680 ± 145	NA
	Logist p50	396	650	568	463
	R^2	1.000	0.816	0.098	0.327
	< 3ms Logist p50	396	650	781	523
	R^2	1.000	0.816	0.223	0.461
Talus	Lowest w Fx	210	904	195	195
	Highest w/o Fx	640	766	864	864
	Logist p50	NA	658	NA	944.2
	R^2	0.035	0.454	0.002	0.102
Tibia/Fibula	Lowest w Fx	625	652	807	625
	Highest w/o Fx	640	766	864	864
	Logist p50	NA	523	NA	813
	R^2	NA	0.670	NA	0.376

Table 13: Summary statistics for peak femur acceleration

Damage Location	Peak Distal Femur Posteroanterior Acceleration (g)	5th-Percentile Female PMHS	75th-Percentile Female PMHS	50th-Percentile Male PMHS	Overall
Calcaneus	Lowest w Fx	239	376	146	146
	Highest w/o Fx	197	429	439	439
	Avg, ± Std.	373 ± 103	441 ± 54	339 ± 149	NA
	Logist p50	218	332	368	320
	R^2	1.000	0.694	0.301	0.426
Talus	Lowest w Fx	176	376	142	142
	Highest w/o Fx	471	429	648	648
Tibia/Fibula	Lowest w Fx	239	376	415	239
	Highest w/o Fx	486	420	648	648

Table 14 presents the results of the point biserial correlation tests. Both vBMD and mass below the knee had a marginally significant relationship with tibia fracture. Peak vertical acceleration of the distal tibia showed a marginally significant relationship with talus fracture and a greatly significant relationship with calcaneus fracture. Peak vertical speed of the distal tibia had a moderately significant relationship with calcaneus fracture. Peak vertical acceleration of the distal femur showed a marginally significant relationship with talus fracture and a greatly significant relationship with calcaneus fracture.

Table 14: Point Biserial Correlations

Damage Location	Parameter	vBMD	Below Knee Mass	Tibia Acceleration	Tibia Speed	Femur Acceleration	Femur Speed
Calcaneus	Point Biserial r	-0.1505	-0.2623	-0.5595	-0.5031	0.6615	0.2134
	95% confidence interval	-0.4044 to 0.1249	-0.5304 to 0.0536	-0.7208 to -0.3408	-0.6808 to -0.2695	0.4785 to 0.7894	-0.0577 to 0.4551
	R^2	0.0227	0.0688	0.3131	0.2531	0.4376	0.0455
	P (two-tailed)	0.2820	0.1021	<0.0001	0.0001	<0.0001	0.1214
	P value summary	ns	ns	****	***	****	ns
Talus	Point Biserial r	-0.0673	-0.1519	-0.3189	-0.2537	0.2869	0.0672
	95% confidence interval	-0.3315 to 0.2068	-0.4425 to 0.1675	-0.5424 to -0.0532	-0.4904 to 0.0178	0.0207 to 0.5151	-0.2042 to 0.3291
	R^2	0.0045	0.0231	0.1017	0.0644	0.0823	0.0045
	P (two-tailed)	0.6323	0.3494	0.0199	0.0668	0.0354	0.6290
	P value summary	ns	ns	*	ns	*	ns
Tibia	Point Biserial r	0.3258	-0.3771	0.0548	0.0810	-0.0702	0.1043
	95% confidence interval	0.0609 to 0.5479	-0.6162 to 0.0744	-0.2187 to 0.3203	-0.1935 to 0.3438	-0.3317 to 0.2014	-0.1681 to 0.3620
	R^2	0.1062	0.1422	0.0030	0.0066	0.0049	0.0109
	P (two-tailed)	0.0173	0.0164	0.6968	0.5642	0.6140	0.4527
	P value summary	*	*	ns	ns	ns	ns

CHAPTER 4

DISCUSSION

Damage Response

Both the immediate and long term effects of lower extremity injuries are a major concern in UBB. The tibia, talus, and calcaneus are of particular concern, since these bones comprise the primary loading path through the leg. Injuries to these regions are prevalent in UBB - Vasquez et al. (2018) reported that injuries to the thigh, lower leg (knee), and foot/ankle were sustained by 8, 28, and 33 percent of individuals who were WIA and 44, 43, and 36 percent of individuals who were KIA, respectively. The devastating long-term effects of calcaneus injuries in particular were described by Ramasamy et al. (2011), who examined a set of forty calcaneus fractures sustained by military personnel during vehicle explosions. At the mean follow-up time of 33.2 months, only two casualties within this dataset were able to return to full military duty, while twenty-three were fit to perform sedentary work or were not able to perform any military duty.

Calcaneus

The calcaneus was the most frequently damaged region of the lower extremities in the current study, affecting fifteen out of twenty lower extremities in Series B (higher-energy floor condition). All calcaneus fractures were classified as AIS 857371.2, meaning the fractures extended into two joint surfaces. They were also classified as Sanders Type IV, meaning there were three or more primary fracture lines with greater than two millimeters of articular displacement, as well as severe comminution. Compression was the primary injury mechanism for calcaneus fractures in this study. This supports the in-theater findings of Danelson et al. (2018), who determined that compression caused 73% of calcaneus fractures in a dataset consisting of mounted UBB attacks.

The comminution of the calcaneus fractures in this study made it difficult to distinguish potential differences in injury patterns between the three PMHS types in the study. Nevertheless, there were notable differences in the frequency of calcaneus fractures between females and males. Series B resulted in just one intact calcaneus out of twelve female calcanei. In contrast, four out of eight male calcanei were intact in Series B. Furthermore, the single intact calcaneus of the female was

associated with severe damage to the ipsilateral tibia and fibula. In contrast, the single case of a male with damage to the ipsilateral ankle-complex in the absence of a calcaneus fracture was minor in nature. These findings could be indicative of potential differences in fracture tolerance between females and males for the foot and ankle. This has been reported previously by Funk et al. (2002), who found that a 50% risk of injury due to blunt axial loading of the foot and ankle of a 45 year old was associated with an 8.3-kN tibia load for 50^{th}-percentile males and just 5 kN for 5^{th}-percentile females.

Severe calcaneus fractures, such as those observed in the current study, are a sign of high-energy trauma and typically have associated injuries to the ipsilateral lower extremity. Danelson et al. (2018) reported that 71% of casualties who sustained an injury to the leg or foot sustained multiple fractures to that lower extremity. Similarly, Ramasamy et al. (2011) reported that 85% of calcaneus fractures sustained by thirty casualties in vehicle explosions involved injuries to the ipsilateral foot and ankle complex. Associated injury regions included the tibia (67.5%), talus (20%), midfoot (52.5%), and forefoot (27.5%). Similar to these reports, the calcaneus fractures in Series B of the current study were frequently associated with multiple fractures to the ipsilateral lower extremity. The fifteen calcaneus fractures were accompanied by fractures of five tibiae, seven tali, four midfoot bones, and three forefoot bones.

Talus

In general, the tali in the current study remained relatively intact, with almost all of the damage being minor. Eight out of nine talus damage cases were coded as AIS 857261.2, meaning the fracture extended into one joint surface of the talar body. In two cases, the talus remained completely intact and was associated with damage to the tibia and calcaneus. Similarly, there were two cases in which the talus sustained minor damage that was associated with major damage of the tibia and calcaneus. These results are corroborated by Chirvi et al. (2017) who produced tibia and calcaneus fractures in cadaver leg specimens in UBB conditions on the VertAc device (Yoganandan et al., 2015). In that study, most of the talus and tibial plafond damage occurred in association with additional hindfoot injuries.

In the current study, there was only one instance of severe talus damage. This case was associated with a crushed calcaneus and no damage to the distal leg. It was classified as a Hawkins Type I, which is a non-displaced fracture of the talar neck. Talar neck fractures such as this one are usually associated with high-energy input and are particularly at risk for avascular necrosis (Stiegelmar et al., 2001).

Interestingly, five talus fractures occurred in the absence of damage to the distal tibia, suggesting that sustained loading of the talus without fracture of the distal tibia is possible. This also suggests that an intact talus is needed for distal tibia fractures to occur. Only one talus fracture occurred in the absence of a calcaneus or tibia fracture, however the damage was minor. Isolated fractures of the talus with significant bone loss are rare - typically talus injuries are associated with nearby fractures and soft tissue damage (Tintle et al., 2010).

Differences in the frequency of talus damage between females and males were identified in the current study. During Series B, all females sustained some form of damage to one or both tali, while only one male sustained damage to the talus. The one case of major damage to the talus occurred in a 5^{th}-percentile female. These results are not unexpected. In a characterization of talus morphology from CT images, Gorman et al. (2016) reported that sex is a significant predictor of talus depth, width, cross-sectional area and radius. A supplementary investigation of the NASS-CDS database for frontal crashes between 2004 and 2013 revealed that sex is a significant predictor of talus injury. The authors proposed that the increased risk of talus fractures for females can be attributed the tali of females generally being smaller than those of men.

Tibia and Fibula

Four lower extremities sustained minor damage of the distal tibia that was coded as AIS 854361.2, meaning the fractures were partial articular. The AO/OTA classification for these fractures was OTA 43-B1, designating a pure split. Three lower extremities incurred severe crushing of the distal portion of the tibia with substantial loss of height. These cases were coded as AIS 854371.2, since they involved complete articular fractures of the distal tibia. The AO/OTA classification for these fractures was OTA type 43-C3, indicating that they were articular and multi-fragmentary. Bone loss and tibial fracture patterns have been cited as two of the most influential factors in the decision

to salvage or amputate a limb according to an investigation of Lower Extremity Assessment Project (LEAP) data by Swiontkowski (2002), and are therefore of utmost concern in UBB scenarios.

All fibula factures were coded as AIS 854471.2, meaning they occurred above the joint (suprasyndesmotic) and were isolated to the head, shaft, or neck. They were also categorized as Danis-Weber classification C, meaning they were proximal to the syndesmosis. Two of the fibula fractures were also classified as OTA 44-C1, which are simple diaphyseal fractures of the fibula. All three fibula fractures were associated with the three cases of major damage to the tibia. This type of fracture could have involved an eversion component, with the fibula being driven up through the tibiofibular syndesmosis, or general instability after distal tibia fracture.

The results of the current study illustrate differences in the frequency and severity of tibia and fibula fractures between females and males. Six female PMHS incurred both major and minor damage to the tibia, while just one male sustained minor damage to the tibia. Only 75th-percentile females sustained major damage of the distal tibia and associated damage to the fibula.

Differences in damage outcome between females and males in the current study may be attributed to differences in bone quantity and quality. Jepsen et al. (2011) examined the robustness and mechanical strength of tibiae using a dataset of pQCT images from females and males. Robustness, which is the total surface area divided by bone length, provides a quantitative description of transverse bone growth with respect to bone length. From a geometrical standpoint, bones that are slender (i.e. narrow relative to length) have a higher risk of fracture in a loading scenario. In the study, it was found that the tibiae of males are 40.9% stiffer than those of females, females have about 10% less cortical area relative to body size, and the tibiae of males are more robust, regardless of body size.

Midfoot

In the current study, midfoot fractures occurred to the navicular and cuboid. Midfoot fractures are of concern, since these bones play an essential role in maintaining the structural integrity of the arches of the foot.

All five navicular damage cases involved non-displaced fractures of the beak. Three of the navicular fractures were coded as AIS 857461.2, since the fracture line extended into one joint surface, while the remaining two navicular fractures were coded as AIS 857451.2, since they were extra-articular. Fractures of the navicular body have been identified as indicators of high-energy traumatic injury mechanisms (Eichenholtz and Levine, 1964).

Two cuboid fractures were produced in the current study. These fractures were located on the lateral portion of the bone and were associated with navicular damage. The cuboid fractures were coded as AIS 857661.2, meaning the fracture line extended into one joint surface.

Danelson et al. (2018) determined that damage to the midfoot during UBB events is likely due to a primary injury mechanism of compression, with a secondary mechanism of differential loading of the foot (i.e. higher vertical displacement of the forefoot relative to the hindfoot due to the deformation of the floor).

Fractures similar to those observed during the current study were produced during Task 4.2 testing on the ALF (Danelson et al., 2015). The conditions of test MS7 produced damage that was not previously seen during that test series. Namely, tarsal bones were damaged, including the navicular, cuboid, and cuneiforms. The tarsal fractures were not displaced, but the bones were fragmented (looking intact upon first examination, but separated into pieces upon further dissection). This outcome was attributed to the implementation of a deformable floor plate that was constructed of a softer material than what was used in previous tests. This resulted in greater floor deformation, and presumably greater duration of boot-floor contact, and greater rate of floor deformation.

Forefoot

In the current study, forefoot damage occurred to the metatarsals and phalanges. Damage to the metatarsals consistently occurred to the proximal portion of the third, fourth, and fifth metatarsals. Some metatarsal fractures were coded as AIS 858163.2, indicating that they were partial articular, while others were coded as AIS 858173.2, meaning they were complete articular. A single case of

damage to the phalanges occurred to the proximal portion of the fifth phalanx and was coded as AIS 858163.2 (partial articular).

The nature of the forefoot damage in the current study is consistent with previously reported cases of high energy impacts to the plantar surface of the foot. Danelson et al. (2015) produced damage to the forefoot on the ALF, which included mid-diaphysis fractures of the second through fourth metatarsals in one foot, and proximal fractures of the fifth metatarsal in two feet. This is in contrast to the current study, in which all forefoot damage only occurred to the proximal portion of the metatarsals. Harris et al. (2000) observed damage throughout all five metatarsal bones in booted PMHS lower extremity specimens when mines were detonated directly beneath the heel and in-line with the tibia. Similar to the current study, these fractures occurred at the base of the metatarsals. To produce damage at the base of the metatarsals in PMHS legs, Smith et al. (2005) found it necessary to implement higher floor speeds (16 m/s) for axial impacts applied posterior to the ball of the foot. It was postulated that the nominal position (zero degrees of dorsiflexion) allows the structures of the foot, namely the arches and soft tissues, to better absorb the impact. It follows that UBB scenarios are capable of producing injuries in the nominal position, since the energy levels in this realm are much greater than those seen in automotive crashes.

Metatarsal fractures are commonly the result of direct trauma, such as crushing injuries (Stiegelmar et al., 2001). Danelson et al. (2018) reported that 54% of fractures of the metatarsals and phalanges occurred due to compression alone – namely an upward load on the plantar surface of the forefoot. Danelson et al. (2018) also reported that injuries of the forefoot from UBB attacks did not trend towards a particular floor input category (Extended Time with Decreased Magnitude vs. standard). Interestingly, the forefoot fractures in the current study occurred exclusively on the left lower extremity, which is positioned closer to the central location of the charge beneath the test fixture. By design, the interaction between the foot and the floor is different between the right and left lower extremity, which may have influenced the damage outcome.

Femur

In the current study, the left femur sustained a complete fracture in four cases. One case was related to a region of cancer in the proximal aspect of the bone. The remaining fractures were not

associated with a particular damage pattern to the distal portion of the lower extremity. One male sustained a spiral wedge fracture of the left femur due to a combination of bending and torsion. The torsional component potentiated this damage, which resulted from inertial loading on the thigh by the lower extremity. A second 50th-percentile male sustained a fragmented wedge fracture of the femur from a mechanism similar to that of the first male. A 5th-percentile female sustained a segmented bending fracture of the left femur that resulted from bending, with torsion being a possible contributor. This female had relatively lower mass lower extremities and relatively higher peak vertical acceleration of the femur. This, in combination with potentially lower bone strength, could have made an inertial fracture more likely for the female, even in the absence of appreciable torsion.

Kinematics Response

Video Data

Inspection of high-speed video reveals that as the floor deforms upwards, the plantar surface of the boot is compressed, followed by the ankle. Once the foot and ankle compliance is exhausted, the knee begins to translate vertically and the ankle decompresses. When the booted foot leaves the floor, the ankle dorsiflexes. The shank remains approximately vertical initially, while the knee and hip joints flex. Eventually, the knee begins to extend and the ankle plantar flexes, as the hip continues to flex. The hip occasionally externally rotates later in the event.

During the test event, the floor plate on the ALF does not translate upwards as a level surface, but rather, it undergoes greater displacement centrally. This is due to the central location of the charge. As a result, the floor surface is slightly slanted in the coronal plane, sometimes resulting in marginal eversion and inversion of the inboard and outboard subtalar joints, respectively. In addition, the maximum displacement of the left lower extremity is higher than the right lower extremity. This is more noticeable in Series B with the higher-energy floor condition, since greater floor deformation occurs sooner in the event. Differences in floor input between the inboard and outboard lower extremities (e.g. variations in displacement, rate of displacement, and/or energy level) may be responsible for the observed differences in injury pattern. No gross differences in kinematics were observed between the PMHS groups in the video data.

Peak Acceleration

There is a strong correlation between increased peak axial (global vertical) acceleration of the distal tibia and increased incidence of calcaneus fractures (p-value <0.0001) in the current study. There is also a strong correlation between increased peak posteroanterior (global vertical) acceleration of the distal femur and increased incidence of calcaneus fractures (p-value <0.0001). When the energy input is great enough to cause the severe calcaneus fractures observed in this study, it follows that these cases would be associated with greater peak vertical acceleration of the lower extremity. In the automotive realm, greater acceleration of the toe pan has been shown to result in injuries of the foot and ankle as well (Kallina et al., 1995).

Injury risk as a function of peak tibia acceleration is not typically discussed in the literature. However, Klopp et al. (1997) reported that fifty-percent probability of lower extremity injury is associated with a calcaneus acceleration of 216-g in a study that subjected the plantar surface of fifty male PMHS lower extremities to pendulum impacts. The results of the current study show that a fifty-percent probability of calcaneus damage is associated with 568-g peak distal tibia axial (global vertical) acceleration for a 50^{th}-percentile male. The differences in injury risk are likely due to differences between the acceleration pulses used for comparison (calcaneus acceleration in Klopp et al. vs. tibia acceleration in the current study), as well as differences in loading and time-to-peak loading. Klopp et al. (1997) included loads that ranged from roughly 3600-N to almost 9500-N, while time-to-peak ranged from roughly 5-ms to 22-ms. In the current study, several data points are associated with comparable time-to-peak for tibia peak vertical acceleration (3 to 6-ms). At these durations, calcaneus fractures occur in the range of 200 to 400-g.

The relationship between peak acceleration of the lower extremity and the incidence of fracture in the current study is likely influenced by the time taken to reach the peak acceleration (time-to-peak). Greater peak distal tibia axial (global vertical) acceleration is associated with calcaneus fracture for shorter acceleration time-to-peak, while lower peak tibia acceleration levels can result in calcaneus fracture if there is a longer time-to-peak. This result is also observed for floor acceleration in the current study. From this it is deduced that lower accelerations must be applied for a longer period to provide enough energy to produce fracture. Danelson et al. (2015) observed a similar trend for peak distal femur global vertical acceleration. Lower extremity damage was

associated with higher peak femur accelerations with shorter time-to-peak. Additionally, one of the lower peak acceleration damage cases had a longer time-to-peak, similar to damage associated with lower accelerations in the current study.

The significance of the relationship between increased peak global vertical acceleration of the lower extremity and increased fracture incidence of the talus is weak for both tibia acceleration (p-value 0.0199) and femur acceleration (p-value 0.0354). Damage to the talus was typically much less severe than damage to the calcaneus. Furthermore, there are far fewer talus fractures than calcaneus fractures occurring at the higher accelerations within these data. This could suggest that the talus generally has higher fracture tolerance than the calcaneus. In addition, fracture of the talus may be sensitive to the direction of loading (orientation of the talus) as well. The severe talus damage case that occurred at lower peak tibia vertical acceleration may indicate reduced fracture tolerance in that 5^{th}-percentile female. The incidence of tibia damage did not have a significant relationship with any lower extremity kinematics. There was a very low number of tibia fractures within this study.

Peak Speed

Peak tibia axial (global vertical) speed was strongly correlated to increased incidence of calcaneus fracture (p-value 0.0001) in the current study. Otherwise, peak tibia and femur global vertical speed do not appear to have a relationship with fracture incidence. Yoganadan et al. (2016) also found that foot and ankle injuries occur in association with higher tibia speed in a study that subjected seventeen PMHS leg specimens to UBB conditions. Peak axial speeds were 11.3 m/s for fracture and 9.0 m/s for non-fracture. Time-to-peak force ranged from 2.4 to 5.2-ms for the cases with damage.

In contrast to the current study, Schueler et al. (1995) did not find global vertical acceleration of the distal tibia to be a significant predictor of lower extremity injury in twenty-four plantar foot impacts to whole-body cadavers; however, speed was a significant predictor. A 35-km/h (9.72 m/s) or greater impact speed was associated with a significant "relative risk of leg injuries." Although not statistically significant, the calcaneus fracture results of the current study are in agreement. Nearly all calcaneus fractures occur above 10-m/s peak floor speed, regardless of the time-to-peak

floor speed. Danelson et al. (2015) reported a potential division of damage and non-damage lower extremity cases near 15 m/s peak floor speed, but this study evaluated male PMHS only, which may have increased this threshold.

Peak speed typically occurs much later than the fractures observed in this study (left censored). Therefore, peak speed is not associated with fracture other than reflecting the amount of energy in the segment/system. Uncensored speed data might produce a different result. Conversely, peak acceleration typically occurs much closer to the time of fracture, and is more closely related to the force applied to the bones. Of course, the acceleration is influenced by the effective mass of the portion of the lower extremity being accelerated, as well as mass coupling and recruitment effects associated with the soft tissues.

Mass below the Knee and Bone Mineral Density

Mass appears to be an important driver of kinematics. In the current study, lower extremities having lower below-knee mass reached higher accelerations and speeds, earlier in the event. The 50^{th}-percentile males were in the higher range of lower extremity mass, while the 75^{th}-percentile females and 5^{th}-percentile females fell within a lower range than the 50^{th}-percentile males. The mass of the females is comparable between sizes. Accordingly, females attain higher femur and tibia global vertical speeds than the 50^{th}-percenitle males in Series A, the results for which are not confounded by the influence of damage. The 5^{th}-percentile females attain higher vertical femur speed than the 75^{th}–percentile females in Series A. However, the 75^{th}-percentile females fall in a lower range of mass below the knee than the 5^{th}-percentile females. The phenomenon might be related to the nature of the engagement of the femur and the mass of the thigh.

Females have been shown to have significantly greater amounts of body fat than males for the same BMI. In addition, with increasing BMI, males increase visceral fat in the upper abdomen, while females increase subcutaneous fat in the hips and buttocks (Gallagher et al., 1996). The amount of soft tissue mass in the lower extremities influences phenomena associated with instantaneous effective mass and mass recruitment throughout the duration of the event (i.e. the degree of coupling between the bone and soft tissue of the leg).

Lower extremity mass also affects the interaction between the boot and the floor. The heavier lower extremities exhibit a more pronounced bimodal acceleration and second order speed response of the femur at the higher energies in Series B. It is postulated that the heavier extremities do not accelerate quickly enough to avoid a subsequent interaction with the rapidly approaching floor.

Interestingly, 75th-percentile female tibia fracture cases show a moderate relationship ($R^2 = 0.310$) for peak axial acceleration of the tibia increasing as leg mass increases. This relationship strengthens if only the more severe fractures are considered ($R^2 = 0.588$). This result could be related to decoupling between portions of the distal tibia due to fracture, as well as the trend of decreasing vBMD for increasing leg mass seen in the 75th-percentile females. In other words, the association between lower vBMD and greater fracture incidence and extent may increase compromise of the tibia, resulting in higher distal tibia axial acceleration.

The 75th-percentile female tibia fracture cases show a moderate relationship ($R^2 = 0.687$) for peak distal femur acceleration decreasing as below-knee mass increases. Again, this relationship becomes strong if only the more severe fractures are considered ($R^2 = 0.996$). Since the fractures occur near the tibia motion block and not the femur motion block, femur acceleration should be expected to be less influenced by the presence of fracture. These observations must be considered carefully, as there are so few data points and so many factors contributing to fracture.

The influence of mass on damage outcome is not well understood, since it is confounded by potential differences in the quality and quantity of bone present. Regardless, the tibia damage observed in the current study was weakly associated with lower extremities with lower mass below the knee (p-value 0.0164). This result was influenced most by the 75th-percentile female responses, which had a lower range of mass below the knee, and a much greater incidence of major tibia damage compared to the other specimen categories.

Increased risk of fracture is not expected to coincide with decreased mass. Blunt trauma of the lower extremities in general is more likely to occur in people who are obese (BMI $\geq$ 30 kg/m^2) (Boulanger et al., 1992). In addition, BMI has been shown to be associated with injury risk in the

automotive realm (Arbabi et al., 2003) and obese drivers are more prevalent among those who sustain lower extremity injuries automotive crashes (Ye et al., 2015). Mass of the lower extremities alone does not fully explain the damage trends that were observed in the current study.

Some trends observed in the current study may suggest that vBMD does not necessarily increase with leg mass. This is in contrast to the reporting of Hardy et al., (2001), in which increased upper extremity mass was shown to be associated with increased radius and ulna strength, and reduced likelihood of forearm fracture. In this study, the relationship between lower vBMD and higher mass below the knee is non-existent in 50th-percentile males (R^2 0.005), weak in 5th-percentile females (R^2 0.094), and moderate in 75th-percentile females (R^2 0.325). This might imply that heavier individuals may be less active during their lifetime, resulting in lower bone density. This may also suggest that greater bone quantity does not necessarily follow from greater bone quality. Both quantity and quality of bone contribute to bone strength. Measures such as robustness (Jepsen et al., 2011) and mineral content (Hardy et al., 2001) are more closely related to bone strength. The rate of mineralization is not related to strength, as all bone has the same calcium composition, resulting in the same percentage ash weight when burned (roughly 65%).

If only damaged tibiae for 75th-percentile females are considered, there is a strong trend (R^2 = 0.896) toward decreased vBMD for increased leg mass. This suggests that even heavier lower extremities can be damaged when the vBMD is low, implying a greater importance of bone density than lower extremity mass relative to injury occurrence. Yoganandan et al. (2017) reported that qCT-based calcaneus BMD of male PMHS specimens was a significant covariate in a survival model of calcaneus injury probability curves under UBB loading conditions. In the current study, the 75th-percentile female data demonstrate a trend toward increased likelihood of tibia fracture as vBMD decreases (p-value 0.0173). McMaster et al. (2000) noted that PMHS specimens that did not sustain fractures had relatively higher BMD in a study that subjected PMHS lower extremities to injurious level axial loading to simulate injuries sustained in frontal crashes.

Study Limitations

A potential limitation of this study is the use of peak values of acceleration and speed. Load on the lower extremities, which is commonly used as an injury metric, could not be measured in this

study. Implanting a load cell in the tibia, which is a current practice in the field, would interfere with the damage outcome of the tibia. A metric that characterizes the overall response of the lower extremity, rather than a single peak, may be more useful in this application. For example, the average distal forearm speed (ADFS) injury criterion introduced by Hardy et al. (1997) is calculated by finding the slope of the integrated distal forearm speed between 10 and 90-percent of the peak forearm displacement at or before 12-ms. This is similar in principal and execution to the Average Spine Acceleration (ASA) presented by Cavanaugh et al. (1993). In contrast to the current study, which uses single axis measures, ADFS is determined by finding the resultant magnitude of the integrated acceleration traces measured by three accelerometers at the distal radius. The current study uses vertical kinematics measures only because there is little rotation compared to the oblique postures investigated as part of Danelson et al., 2015. Both average distal speed and acceleration could be evaluated for either individual signals or resultants in this study.

The acceleration and speed values analyzed in this study are right censored for non-fracture cases and left censored for fracture cases. Uncensored data could be approximated for the fracture cases in a future analysis. This would result in a reduction of available data points, as the timing of all fracture events cannot be determined with absolute certainty. While fracture timing assessment for the purpose of determining approximately how quickly damaged occurs is reasonable, as little as a 0.1-ms shift can result in different values of acceleration and speed. However, once a robust method of determining fracture timing is established using strain, acceleration, and speed, some of these analyses can be repeated. The nonlinear regressions cannot be conducted using uncensored damage data, as the right censored non-damage peak values will be greater than the uncensored damage values for acceleration and speed.

Another limitation of this study is the performance of the ALF, which was much heavier than it was during previous testing (Danelson et al., 2015) after a redesign for the current study. The current incarnation of the ALF prohibits testing at higher input ranges, particularly input to the seat.

While twenty PMHS contribute to this study, there are three categories of sex/anthropometry and two levels of input to the ALF. That equates to having only three or four specimens within each

group. It is difficult assess true sex and anthropometry difference using this few specimens. Additional data would be helpful to clarify remaining questions and potentially reinforce the trends observed in this study.

Another limitation of this study is the difficulty in determining the influence of specific specimen characteristics on injury outcome due to their interrelatedness. In this study, increased mass below the knee did not relate to increased vBMD, which is unexpected based on previous literature (Hardy et al., 2001). Many of the 75th-percentile female specimens had decreasing vBMD for increasing below-knee mass. This inverse relationship is likely a result of selecting PMHS from a population with a more sedentary lifestyle. In addition, many of the male specimens had relatively diminutive lower extremities.

While DeXA t-score was a controlled selection criterion, vBMD varied considerably, which calls into question the relevance of DeXA. With the limited availability of PMHS falling within the mass and height requirements of this study, an additional exclusion criterion based on body composition (body fat percentage, body mass distribution, etc.) is not feasible.

An additional confounding factor included mass below the knee, which varied within each PMHS group and overlapped between groups. Additional complexity is introduced when variations in bone quality and quantity are considered. While BMD had been shown to be correlated with fracture tolerance, it does not necessarily characterize tissue quality (Jepsen et al., 2011). The combined influence of lower extremity mass, vBMD, bone quality, and bone quantity may skew potential differences in damage tolerance. Robustness and mineral content data could be valuable additions to the analyses.

CHAPTER 5

SUMMARY

This research forms the first biomechanical account of UBB effects on the lower extremities of matched pairs of female and male whole-body PMHS. This effort contributes to the body of knowledge pertaining to high-rate vertical loading of the lower extremities in a seated, nominal posture. The outcomes of this study are summarized below.

- The kinematics response in the global vertical direction varied between the two sexes and three percentiles studied:
    - In Series A (lower-energy floor condition), the tibiae of the 5th- and 75th-percentile females reached higher peak vertical accelerations than those of the 50th-percentile males.
    - In Series A, the general shape and duration of the femur and tibia vertical speeds were similar between females and males. However, the females had higher vertical speeds and they reached those speeds earlier in the event than the males.
    - In Series A, both sexes exhibited an oscillatory square unimodal response in the vertical acceleration response of the femora.
    - In Series B (higher-energy floor condition), the global vertical speeds of the tibiae were approximately twice those in Series A.
    - In Series B, the heavier lower extremities exhibited a second-order effect in the vertical speed of the distal femur.
    - In Series B, the vertical femur acceleration responses of the heavier lower extremities were triangular and bimodal in nature.
- There were no gross differences between female and male PMHS movement observed in the high-speed video.
- The higher-energy floor condition resulted in damage to the femur; tibia; fibula; talus; calcaneus; navicular; cuboid; third, fourth, and fifth metatarsals; and fifth phalange.
- Major damage occurred to the femur, tibia, fibula, talus, and calcaneus.
- Lower extremity damage type, incidence, and extent varied between the two sexes and three percentiles studied:

    - All but one case of tibia damage occurred to females.
    - All major tibia damage occurred to 75th-percentile females.
    - All fibula damage occurred to 75th-percentile females.
    - All but one case of talus damage occurred to females.
    - All midfoot damage occurred to females.
- All calcaneus and tibia fractures occurred within 3 ms of the onset of calcaneus motion.
- Calcaneus fracture is associated with higher peak vertical acceleration of the tibia with a lower time-to-peak. For longer time-to-peak, lower peak tibia acceleration levels can result in calcaneus fracture.
- Few fractures in the combined tibia and fibula category are seen overall. Unlike for the calcaneus and talus, no combined distal tibia and fibula fractures occurred at the lower levels of peak distal tibia axial acceleration observed in this study.
- Increased incidence of calcaneus damage has a strong relationship to both increased peak tibia vertical acceleration and increased peak femur vertical acceleration.
- Increased incidence of calcaneus damage has a moderate relationship with increased peak tibia vertical speed.
- Increased incidence of talus damage has a weak relationship with both increased peak tibia vertical acceleration and increased peak femur vertical acceleration.
- There is a weak relationship between decreased volumetric bone mineral density and increased incidence of tibia damage.
- There is a weak relationship between decreased mass below the knee and increased incidence of tibia damage.
- A fifty-percent probability of calcaneus fracture for less than 3-ms time-to-peak is associated with a 781-g peak tibia vertical acceleration for 50th-percentile males, 650-g for 75th-percentile females, and 396-g for 5th-percentile females.
- Fifty-percent probability of calcaneus fracture, regardless of time-to-peak, is associated with a 368-g peak femur vertical acceleration for 50th-percentile males, 332-g for 75th-percentile females, and 218-g for 5th-percentile females.
- Mass is an important driver of kinematics: Lighter extremities reach higher accelerations and speeds earlier in the event.

- The influence of mass on lower extremity damage is confounded by the quantity and quality of bone present.
- There are important differences between females and males in terms of kinematics and damage responses:
    - The observed differences in kinematics are not considered to be a result of the differences in anatomy/shape, but are more closely tied to specimen size and test input conditions.
    - The observed differences in fracture incidence and extent between the sex/anthropometry categories examined in this study are largely related to quantity and quality of bone (tolerance).

By expanding the knowledgebase of UBB injury data, the results of this study contribute to more accurate assessment and prediction of injuries in the UBB environment. These findings will inform future decisions regarding the requirements for test capabilities that incorporate the female Warfighter. Ultimately, advancements can be made in physical surrogates, injury assessment and prediction criteria, modeling and simulation capabilities, and test methods, which will allow further optimization of military ground vehicles, personal protective equipment, and injury countermeasures. Improvements in these technologies will reduce and/or prevent injuries and deaths among the US Warfighter population, both male and female.

APPENDICES

Appendix A: Anthropometry

Table A1: 50th-percentile male anthropomorphic measurements (cm)

Measure	SA1C1	SA1C2	SA2C1	SA2C2	SB2C1	SB3C1	SB4C1	SB5C1	Avg.	Std.
Stature	182.9	174.6	188.2	181.8	186.9	168.5	178.0	181.6	180.3	6.5
Shoulder Height	157.9	146.1	168.8	157.0	158.6	148.1	150.6	156.6	155.5	7.2
Waist Height	106.3	96.3	110.7	103.3	111.5	97.1	97.9	98.3	102.6	6.2
Crotch Height	88.3	78.8	99.3	81.5	86.0	73.3	78.7	82.4	83.5	7.9
Tibial Height	50.3	48.2	50.6	48.4	49.5	45.2	45.5	47.3	48.1	2.0
Vertex-Symphysion	83.4	88.3	89.0	89.8	98.8	86.8	93.1	87.8	89.6	4.6
Head-Trochanterion	85.7	80.5	87.9	88.4	91.9	79.3	86.5	84.4	85.6	4.2
Shoulder-Elbow	40.3	37.2	40.9	37.9	38.2	35.2	34.7	37.7	37.8	2.2
Forearm-Hand	51.2	47.7	52.6	49.8	53.2	43.0	45.5	47.1	48.7	3.6
Bi-acromial Breadth	37.9	35.4	32.5	29.1	42.0	33.6	38.2	34.8	35.4	4.0
Bi-deltoid Breadth	47.0	41.1	44.1	-	40.6	42.8	42.2	47.1	43.6	2.6
Chest Breadth	32.6	33.6	31.3	32.2	31.9	36.6	34.7	33.2	33.3	1.7
Hip Breadth	36.7	30.6	35.1	34.6	32.5	32.2	30.1	27.8	32.5	2.9
Waist Breadth	34.9	30.8	32.5	32.4	31.5	30.7	32.8	33.1	32.3	1.4
Trochanter Breadth	37.4	34.0	35.9	36.5	36.8	31.5	34.8	34.2	35.1	1.9
Chest Depth	25.4	21.3	18.5	18.9	17.8	24.3	19.2	17.9	20.4	2.9
Waist Depth	24.5	23.0	20.0	17.4	17.0	21.8	16.9	15.2	19.5	3.4
Buttock Depth	18.8	20.6	16.9	17.5	16.5	17.8	17.2	18.4	18.0	1.3
Head Height	24.1	21.8	23.4	20.7	22.8	23.1	22.9	23.6	22.8	1.1
Head Breadth	15.0	14.7	16.2	15.9	16.6	15.3	14.5	15.7	15.5	0.7
Bi-zygomatic Breadth	12.0	14.6	14.2	14.0	11.5	13.2	12.6	14.0	13.3	1.1
Head Length	20.6	19.8	20.8	19.2	18.5	18.8	19.9	19.1	19.6	0.8
Menton-Sellion	12.0	12.0	12.6	12.8	13.2	12.7	12.4	11.8	12.4	0.5
Foot Breadth	9.3	9.2	8.7	10.1	8.3	7.9	8.4	8.9	8.8	0.7
Ankle Height	10.8	9.9	14.2	11.6	10.2	10.7	11.7	11.3	11.3	1.3
Foot Length	24.3	24.8	27.5	24.8	23.9	23.3	25.6	25.1	24.9	1.3
Neck Circumference	41.5	41.0	46.0	35.3	38.2	54.0	37.0	41.5	41.8	5.9
Scye Circumference	57.3	45.5	43.5	38.5	41.8	42.5	43.3	45.0	44.7	5.5
Bicep Circumference	30.5	25.0	29.5	24.7	31.9	26.8	27.0	29.8	28.1	2.6
Elbow Circumference	28.7	25.5	29.5	26.0	29.7	26.3	25.9	26.7	27.3	1.7
Forearm Circumference	28.4	24.0	28.0	20.5	29.3	24.3	25.2	27.4	25.9	2.9
Wrist Circumference	17.5	17.5	17.0	15.7	19.1	17.2	17.2	16.4	17.2	1.0
Thigh Circumference	62.5	47.0	61.0	47.5	53.6	55.5	49.9	57.0	54.2	5.9
Distal Thigh Circumference	40.0	39.8	39.1	35.5	41.6	34.5	38.7	37.2	38.3	2.4
Knee Circumference	37.1	39.2	43.0	27.0	43.1	34.9	38.2	37.5	37.5	5.1
Calf Circumference	40.7	28.6	31.1	35.5	35.3	25.1	33.5	34.3	33.0	4.8
Ankle Circumference	22.3	20.6	21.4	18.5	25.9	18.3	22.2	19.9	21.1	2.5
Chest Circumference	104.4	100.8	96.3	90.8	93.9	110.8	90.6	92.3	97.5	7.3
Waist Circumference	100.0	94.5	92.0	87.0	83.3	94.2	88.5	89.8	91.2	5.2
Buttocks Circumference	110.5	93.6	100.9	92.8	100.0	93.5	91.5	96.8	97.5	6.3

Table A2: 75th-percentile female anthropomorphic measurements (cm)

Measure	SA3C1	SA4C1	SA5C1	SB1C1	SB3C2	SB4C2	Avg.	Std.
Stature	170.9	161.4	164.1	166.6	164.3	162.9	165.0	3.4
Shoulder Height	147.5	137.1	144.9	146.0	140.1	139.9	142.5	4.1
Waist Height	96.2	89.9	91.1	92.9	91.3	86.3	91.3	3.3
Crotch Height	81.2	71.7	74.2	75.2	78.7	93.7	79.1	7.9
Tibial Height	42.7	41.6	42.0	44.2	41.2	41.3	42.2	1.1
Vertex-Symphysion	84.4	80.9	82.1	82.9	83.7	85.8	83.3	1.7
Head-Trochanterion	81.6	78.2	85.3	83.1	80.7	80.3	81.5	2.4
Shoulder-Elbow	36.8	32.5	34.2	32.2	34.8	34.1	34.1	1.7
Forearm-Hand	45.3	42.1	44.7	43.4	43.6	42.1	43.5	1.3
Bi-acromial Breadth	31.4	-	26.6	35.0	36.6	31.8	32.3	3.9
Bi-deltoid Breadth	39.7	25.9	42.3	39.8	39.4	45.4	38.8	6.7
Chest Breadth	32.9	26.2	30.0	34.5	29.4	31.6	30.7	2.9
Hip Breadth	31.5	34.4	33.3	32.4	29.6	30.4	31.9	1.8
Waist Breadth	36.8	39.0	37.7	35.8	35.9	30.3	35.9	3.0
Trochanter Breadth	38.8	41.7	37.3	37.2	40.3	30.3	37.6	4.0
Chest Depth	20.3	16.6	17.6	18.1	16.1	19.5	18.0	1.6
Waist Depth	19.8	16.4	18.4	17.6	16.0	19.8	18.0	1.6
Buttock Depth	17.5	16.9	17.8	16.6	16.2	19.2	17.4	1.1
Head Height	22.6	21.3	19.1	21.4	22.5	20.5	21.2	1.3
Head Breadth	15.4	14.6	14.4	15.2	14.2	14.6	14.7	0.5
Bi-zygomatic Breadth	11.8	11.0	14.2	14.8	12.5	12.4	12.8	1.4
Head Length	18.5	18.6	18.2	18.6	17.7	17.8	18.2	0.4
Menton-Sellion	10.4	11.6	11.9	11.2	11.8	9.5	11.1	0.9
Foot Breadth	8.2	7.5	8.6	7.6	8.2	6.1	7.7	0.9
Ankle Height	9.8	7.7	10.4	9.2	8.6	10.1	9.3	1.0
Foot Length	24.2	22.1	24.0	21.9	21.7	21.0	22.5	1.3
Neck Circumference	34.9	29.6	35.0	35.2	35.4	46.2	36.1	5.4
Scye Circumference	43.4	39.2	41.2	38.0	39.8	43.8	40.9	2.3
Bicep Circumference	25.2	28.7	33.2	24.8	29.2	26.9	28.0	3.1
Elbow Circumference	23.2	24.4	26.2	22.3	25.6	24.3	24.3	1.4
Forearm Circumference	20.3	23.1	26.5	21.4	20.1	22.7	22.3	2.4
Wrist Circumference	14.9	14.0	14.5	15.1	14.6	15.3	14.7	0.5
Thigh Circumference	56.8	62.6	58.4	56.0	60.9	49.7	57.4	4.5
Distal Thigh Circumference	37.8	38.5	40.6	39.5	40.3	37.8	39.1	1.2
Knee Circumference	35.6	38.0	42.7	34.6	40.9	37.5	38.2	3.1
Calf Circumference	28.1	33.2	31.3	30.7	31.3	30.1	30.8	1.7
Ankle Circumference	23.3	20.3	19.5	19.0	20.5	17.4	20.0	2.0
Chest Circumference	91.8	83.2	88.0	96.8	85.9	95.4	90.1	5.4
Waist Circumference	102.0	100.8	100.7	102.5	104.3	87.2	99.6	6.2
Buttocks Circumference	105.3	106.9	100.5	101.0	103.5	88.2	100.9	6.7

Table A3: 5th-percentile female anthropometric measurements (cm)

Measure	SA3C2	SA5C2	SA6C1	SB1C2	SB2C2	SB5C2	Avg.	Std.
Stature	159.2	162.3	163.1	171.6	160.3	159.1	162.6	4.7
Shoulder Height	137.3	141.0	137.4	148.0	136.9	134.1	139.1	4.9
Waist Height	87.7	88.2	89.8	103.8	93.9	85.4	91.4	6.7
Crotch Height	73.1	70.0	73.7	82.3	72.3	71.4	73.8	4.4
Tibial Height	39.7	41.7	41.7	43.0	42.9	41.6	41.7	1.2
Vertex-Symphysion	80.9	84.6	81.5	85.2	87.5	84.3	84.0	2.4
Head-Trochanterion	77.1	78.9	78.7	80.1	80.2	80.5	79.2	1.3
Shoulder-Elbow	33.6	33.5	34.1	36.7	31.0	32.0	33.5	2.0
Forearm-Hand	40.4	42.6	45.1	44.1	38.6	41.7	42.1	2.4
Bi-acromial Breadth	25.8	25.7	33.9	27.6	33.7	29.6	29.4	3.7
Bi-deltoid Breadth	35.7	42.6	42.1	38.6	31.8	35.9	37.8	4.2
Chest Breadth	27.3	31.9	30.2	28.4	26.8	24.9	28.2	2.5
Hip Breadth	23.6	31.5	29.6	24.9	26.1	23.4	26.5	3.3
Waist Breadth	26.5	34.2	32.7	27.4	29.8	25.5	29.4	3.5
Trochanter Breadth	31.2	35.3	33.9	33.4	38.1	26.8	33.1	3.8
Chest Depth	16.9	17.3	15.5	14.7	16.0	13.6	15.7	1.4
Waist Depth	17.3	18.4	14.5	17.0	15.7	13.4	16.1	1.9
Buttock Depth	16.9	16.5	15.2	17.2	15.6	12.7	15.7	1.6
Head Height	21.0	20.1	19.0	21.5	20.2	20.1	20.3	0.9
Head Breadth	14.0	14.3	14.3	14.8	13.7	13.8	14.2	0.4
Bi-zygomatic Breadth	10.6	11.7	12.9	14.4	11.8	12.9	12.4	1.3
Head Length	17.7	18.8	17.4	18.3	16.8	18.7	18.0	0.8
Menton-Sellion	10.8	11.0	10.3	10.7	9.9	10.2	10.5	0.4
Foot Breadth	8.3	8.2	7.7	8.0	7.5	8.5	8.0	0.4
Ankle Height	9.0	11.0	9.6	9.7	7.5	9.8	9.4	1.1
Foot Length	22.1	23.0	20.9	21.1	21.8	22.6	21.9	0.8
Neck Circumference	31.4	35.9	32.6	31.8	32.5	27.0	31.9	2.9
Scye Circumference	32.2	44.6	34.6	37.0	34.1	31.0	35.6	4.9
Bicep Circumference	23.3	27.0	25.5	23.6	28.6	18.6	24.4	3.5
Elbow Circumference	21.6	23.5	25.4	22.8	23.4	20.2	22.8	1.8
Forearm Circumference	18.8	21.8	24.5	21.3	22.6	18.9	21.3	2.2
Wrist Circumference	14.4	14.5	15.2	14.2	14.4	14.0	14.4	0.4
Thigh Circumference	45.9	55.4	49.1	52.7	57.3	42.5	50.5	5.7
Distal Thigh Circumference	31.7	36.9	38.1	34.1	42.5	27.5	35.1	5.2
Knee Circumference	32.4	35.2	36.9	33.4	38.7	29.9	34.4	3.2
Calf Circumference	27.5	31.2	29.9	28.2	35.5	22.7	29.2	4.3
Ankle Circumference	22.9	17.8	18.7	21.6	21.5	19.0	20.2	2.0
Chest Circumference	78.9	91.6	82.8	80.6	78.1	67.1	79.8	7.9
Waist Circumference	85.1	93.4	87.9	88.4	80.2	71.4	84.4	7.7
Buttocks Circumference	87.0	94.7	89.8	90.2	99.5	73.4	89.1	8.9

Appendix B: Catalog of PMHS Damage Data

Table B1: MS1 autopsy summary

Crew 1: PMHS-SM91 (50M)	-
None	-

Table B2: MS4 autopsy summary

Crew 1: PMHS-6541 (50M)	-
Hindfoot: Calcaneus, crushed, bilateral	-

Table B3: MS5 autopsy summary

Crew 1: PMHS-SM85 (50M)	Crew 2: PMHS-SM90 (50M)
Hindfoot: Calcaneus, crushed, RT	None

Table B4: MS7 autopsy summary

Crew 1: PMHS-6504 (50M)	-
Hindfoot: Talus, Fx, minor/focal neck compression, LT Calcaneus, crushed, bilateral Midfoot: Navicular, Fx, bilateral Forefoot: Metatarsals 2-3, Fx, RT Metatarsal 4, Fx, RT Metatarsal 5, Fx, LT	-

Table B5: MS11 autopsy summary

Crew 1: PMHS-SM94 (50M)	-
Hindfoot: Talus, Fx, complete, LT Calcaneus, crushed, bilateral	-

Table B6: MS14 autopsy summary

Crew 1: PMHS-6601 (50M)	-
Hindfoot: Talus, 2 Fx, minor posteromedial articular surface chip and minor/focal neck compression, RT Calcaneus, crushed, RT	-

Table B7: SA1 autopsy summary

Crew 1: PMHS-SM117 (50M)	Crew 2: PMHS-SM118 (50M)
None	None

Table B8: SA2 autopsy summary

Crew 1: PMHS-SM120 (50M)	Crew 2: PMHS-SM119 (50M)
None	None

Table B9: SA3 autopsy summary

Crew 1: PMHS-SF127 (75F)	Crew 2: PMHS-SF126 (5F)
None	Thigh: Femur, Fx, proximal, LT

Table B10: SA4 autopsy summary

Crew 1: PMHS-SF128 (75F)	Crew 2: ATD-HIII 5th-female
None	NA

Table B11: SA5 autopsy summary

Crew 1: PMHS-SF131 (75F)	Crew 2: PMHS-SF132 (5F)
None	None

Table B12: SA6 autopsy summary

Crew 1: PMHS-SF133 (5F)	Crew 2: ATD-HIII 5th-female
Hindfoot: Talus, Fx, facies articularis navicularis, partial, LT	NA

Table B13: SB1 autopsy summary

Crew 1: PMHS-SF138 (75F)		Crew 2: PMHS-SF134 (5F)	
Leg:	Tibia, Fx, pilon, distal, RT	Thigh:	Femur, Fx, mid-diaphysis, LT
	Tibia, crush Fx, distal, LT	Leg:	Tibia, Fx, pilon, distal, LT
	Fibula, Fx, articular surface of lateral malleolus, LT	Hindfoot:	Talus, Fx, partial transection, RT
Hindfoot:	Talus, 2 Fx, posterolateral tubercle and facies articularis navicularis, RT		Calcaneus, crushed, bilateral
		Midfoot:	Navicular, Fx, beak, LT
		Forefoot:	Metatarsal 5, Fx, proximal, LT
	Calcaneus, crushed, RT		
Midfoot:	Navicular, Fx, beak, bilateral		
	Cuboid, Fx, lateral portion of posterior surface, RT		
	Cuboid, Fx, posterior border of dorsal surface, LT		
Forefoot:	Metatarsal 4, Fx, base, LT		
	Metatarsal 5, Fx, base, LT		
	Phalanx 5, Fx, base, LT		

Table B14: SB2 autopsy summary

Crew 1: PMHS-SM140 (50M)		Crew 2: PMHS-SF135 (5F)	
Thigh:	Femur, Fx, mid-diaphysis, LT	Hindfoot:	Talus, Fx, lateral aspect of posterior calcaneal articular surface, LT
Hindfoot:	Calcaneus, crushed, bilateral		Calcaneus, crushed, bilateral
Forefoot:	Metatarsal 4, Fx, base, LT	Midfoot:	Navicular, Fx, beak, RT

Table B15: SB3 autopsy summary

Crew 1: PMHS-SM141 (50M)		Crew 2: PMHS-SF142 (75F)	
Hindfoot:	Calcaneus, crushed, LT	Leg:	Tibia, crush Fx, distal, LT
			Fibula, 2 Fx, distal diaphysis and head, LT
		Hindfoot:	Talus, multiple Fx, posterior calcaneal articular surface, facies malleolus lateralis, facies malleolaris medialis, RT
			Talus, cartilage damage, LT
			Calcaneus, crushed, bilateral
		Midfoot:	Navicular, Fx, beak, RT

Table B16: SB4 autopsy summary

Crew 1: PMHS-SM145 (50M)		Crew 2: PMHS-SF148 (75F)	
Leg:	Tibia, Fx, plafond, RT	Leg:	Tibia, Fx, pilon, RT
Hindfoot:	Talus, cartilage damage trochlear surface, Fx posterolateral tubercle, RT		Tibia, crush Fx, LT
			Fibula, Fx, distal diaphysis, LT
		Hindfoot:	Talus, multiple Fx, anterolateral aspect of trochlear surface, lateral process, facies malleolus lateralis, LT
	Calcaneus, crushed, LT		Calcaneus, crushed, bilateral
		Forefoot:	Metatarsal 3, Fx, base, LT
			Metatarsal 4, Fx, base, LT
			Metatarsal 5, Fx, base, LT

Table B17: SB5 autopsy summary

Crew 1: PMHS-SM150 (50M)	Crew 2: PMHS-SF151 (5F)
Thigh: Femur, Fx, mid-diaphysis, LT	Hindfoot: Talus, Fx, posterolateral tubercle, RT Calcaneus, crushed, bilateral

Damage Coding

Series A: Shot 3 Crew 2 – PMHS-SF126 (5F)

- Femur, left – proximal shaft fx
  - AIS: 853251.3 simple; spiral; oblique; transverse; Winquist I
  - BioPT Bin: Femur shaft fracture (simple; OTA Type 32-A; Winquist I)
  - OTA 32-A2 oblique

Series A: Shot 6 Crew 1 – PMHS-SF133 (5F)

- Talus, left - partial neck fx (medial/dorsal aspect)
  - AIS: 857261.2 fracture line into one joint surface; talus body
  - BioPT Bin 2: talus fx non-displaced or simple displacement; Hawkins Type-I, II)
  - No Hawkins classification, not a neck fracture

Series B: Shot 1 Crew 1 – PMHS-SF138 (75F)

- Distal tibia, right - pilon fx
  - AIS: 854361.2 distal tibia partial articular
  - BioPT Bin 6: distal tibia fracture (partial articular; simple pilon; OTA Type 43-B)
  - OTA 43-B1 pure split
- Talus, right – 2 chip fx: posterolateral tubercle and facies articularis navicularis
  - AIS: 857261.2 fracture line into one joint surface; talus body
  - BioPT Bin 2: Talus fracture (fx non-displaced or simple displacement; Hawkins Type-I, II)
  - No Hawkins classification, not a neck fracture
- Calcaneus, right - crushed
  - AIS: 857371.2 fracture line into ≥ 2 joint surfaces
  - BioPT Bin 5: calcaneus fracture (comminuted crush, comminuted, Sanders Type-III, Type-IV)
  - Sanders Type IV, 3 or more fracture lines
- Navicular, right – fx of beak
  - AIS: 857461.2 fracture line into two joint surfaces

    - BioPT Bin 1: Tarsal bone fracture (navicular, cuboid, and cuneiforms)
- Cuboid, right - fx of lateral portion of posterior surface
    - AIS: 857661.2 fracture line into one joint surface
    - BioPT Bin 1: Tarsal bone fracture (navicular, cuboid, and cuneiforms)
- Distal tibia, left - compression fx
    - AIS: 854371.2 distal tibia complete articular
    - OTA type 43-C3 articular multi-fragmentary
    - BioPT Bin 7: distal tibia fracture (complete articular; comminuted pilon; OTA Type 43-C)
- Distal fibula, left - oblique fx
    - AIS: 854471.2 above joint (suprasyndesmotic); isolated shaft, head, or neck; Weber C
    - BioPT Bin 10: Distal fibula fracture (simple, complex bimalleolar)
    - Weber classification: C
- Navicular, left - fx of beak
    - AIS: 857461.2 fracture line into two joint surfaces
    - BioPT Bin 1: tarsal bone fracture (navicular, cuboid, and cuneiforms)
- Cuboid, left – chip of posterior border of dorsal surface
    - AIS: 857661.2 fracture line into one joint surface
    - BioPT Bin 1: tarsal bone fracture (navicular, cuboid, and cuneiforms)
- 4^{th} metatarsal, left - chip on superior edge of articular surface for 5^{th} metatarsal
    - AIS: 858163.2 partial articular
- 5^{th} metatarsal, left - crushed proximal portion
    - AIS: 858173.2 complete articular
- 5^{th} proximal phalange, left – fx of articular surface for 5^{th} metatarsal
    - AIS: 858163.2 partial articular

Series B: Shot 1 Crew 2 – PMHS-SF134 (5F)

- Talus, right – partial transection at neck
    - AIS: 857261.2 fracture line into one joint surface; talus body
    - BioPT Bin 2: talus fracture (fx non-displaced or simple displacement; Hawkins Type-I, II)

- Hawkins type I- non displaced fracture of talar neck

- Calcaneus, right - crushed
  - AIS: 857371.2 fracture line into ≥ 2 joint surfaces
  - BioPT Bin 5: calcaneus fracture (comminuted crush, comminuted, Sanders Type-III, Type-IV)
  - Sanders Type IV, 3 or more fracture lines
- Femur, left - shaft fx
  - AIS: 853271.3 complex; comminuted; segmental; Winquist IV
  - BioPT Bin 3: femur shaft fracture (complex; OTA Type 32-C; Winquist IV)
  - OTA 32-C2: complex- segmental
  - Winquist IV
- Tibia, left - pilon fx
  - AIS: 854361.2 distal tibia, partial articular
  - BioPT Bin 6: distal tibia fracture (partial articular; simple pilon; OTA Type 43-B)
  - OTA 43-B1 pure split
- Calcaneus, left - crushed
  - AIS: 857371.2 fracture line into ≥ 2 joint surfaces
  - BioPT Bin 5: calcaneus fracture (comminuted crush, comminuted, Sanders Type-III, Type-IV)
  - Sanders Type IV, 3 or more fracture lines
- Navicular, left – fx of beak
  - AIS: 857461.2 navicular fracture, fracture line into two joint surfaces
  - BioPT bin 1: tarsal bone fracture (navicular, cuboid, and cuneiforms)
- 5^{th} metatarsal, left – fx of proximal articular surface
  - AIS 858163.2 partial articular

Series B: Shot 2 Crew 1 – PMHS-SM140 (50M)

- Calcaneus, right - crushed
  - AIS: 857371.2 fracture line into ≥ 2 joint surfaces
  - BioPT Bin 5: Calcaneus fracture (comminuted crush, comminuted, Sanders Type-III, Type-IV)

- Sanders Type IV, 3 or more fracture lines

- Femur, left - shaft fx
  - AIS: 853261.3 wedge; "butterfly"; Winquist II or III
  - BioPT Bin 2: femur shaft fracture (wedge; OTA Type 32-B; Winquist II/III)
  - OTA Bin 32-B1 spiral wedge
- Calcaneus, left - crushed
  - AIS: 857371.2 fracture line into ≥ 2 joint surfaces
  - BioPT Bin 5: calcaneus fracture (comminuted crush, comminuted, Sanders Type-III, Type-IV)
  - Sanders Type IV, 3 or more fracture lines
- 4^{th} metatarsal, left – fx of proximal articular surface
  - AIS 858163.2 partial articular

Series B: Shot 2 Crew 2 – PMHS-SF135 (5F)

- Calcaneus, right - crushed
  - AIS: 857371.2 fracture line into ≥ 2 joint surfaces
  - BioPT Bin 5: calcaneus fracture (comminuted crush, comminuted, Sanders Type-III, Type-IV)
  - Sanders Type IV, 3 or more fracture lines
- Navicular, right – fx of lateral border of dorsal surface
  - AIS: 857451.2 extra articular (coronal body split, no joint involvement)
  - BioPT Bin 1: tarsal bone fracture (navicular, cuboid, and cuneiforms)
- Talus, left – fx of lateral aspect of posterior calcaneal articular surface
  - AIS: 857261.2 fracture line into one joint surface; talus body
  - BioPT Bin 2: talus fracture (fx non-displaced or simple displacement; Hawkins Type-I, II)
  - No Hawkins classification, not a neck fracture
- Calcaneus, left - crushed
  - AIS: 857371.2 fracture line into ≥ 2 joint surfaces
  - BioPT Bin 5: Calcaneus fracture (comminuted crush, comminuted, Sanders Type-III, Type-IV)

- Sanders Type IV, 3 or more fracture lines

Series B: Shot 3 Crew 1 – PMHS-SM141 (50M)

- Calcaneus, left – crushed
  - AIS: 857371.2 fracture line into ≥ 2 joint surfaces
  - BioPT Bin 5: calcaneus fracture (comminuted crush, comminuted, Sanders Type-III, Type-IV)
  - Sanders Type IV, 3 or more fracture lines

Series B: Shot 3 Crew 2 – PMHS-SF142 (75F)

- Talus, right - 3 fx: posterior calcaneal articular surface, facies malleolus lateralis, and facies malleolaris medialis
  - AIS: 857261.2 fracture line into one joint surface; talus body
  - BioPT Bin 2: talus fracture (fx non-displaced or simple displacement; Hawkins Type-I, II)
  - No Hawkins classification, not a neck fracture
- Calcaneus, right - crushed
  - AIS: 857371.2 fracture line into ≥ 2 joint surfaces
  - BioPT Bin 5: calcaneus fracture (comminuted crush, comminuted, Sanders Type-III, Type-IV)
  - Sanders Type IV, 3 or more fracture lines
- Navicular, right – fx of beak
  - AIS: 857461.2 fracture line into two joint surfaces
  - BioPT Bin 1: tarsal bone fracture (navicular, cuboid, and cuneiforms)
- Distal tibia, left - shattered
  - AIS: 854371.2 distal tibia complete articular
  - BioPT Bin 7: distal tibia fracture (complete articular; comminuted pilon; OTA Type 43-C)
  - OTA Type 43-C3 articular multi-fragmentary
- Fibula, left - 2 fx: head and distal shaft

    - AIS: 854471.2 fibula above joint (suprasyndesmotic); isolated shaft, head or neck; Weber C
    - BioPT Bin- no bin
    - OTA 44-C1 fibular diaphyseal fracture, simple
    - Weber C
- Talus, left - cartilage damage
    - AIS- no code for cartilage damage
- Calcaneus, left - crushed
    - AIS: 857371.2 fracture line into ≥ 2 joint surfaces
    - BioPT Bin 5: calcaneus fracture (comminuted crush, comminuted, Sanders Type-III, Type-IV)
    - Sanders Type IV, 3 or more fracture lines

Series B: Shot 4 Crew 1 – PMHS-SM145 (50M)

- Tibia, right – minor damage to the anterior and posterior margins of plafond
    - AIS: 854361.2 distal tibia, partial articular
    - BioPT Bin 6: distal tibia fracture (partial articular; simple pilon; OTA Type 43-B)
    - OTA 43-B1 pure split
- Talus, right - cartilage damage to posterolateral portion of trochlear surface; fx of posterior process
    - AIS: 857261.2 fracture line into one joint surface; talus body
    - BioPT Bin 2: talus fracture (fx non-displaced or simple displacement; Hawkins Type-I, II)
    - No Hawkins classification, not a neck fracture
- Calcaneus, left – crushed (separation of sustentaculum tali and general anterior-posterior segmentation resulting in four large pieces and associated chips)
    - AIS: 857371.2 fracture line into ≥ 2 joint surfaces
    - BioPT Bin 5: calcaneus fracture (comminuted crush, comminuted, Sanders Type-III, Type-IV)
    - Sanders Type IV, 3 or more fracture lines

Series B: Shot 4 Crew 2 – PMHS-SF148 (75F)

- Tibia, right – pilon fx (cartilage damage on posterior lateral aspect. Reaches bone, but there is negligible bone damage, 12 mm length)
  - AIS: 854361.2 distal tibia, partial articular
  - BioPT Bin 6: distal tibia fracture (partial articular; simple pilon; OTA Type 43-B)
  - OTA 43-B1 pure split
- Calcaneus, right – crushed (sectioning of the dorsal half and crushing of the plantar half)
  - AIS: 857371.2 fracture line into ≥ 2 joint surfaces
  - BioPT Bin 5: calcaneus fracture (comminuted crush, comminuted, Sanders Type-III, Type-IV)
  - Sanders Type IV, 3 or more fracture lines
- Tibia, left – crushed (stellate fx pattern beginning at tibia plafond propagating 6 cm with general crushing of the distal tibia generating several fragments ranging from 15 mm to 4 cm in length with multiple small chips. Largest segments were both medial and lateral)
  - AIS: 854371.2 distal tibia complete articular
  - BioPT Bin 7: distal tibia fracture (complete articular; comminuted pilon; OTA Type 43-C)
  - OTA type 43-C3 articular multi-fragmentary
- Fibula, left - transverse fx (9 cm from distal end; slight angulation from medial distal to lateral proximal)
  - AIS: 854471.2 above joint (suprasyndesmotic); isolated shaft, head or neck; Weber C
  - BioPT Bin 10: distal fibula fracture (simple, complex bimalleolar)
  - Weber classification: C
  - OTA 44-C1: fibular diaphyseal fracture, simple
- Talus, left - two lateral evulsions (both triangular: one at anterior portion of superior articular surface, 12 mm on a side; one at the junction between lateral and inferior articular surfaces, 15 mm on a side)
  - AIS: 857261.2 fracture line into one joint surface; talus body
  - BioPT Bin 2: talus fracture (fx non-displaced or simple displacement; Hawkins Type-I, II)
  - No Hawkins classification, not a neck fracture

- Calcaneus, left - Crushed (one primary anterior-posterior fx through calcaneal sulcus, 4 cm; producing two anterior-medial chips, 2.5 cm and 1.5 cm; involving the middle articular surface and separating the anterior articular surface. Posterior cortical chip on dorsal surface located 1 cm from posterior aspect, 7 mm wide)
  - AIS: 857371.2 fracture line into ≥ 2 joint surfaces
  - BioPT Bin 5: calcaneus fracture (comminuted crush, comminuted, Sanders Type-III, Type-IV)
  - Sanders Type IV, 3 or more fracture lines
- 3rd metatarsal, left - proximal articular surface crushed (dominant horizontal fracture, 18 mm; dorsal part separated from ventral)
  - AIS 858163.2 complete articular
- 4th metatarsal, left - proximal articular surface crushed (horizontal fx propagating to mid-diaphysis)
  - AIS: 858173.2 complete articular
- 5th metatarsal, left - proximal lateral chip. Triangular with base being 5 mm and sides being 3 mm
    - AIS 858163.2 partial articular

Series B: Shot 5 Crew 1 – PMHS-SM150 (50M)

- Femur, left – shaft fx
  - AIS: 853261.3 wedge; "butterfly"; Winquist II or III
  - BioPT Bin 2: Femur shaft fracture (wedge; OTA Type 32-B; Winquist II/III)
  - OTA Bin 32-B3 fragmentary wedge

Series B: Shot 5 Crew 2 – PMHS-SF151 (5F)

- Talus, right – posterior chip on articular surface for calcaneus (4 pieces ~5 mm each)
  - AIS: 857261.2 fracture line into one joint surface; talus body
  - BioPT Bin 2: Talus fracture (fx non-displaced or simple displacement; Hawkins Type-I, II)
  - No Hawkins classification, not a neck fracture

- Calcaneus, right – crushed (general crushing of plantar half and sectioning of dorsal half; large posterior chip, 5 x 2 x 3 cm; several smaller chips ranging from 2-4 cm in length from superolateral and superomedial aspect)
    - AIS: 857371.2 fracture line into ≥ 2 joint surfaces
    - BioPT Bin 5: Calcaneus fracture (comminuted crush, comminuted, Sanders Type-III, Type-IV)
    - Sanders Type IV, 3 or more fracture lines
- Calcaneus, left – crushed (general crushing of plantar half and sectioning of dorsal half; large posterior chip, 5 x 3 x 3 cm; several smaller chips ranging from 1-3 cm in length from superolateral and superomedial aspect; splitting of the articular surface for the cuboid)
    - AIS: 857371.2 fracture line into ≥ 2 joint surfaces
    - BioPT Bin 5: Calcaneus fracture (comminuted crush, comminuted, Sanders Type-III, Type-IV)
    - Sanders Type IV, 3 or more fracture lines

Appendix C: Video Frame Sequences

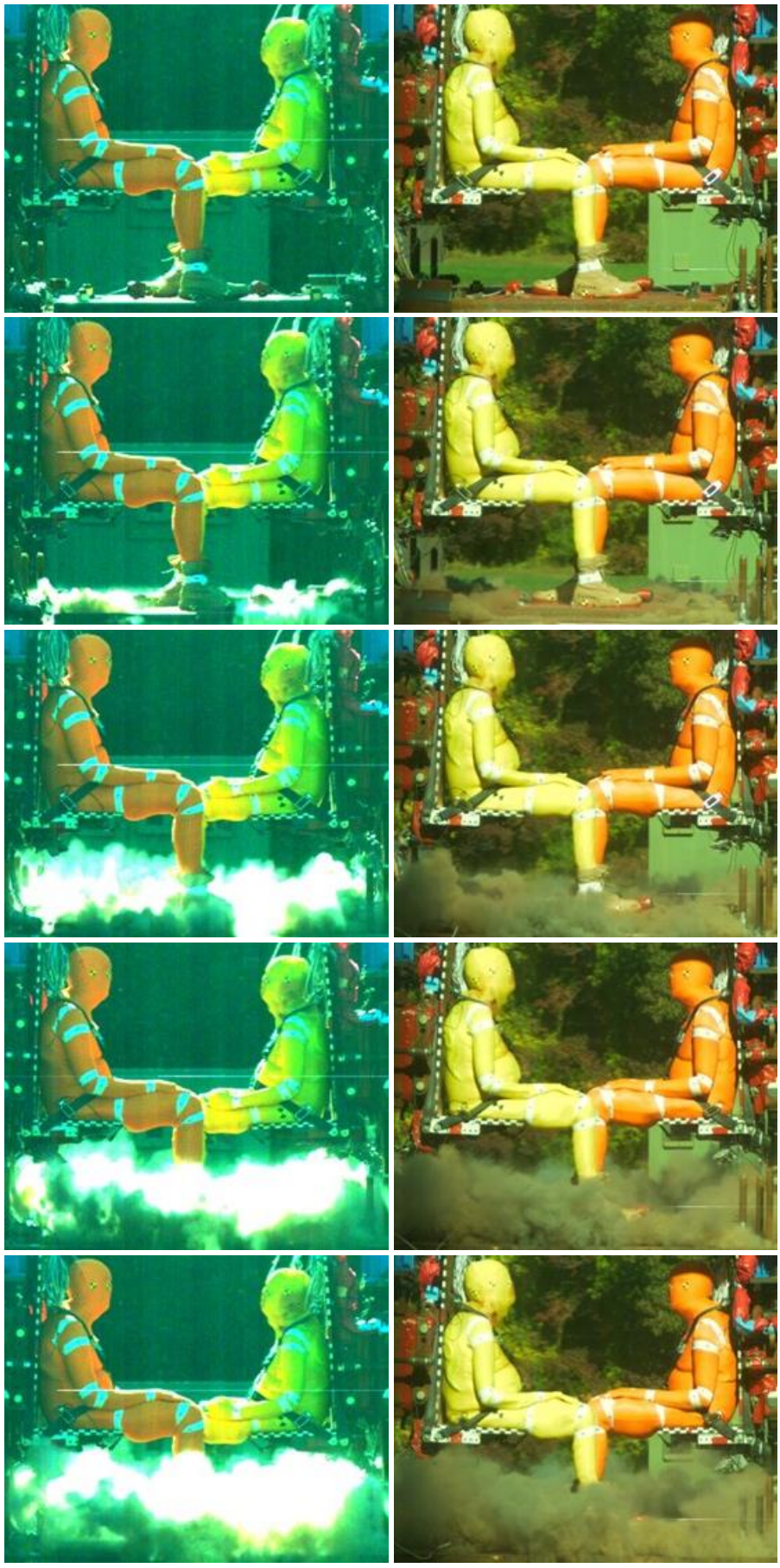

Figure C1: SA1 lateral view. Crew 1 PMHS-SM117 (50M) left; Crew 2: PMHS-SM118 (50M) right.

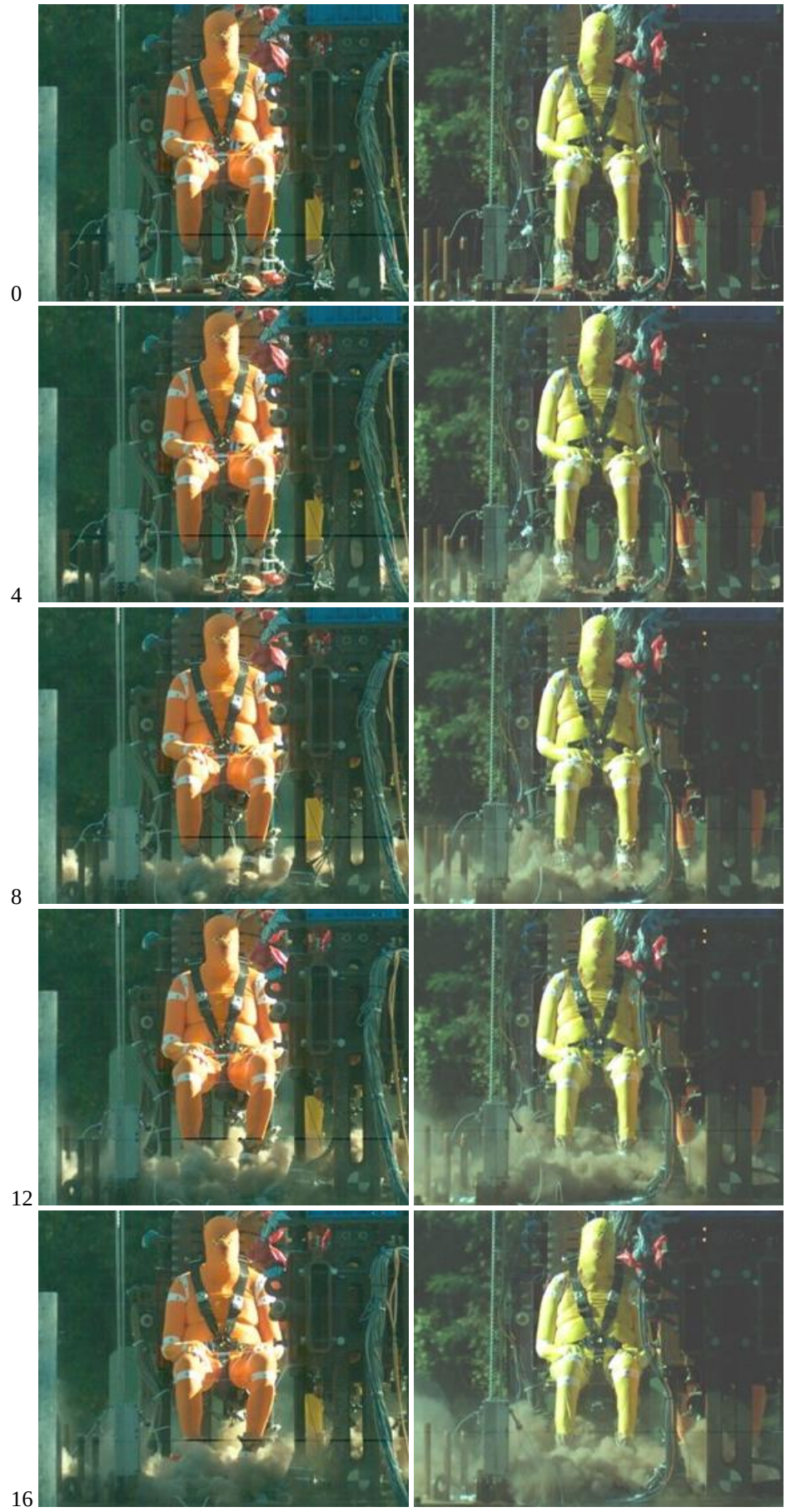

Figure C2: SA1 coronal view. Crew 1: PMHS-SM117 (50M) left; Crew 2: PMHS-SM118 (50M) right.

Figure C3: SA1 mid-event and late-event. Crew 1: PMHS-SM117 (50M) left; Crew 2: PMHS-SM118 (50M) right.

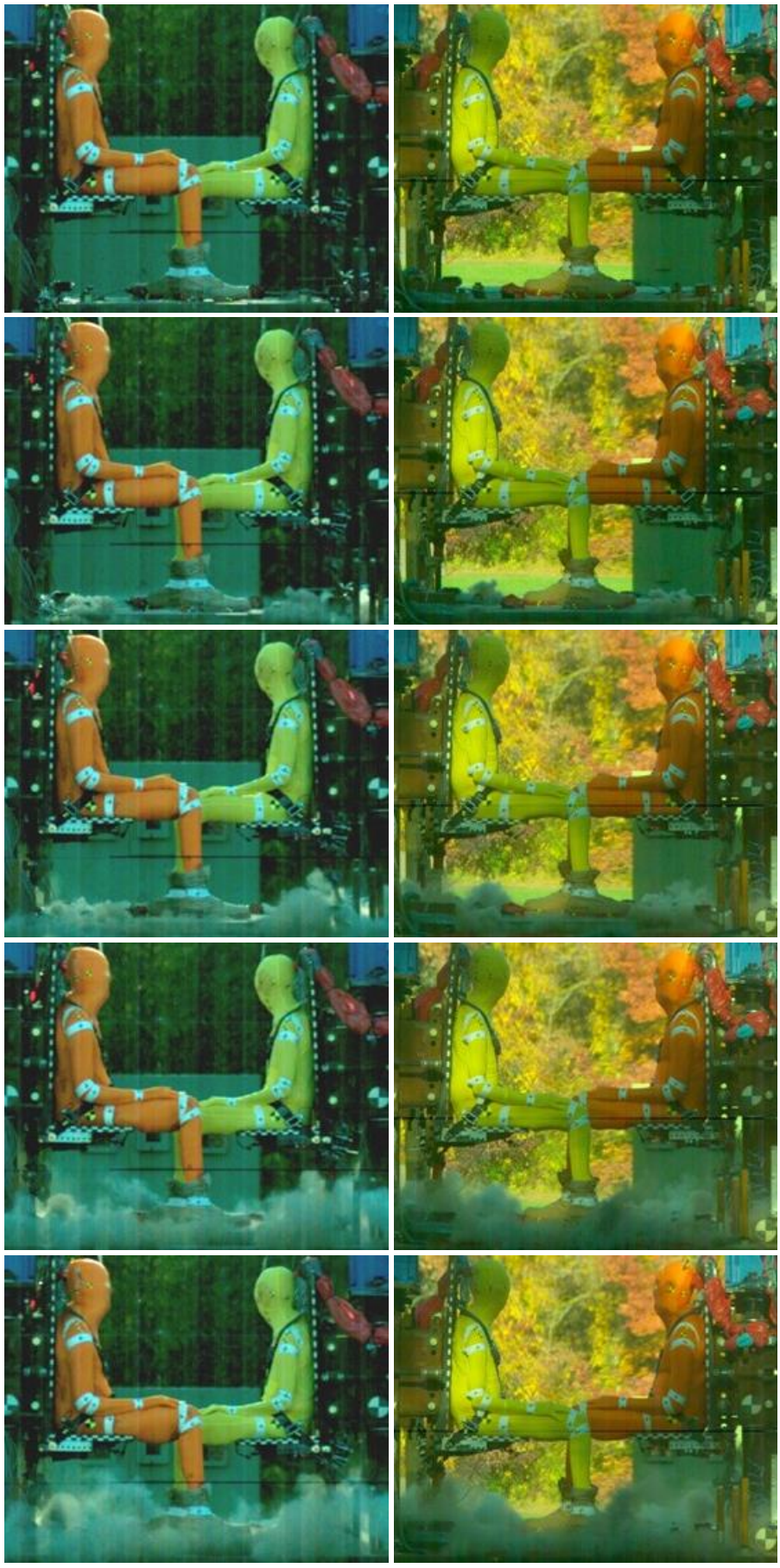

Figure C4: SA2 lateral view. Crew 1: PMHS-SM120 (50M) left; Crew 2: PMHS-SM119 (50M) right.

Figure C5: SA2 coronal view. Crew 1: PMHS-SM120 (50M) left; Crew 2: PMHS-SM119 (50M) right.

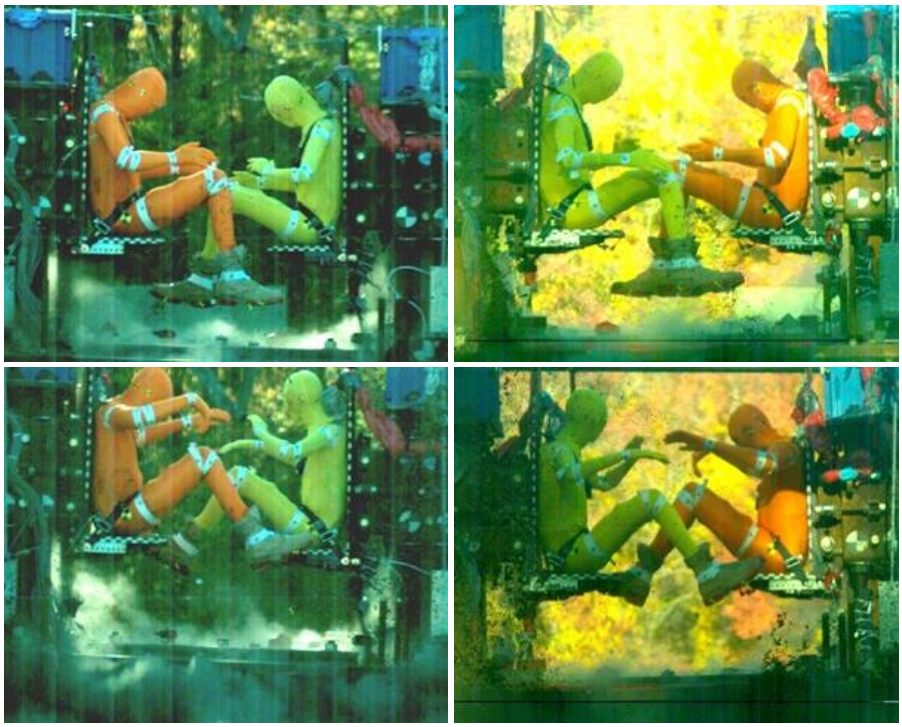

Figure C6: SA2 mid-event and late-event. Crew 1: PMHS-SM120 (50M) left; Crew 2: PMHS-SM119 (50M) right.

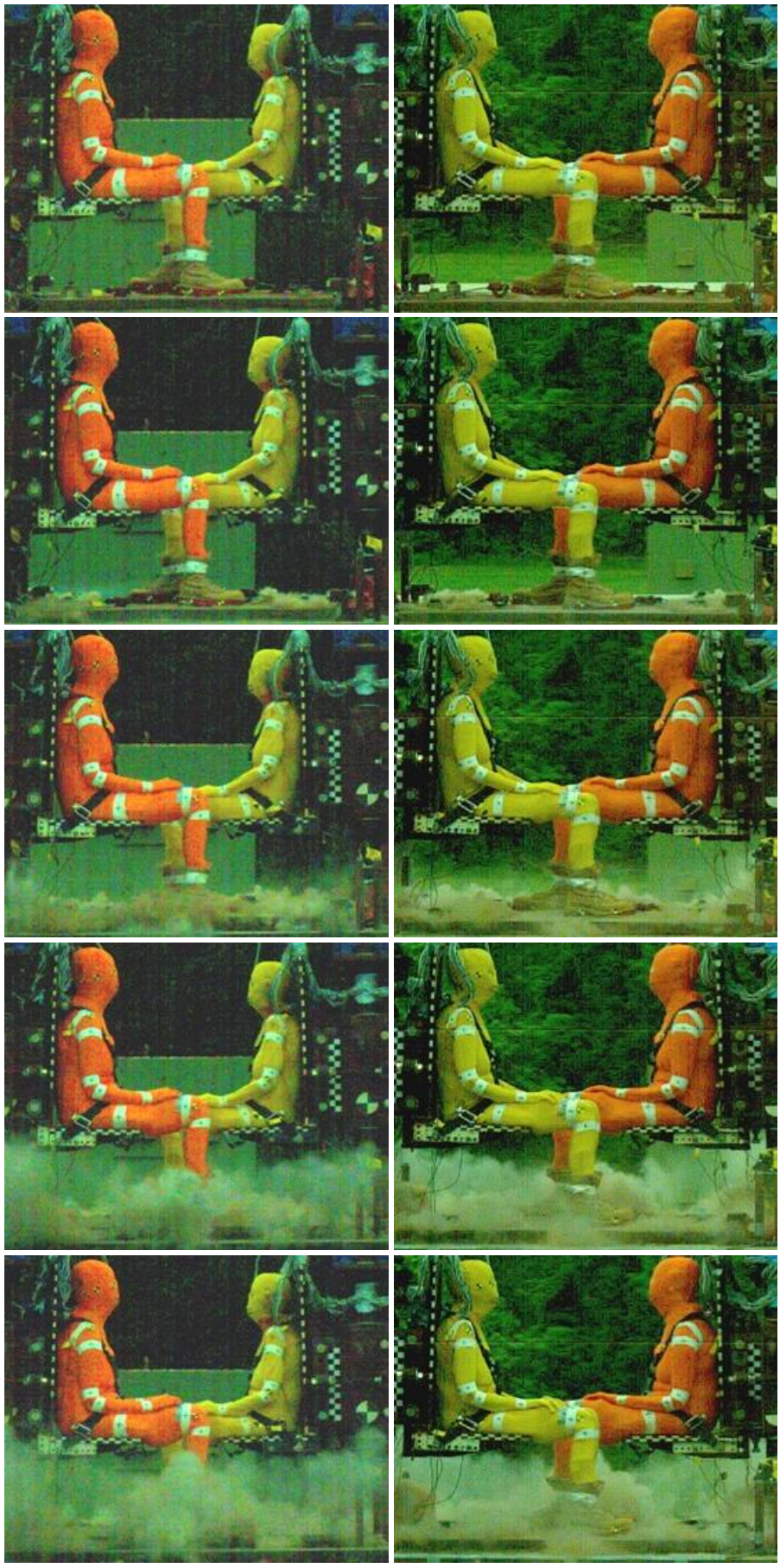

Figure C7: SA3 lateral view. Crew 1: PMHS-SF127 (75F) left; Crew 2: PMHS-SF126 (5F) right.

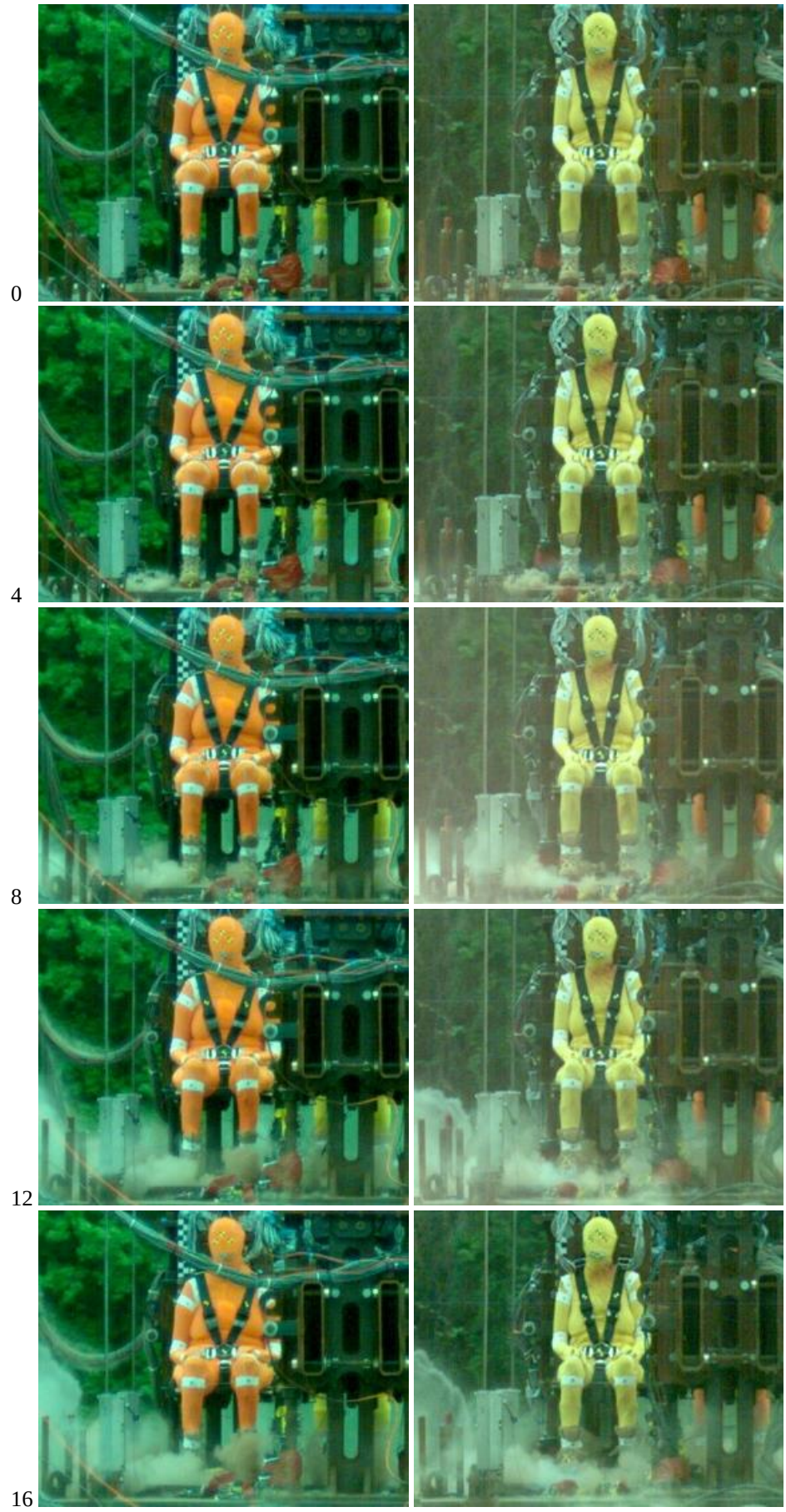

Figure C8: SA3 coronal view. Crew 1: PMHS-SF127 (75F) left; Crew 2: PMHS-SF126 (5F) right.

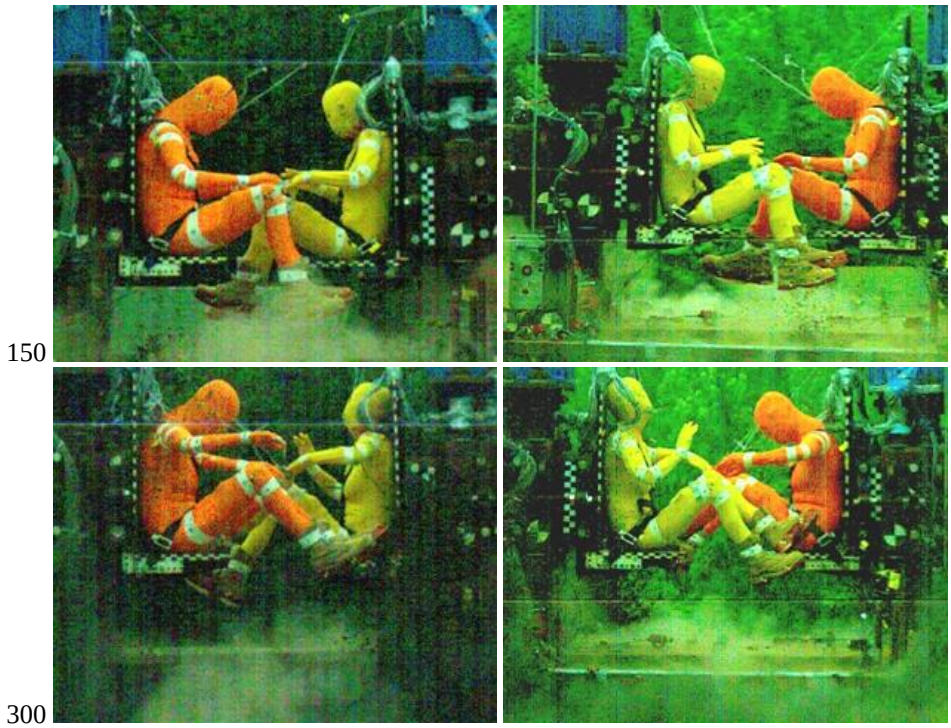

Figure C9: SA3 mid-event and late-event. Crew 1: PMHS-SF127 (75F) left; Crew 2: PMHS-SF126 (5F) right.

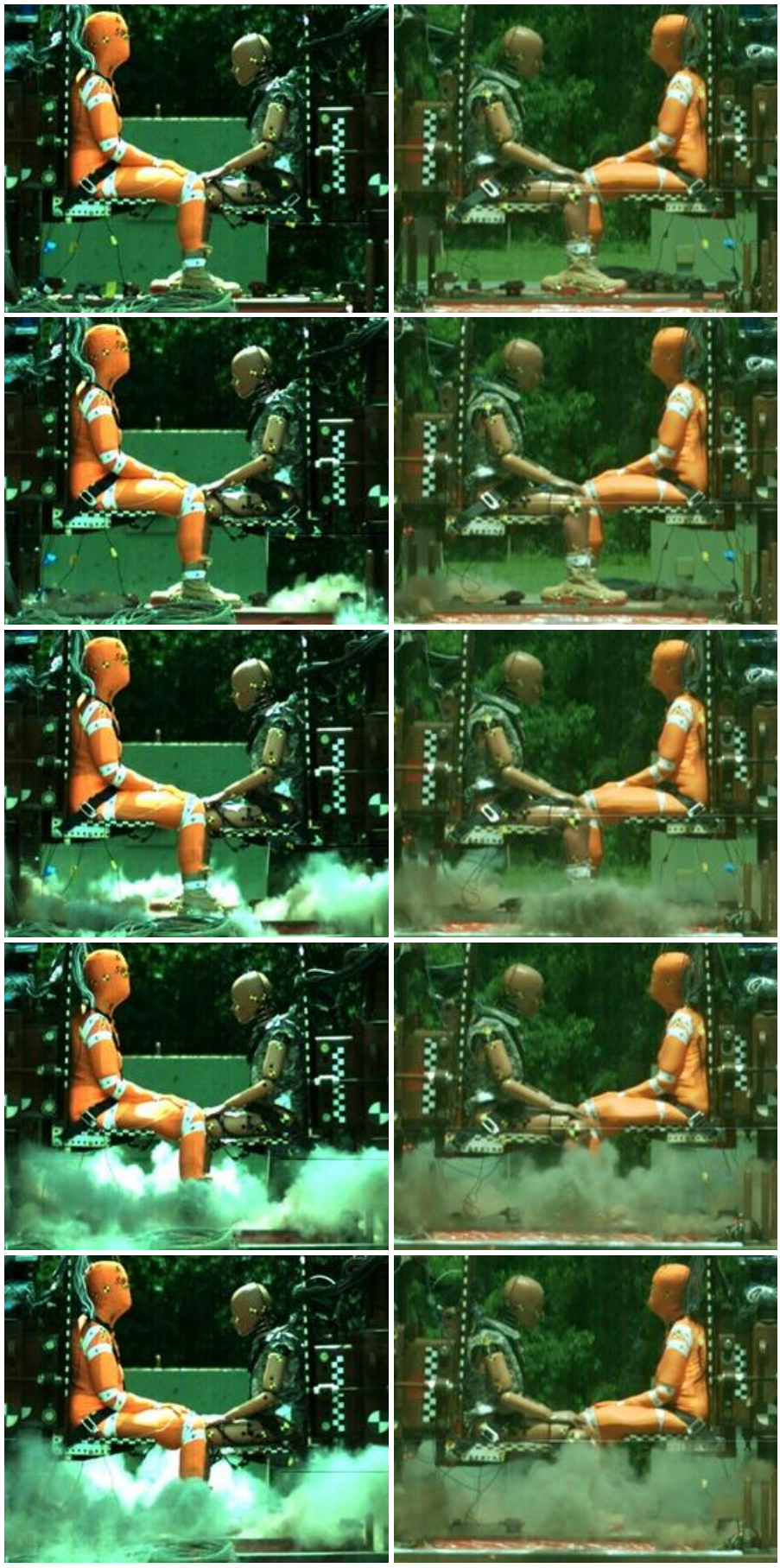

Figure C10: SA4 lateral view. Crew 1: PMHS-SF128 (75F) left; Crew 2: ATD-HIII 5th female right.

Figure C11: SA4 coronal view. Crew 1: PMHS-SF128 (75F) left; Crew 2: ATD-HIII 5th female right.

Figure C12: SA4 mid-event and late-event. Crew 1: PMHS-SF128 (75F) left; Crew 2: ATD-HIII 5th female right.

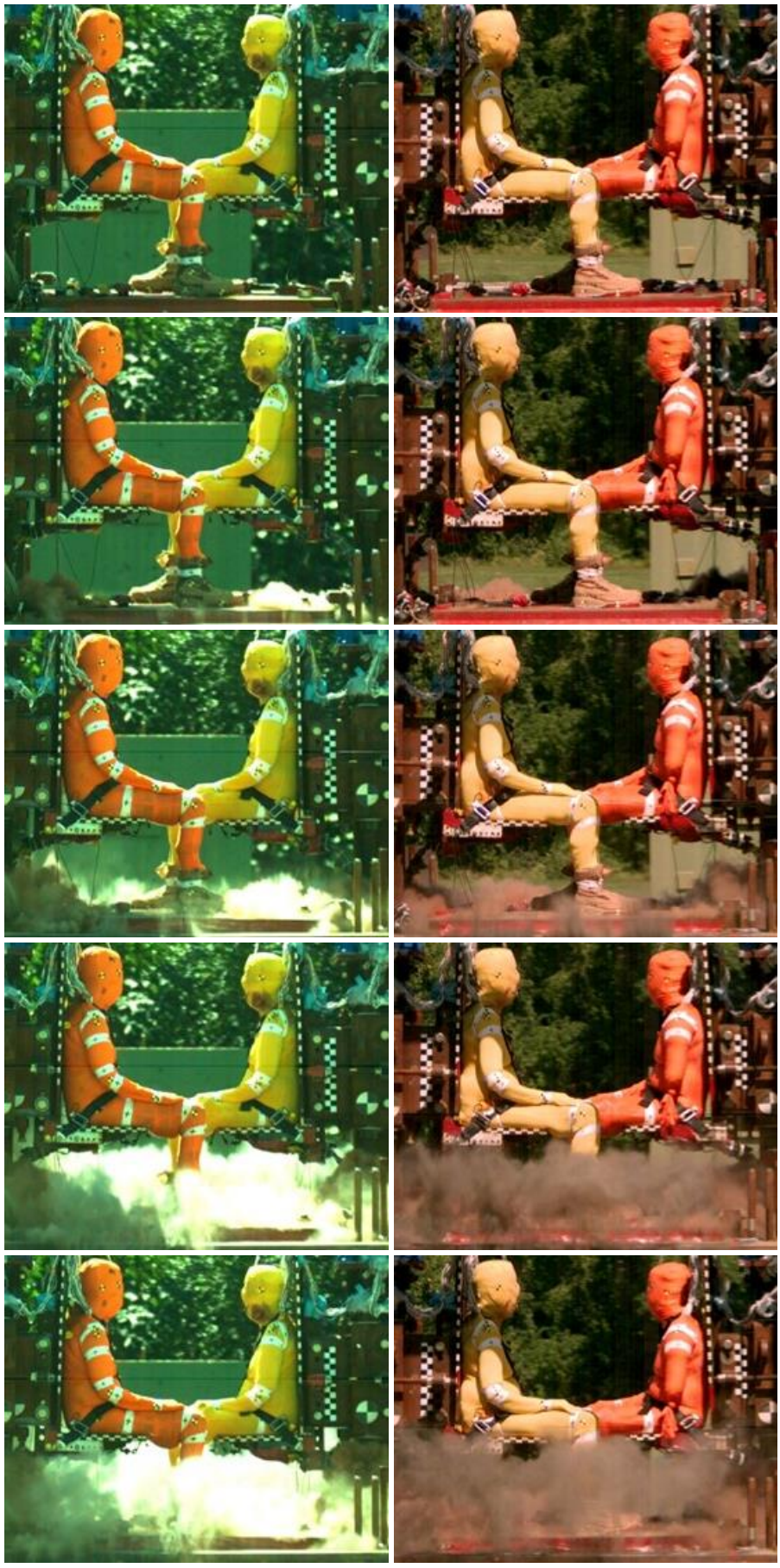

Figure C13: SA5 lateral view. Crew 1: PMHS-SF131 (75F) left; Crew 2: PMHS-SF132 (5F) right.

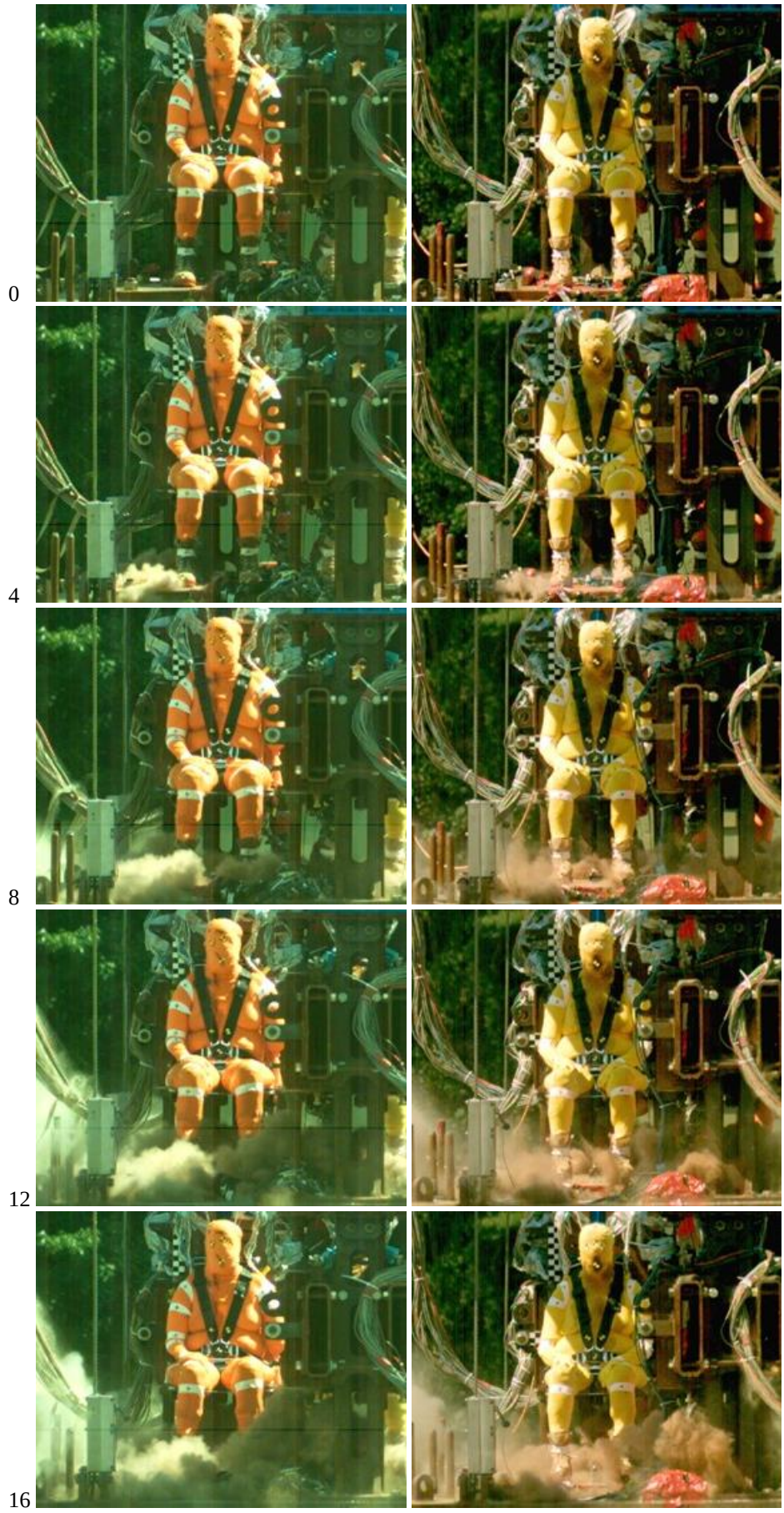

Figure C14: SA5 coronal view. Crew 1: PMHS-SF131 (75F) left; Crew 2: PMHS-SF132 (5F) right.

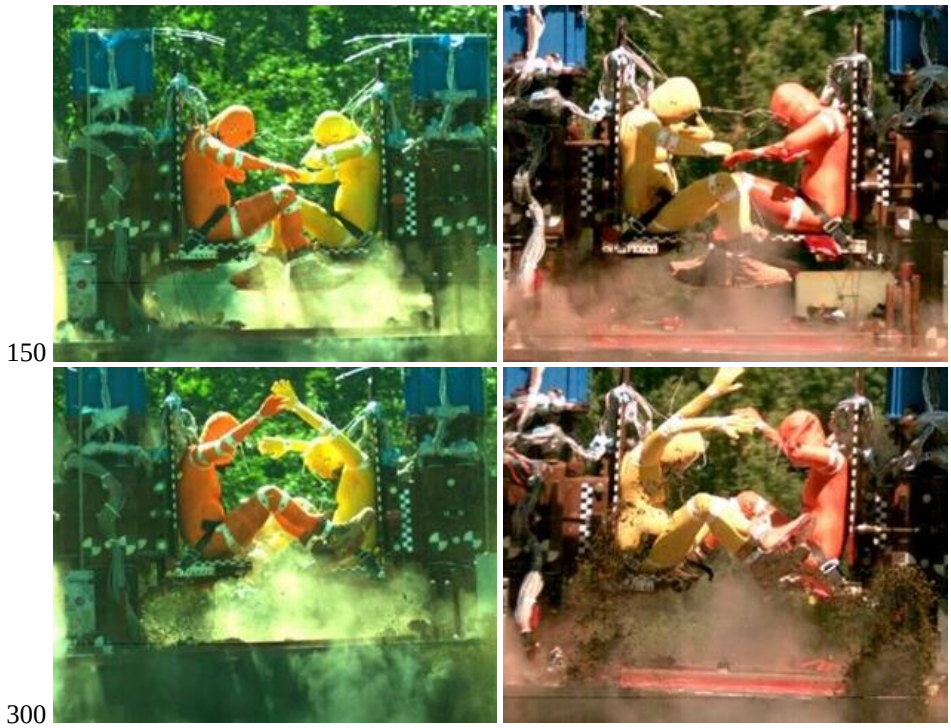

Figure C15: SA5 mid-event and late-event. Crew 1: PMHS-SF131 (75F) left; Crew 2: PMHS-SF132 (5F) right.

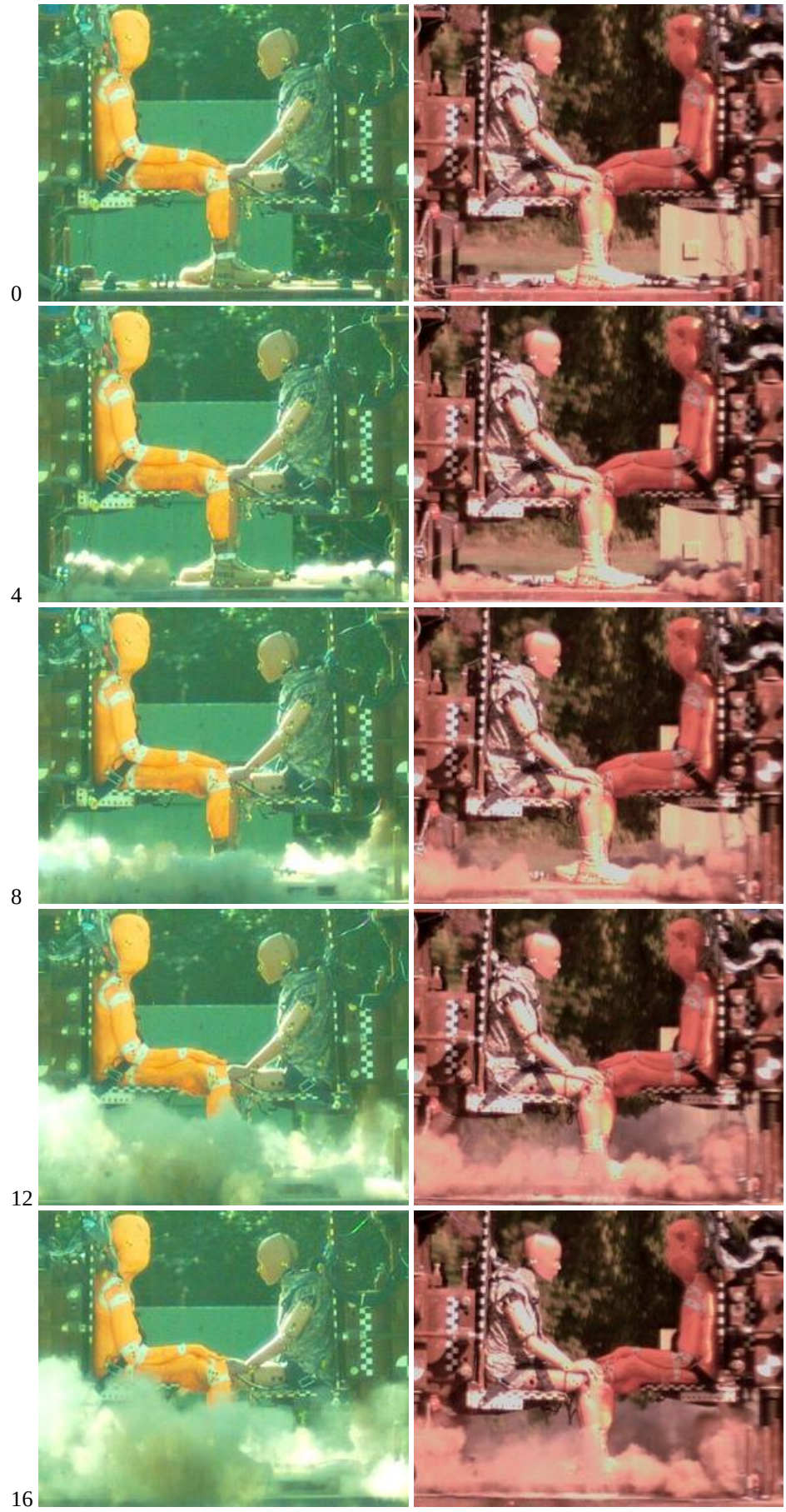

Figure C16: SA6 lateral view. Crew 1: PMHS-SF133 (5F) left; Crew 2: ATD-HIII 5th female right.

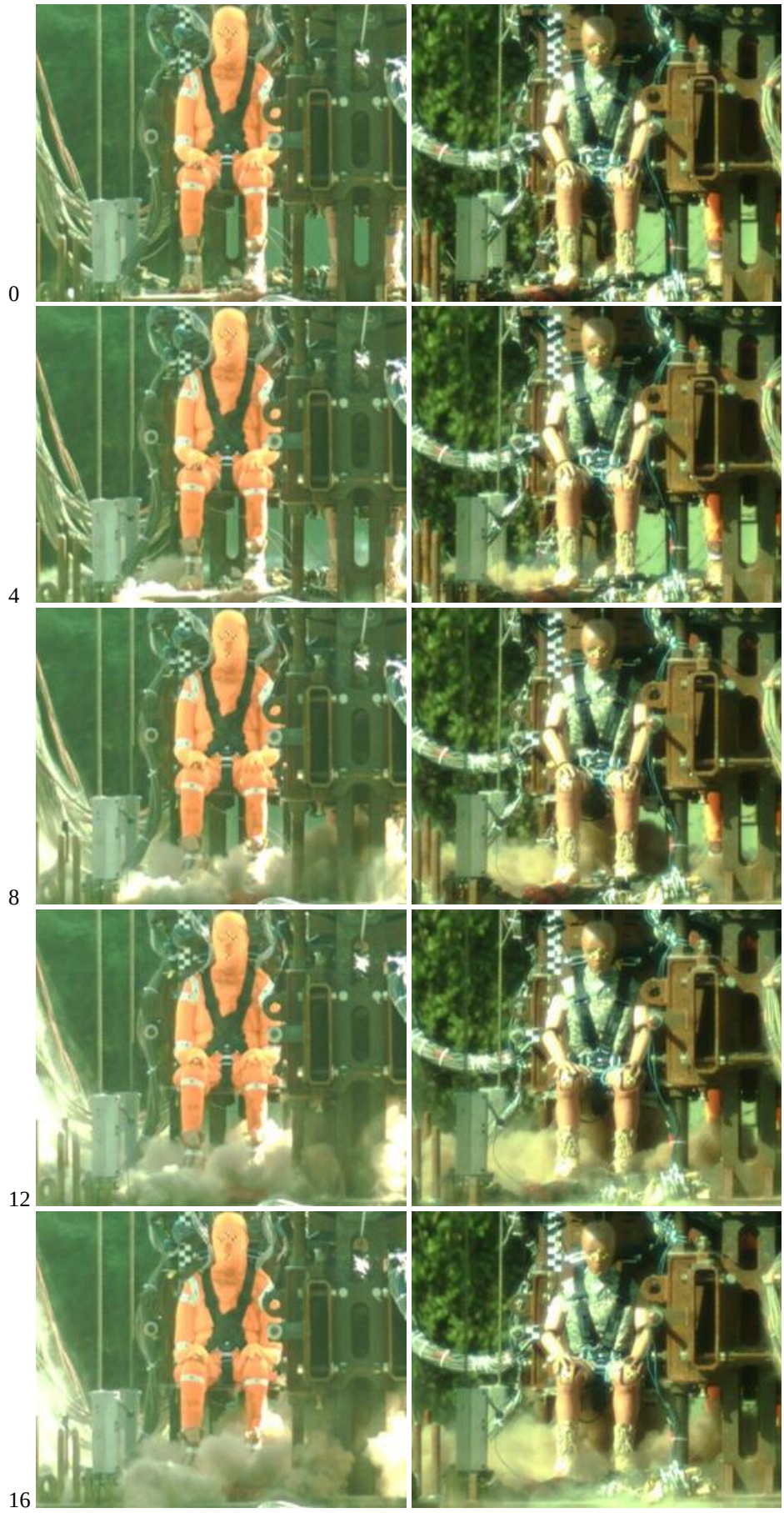

Figure C17: SA6 coronal view. Crew 1: PMHS-SF133 (5F) left; Crew 2: ATD-HIII 5th female right.

Figure C18: SA6 mid-event and late-event. Crew 1: PMHS-SF133 (5F) left; Crew 2: ATD-HIII 5th female right.

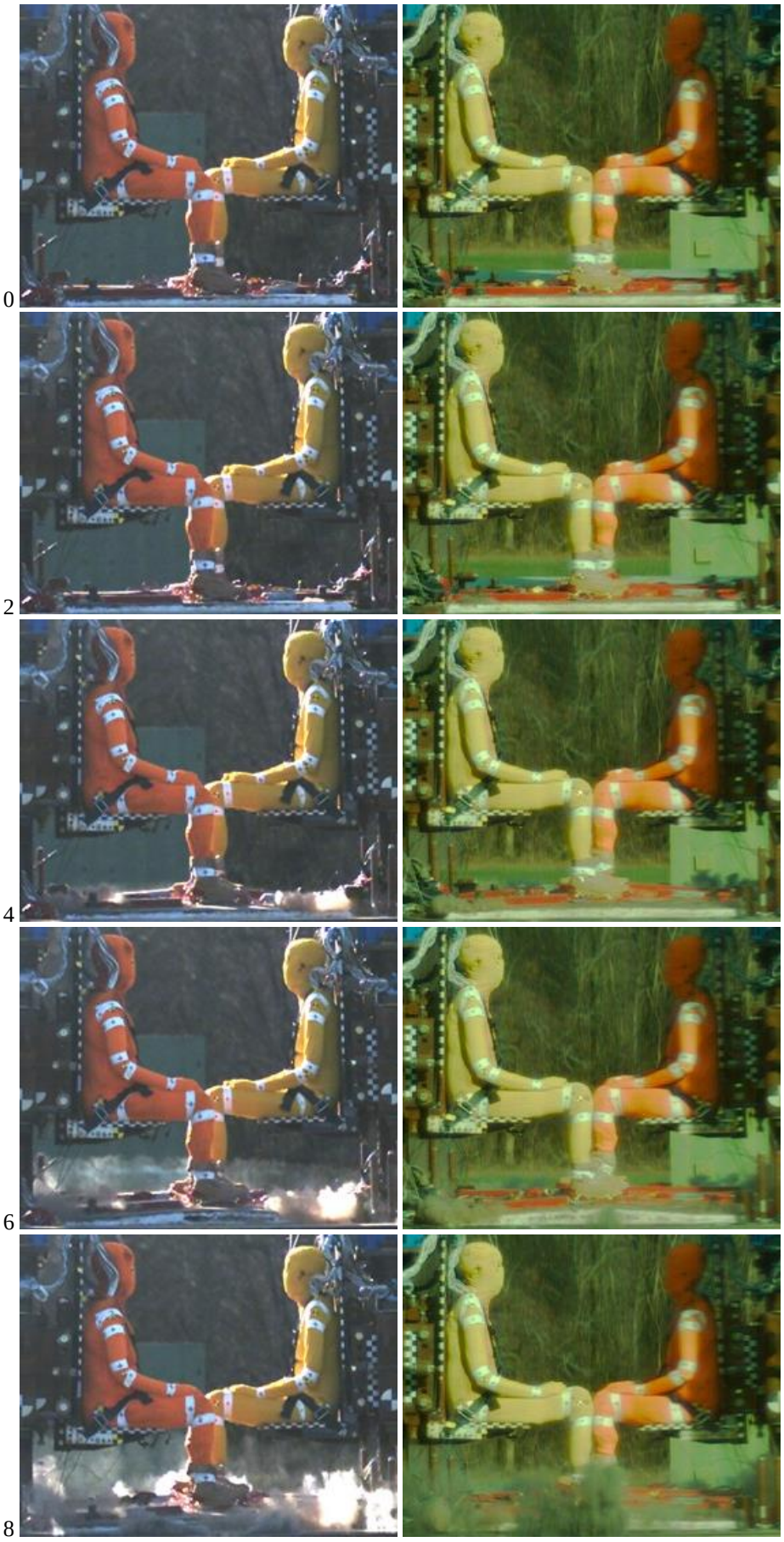

Figure C19: SB1 lateral view. Crew 1: PMHS-SF138 (75F) left; Crew 2: PMHS-SF134 (5F) right.

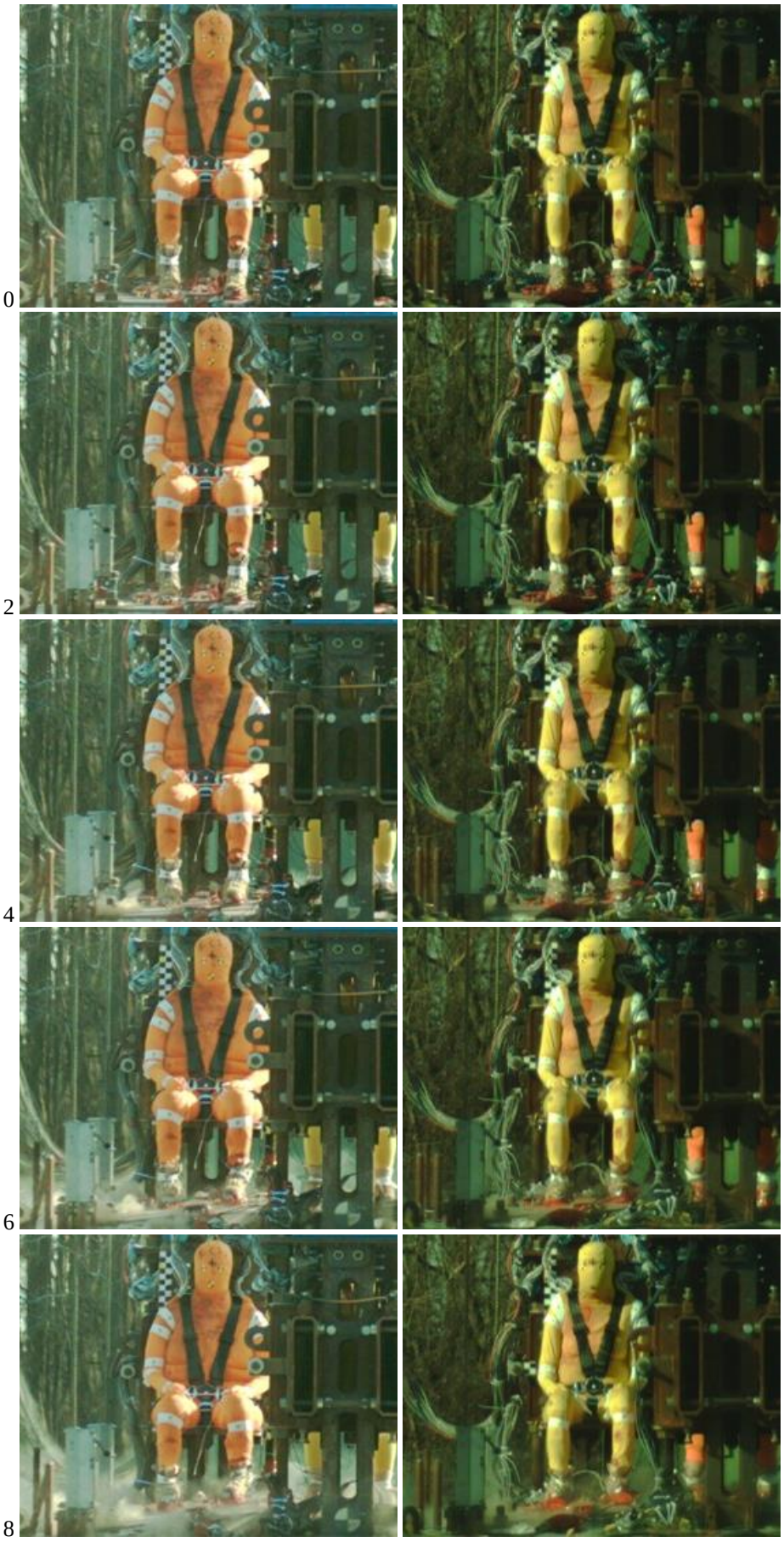

Figure C20: SB1 coronal view. Crew 1: PMHS-SF138 (75F) left; Crew 2: PMHS-SF134 (5F) right.

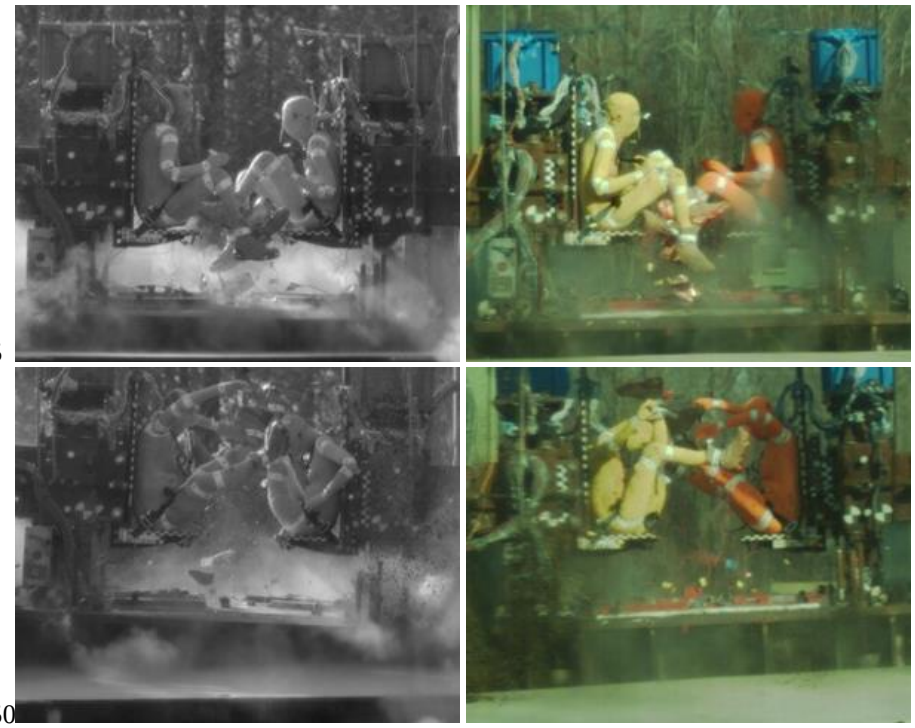

Figure C21: SB1 mid-event and late-event. Crew 1: PMHS-SF138 (75F) left; Crew 2: PMHS-SF134 (5F) right.

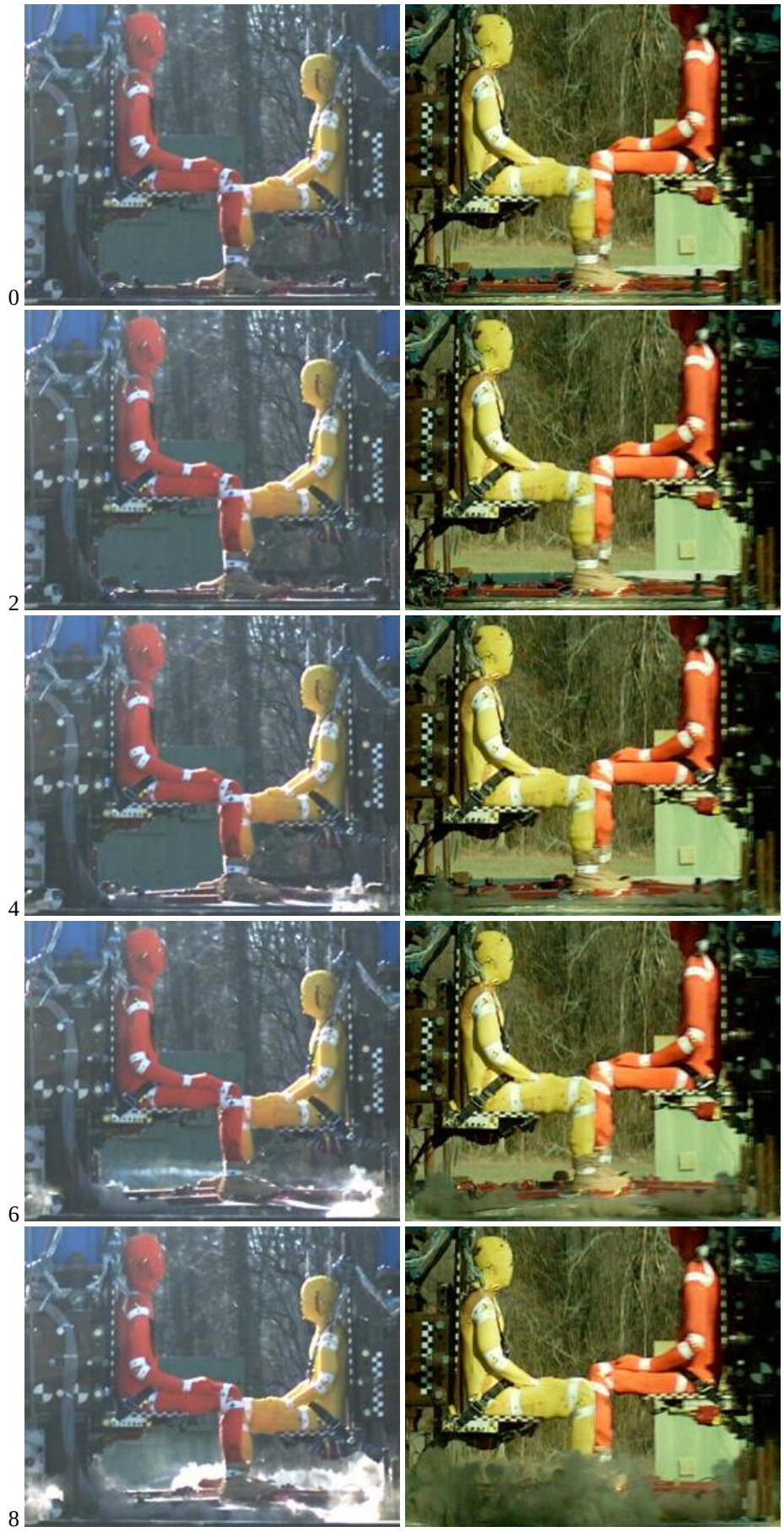

Figure C22: SB2 lateral view. Crew 1: PMHS-SM140 (50M) left; Crew 2: PMHS-SF135 (5F) right.

Figure C23: SB2 coronal view. Crew 1: PMHS-SM140 (50M) left; Crew 2: PMHS-SF135 (5F) right.

Figure C24: SB2 mid-event and late-event. Crew 1: PMHS-SM140 (50M) left; Crew 2: PMHS-SF135 (5F) right.

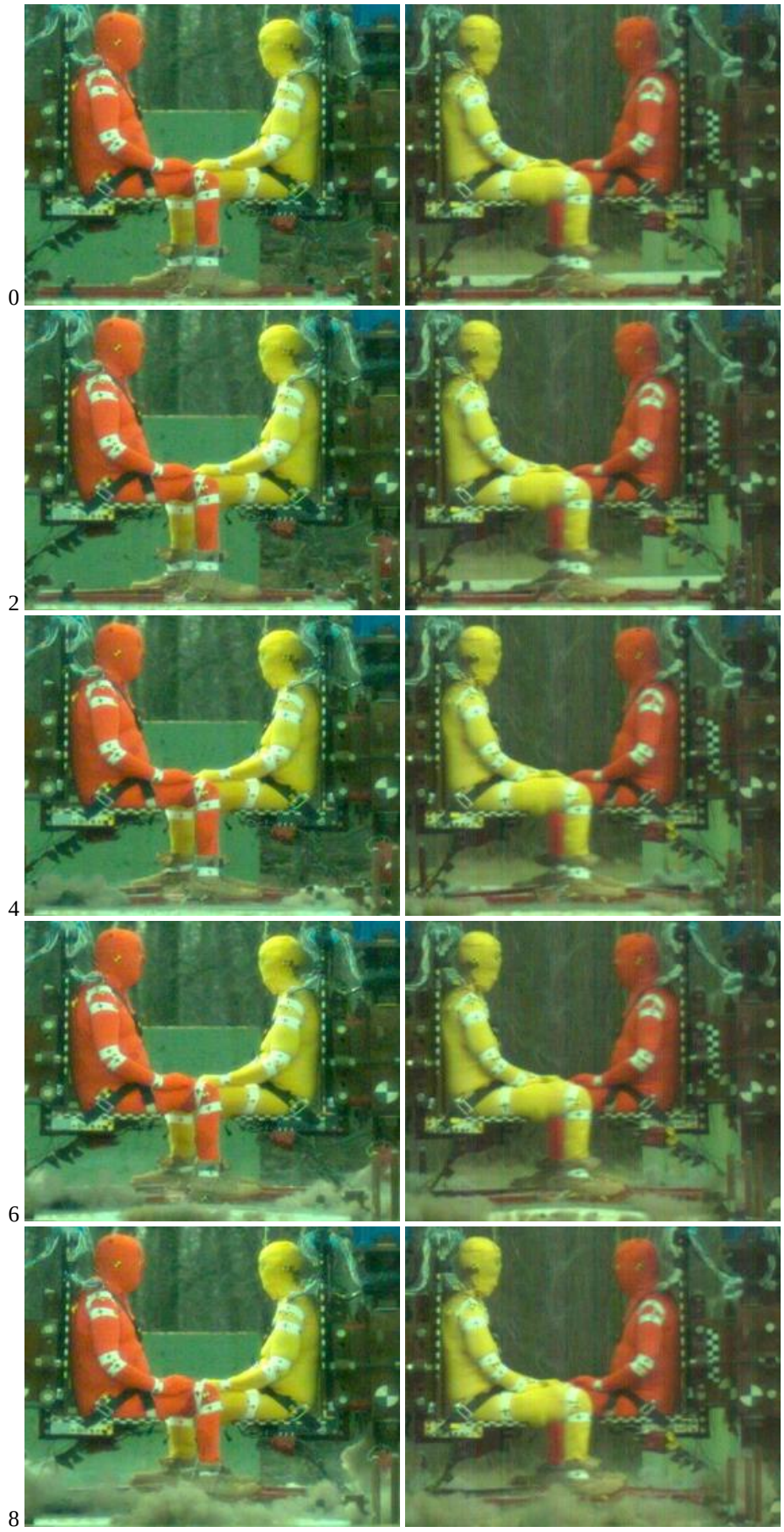

Figure C25: SB3 lateral view. Crew 1: PMHS-SM141 (50M) left; Crew 2: PMHS-SF142 (75F) right.

Figure C26: SB3 coronal view. Crew 1: PMHS-SM141 (50M) left; Crew 2: PMHS-SF142 (75F) right.

Figure C27: SB3 mid-event and late-event. Crew 1: PMHS-SM141 (50M) left; Crew 2: PMHS-SF142 (75F) right.

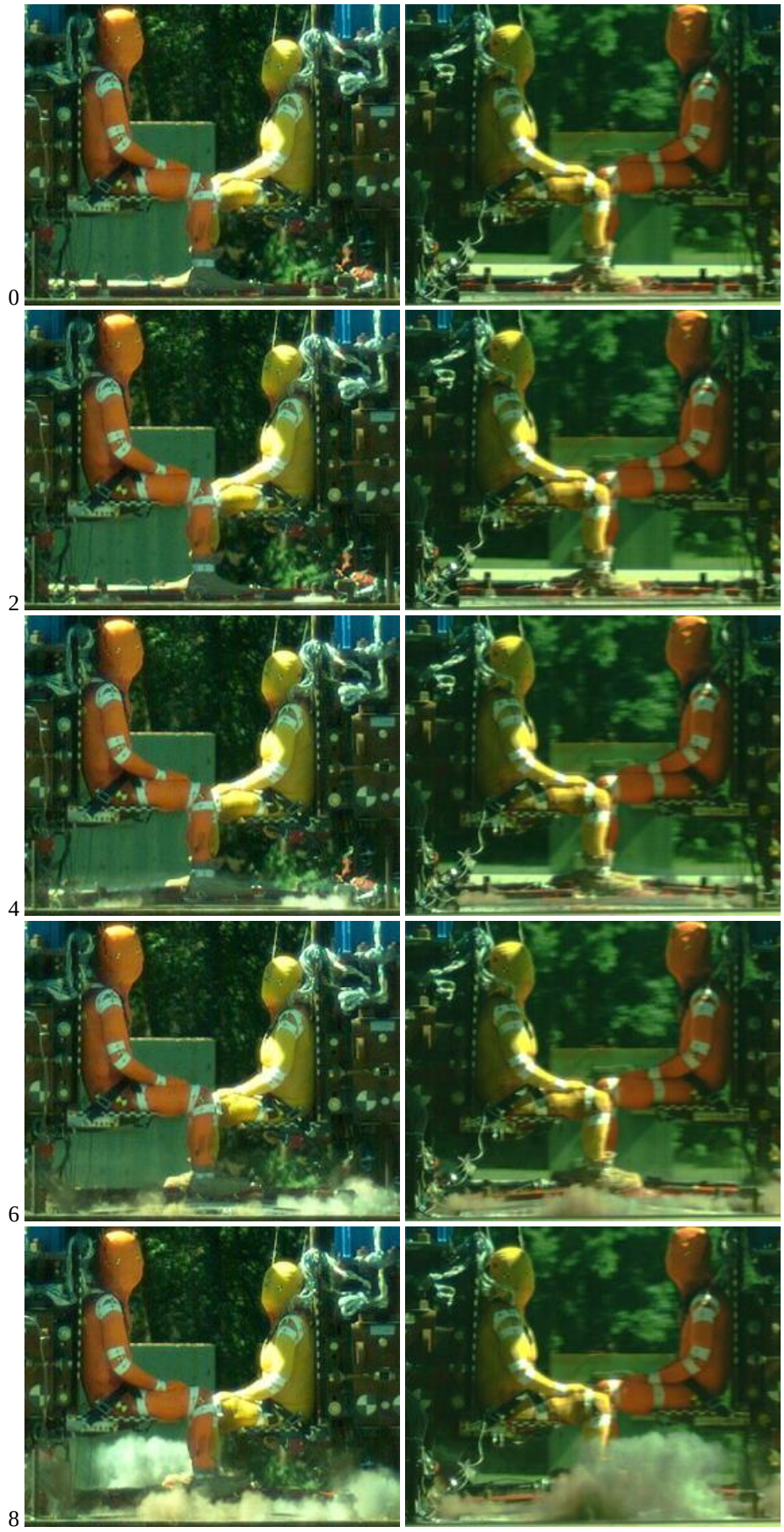

Figure C28: SB4 lateral view. Crew 1: PMHS-SM145 (50M) left; Crew 2: PMHS-SF148 (75F) right.

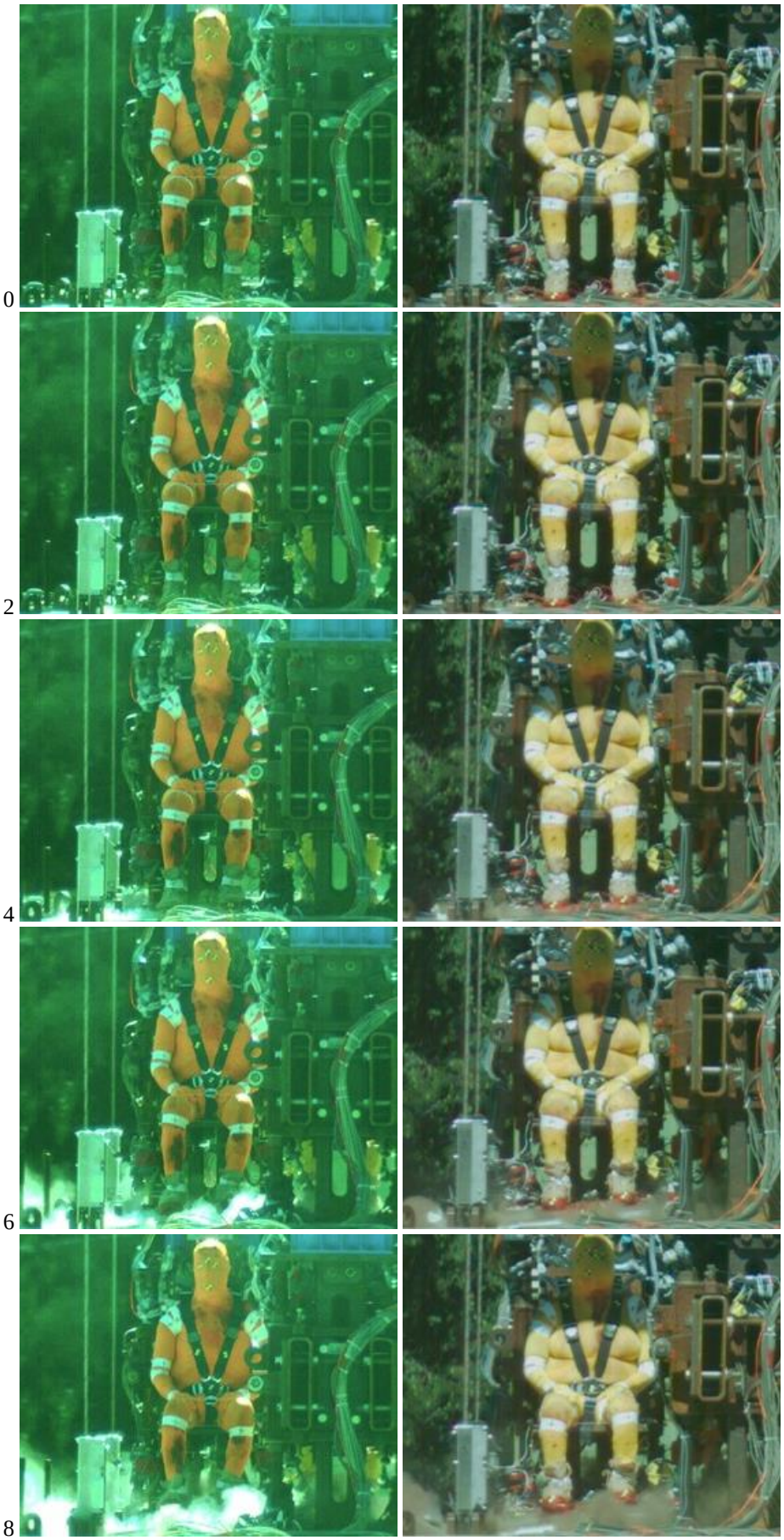

Figure C29: SB4 coronal view. Crew 1: PMHS-SM145 (50M) left; Crew 2: PMHS-SF148 (75F) right.

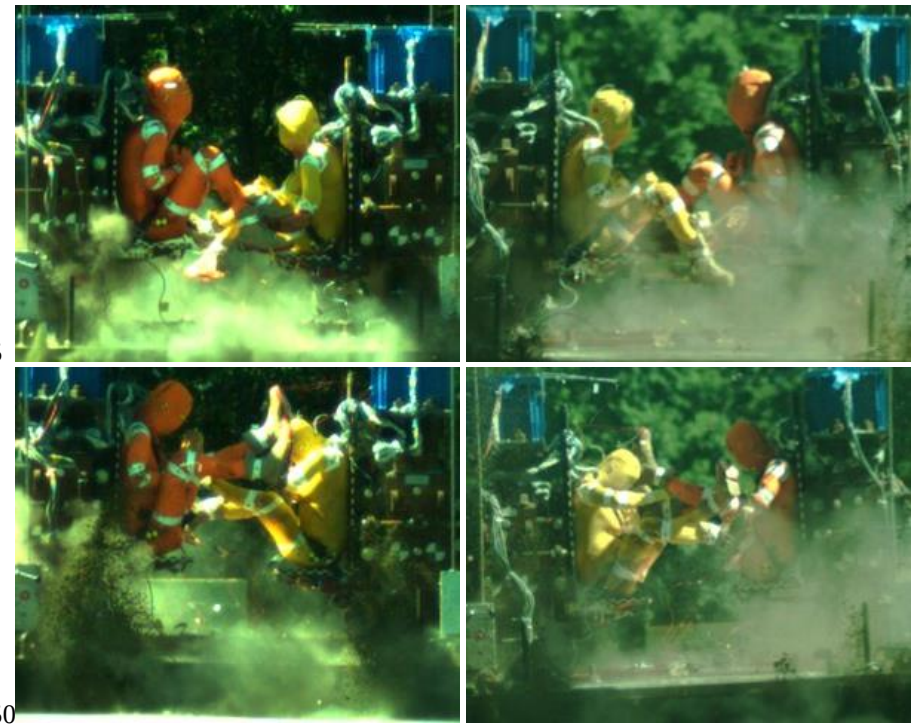

Figure C30: SB4 mid-event and late-event. Crew 1: PMHS-SM145 (50M) left; Crew 2: PMHS-SF148 (75F) right.

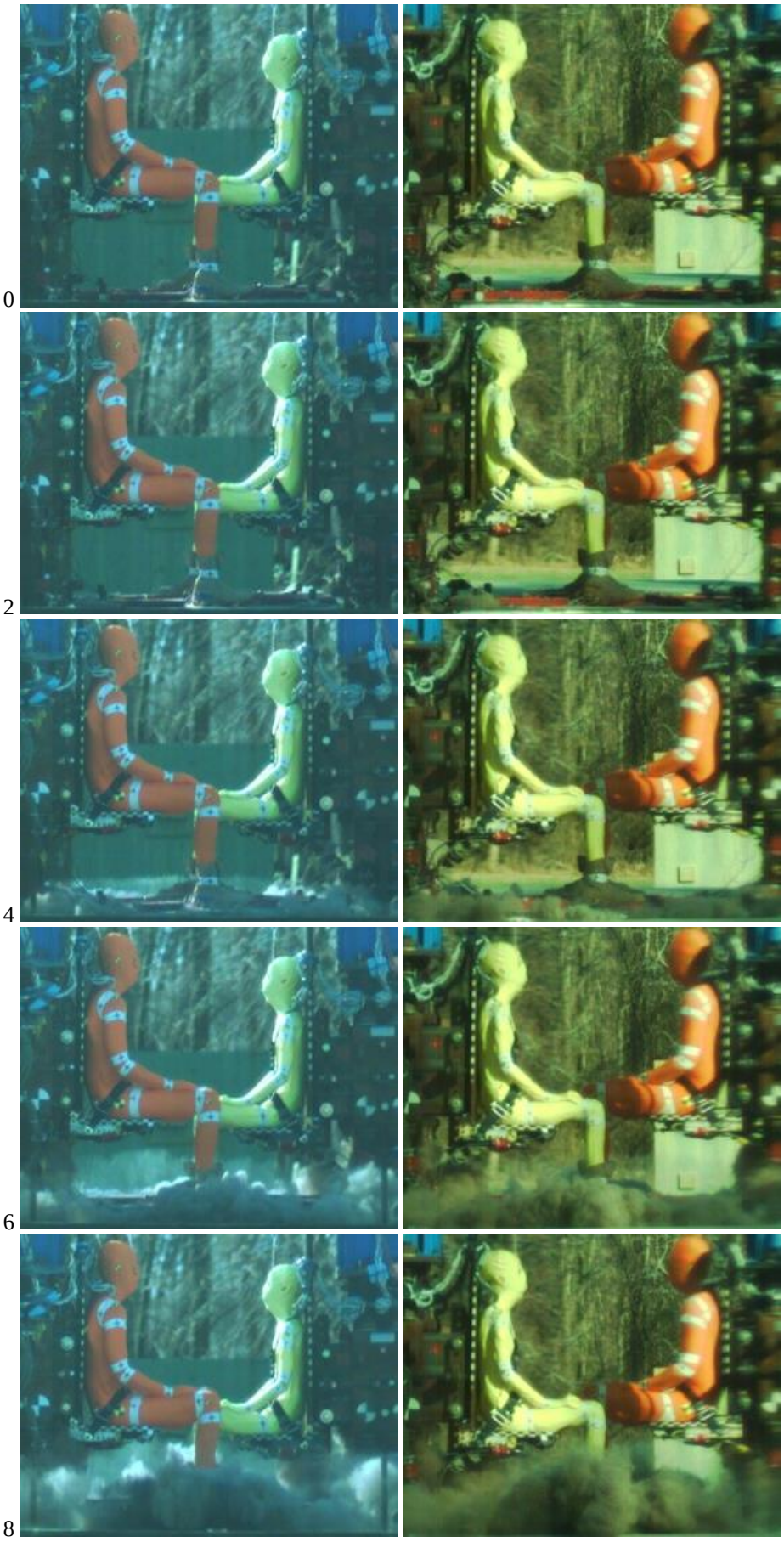

Figure C31: SB5 lateral view. Crew 1: PMHS-SM150 (50M) left; Crew 2: PMHS-SF151 (5F) right.

Figure C32: SB5 coronal view. Crew 1: PMHS-SM150 (50M) left; Crew 2: PMHS-SF151 (5F) right.

Figure C33: SB5 mid-event and late-event. Crew 1: PMHS-SM150 (50M) left; Crew 2: PMHS-SF151 (5F) right.

Appendix D: Lower Extremity Response Traces

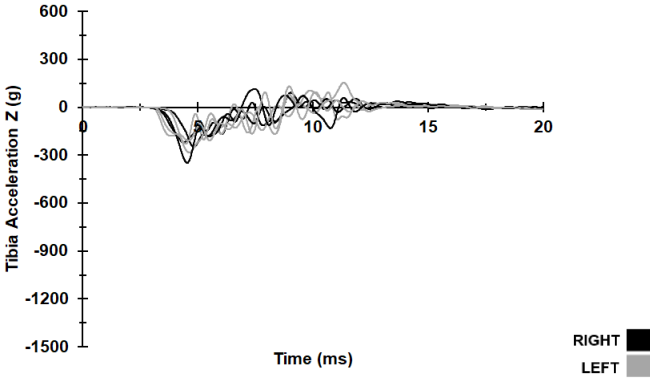

Figure D1: Series A 5th-percentile female distal tibia Z-axis acceleration.

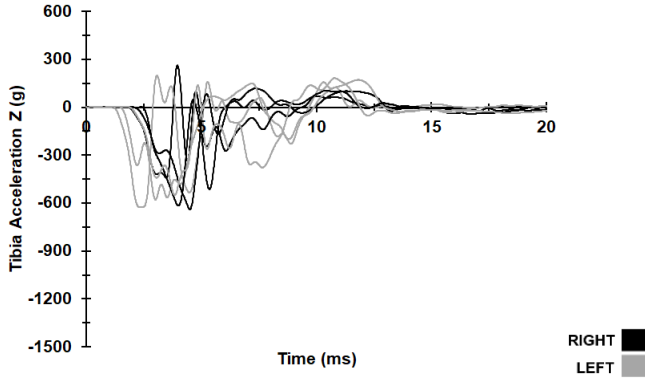

Figure D2: Series B 5th-percentile female distal tibia Z-axis acceleration.

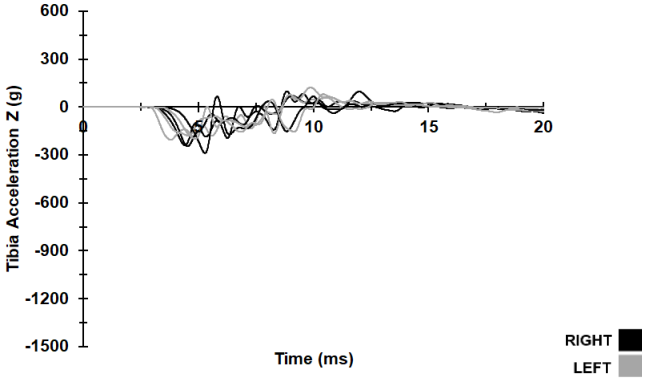

Figure D3: Series A 75th-percentile female distal tibia Z-axis acceleration.

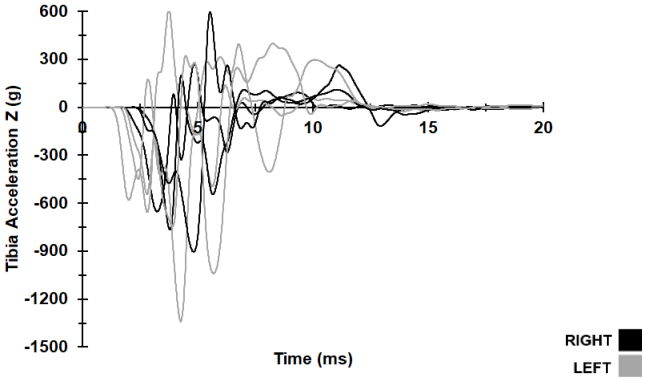

Figure D4: Series B 75th-percentile female distal tibia Z-axis acceleration.

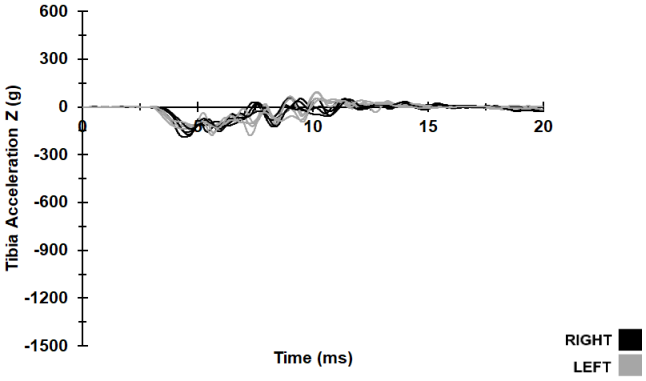

Figure D5: Series A 50th-percentile male distal tibia Z-axis acceleration.

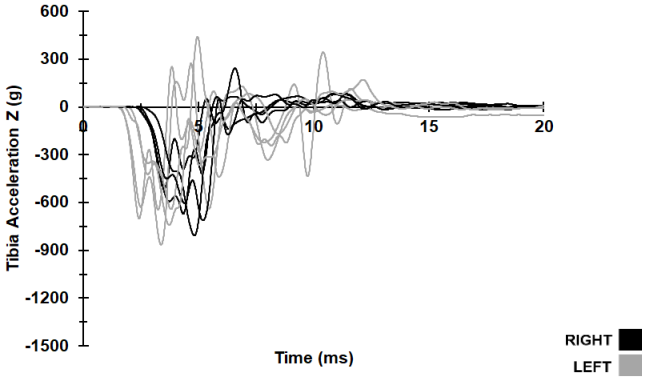

Figure D6: Series B 50th-percentile male distal tibia Z-axis acceleration.

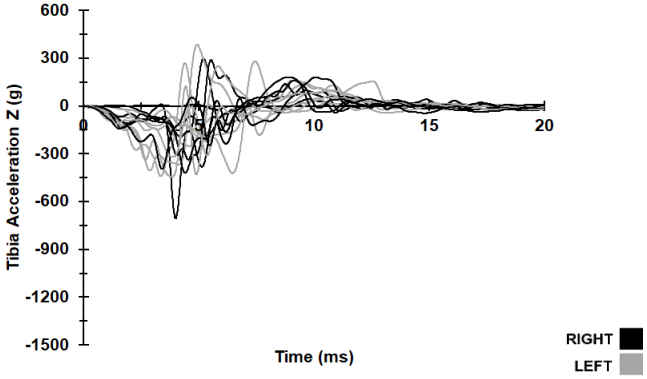

Figure D7: 4.2 Series 50th-percentile male distal tibia Z-axis acceleration.

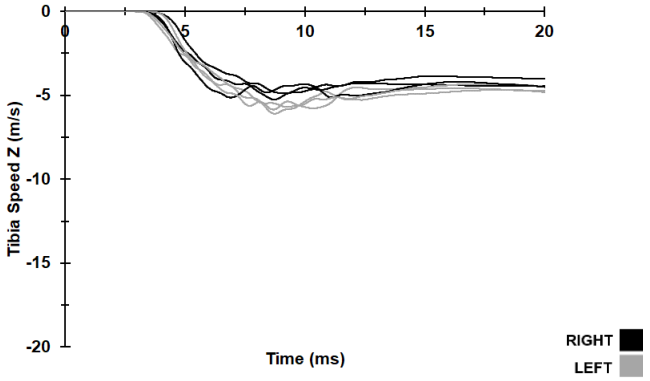

Figure D8: Series A 5th-percentile female distal tibia Z-axis speed.

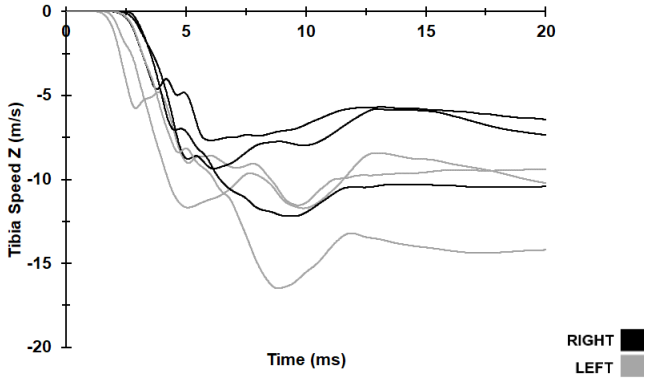

Figure D9: Series B 5th-percentile female distal tibia Z-axis speed.

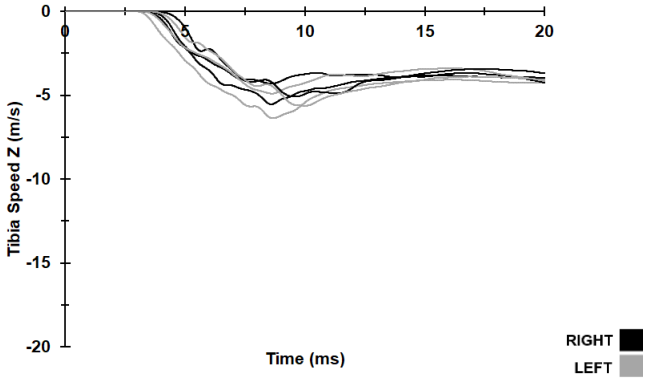

Figure D10: Series A 75th-percentile female distal tibia Z-axis speed.

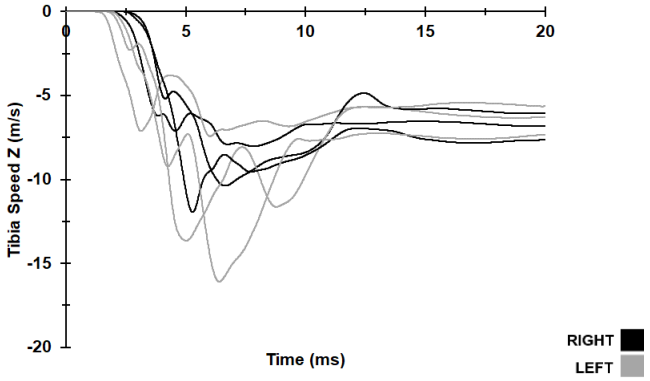

Figure D11: Series B 75th-percentile female distal tibia Z-axis speed.

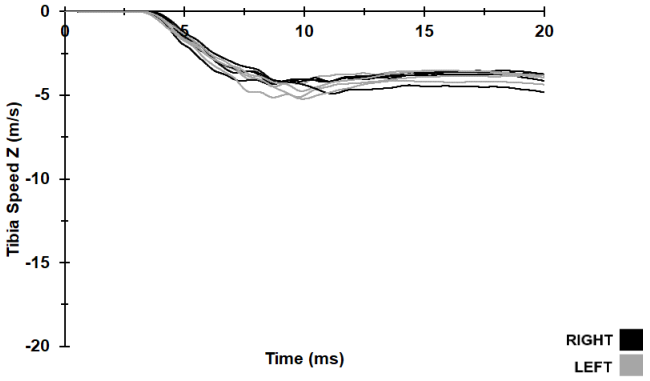

Figure D12: Series A 50th-percentile male distal tibia Z-axis speed.

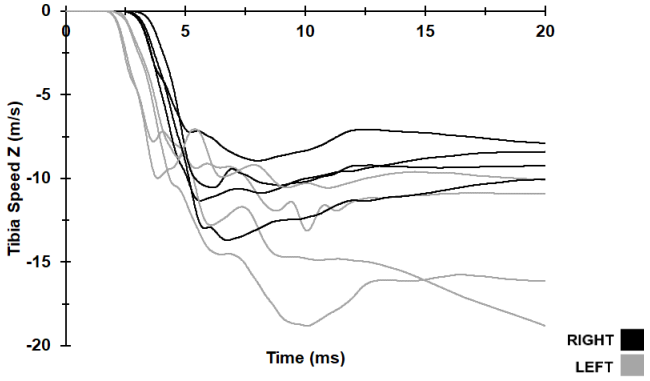

Figure D13: Series B 50th-percentile male distal tibia Z-axis speed.

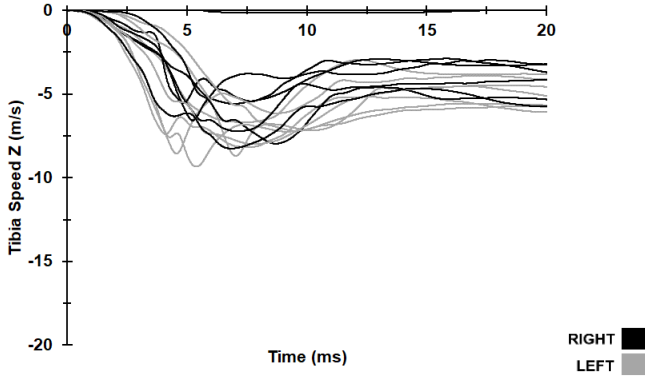

Figure D14: 4.2 Series 50th-percentile male distal tibia Z-axis speed.

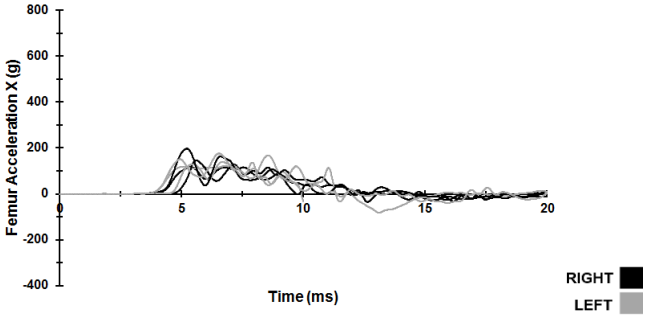

Figure D15: Series A 5th-percentile female distal femur X-axis acceleration.

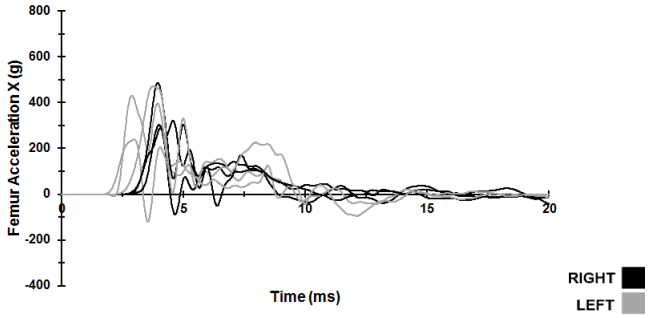

Figure D16: Series B 5th-percentile female distal femur X-axis acceleration.

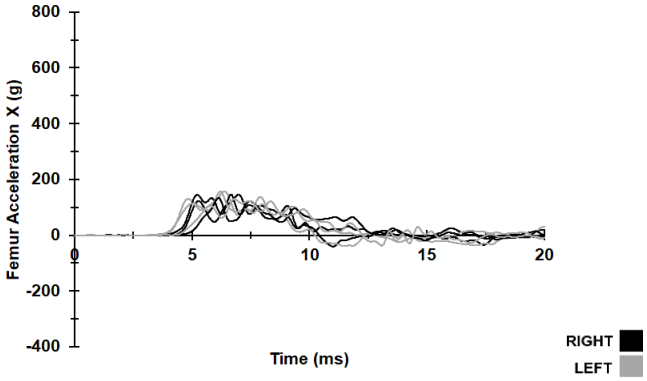

Figure D17: Series A 75th-percentile female distal femur X-axis acceleration.

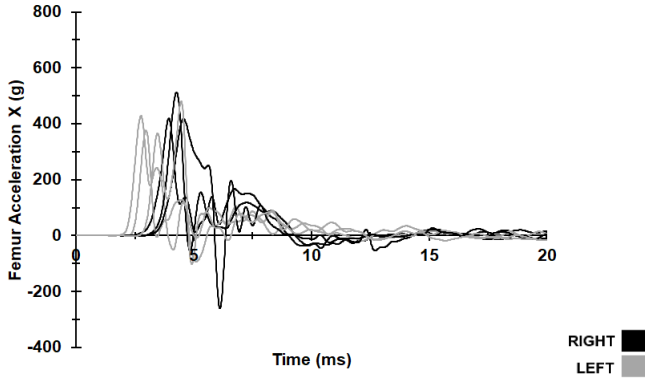

Figure D18: Series B 75th-percentile female distal femur X-axis acceleration.

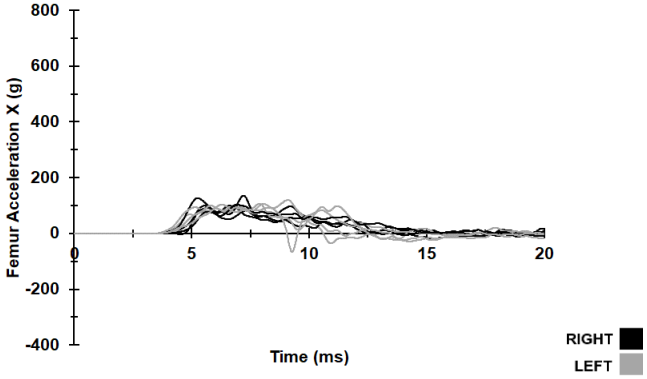

Figure D19: Series A 50th-percentile male distal femur X-axis acceleration.

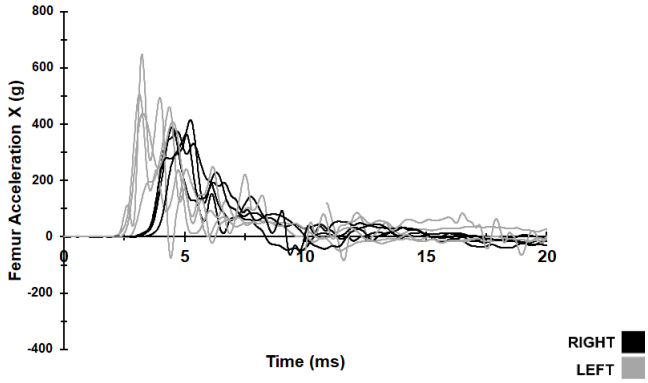

Figure D20: Series B 50th-percentile male distal femur X-axis acceleration.

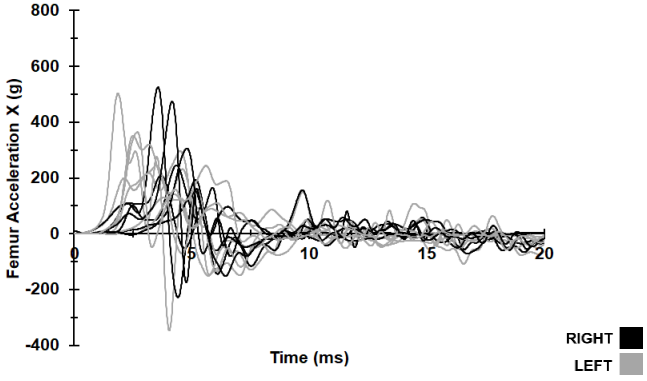

Figure D21: 4.2 Series 50th-percentile male distal femur X-axis acceleration.

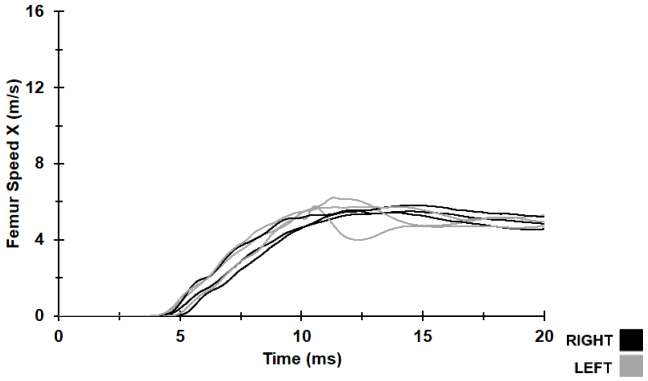

Figure D22: Series A 5th-percentile female distal femur X-axis speed.

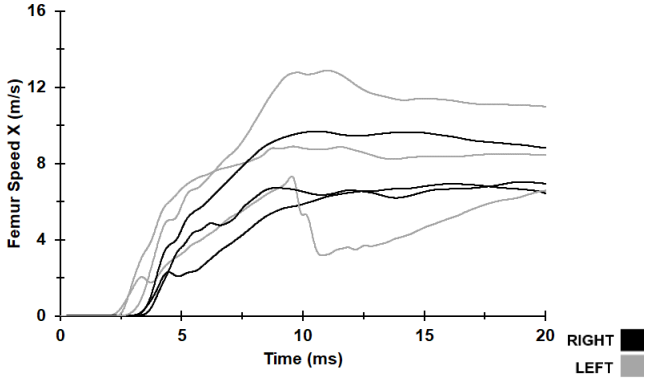

Figure D23: Series B 5th-percentile female distal femur X-axis speed.

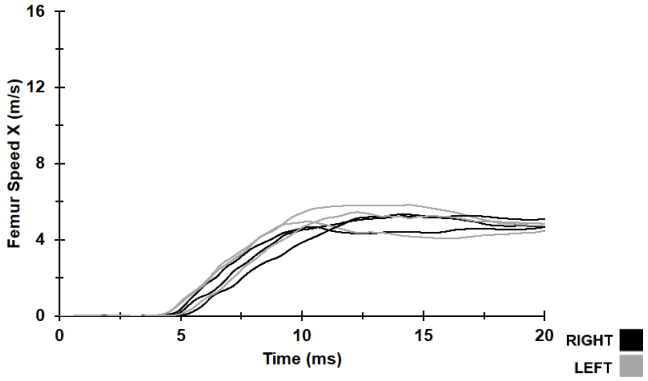

Figure D24: Series A 75th-percentile female distal femur X-axis speed.

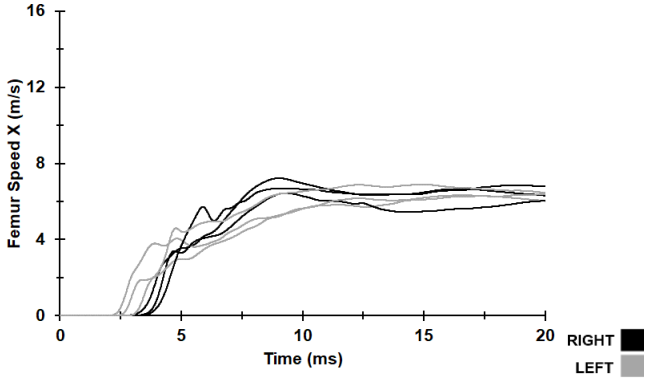

Figure D25: Series B 75th-percentile female distal femur X-axis speed.

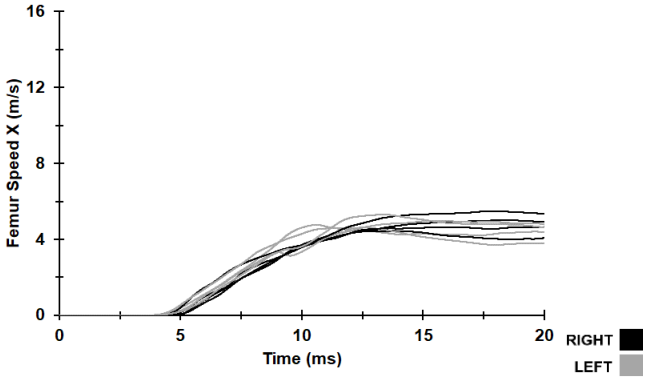

Figure D26: Series A 50th-percentile male distal femur X-axis speed.

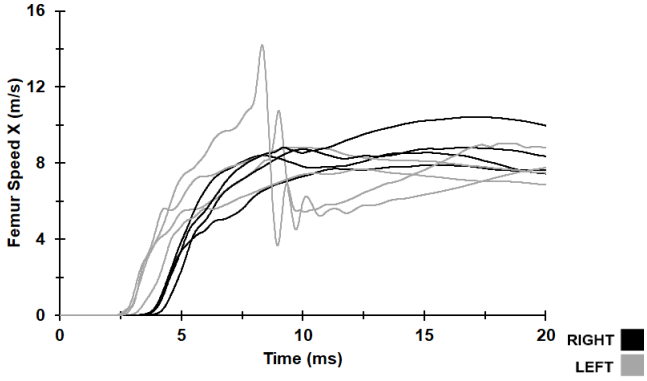

Figure D27: Series B 50th-percentile male distal femur X-axis speed.

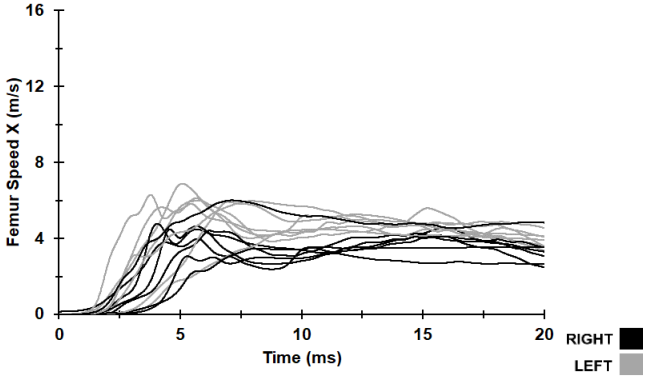

Figure D28: 4.2 Series 50th-percentile male distal femur X-axis speed.

Appendix E: Lower Extremity Response Envelopes

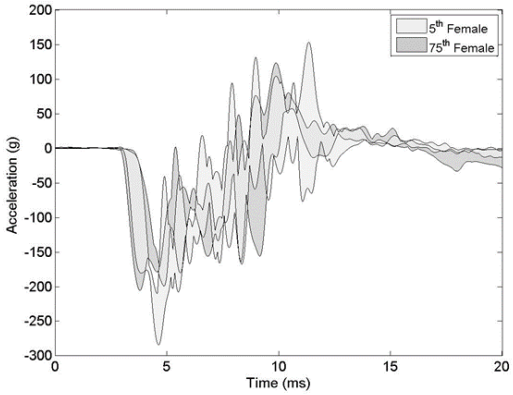

Figure E1: Series A left tibia Az 5th- and 75th-percentile females.

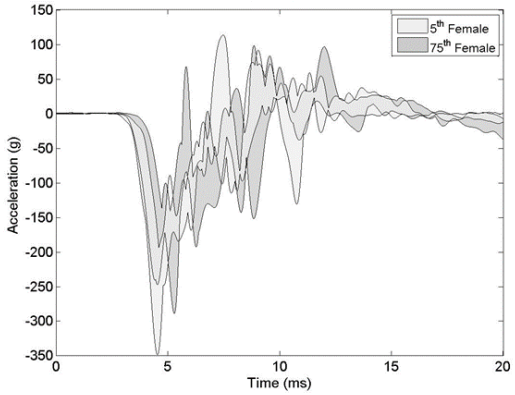

Figure E2: Series A right tibia Az 5th- and 75th-percentile females.

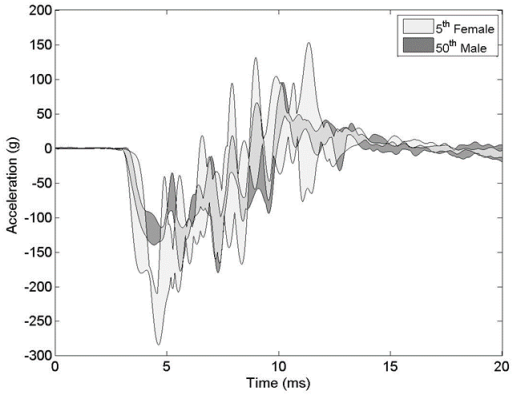

Figure E3: Series A left tibia Az 5th-percentile females and 50th-percentile males.

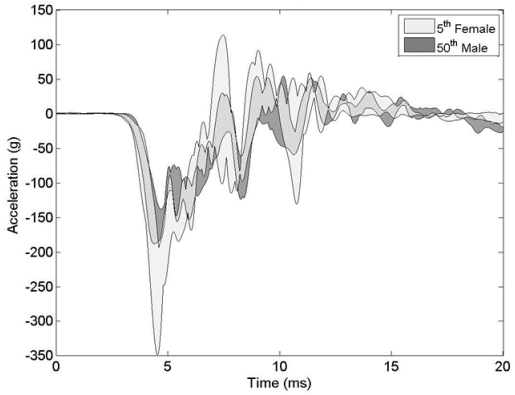

Figure E4: Series A right tibia Az 5th-percentile females and 50th-percentile males.

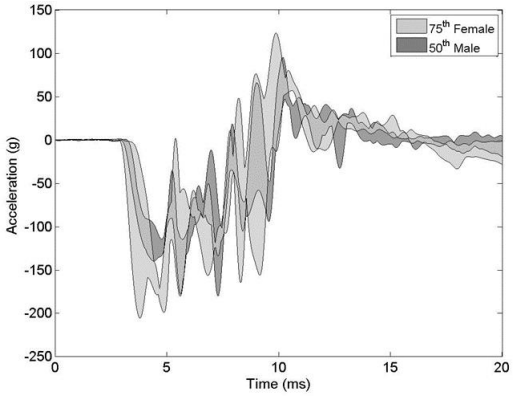

Figure E5: Series A left tibia Az 75th-percentile females and 50th-percentile males.

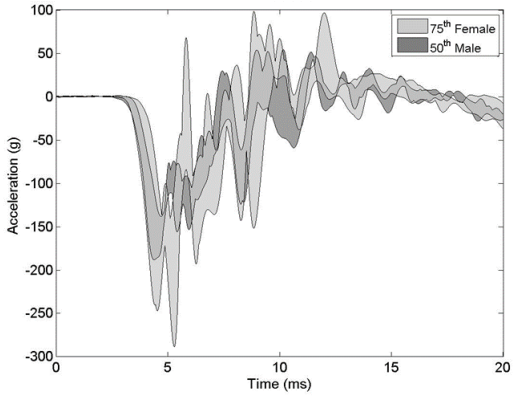

Figure E6: Series A right tibia Az 75th-percentile females and 50th-percentile males.

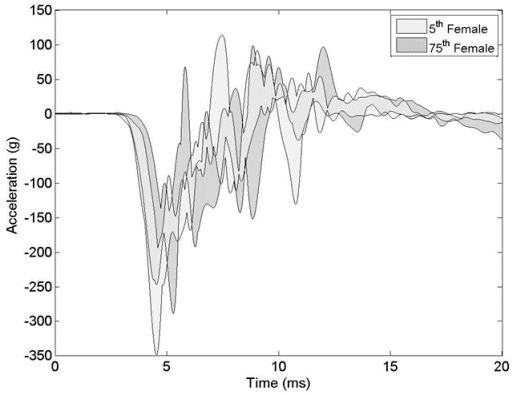

Figure E7: Series A right tibia Az 5th- and 75th-percentile females.

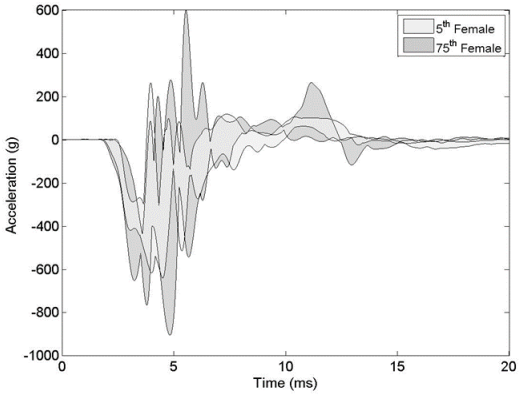

Figure E8: Series B right tibia Az 5th- and 75th-percentile females.

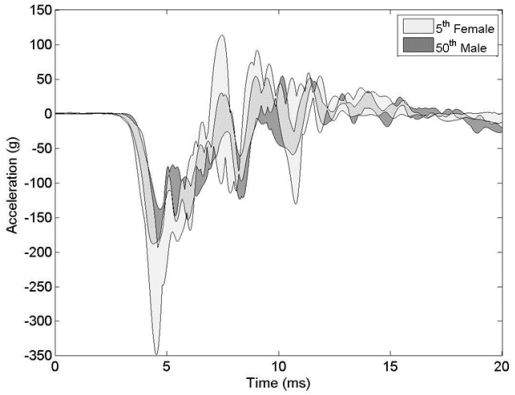

Figure E9: Series A right tibia Az 5th-percentile females and 50th-percentile males.

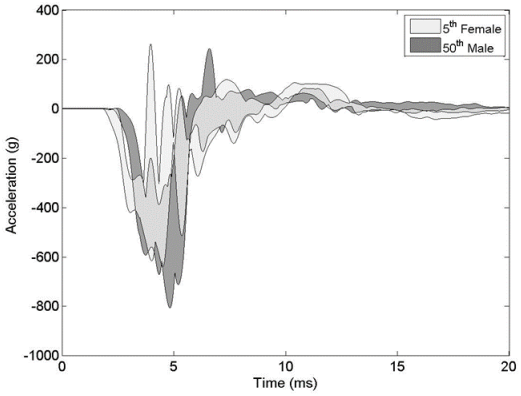

Figure E10: Series B right tibia Az 5th-percentile females and 50th-percentile males.

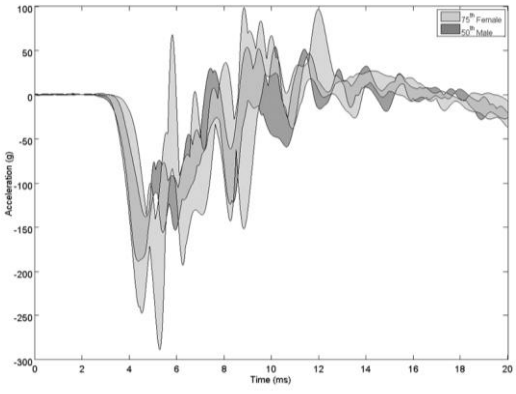

Figure E11: Series A right tibia Az 75th-percentile females and 50th-percentile males.

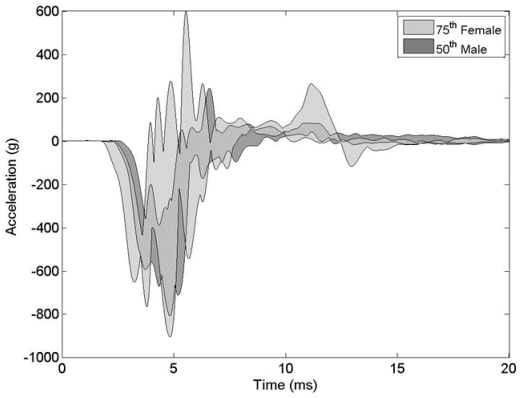

Figure E12: Series B right tibia Az 75th-percentile females and 50th-percentile males.

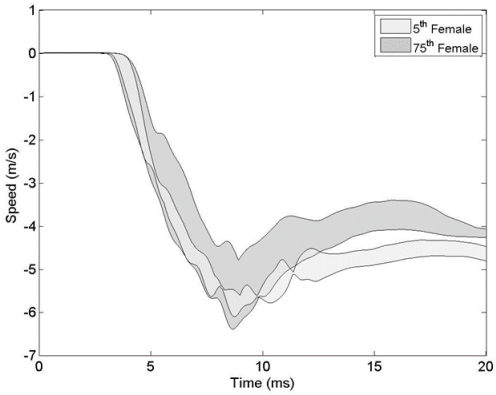

Figure E13: Series A left tibia Vz 5th- and 75th-percentile females.

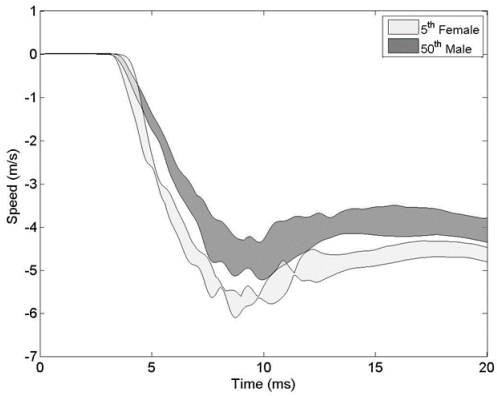

Figure E14: Series A left tibia Vz 5th-percentile females and 50th-percentile males.

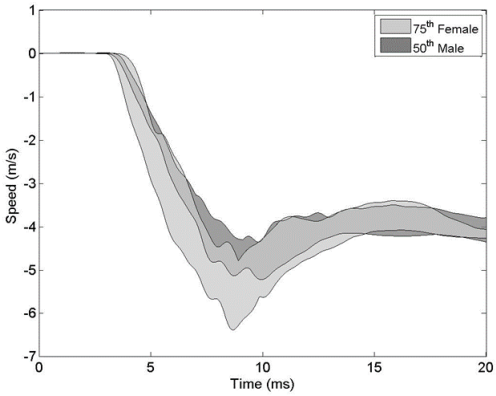

Figure E15: Series A left tibia Vz 75th-percentile females and 50th-percentile males.

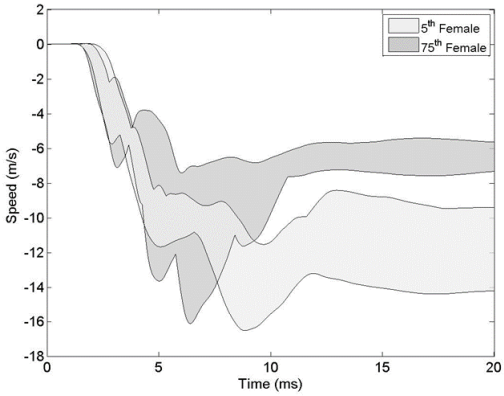

Figure E16: Series B left tibia Vz 5th- and 75th-percentile females.

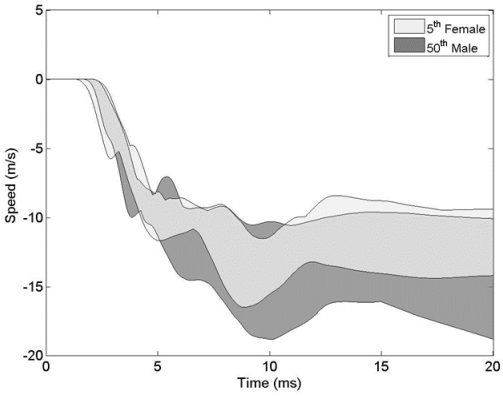

Figure E17: Series B left tibia Vz 5th-percentile females and 50th-percentile males.

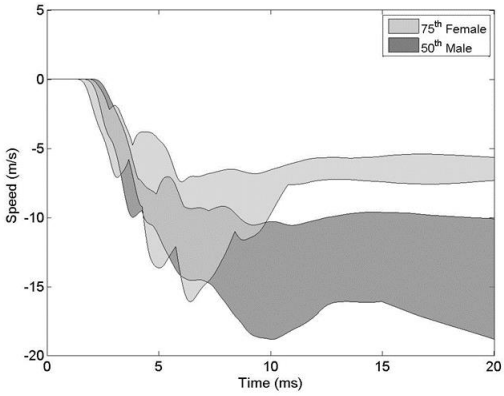

Figure E18: Series B left tibia Vz 75th-percentile females and 50th-percentile males.

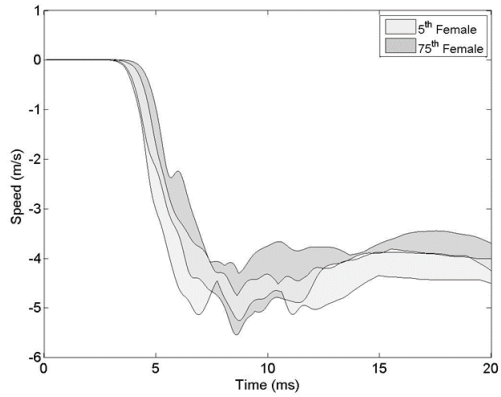

Figure E19: Series A right tibia Vz 5th- and 75th-percentile females.

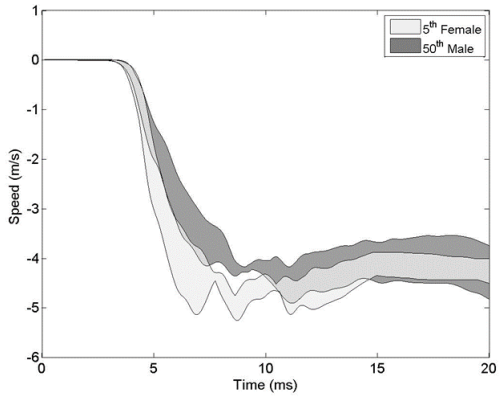

Figure E20: Series A right tibia Vz 5th-percentile females and 50th-percentile males.

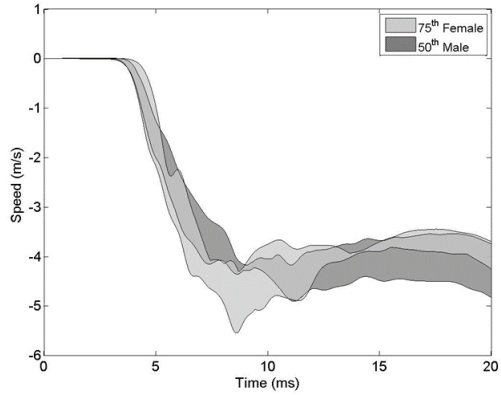

Figure E21: Series A right tibia Vz 75th-percentile females and 50th-percentile males.

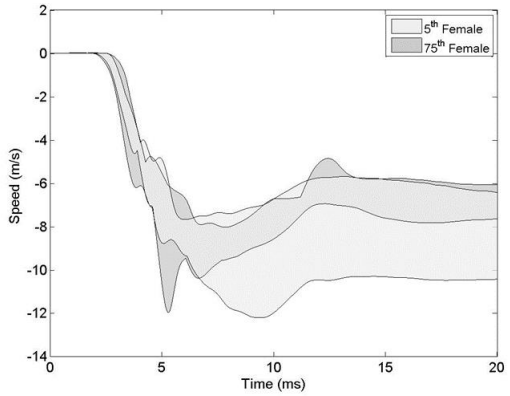

Figure E22: Series B right tibia Vz 5th- and 75th-percentile females.

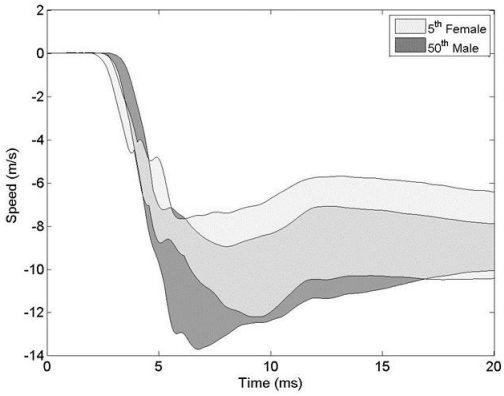

Figure E23: Series B right tibia Vz 5th-percentile females and 50th-percentile males.

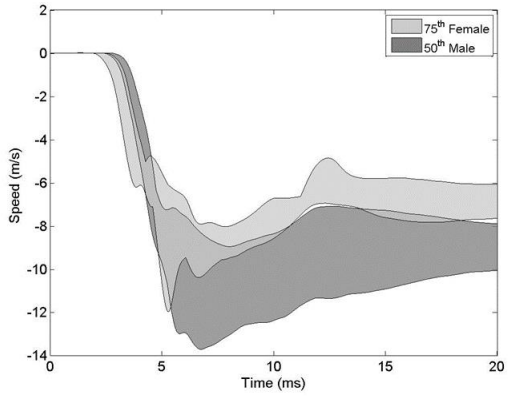

Figure E24: Series B right tibia Vz 75th-percentile females and 50th-percentile males.

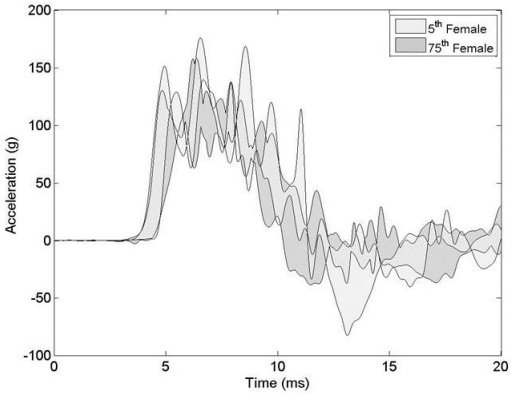

Figure E25: Series A left femur Ax 5th- and 75th-percentile females.

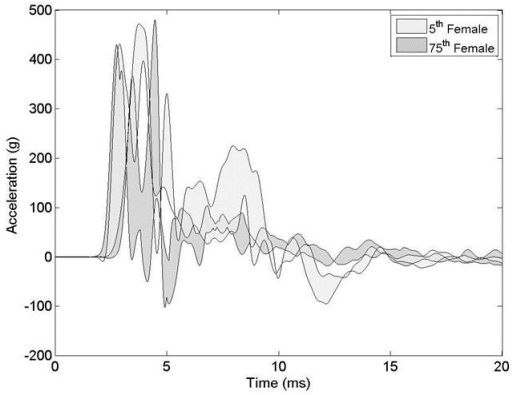

Figure E26: Series B left femur Ax 5th- and 75th-percentile females.

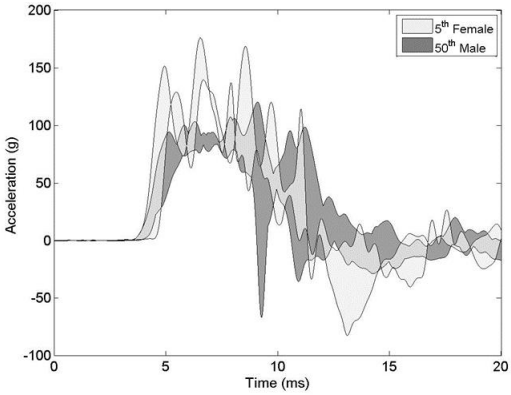

Figure E27: Series A left femur Ax 5th-percentile females and 50th-percentile males.

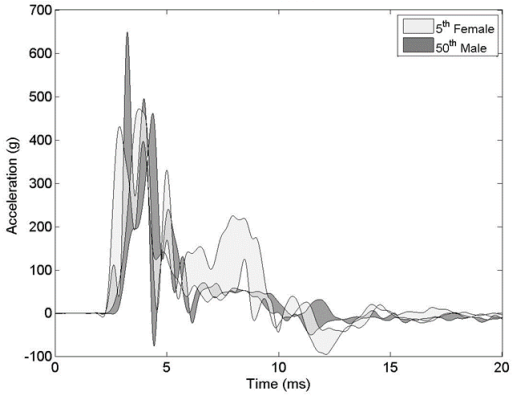

Figure E28: Series B left femur Ax 5th-percentile females and 50th-percentile males.

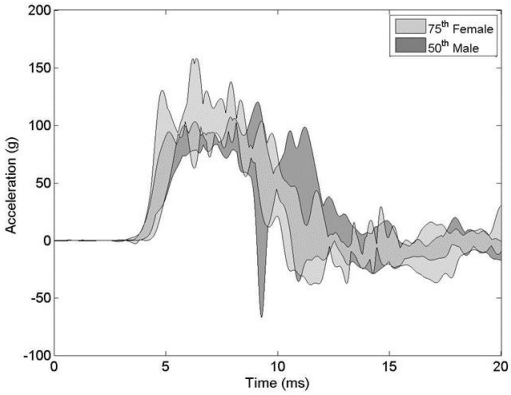

Figure E29: Series A left femur Ax 75th-percentile females and 50th-percentile males.

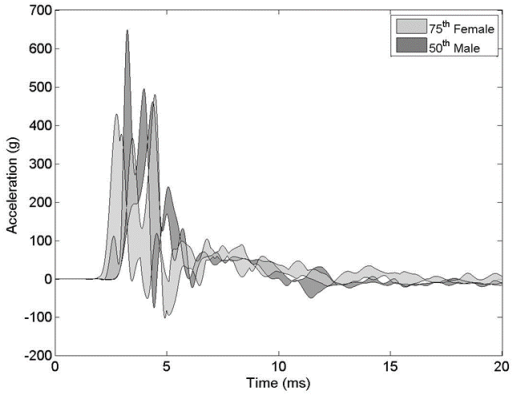

Figure E30: Series B left femur Ax 75th-percentile females and 50th-percentile males.

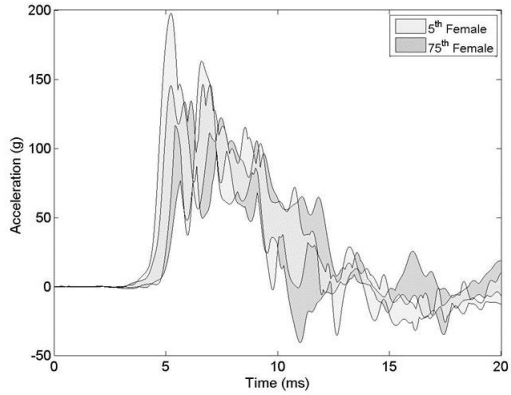

Figure E31: Series A right femur Ax 5th- and 75th-percentile females.

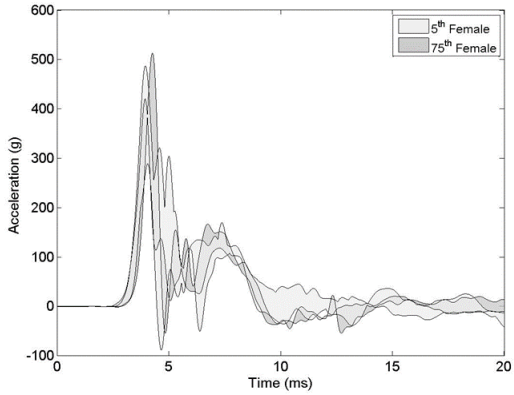

Figure E32: Series B right femur Ax 5th- and 75th-percentile females.

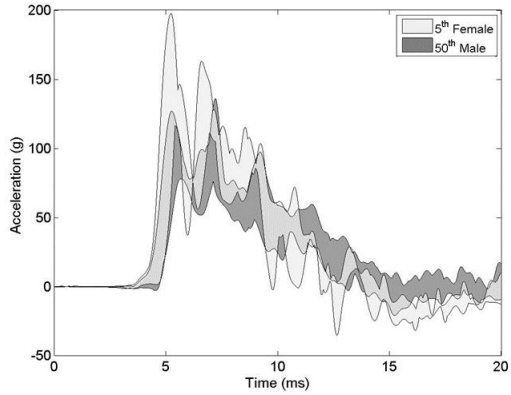

Figure E33: Series A right femur Ax 5th-percentile females and 50th-percentile males.

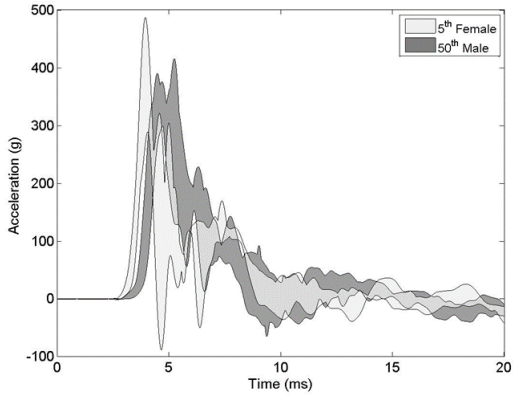

Figure E34: Series B right femur Ax 5th-percentile females and 50th-percentile males.

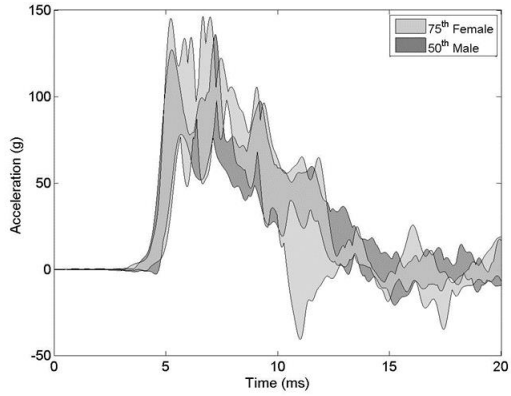

Figure E35: Series A right femur Ax 75th-percentile females and 50th-percentile males.

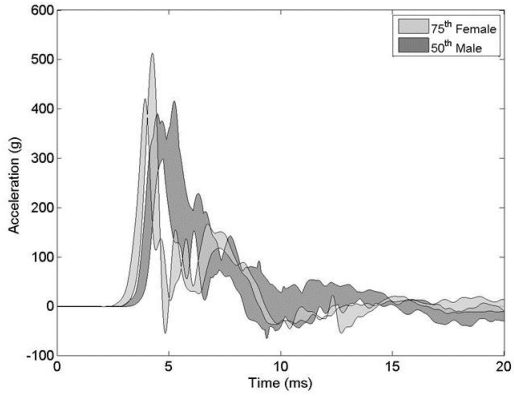

Figure E36: Series B right femur Ax 75th-percentile females and 50th-percentile males.

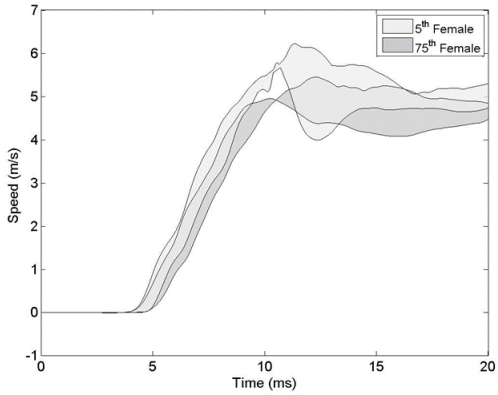

Figure E37: Series A left femur Vx 5th- and 75th-percentile females.

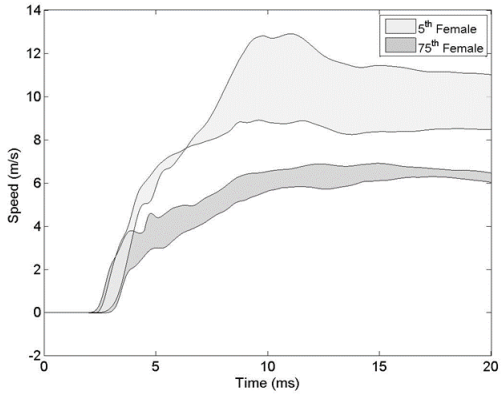

Figure E38: Series B left femur Vx 5th- and 75th-percentile females.

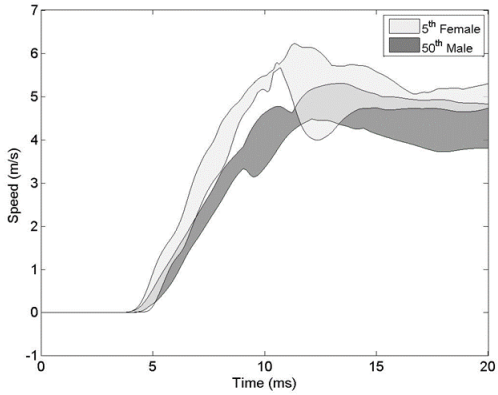

Figure E39: Series A left femur Vx 5th-percentile females and 50th-percentile males.

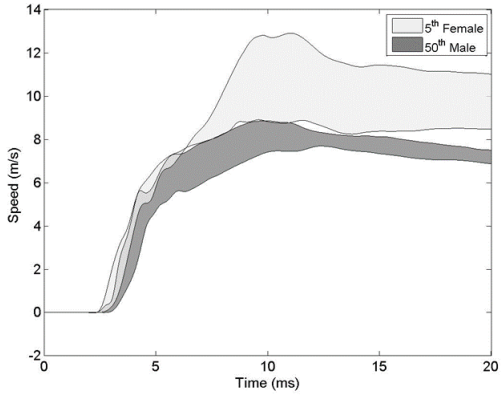

Figure E40: Series B left femur Vx 5th-percentile females and 50th-percentile males.

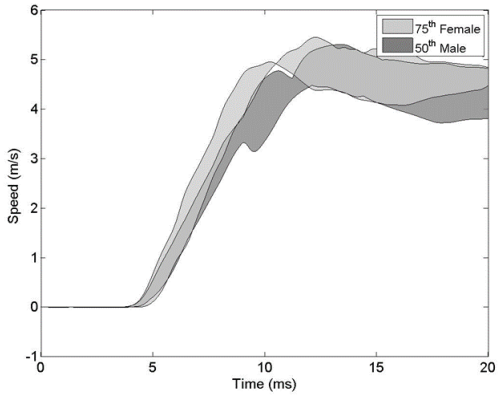

Figure E41: Series A left femur Vx 75th-percentile females and 50th-percentile males.

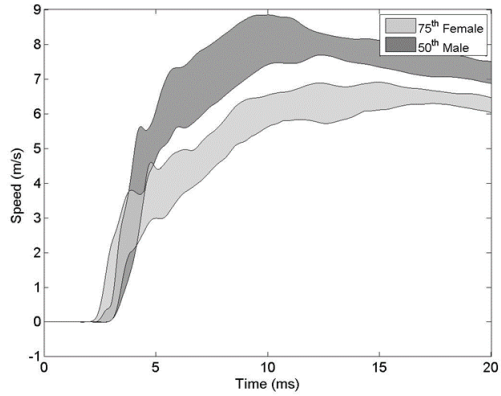

Figure E42: Series B left femur Vx 75th-percentile females and 50th-percentile males.

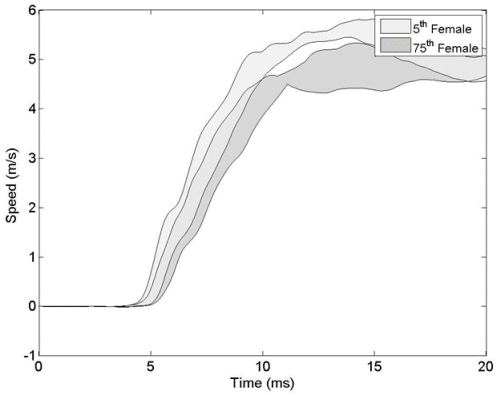

Figure E43: Series A right femur Vx 5th- and 75th-percentile females.

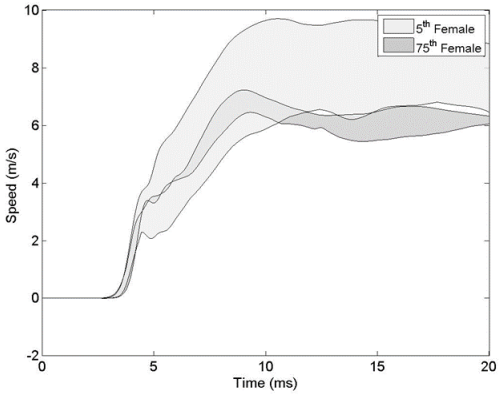

Figure E44: Series B right femur Vx 5th- and 75th-percentile females.

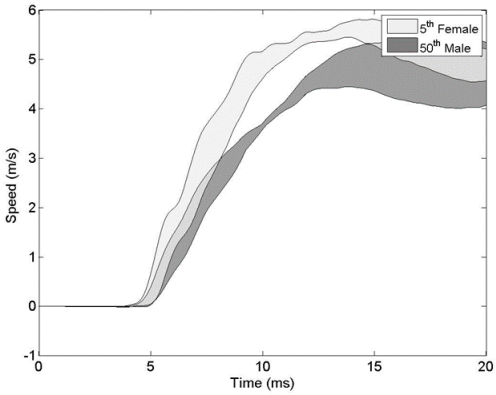

Figure E45: Series A right femur Vx 5th-percentile females and 50th-percentile males.

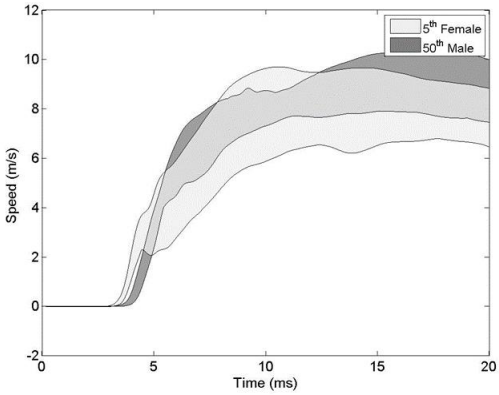

Figure E46: Series B right femur Vx 5th-percentile females and 50th-percentile males.

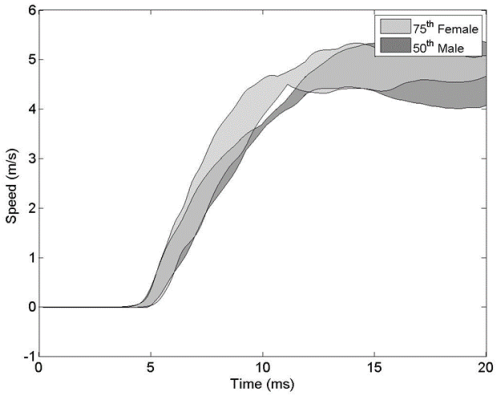

Figure E47: Series A right femur Vx 75th-percentile females and 50th-percentile males.

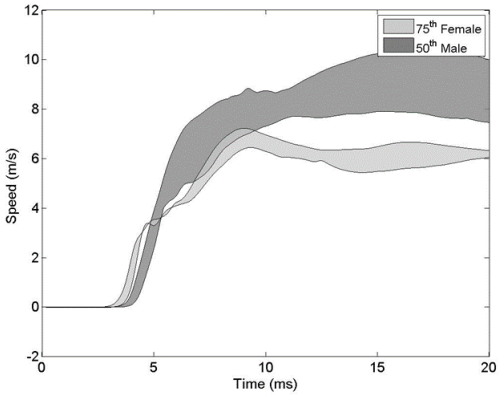

Figure E48: Series B right femur Vx 75th-percentile females and 50th-percentile males.

Appendix F: Peak and Time-to-Peak Values

Table F1: Distal femur posteroanterior (global vertical) peak and TTP values

Shot	Crew	Side	Peak Acc. (g)	Acc. TTP (ms)	Peak Speed (m/s)	Speed TTP (ms)
MS1	1	R	208.461	3.320	3.978	5.320
MS1	1	L	297.187	4.370	6.884	4.940
MS4	1	R	524.956	2.830	4.772	3.310
MS4	1	L	503.365	1.660	6.294	3.570
MS5	2	R	246.008	2.910	4.409	4.760
MS5	2	L	244.305	2.300	6.003	4.550
MS11	1	R	193.376	3.590	3.462	6.530
MS11	1	L	141.879	2.480	4.471	8.620
MS14	1	R	306.222	2.340	3.223	8.800
MS14	1	L	244.153	3.990	5.924	5.340
MS5	1	R	475.438	3.480	4.635	4.970
MS5	1	L	352.182	2.010	6.114	5.150
MS7	1	R	277.126	2.830	6.007	6.630
MS7	1	L	364.245	1.690	5.973	6.950
SA1	1	R	99.301	1.680	4.651	11.940
SA1	1	L	76.181	1.870	4.768	6.950
SA1	2	R	126.782	1.640	4.446	10.140
SA1	2	L	94.143	1.560	4.62	8.930
SA2	1	R	92.195	1.160	5.024	14.000
SA2	1	L	99.829	1.870	4.991	11.380
SA2	2	R	77.908	1.560	5.465	13.400
SA2	2	L	103.026	2.510	5.297	9.560
SA3	1	R	145.715	2.690	5.231	9.840
SA3	1	L	157.742	2.530	5.813	8.760
SA3	2	R	116.638	1.480	5.498	10.560
SA3	2	L	122.054	3.220	5.774	6.960
SA4	1	R	146.013	3.360	4.679	7.090
SA4	1	L	157.410	2.930	4.948	6.950
SA5	1	R	133.976	1.890	5.327	9.960
SA5	1	L	129.458	2.500	5.443	7.940
SA5	2	R	146.051	1.680	5.502	8.440
SA5	2	L	128.510	1.620	6.213	7.470
SA6	1	R	197.277	1.710	5.807	11.380
SA6	1	L	175.647	2.980	5.743	8.650

Table F2: Distal femur posteroanterior (global vertical) peak and TTP values, continued

Shot	Crew	Side	Peak Acc. (g)	Acc. TTP (ms)	Peak Speed (m/s)	Speed TTP (ms)
SB1	1	R	419.586	1.460	7.216	6.540
SB1	1	L	428.892	0.950	5.819	9.580
SB1	2	R	288.399	1.370	6.564	9.950
SB1	2	L	239.149	1.150	7.332	7.710
SB2	1	R	389.409	1.460	7.706	8.310
SB2	1	L	506.764	1.040	10.748	6.920
SB2	2	R	320.668	1.690	6.725	6.000
SB2	2	L	430.381	0.630	8.897	7.350
SB3	1	R	375.330	1.790	8.408	5.420
SB3	1	L	648.082	0.990	8.834	7.730
SB3	2	R	512.328	1.330	6.440	6.360
SB3	2	L	376.140	0.680	6.169	9.990
SB4	1	R	415.015	1.920	8.728	6.650
SB4	1	L	460.709	1.650	7.681	9.620
SB4	2	R	417.961	1.490	6.689	6.260
SB4	2	L	479.456	1.800	6.875	9.610
SB5	1	R	364.205	1.990	10.432	14.080
SB5	1	L	438.801	0.910	14.211	5.970
SB5	2	R	486.027	1.110	9.685	7.640
SB5	2	L	471.136	1.440	12.887	8.680

Table F3: Distal tibia axial (global vertical) peak and TTP values

Shot	Crew	Side	Peak Acc. (g)	Acc. TTP (ms)	Peak Speed (m/s)	Speed TTP (ms)
MS1	1	R	-186.882	5.640	-5.583	7.200
MS1	1	L	-252.886	4.870	-6.680	7.590
MS4	1	R	-704.500	3.750	-5.513	4.600
MS4	1	L	-441.634	3.570	-8.167	7.650
MS5	2	R	-421.006	4.200	-6.575	5.030
MS5	2	L	-406.086	2.770	-8.555	4.450
MS11	1	R	-25.113	1.950	-0.155	3.390
MS11	1	L	-194.703	4.860	-7.169	9.640
MS14	1	R	-382.193	5.300	-7.964	8.860
MS14	1	L	-290.889	5.060	-8.696	6.090
MS5	1	R	-337.618	4.420	-7.226	6.920
MS5	1	L	-444.283	3.670	-9.334	5.220
MS7	1	R	-395.730	3.530	-8.254	6.950
MS7	1	L	-321.189	3.740	-7.983	7.690
SA1	1	R	-175.213	1.600	-4.297	5.690
SA1	1	L	-126.822	1.690	-4.489	5.730
SA1	2	R	-188.402	1.830	-4.356	6.080
SA1	2	L	-177.897	2.630	-5.134	5.720
SA2	1	R	-159.298	1.270	-4.178	7.750
SA2	1	L	-162.564	2.430	-4.754	6.610
SA2	2	R	-138.442	1.840	-4.902	8.300
SA2	2	L	-131.930	2.750	-5.223	6.800
SA3	1	R	-240.517	1.700	-5.541	5.870
SA3	1	L	-205.525	0.900	-6.383	5.760
SA3	2	R	-220.877	1.640	-5.251	5.980
SA3	2	L	-230.859	1.790	-6.095	6.040
SA4	1	R	-247.145	1.440	-4.309	5.490
SA4	1	L	-178.833	1.470	-4.908	5.530
SA5	1	R	-288.520	1.980	-5.081	6.260
SA5	1	L	-199.138	1.910	-5.629	7.040
SA5	2	R	-248.247	1.820	-4.883	6.120
SA5	2	L	-284.223	1.560	-5.779	7.250
SA6	1	R	-348.439	1.650	-5.132	4.010
SA6	1	L	-210.399	1.930	-5.849	6.020

Table F4: Distal tibia axial (global vertical) peak and TTP values, continued

Shot	Crew	Side	Peak Acc. (g)	Acc TTP (ms)	Peak Speed (m/s)	Speed TTP (ms)
SB1	1	R	-651.741	1.470	-8.027	6.040
SB1	1	L	-656.175	1.620	-7.430	4.820
SB1	2	R	-440.902	1.620	-7.672	4.170
SB1	2	L	-625.181	1.140	-11.540	8.480
SB2	1	R	-514.671	1.260	-8.948	5.740
SB2	1	L	-699.819	0.950	-13.128	8.600
SB2	2	R	-640.154	2.410	-9.358	4.050
SB2	2	L	-578.595	1.510	-11.723	8.380
SB3	1	R	-670.568	2.090	-11.340	3.350
SB3	1	L	-864.074	1.790	-14.690	7.470
SB3	2	R	-765.538	1.460	-10.380	4.300
SB3	2	L	-1339.706	2.620	-13.649	3.370
SB4	1	R	-806.717	2.230	-10.559	3.550
SB4	1	L	-642.018	1.890	-10.574	9.000
SB4	2	R	-904.036	2.520	-11.958	2.970
SB4	2	L	-746.411	2.120	-16.089	4.610
SB5	1	R	-711.749	3.320	-13.699	4.860
SB5	1	L	-741.375	1.940	-18.813	8.260
SB5	2	R	-616.479	2.060	-12.199	7.380
SB5	2	L	-550.241	1.940	-16.494	6.920

Table F5: Floor peak and TTP values

Shot	Crew	Side	Peak Acc (g)	Acc TTP (ms)	Peak Speed (m/s)	Speed TTP (ms)
MS1	1	R	1245.02	3.03550	7.276	3.11400
MS1	1	L	2140.97	2.11550	14.233	3.29900
MS4	1	R	1452.94	2.52550	10.964	4.14550
MS4	1	L	3506.27	2.18800	18.100	3.40000
MS5	2	R	1910.91	2.66500	8.362	2.78750
MS5	2	L	2527.19	2.32500	17.049	3.44250
MS11	1	R	1217.29	7.02800	9.335	7.22800
MS11	1	L	1357.92	4.16850	11.745	4.50350
MS14	1	R	1296.61	5.94200	13.297	7.24300
MS14	1	L	956.28	3.34000	11.391	5.61750
MS5	1	R	1525.77	2.36850	17.608	5.84250
MS5	1	L	2527.19	2.32500	17.049	3.44250
MS7	1	R	2071.35	4.91050	17.101	5.88700
MS7	1	L	2624.58	3.13800	16.109	4.20400
SA1	1	R	4477.667	1.75500	23.61	2.95150
SA1	1	L	377.408	0.50700	0.44	0.56750
SA1	2	R	3320.357	1.65850	24.57	2.81700
SA1	2	L	1051.171	0.49150	1.21	0.55050
SA2	1	R	2066.118	1.05900	7.58	2.22700
SA2	1	L	4974.786	1.30250	6.84	1.39700
SA2	2	R	2088.155	1.88050	10.35	2.81350
SA2	2	L	6226.921	0.80500	9.61	0.91950
SA3	1	R	1164.307	1.39450	7.96	2.55450
SA3	1	L	4140.348	1.11350	8.92	1.27050
SA3	2	R	1395.733	1.82600	6.50	2.11050
SA3	2	L	4063.064	0.98500	9.45	1.15400
SA4	1	R	-	-	-	-
SA4	1	L	5938.746	1.26450	14.63	2.53200
SA5	1	R	1179.580	2.03650	7.48	2.55100
SA5	1	L	3685.292	1.29200	7.21	1.44700
SA5	2	R	1109.231	1.43250	6.97	2.63250
SA5	2	L	3065.502	1.22850	5.53	1.35450
SA6	1	R	1912.533	1.83200	8.04	2.36550
SA6	1	L	4062.648	1.32950	9.63	1.52150

Table F6: Floor peak and TTP values, continued

Shot	Crew	Side	Peak Acc (g)	Acc TTP (ms)	Peak Speed (m/s)	Speed TTP (ms)
SB1	1	R	1447.710	2.24800	6.31	2.69050
SB1	1	L	5547.138	1.36050	10.44	1.47800
SB1	2	R	1272.141	1.82500	6.75	1.90650
SB1	2	L	5335.492	1.38300	10.46	1.51450
SB2	1	R	2561.963	1.61850	21.15	3.38100
SB2	1	L	5207.308	0.62400	36.99	2.77250
SB2	2	R	2518.804	1.24650	18.41	2.88750
SB2	2	L	3575.910	0.48700	16.24	2.53350
SB3	1	R	2543.754	1.28000	17.14	2.90050
SB3	1	L	-	-	-	-
SB3	2	R	2100.286	1.82350	17.16	2.97850
SB3	2	L	-	-	-	-
SB4	1	R	2961.416	1.82350	20.40	2.98450
SB4	1	L	1116.212	0.47750	1.27	0.53650
SB4	2	R	2933.657	1.80300	24.66	2.83400
SB4	2	L	-	-	-	-
SB5	1	R	2497.572	1.73450	18.09	2.96550
SB5	1	L	-	-	-	-
SB5	2	R	1977.082	1.27050	16.87	2.94550
SB5	2	L	-	-	-	-

REFERENCES

AAAM (2008) The Abbreviated Injury Scale 2005 Update 2008. Des Plaines, IL. 1981-2000.

Alvarez, J. (2011) Epidemiology of Blast Injuries in Current Operations, *In: A Survey of Blast Injury across the Full Landscape of Military Science RTO-MP-HFM-207*, Halifax, Canada, NATO Science and Technology Organization.

AO/OTA Fracture and Dislocation Compendium (2018). Journal of Orthopaedic Trauma, 32(1).

Arbabi S., Wahl W. L., Hemmila, M. R., Kohoyda-Inglis, C., Taheri, P. A., Wang, S. C. (2003). The cushion effect. *Journal of Trauma*, 54, 1090 – 1093.

Bailey, A. M., Perry, B. J., Salzar, R. S. (2017). Response and injury of the human leg for axial impact durations applicable to automotive intrusion and underbody blast environments. International Journal of Crashworthiness, 1–9.

Barbir, A. (2005). Validation of lower limb surrogates as injury assessment tools in floor impacts due to anti-vehicular landmine Explosions. *Master Thesis*, Wayne State University, Detroit, USA.

Begeman, P. and Aekbote, K. (1996). Axial load strength and some ligament properties of the ankle joint, *Injury Prevention though Biomechanics Symposium*.

Begeman, P. and Prasad, P. (1990). Human Ankle Impact Response in Dorsiflexion, *Society of Automotive Engineers*, SAE Paper 902308.

Bieler, D., Hentsch, S., Franke, A., Kollig, E. (2011). Current Strategies for the Treatment of Blast Injuries to the Extremities, In: *A Survey of Blast Injury across the Full Landscape of Military Science RTO-MP-HFM-207*, Halifax, Canada, NATO Science and Technology Organization.

Boulanger, B. R., Milzman D., Mitchell K., Rodriguez A. (1992). Body habitus as a predictor of injury pattern after blunt trauma. *Journal of Trauma*, 33, 228 – 232.

Cavanaugh, J. M., Zhu, Y., Huang, Y., King, A. (1993). Injury and Response of the Thorax in Side Impact Cadaveric Tests. *Stapp Car Crash Conference*, 199 – 222.

Champion, H. R., Holcomb, J. B., Young, L. A. (2009). Injuries from Explosions: Physics, Biophysics, Pathology, and Required Research Focus. *Journal of Trauma*, 66, 1468 - 77.

Chirvi, S., Pintar, F., Yoganandan, N., Banerjee, A., Schlick, M., Curry, W., Voo, L. (2017). Human Foot-Ankle Injuries and Associated Risk Curves from Under Body Blast Loading Conditions. *Stapp Car Crash Journal*, 61, 157 – 173.

Cimpoeru, S. J., Phillips, P., and Ritzel, D. V. (2017). Blast Physics and Vehicle Response. In M. Franklyn & P. V. S. Lee (Eds.), *Military Injury Biomechanics the Cause and Prevention of Impact Injuries* (pp. 19 – 34). Boca Raton, FL: CRC Press.

Danelson K. A., Kemper A. R., Mason M. J., Tegtmeyer M., Swiatkowski S. A., Bolte J. H., Hardy W. N. (2015). Comparison of ATD to PMHS Response in the Under-Body Blast Environment. *Stapp Car Crash Journal*, 59, 445-520.

Danelson, K., Watkins, L., Hendricks, J., Frounfelker, P., WIAMan Case Review Team, Pizzolato-Heine, K., Valentine, R., Loftis, K. (2018). Analysis of the Frequency and Mechanism of Injury to Warfighters in the Under-body Blast Environment. *Stapp Car Crash Journal*, 62, 489-513.

Dischinger, P. C., Kufera, J. A., Ho, S. M., Ryb, G. E., Wang, S. (2016). On equal footing: Trends in Ankle/Foot Injuries for Men vs. Women. *Traffic Injury Prevention*, 17(1), 150-155.

Dischinger, P. C., Read, K. M., Kufera, J. A., Kerns, T. J., Burch, C. A., Jawed, N., Ho, S. M., Burgess, A. R. (2004). Consequences and Costs of Lower-Extremity Injuries. *48th Annual Proceedings of the Association for the Advancement of Automotive Medicine*, 48, 339 - 53.

Dosquet, F., Nies, O., Lammer, C. (2004). Test methodology for protection of vehicles occupants against IED. *18th Symposium of Military Aspects of Shock and Blast, Bad Reichenhall, Germany*.

Dougherty, A. L., Mohrle, C. R., Galarneau, M. R., Woodruff, S. I., Dye, J. L., Quinn, K. H. (2009). Battlefield extremity injuries in Operation Iraqi Freedom. *Injury, Int. J. Care Injured*, 40, 772–777.

Dye, J. L., Eskridge, S. L., Tepe, V., Clouser, M. C., Galarneau, M. (2016). Characterization and Comparison of Combat-Related Injuries in Women During OIF and OEF. *Military Medicine*, 181, 92 – 98.

Eichenholtz, S. N., Levine, D. B. (1964). Fractures of the tarsal navicular bone. *Clinical Orthopaedics and Related Research*, 34, 142 – 57.

Eskridge, S.L., Macera, C.A., Galarneau, M.R., Holbrook, T.L., Woodruff, S.I., MacGregor, A.J., Morton, D.J., Shaffer, R.A., (2012). Injuries from combat explosions in Iraq: Injury type, location, and severity. *International Journal of the Care of the Injured*, 43, 1678 – 1682.

Evans, L (2001). Female Compared with Male Fatality Risk from Similar Physical Impacts. *The Journal of Trauma Injury, Infection, and Critical Care*, 50(2), 281-288.

Foret-Bruno, J.Y., Faverjon, G., Brun-Cassan, F., Tarriere, C. (1990). Females More Vulnerable than Males in Road Accidents. *FISITA Congress XXIII The Promise of New Technology in the Automotive Industry, SAE*.

Funk, J. R., Crandall, J. R., Tourret, L. J., MacMahon, C. B., Bass, C. R., Patrie, J. T., Khaewpong, N. and Eppinger, R. H. (2002). The Axial Injury Tolerance of the Human Foot/Ankle Complex and the Effect of Achilles Tension. *Journal of Biomechanical Engineering*, 124, 750 - 757.

Gallagher D., Visser M., Sepúlveda, D., Pierson R. N., Harris T., Heymsfield S. B. (1996). How useful is body mass index for comparison of body fatness across age, sex, and ethnic groups? *American Journal of Epidemiology*, 143(3), 228 – 239.

Gallenberger, K., Yoganandan, N., Pintar, F. A. (2013). Biomechanics of foot/ankle trauma with variable energy impacts. Annals in Advancement of Automotive Medicine, 57, 123 – 132.

Gilroy, A. M., MacPherson, B. R., Ross, L. M. (2012). *Atlas of Anatomy: Second Edition.* Stuttgart: Thieme.

Gordon, C. C., Blackwell, C. L., Bradtmiller, B., Parham, J. L., Barrientos, P., Paquette, S. P., Corner, B. D., Carson. J. M., Venezia, J. C., Rockwell, B. M., Michael Mucher, M., Kristensen, S. (2012). Anthropometric survey of us army personnel methods and summary statistics. *Technical Report Natick/TR-15/007*.

Gorman, D., Handy, E., Wang, S., Irwin, A. L., Wang, S. (2016). Morphomics and the Talus. *Stapp Car Crash Journal*, 60, 287 - 300.

Griffin, L.V., Harris, R. M., Hayda, R. A. and Rountree, M. S. (2001), Loading Rate and Torsional Moments Predict Pilon Fractures for Antipersonnel Blast Mine Loading. *International Conference on the Biomechanics of Impacts* in Isle of Man, UK.

Hamill, J., Knutzen K. M., Derrick T.R. (2015). *Biomechanical Basis of Human Movement: Fourth Edition*. Philadelphia: Wolters Kluwer.

Hardy, W.N., Schneider, L.W., Rouhana, S.W. (2001). Abdominal Impact Response to Rigid-Bar, Seatbelt, and Airbag Loading. *Stapp Car Crash Journal*, 45, 1 – 31.

Hardy, W.N., Schneider, L.W., Rouhana, S.W. (2001). Prediction of Airbag-Induced Forearm Fractures and Airbag Aggressivity. *Stapp Car Crash Conference Journal*, 45, 511-534.

Harris, R., Rountree, M., Griffin, L. V., Hayda, R. A., Bice, T., Mannion, S. J. (2000). Final Report of the Lower Extremity Assessment Program. U.S. Army Institute of Surgical Research. Fort Sam, Houston, TX.

Hawkins, L. G. (1970). Fractures of the neck of the talus. *Journal of Bone and Joint Surgery*, 52(5), 991 - 1002.

Henderson, K., Bailey, A., Christopher, J., Brozoski, F., Salzar, R. (2013). Biomechanical response of the lower leg under high rate loading. *International Conference on the Biomechanics of Impacts* in Gothenburg, Sweden.

Jepsen, K. J., Centi, A., Duarte, G. F., Galloway, K., Goldman, H., Hampson, N., Lappe, J. M., Cullen, D. M., Greeves, J., Izard, R., Nindl, B. C., Kraemer, W. J., Negus, C. H., Evans, R. K. (2011). Biological Constraints That Limit Compensation of a Common Skeletal Trait Variant Lead to Inequivalence of Tibial Function Among Healthy Young Adults. *Journal of Bone and Mineral Research*, 26(12), 2872 - 2885.

Kallina, I., Scheunert, D., Scheerer, J., Breitner, R., Zeidler, F. (1995). Significance for the Occupants - Assessment in Tests - Injury Prevention. *International Conference on Pelvic and Lower Extremity Injuries*, Washington, DC.

Kemper, A. K., Stitzel, J., Duma, S., Matsuoka, F., Masuda, M. (2005). Biofidelity of the SID-IIs and a Modified SID-IIs Upper Extremity: Biomechanical Properties of the Human Humerus. *In 19th International Technical Conference on the Enhanced Safety of Vehicles (ESV)*, Washington DC, United States.

Kitagawa, Y., Ichikawa, H., King, A.I., Levine, R. S. (1998). A severe ankle and foot injury in frontal crashes and its mechanism. *Society of Automotive Engineers*, Paper 983145.

Klopp, G., Crandall, J., Hall, G., Pilkey, W., Hurwitz, S. and Kuppa, S. (1997). Mechanisms of injury and injury criteria for the human foot and ankle in dynamic axial impacts to the foot. *International Conference Proceedings* in Hanover, Germany. 73 - 86.

Kuppa, S., Wang, J., Haffner, M., Eppinger, R. (2001). Lower Extremity Injuries and Associated Injury Criteria. *17th International Technical Conference on the Enhanced Safety of Vehicles in Amsterdam, The Netherlands*, National Highway Traffic Safety Administration, Washington, D.C.

Laidlaw P. P. (1904). The varieties of the os calcis. *Journal of Anatomy and Physiology*, 38(2), 133 - 143.

Loftis, K. and Gillich, P. J. (2014). Trauma Comparison of Civilian Automotive with Military Combat Injuries. *Short Communications from AAAM's 58th Annual Scientific Conference, Traffic Injury Prevention*, 15, sup 1, 256 - 9.

Masouros, S., Ramasamy, A., Newell, N., Clasper, J. C. (2013). Design of a Traumatic Injury Simulator for Assessing Lower Limb Response to High Loading Rates. *Annals of Biomedical Engineering*, April, DOI: 10.1007/s10439-013-0814-6

McKay, B. J., Bir, C. A. (2009). Lower extremity injury criteria for evaluating military vehicle occupant injury in underbelly blast events. *Stapp Car Crash Journal*, 53, 229 - 249.

McMaster, J., Parry, M., Wallace, W. A., Wheeler, L., Owen, C., Lowne, R., Oakley, C., Roberts, A. (2000). Biomechanics of ankle and hindfoot injuries in dynamic axial loading. *Stapp Car Crash Journal*, 44, 357 – 377.

Miller, C., Rupp, J., Humm, J., Alai, A., Kang, Y.S., Dooley, C., Sherman, D., Marcus, I., Bigler, B. (2015). Signal Conversion Tiger Team [ScoTT] Recommendations for Anatomical Reference Rev. 0.6 (under review).

Morris, A., Thomas, P., Taylor, A., Wallace, W. (1997). Mechanisms of Fractures in Ankle and Hind-Foot Injuries to Front Seat Car Occupants - An In-Depth Accident Data Analysis, *SAE Technical Paper 973328*.

Newell, N., Masouros, S. D., Ramasamy, A., Bonner, T. J., Hill, A. M., Clasper, J. C., Bull, A. M. J. (2012). Use of cadavers and anthropometric test devices (ATDs) for assessing lower limb injury outcome from under-vehicle explosions. *International Conference on the Biomechanics of Impacts* in Dublin, Ireland.

Nusholtz, G., Kaiker, P. (1994). Abdominal Response to Steering Wheel Loading. *Proceedings of the 14th International Technical Conference on Enhanced Safety of Vehicles*, 118-127.

Owens, B. D., Kragh, J. F., Jr., Macaitis, J., Svoboda, S. J., Wenke, J. C. (2007). *Journal of Orthopaedic Trauma*, 21, 254 – 257.

Owens, B. D., Kragh, J. F., Jr., Wenke, J. C., Macaitis, J., Wade, C. E., Holcomb, J. B. (2008). Combat Wounds in Operation Iraqi Freedom and Operation Enduring Freedom. *The Journal of Trauma Injury, Infection, and Critical Care*, 64(2), 295-299.

Perry, J. (1983). Anatomy and Biomechanics of the Hindfoot. *Clinical Orthopaedics and Related Research*. 9 – 15.

Petit, P., Portier, L., Foret-Bruno, J., Trosseille, X., Parenteau, C., Coltat, J., Tarriere, C., Lassau, J. (1997). Quasistatic characterization of the human foot-ankle joints in a simulated tensed state and updated accidentological data. *International Conference on the Biomechanics of Impact* in Dublin, Ireland, 363 – 376.

Pietsch, H. A, Bosch, K. E., Weyland, D. R., Spratley, E. M., Henderson, K. A., Salzar, R. S., Smith, T. A., Sagara, B. M., Demetropoulos, C. K., Dooley, C. J., Merkle, A. C. (2016). Evaluation of WIAMan Technology Demonstrator Biofidelity Relative to Sub-Injurious PMHS Response in Simulated Under-body Blast Events. *Stapp Car Crash Journal*, 60, 199-246.

Pintar, F. A., Schlick, M. B., Yoganandan, N., Voo, L., Merkle, A. C., Kleinberger, M. (2016). Biomechanical Response of Military Booted and Unbooted Foot-Ankle-Tibia from Vertical Loading. Stapp Car Crash Conference, 247 - 285.

Powers, R. (2016). The Cost of War. Retrieved from: thebalance.com.

Quenneville, C., Fraser, G., and Dunning, C. (2010) Development of an Apparatus to Produce Fractures From Short-Duration High-Impulse Loading With an Application in the Lower Leg. *ASME Journal of Biomechanical Engineering*, 132(1), 014502.

Ramasamy A., Hill A. M., Hepper A. E., Bull A. M. J., Clasper J. C. (2009). Blast Mines: Physics, Injury Mechanisms and Vehicle Protection. *Journal of the Royal Army Medical Corps*, 155(4), 258-64.

Ramasamy, A., Hill, A. M., Phillip, R., Gibb, I., Bull, A. M. J., Clasper, J. C. (2011). The Modern "Deck-Slap" Injury – Calcaneal Blast Fractures from Vehicle Explosions. *The Journal of Trauma Injury, Infection, and Critical Care*, 71, 1694 – 1698.

Rammelt, S. and Zwipp, H. (2006). Calcaneus Fractures. *Trauma*, 8, 197–212.

Roberts, D., Donnelly, B., Severin, C., Medige, J. (1993). Injury mechanisms and tolerance of the human ankle joint. *Centers for Disease Control*.

Rupp, J., Reed, M. (2015). WIAMan Bio PT PMHS Positioning Procedure guidelines. Rev. 0.7 (under review).

Sanders, R., Fortin, P., DiPasquale, T., Walling, A. (1993). Operative treatment in 120 displaced intraarticular calcaneal fractures. Results using a prognostic computed tomography scan classification. *Clinical Orthopaedics and Related Research*, 290, 87 - 95.

Sarrafian, S. K. *Kelikian, A. S. (editor).* (2011). *Sarrafian's Anatomy of the Foot and Ankle: Third Edition*. Philadelphia: Lippincott Williams & Wilkins.

Schueler, F., Mattern, R., Zeidler, F., Zeidler, F., Scheunert, D. (1995). Injuries of the lower legs –foot, ankle joint, tibia; mechanisms, tolerance limits, injury-criteria evaluation of a recent biomechanic experiment-series. *International Research Council on the Biomechanics of Injury*, 33 - 45.

Seipel, R. C., Pintar, F. A., Yoganandan, N., Boynton, M. D. (2001), Biomechanics of Calcaneal Fractures: a model for the motor vehicle. *Clinical Orthopaedics and Related Research*, 338, 218 - 224.

Smith, B. R., Begeman, P. C., Leland, R., Meehan, R., Levine, R. S., Yang, K. H., King, A. I. (2005). A Mechanism of Injury to the Forefoot in Car Crashes. *Traffic Injury Prevention*, 6:2, 156 - 169.

Society of Automotive Engineers. (2014). Standard J211/1 Instrumentation for Impact Test - Part 1 - Electronic Instrumentation. Warrendale, PA.

Stiegelmar, R., McKee, M. D., Waddell, J. P., Schemitsch, E.H. (2001). Outcome of Foot Injuries in Multiply Injured Patients. *Foot and Ankle Trauma*, 32(1), 193 – 204.

Swiontkowskie, M. F., MacKenzie, E. J., Bosse, M. J., Jones, A. L., Travison, T. (2002). Factors Influencing the Decision to Amputate or Reconstruct after High-Energy Lower Extremity Trauma. *The Journal of Trauma Injury, Infection, and Critical Care*, 52, 641 - 9.

Tintle, S. M., Forsberg, J. A., Keeling, J. J., Shawen, S. B., Potter, B. K. (2010). Lower Extremity Combat-Related Amputations. *Journal of Surgical Orthopaedic Advances*, 19(1), 35-43.

Tintle, S. M., Keeling, J., et al. (2010). Combat Foot and Ankle Trauma. *Journal of Surgical Orthopaedic Advances*, 19(1), 70 – 76.

VanDenBogart A. J., Read L., Nigg, B. M. (1999). An analysis of hip joint loading during walking running, and skiing. *Medicine & Science in Sports and exercise*, 31, 131-142.

Vasquez, K. B., Brozoski, F. T., Logsdon, K. P., Chancey, V. C. (2018). Retrospective Analysis of Injuries in Underbody Blast Events: 2007–2010. *Military Medicine*, 183, 3/4, 347 – 352.

Weber, B.G. (1972). *Die verletzungen des oberen sprunggelenkes: second edition*. Bern, Switzerland: Huber.

Welsh, R., Lenard, J. (2001). Male and Female Car Drivers - Difference in Collision and Injury Risks. *Proceedings of the 45th Annual AAAM Conference*, 24-26.

Ye X., Poplin G., Bose D., Forbes, A., Hurwitz, S., Shaw, G., Crandall, J. (2015). Analysis of Crash Parameters and Driver Characteristics Associated with Lower Limb Injury. *Accident Analysis and Prevention*, 83, 37 – 46.

Yoganandan N., Chirvi S., Pintar F. A., Uppal H., Schlick M., Banerjee A., Voo L., Merkle A., Kleinberger M. (2016). Foot-Ankle Fractures and Injury Probability Curves from Post-mortem Human Surrogate Tests. *Annals of Biomedical Engineering*, 44, 2937 - 2947.

Yoganandan, N., Chirvi, S., Voo, L., DeVogel, N., Pintar, F. A., Banerjee, A. (2017). Foot-ankle complex injury risk curves using calcaneus bone mineral density data. *Journal of the Mechanical Behavior of Biomedical Materials*, 72, 246 – 251.

Yoganandan, N., Pintar, F. A., Boyton M., Begeman, P., Prasad, P., Kuppa, S. M., Morgan, R. M. Eppinger, R. H. (1996). Dynamic Axial Tolerance of the Human Foot-Ankle Complex. *Society of Automotive Engineers*, 207 – 218.

Yoganandan N., Pintar, F. A., Gennarelli, T. A., Seipel, R. C., Marks, R. M. (1999). Biomechanical Tolerance of Calcaneal Fractures. *43rd Annual AAAM Conference*, Association for the Advancement of Automotive Medicine, Barcelona, Spain, 345 - 356

Yoganandan N., Pintar F. A., Schlick M., Humm J. R., Voo L., Merkle A., Kleinberger M. (2015). Vertical accelerator device to apply loads simulating blast environments in the military to human surrogates. *Journal of Biomechanics*, 48, 3534 - 3538.